Physik-Department

Measurement of the production cross section of heavy quark jets in association with a W boson with the ATLAS detector at the LHC

Dissertation
von
Marco Vanadia

München
Juni 2013

TECHNISCHE
UNIVERSITÄT
MÜNCHEN

Max-Planck-Institut für Physik
(Werner-Heisenberg-Institut)

TECHNISCHE UNIVERSITÄT MÜNCHEN

Max-Planck-Institut für Physik
(Werner-Heisenberg-Institut)

Lehrstuhl für Experimentalphysik

Measurement of the production cross section of heavy quark jets in association with a W boson with the ATLAS detector at the LHC

Marco Vanadia

Vollständiger Abdruck der von der Fakultät für Physik der Technischen Universität München zur Erlangung des akademischen Grades eines

Doktors der Naturwissenschaften (Dr. rer. nat.)

genehmigten Dissertation.

Vorsitzender: Univ-Prof. Dr. M. Beneke
Prüfer der Dissertation:
1. Priv.-Doz. Dr. H. Kroha
2. Univ-Prof. Dr. L. Oberauer

Die Dissertation wurde am 05.06.2013 bei der Technischen Universität München eingereicht und durch die Fakultät für Physik am 12.06.2013 angenommen.

Abstract

In this thesis the production of a W boson in association with heavy-quark jets has been studied in proton-proton collisions at a centre-of-mass energy of 7 TeV with the ATLAS detector at the Large Hadron Collider (LHC).

For the identification of the W bosons and of the heavy quarks their semileptonic decays have been used. For this purpose, detailed studies of the muon reconstruction efficiencies of the ATLAS detector have been performed.

The associated production of a W boson with bottom quark jets represents an important background for searches for the Higgs boson and beyond Standard Model physics. It is therefore important to verify experimentally the Standard Model predictions for this process in the new energy regime of the LHC. The cross sections for W boson production together with a b-jet and zero or one additional jet have been measured for the first time at LHC energies and were found to be consistent with next-to-leading order QCD predictions.

The W boson production in association with a charm quark jet is of particular interest because of the sensitivity to the strange quark content of the proton which is still rather poorly constrained by experiments. The cross section measurements for this process in this thesis are an important input for the determination of the strange quark parton density function in the energy regime of the LHC.

Contents

Nothing is insoluble. Nothing is hopeless.
Not while there's life.
(Alan Moore, Watchmen)

Introduction

The Large Hadron Collider (LHC) at CERN is currently the largest particle accelerator in the world. Located near Geneva, in a 27.5 km long underground tunnel, after nearly two decades of planning and construction it started colliding protons steadily at a centre-of-mass energy of $\sqrt{\text{s}}$=7 TeV since March 2010, an energy never reached before at particle colliders. In 2012 the centre-of-mass energy was raised to $\sqrt{\text{s}}$=8 TeV. In early 2013 the LHC went into shutdown for upgrades to increase beam energy and instantaneous luminosity. The LHC is the culmination of the physics experiments which tested and confirmed the Standard Model of particle physics in this and the last century shaping our knowledge of the most fundamental constituents of matters in the Universe.

The Standard Model is a theory of the electroweak and strong interactions between elementary particles which has been developed to its present form in the 1960s and 70s, with quarks and leptons as fundamental constituents of matter and local gauge boson fields as mediator of the interactions. The Standard Model successfully describes the experimental results obtained up to now and foreshadowed the existence of new phenomena and particles which were observed in the years following its formulation, as the the neutral weak current discovered with the Gargamelle bubble chamber at the CERN Proton Synchrotron and the W and Z bosons discovered by the UA1 and UA2 experiments at the CERN Super Proton Synchrotron. Many other experimental results in the last decades strengthened the Standard Model description and shaped our current knowledge of the fundamental constituents of matter with the discovery of new elementary particles: the charm quark (at the Stanford Linear Accelerator Center and at the Brookhaven National Laboratory), the bottom quark (by the E288 experiment at Fermilab), the τ lepton (at the Stanford Linear Accelerator Center), the gluons (at DESY laboratories), the top quark (by the CDF and D0 experiments at the proton-antiproton collider Tevatron at Fermilab) and the τ neutrino (by the DONUT experiment at the Tevatron).

The measurements performed by the experiments at the Tevatron and at the CERN Large Electron Positron (LEP) collider provided tests of the Standard Model with unprecedented precision. The last missing piece of the Standard Model was one of its cornerstones: the spinless Higgs boson which is related to the mechanism providing masses to the elementary particles without violating local gauge invariance. The search for this particle lasted for decades as the Standard Model makes no precise prediction for its mass.

Finally, on July 4th 2012, the ATLAS and the CMS experiments at the LHC announced the discovery of a new particle with a mass of about 125 GeV/c^2 and the characteristics of the Higgs boson.

The experiments at the LHC test also other predictions of the Standard Model with high precision and at the highest energies reached by accelerators so far.
ATLAS is a general-purpose detector designed to study proton-proton interactions at the LHC with a very wide research program including Higgs boson searches, precision measurements of the strong and electroweak interactions, top quark physics, flavour physics, and searches for new physics beyond the Standard Model. In this thesis the cross sections for the production of a W boson in association with heavy charm and bottom quark jets predicted by the Standard Model has been measured with data collected by the ATLAS experiment in 2010 and 2011. These measurements probe the perturbative calculations and Monte Carlo descriptions of such processes, which are particularly relevant because these productions represent important background for many Standard Model and beyond Standard Model studies. Furthermore, the study of charm jets produced together with W bosons provide important information on the strange quark content of the proton which is currently known with high uncertainties.

In Chapter 1 a brief introduction to the Standard Model is given. Chapter 2 gives an overview of the phenomenology of weak boson production at the LHC with particular focus on $W+$ jets production. In Chapter 3 the LHC and the ATLAS detector are described, while in Chapter 4 an overview of the algorithms used for the evaluation of the trajectories and the energies of particles, hadron jets and other observables is given. Chapter 5 presents a detailed study of the performance of the ATLAS muon spectrometer and of the muon identification in data, which are important for the measurements presented in this thesis and for many other measurements by the ATLAS experiment involving muons. Chapter 6 describes the cross section measurement for the associated production of a W boson together with at least one bottom quark jet using data collected in 2010 [1]. In Chapter 7 the cross section measurement using data collected in 2011 for the production of a W boson in association with a charm quark jet is explained [2]. Both cross section measurements have been produced by small analysis teams and are described in the respective chapters with particular focus on the major contribution of this work.

Conventions

Throughout the thesis, the International System of Units [3, 4] is used. The speed of light, however, is fixed to $c = 1$. Thus, masses, momenta and energies are expressed in the same units, namely the eV = $1.602176565(35) \cdot 10^{-19}$ J. Charges are expressed in units of the electron charge.

Chapter 1

The Standard Model of Strong and Electroweak Interactions

The *Standard Model* [5, 6, 7, 8] is our present best theory of the fundamental interactions intercurring between elementary particles. It is extremely successful in describing the experimental results of particle physics with high precision. Three of the four known interactions are described by the Standard Model (see Table 1.1):

- the *strong interaction* responsible for the binding of quarks in hadrons and of the nucleons in nuclei,
- the *weak interaction* responsible for instance for the radioactive β^- decays,
- and the *electromagnetic interaction*, responsible for the interactions between charged particles.

The Standard Model is a relativistic quantum field theory invariant under the local gauge transformation group

$$SU(3)_C \otimes SU(2)_L \otimes U(1)_Y \tag{1.1}$$

with the $SU(3)_C$ symmetry group of the strong interaction and the $SU(2)_L \otimes U(1)_Y$ group describing the electroweak interactions. The Standard Model comprises 12 elementary fermions, the gauge bosons of the $SU(3)_C \otimes SU(2)_L \otimes U(1)_Y$ interactions between the fermions and the Higgs boson responsible for the $SU(2)_L \otimes U(1)_Y$ symmetry breaking which provides mass terms for the weak gauge bosons. These components are summarized in Table 1.2. All particles have a corresponding anti-particle with opposite charge and the same mass as a consequence of CPT invariance [9, 10, 11, 12].

The Standard Model particles are described by the following quantum fields:

- Spinor fields Ψ for the fermions.

- Vector gauge fields G^a, B, W^i for the gluons and the electroweak bosons.
- The Scalar Higgs boson field Φ.

The brief review of the Standard Model presented in this chapter is based on [13, 14, 15].

Table 1.1: Fundamental interactions

Interaction	Range [m]	Mediators	Relative strength
Strong	10^{-15}	gluons	1
Weak	10^{-18}	$W^{\pm}$ and Z^0 bosons	10^{-13}
Electromagnetic	∞	photon	10^{-2}
Gravitational	∞	graviton (not discovered yet)	10^{-38}

Table 1.2: Elementary particles in the Standard Model

	Fermions (spin 1/2)			Bosons (spin 1)	Boson (spin 0)
Quarks	u	c	b	$W^{\pm}$	Higgs boson
	d	s	t	Z^0	
Leptons	ν_e	ν_μ	ν_τ	γ^0	
	e	μ	τ	gluons	

1.1 Electroweak interactions

In the Standard Model, the electroweak interaction is described by the symmetry group

$$SU(2)_L \otimes U(1)_Y \ . \tag{1.2}$$

As introduced first by Glashow in 1961 [5], three conserved weak currents are related to the generators of the *weak isospin* group $SU(2)_L$ and one to the *weak hypercharge* group $U(1)_Y$. The observed charged weak currents can be identified as a combination of two $SU(2)_L$ currents, while the neutral weak and the electromagnetic currents are derived from a mixing of the $SU(2)$ and $U(1)$ currents.

The weak hypercharge Y is related to the electric charge Q and the third component of the weak isospin I by:

$$Y = 2(Q - I_3) \ . \tag{1.3}$$

The elementary fermions included in the Standard Model are arranged in weak isospin multiplets (see Table 1.3). The weak gauge bosons fields generated by the $SU(2)_L$ symmetry group couple only with left-handed fermions, which are included in isospin doublets. Right-handed leptons and quarks represent isospin singlets. Right-handed neutrinos would be non-interacting particles and are therefore not included in the Standard Model.

Table 1.3: Quantum numbers of the elementary fermions in the Standard Model. The subscript L indicates left-handed particles, the subscript R indicates right-handed particles.

	Fermions			I	I_3	Y	Q
quarks	$\begin{pmatrix}u\\d\end{pmatrix}_L$	$\begin{pmatrix}c\\s\end{pmatrix}_L$	$\begin{pmatrix}t\\b\end{pmatrix}_L$	1/2	1/2	1/3	2/3
				1/2	-1/2	1/3	-1/3
	u_R	c_R	t_R	0	0	4/3	2/3
	d_R	s_R	b_R	0	0	-2/3	-1/3
leptons	$\begin{pmatrix}\nu_e\\e^-\end{pmatrix}_L$	$\begin{pmatrix}\nu_\mu\\\mu^-\end{pmatrix}_L$	$\begin{pmatrix}\nu_\tau\\\tau^-\end{pmatrix}_L$	1/2	1/2	-1/2	0
				1/2	-1/2	-1/2	-1
	e^-_R	μ^-_R	τ^-_R	0	0	-2	-1

The physical electroweak bosons fields $W^{\pm}, Z^0, A$ are linear combinations of the fields corresponding to the generators of $SU(2)$ and $U(1)$, respectively the isospin triplet $\mathbf{W}_\mu$ and the hypercharge singlet B_μ.

$$W^{\pm,\mu} = \frac{1}{\sqrt{2}}(W_1^\mu \mp iW_2^\mu), \tag{1.4}$$

are the mediators of the charged weak interaction,

$$A^\mu = B^\mu cos(\theta_W) + W_3^\mu sin(\theta_W), \tag{1.5}$$

is the photon field and

$$Z^\mu = -B^\mu sin(\theta_W) + W_3^\mu cos(\theta_W) \tag{1.6}$$

the mediator of the neutral weak interaction. θ_W is the *Weinberg mixing angle* [16].

This model describes the left-handed charged weak currents and the neutral weak and electromagnetic currents interacting both with right-handed and left-handed fermions. The four gauge bosons are massless according to the local gauge symmetry of the interactions. However, the W and Z bosons have experimentally observed masses needed to explain the short range of the weak interactions. Explicit mass terms introduced into the Standard Model Lagrangian would break the gauge invariance and thus the renormalizability of the field theory.

1.2 The Higgs mechanism

The solution for this problem is provided by the Higgs mechanism [17, 18, 19, 20, 21, 22] introduced into the Standard Model by Weinberg [6] and Salam [7] at the end of the 1960s.

The Higgs mechanism employs spontaneous symmetry breaking by introducing gauge boson masses. The Goldstone theorem [23, 24] states that the spontaneous breaking of a global continuous symmetry generates massless Goldstone bosons. The Higgs mechanism involves the spontaneous symmetry breaking of a *local* gauge symmetry, the $SU(2)_L \otimes U(1)_Y$ symmetry of the electroweak interaction.

A new contribution has to be included into the Lagrangian of the Standard Model:

$$\mathcal{L} = (\mathcal{D}_\mu \phi)^\dagger (\mathcal{D}^\mu \phi) - \mu^2 \phi^\dagger \phi - \lambda (\phi^\dagger \phi)^2 \; = (\mathcal{D}_\mu \phi)^\dagger (\mathcal{D}^\mu \phi) - V(\phi) \tag{1.7}$$

with $\mathcal{D}_\mu = \partial_\mu + igI \cdot \mathbf{W}_\mu + i\frac{g'}{2} Y B_\mu$ and g, g' being constants. This term describes the propagation and interaction field of a complex scalar weak isospin doublet field with $Y = 1$. Choosing a potential $V(\phi)$ with $\mu^2 < 0$ and $\lambda > 0$ the ground state is not uniquely defined at $|\phi| = 0$, but any state fulfilling the requirement

$$\phi^\dagger \phi = \frac{-\mu^2}{2\lambda} \equiv \frac{v^2}{2} \; . \tag{1.8}$$

All ground states are connected by gauge transformations. An arbitrary ground state may be chosen, for instance $\phi_0 = \frac{1}{\sqrt{2}} \left(\begin{smallmatrix} 0 \\ v \end{smallmatrix} \right)$. The scalar Higgs field $H(x)$ is a massive excitation from this ground state,

$$\phi(x) = \frac{1}{\sqrt{2}} \left(\begin{smallmatrix} 0 \\ v + H(x) \end{smallmatrix} \right) \; , \tag{1.9}$$

corresponding to a new neutral particle with mass $m_H = \sqrt{-2\mu^2}$. Massless excitations in the form of Goldstone bosons have been eliminated by gauge transformation into longitudinal polarization states of the W and Z^0 bosons. Inserting Eq. 1.9 into the Lagrangian of Eq. 1.7 the following expression is obtained:

$$\begin{aligned} \mathcal{L} =& \frac{1}{2} (\partial_\mu H)^2 - \mu^2 H^2 + \frac{g^2 v^2}{4} W_\mu^+ W^{-\mu} + \frac{v^2 (g^2 + g'^2)}{8} Z_\mu Z^\mu \\ & + \text{boson kinetic energy terms } + \text{higher order terms} \; . \end{aligned} \tag{1.10}$$

The spontaneously generated mass terms for the $W^\pm$ and Z bosons do not violate gauge invariance and the photon remains massless. Mass terms for the fermions are also forbidden by the global $SU(2)_L$ symmetry but can be generated preserving the gauge invariance by introducing a new weak interaction between the fermions and the Higgs field.

1.3 Quantum chromodynamics

The description of the strong interaction between quarks in the Standard Model is based on the $SU(3)_C$ symmetry group, where C stands for the colour charges of the gauge theory of the strong interaction which is therefore called quantum chromodynamics (QCD). The requirement of $SU(3)_C$ local gauge invariance of the Lagrangian of the quarks is satisfied with the introduction of eight massless gauge bosons called *gluons* which mediate the strong interaction between coloured quarks. The non-Abelian structure of the symmetry group leads to self-interaction of the gluons which is responsible for the confinement of quarks and gluons in hadrons.

The difference between the photons, which are not electrically charged, and the weak and strong gauge bosons which carry the non-Abelian gauge charges is very important. Vacuum polarization causes *screening* of the electric charge depending on the momentum transferred in the interaction, while the effect is reverted in the weak and the strong interactions. The electromagnetic coupling rises with decreasing distances, while the weak and the strong coupling decrease, an effect known as *asymptotic freedom.* Quarks in their bound states behave like free particles and perturbative QCD calculations are possible for high-energy processes. At large distances the coupling of the colour interaction becomes strong and perturbative calculations are no longer possible. Furthermore, when separating quarks at large distances, quark-antiquark pairs are created from the vacuum and form bound states with the original ones, a phenomenon called *hadronization.*

1.4 Physics beyond the Standard Model

While the Standard Model successfully describes essentially all experimental observations in the laboratory it leaves many questions unanswered. First of all it contains a large number of parameters which have to be experimentally determined. Extremely precise tuning of the parameters is needed to keep the mass of the Higgs boson at the low values predicted from the electroweak precision measurements at LEP and Tevatron and from the self-consistency of the theory. The Standard Model does not include a quantum theory of gravity, does not provide a description of dark matter and dark energy and cannot explain the observed asymmetry between matter and antimatter in the Universe. Moreover the Standard Model has to be expanded to include neutrino masses for which there is experimental evidence from the observation of neutrino oscillations [25].

There are many extensions of the Standard Model addressing these and other open questions: Grand Unified Theories (GUT), supersimmetry (SUSY), string theory and many others. To find hints for such new physics beyond the Standard Model is one of the many goals of the experiments at the LHC.

Chapter 2

W and *Z* boson production at the LHC

In this chapter a short introduction to the phenomenology of proton-proton collisions will be given, with particular attention to the case of $W^{\pm}$ and Z^0 boson production. A brief overview of the Monte Carlo generators used to simulate the physics processes relevant for this thesis can be found at the end of the chapter.

2.1 Theoretical description of *pp* collisions

The composite nature of the proton is known since the 1950s [26]. According to the Standard Model protons are bound states of two up and one down quark (*valence quarks*) which exchange gluons. In addition there are quark-antiquark pairs of any flavour which are generated from emitted gluons (*sea quarks*).

In the parton model the constituents of the proton are treated as free particles. Each parton carries a fraction x of the proton momentum. The different quark flavours and the gluons have different probabilities for carrying a certain momentum fraction in interactions with a given transferred momentum Q, which are described by the *parton density functions* (PDF) $f(x, Q^2)$. Knowledge of the PDFs is essential for a correct description of proton collisions. In Fig. 2.1 an evaluation of the PDF of the proton is shown: one can see that at high x values the dominant contributions are from the valence quarks, while at low x the gluon contribution dominates and the contributions from sea quarks become more relevant. This behaviour becomes more pronounced for high values of the transferred momentum. The s quark PDF is of particular interest for this thesis (see Chapter 7). In Fig. 2.1 it can be noticed that the predicted s quark contribution is lower compared to the one of the other light sea quarks $\overline{u}$, $\overline{d}$. The three distributions can be expected to be equal in the case of unbroken flavour symmetry. The different masses of the quarks leads to a suppression of the sea quark contributions increasing with the quark mass. The s quark PDF is currently poorly constrained by experimental data.

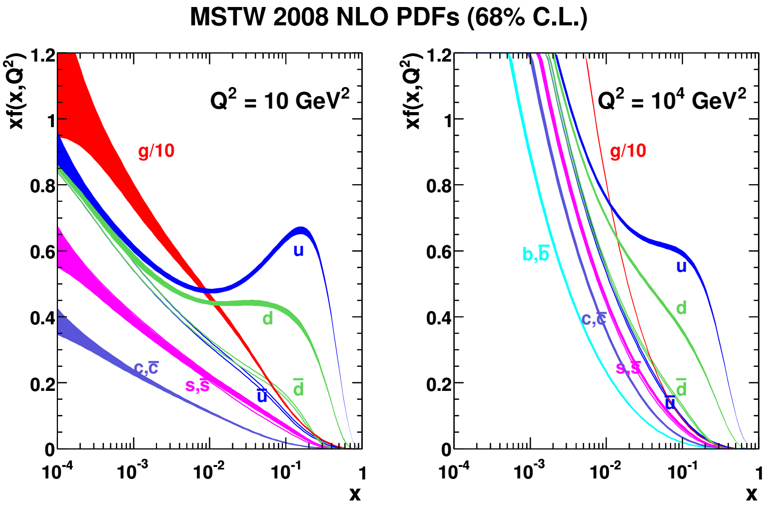

Figure 2.1: Parton distribution functions of the proton for momentum transfers squared of $Q^2 = 10$ GeV^2 and $Q^2 = 10000$ GeV^2 using the `MSTW 2008` parametrization [27].

Most physics analyses in proton-proton collisions are interested in the so-called *hard processes*, with high momentum transfer. In this case, the theoretical description is simpler, because at high energies the interaction between two constituents of the two colliding protons can be factorized and the remaining constituent particles can be considered as only *spectators* of this interaction. In Fig. 2.2 an example of a hard scattering process is given. The interacting quarks or gluons may radiate gluons or photons before the hard interaction producing initial state radiation (ISR). The same particles may be radiated by the final state particles produced in the interaction, a phenomenon known as final state radiation (FSR). The remnants of the protons may undergo soft interactions and may also radiate gluons and photons. All final state particles except the participants in the hard scattering process are called together the *underlying event.* The factorization between the hard interaction and the underlying event is an approximation. No coloured particles can be observed in the final state, due to the characteristics of the strong interaction discussed in Section 1.3, therefore coloured particles produced by the hard scattering must interact with coloured particles in the underlying event to result solely in colourless particles in the final state.

Assuming a generic interaction between two protons A and B and with a and b being the constituents of the protons participating in the hard interaction, the cross section of the overall process $A + B \to c + X$, where c is the outcome of the hard scattering and X the proton remnants, can be expressed in terms of the elementary processes $a + b \to c$ by

$$\sigma_{A+B\to c+X} = \sum_{a,b} \int_0^1 dx_a \int_0^1 dx_b [f_A^a(x_a, Q^2) f_B^b(x_b, Q^2)] \sigma_{a+b\to c} \,. \tag{2.1}$$

The sum is over all the constituents a and b contributing to the production of c. f_A^a and

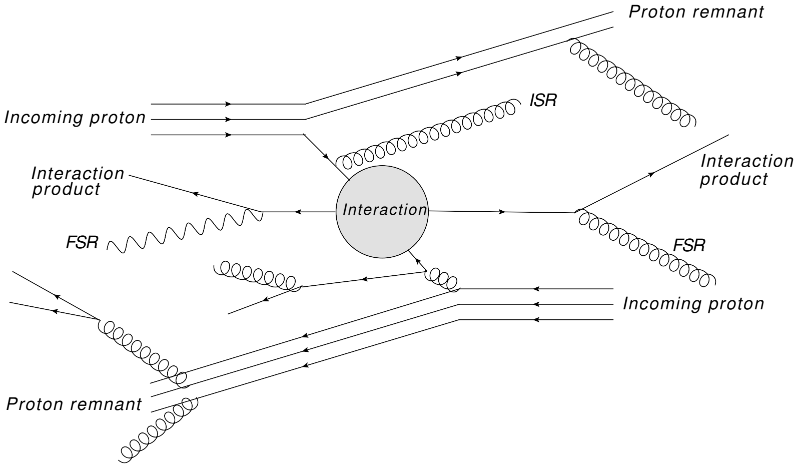

Figure 2.2: Illustration of a proton-proton collision with a hard scattering process between two constituents, a quark and a gluon, of the incoming protons. ISR stands for initial state radiation, FSR for final state radiation.

f_B^b are the PDFs of the proton constituents.

2.2 Overview of $W^{\pm}$ and Z boson production at colliders

The experimental observation of the theoretically predicted $W^{\pm}$ and Z bosons was made in 1983 by the UA1 and UA2 collaborations in proton − anti-proton collisions at the the Super Proton Synchrotron (SPS) [28, 29, 30, 31]. The precision measurements of the Z boson mass were performed by the four experiments ALEPH, DELPHI, L3 and OPAL at the LEP collider [25]. At LEP-I, the Z bosons were produced in resonance at a centre-of-mass energy near the Z boson mass. The Z decay modes are into fermion − anti-fermion pairs with branching ratios (BR) shown in Table 2.1. The leptonic decays $Z \to e^+e^-$ and $Z \to \mu^+\mu^-$ provide a very clear signature for Z bosons production.

The W boson mass measurement is less precise due to the presence of neutrinos in the leptonic decay modes which cannot be detected. The most precise measurements are from LEP-II and from the CDF and D0 experiments at the Tevatron collider [25]. The main properties and decay modes of the W boson are listed in Table 2.1.
Figures 2.3a and 2.3d show the leading order (LO) Feynman diagrams for the W/Z production at hadron colliders. It is known since the end of the '70s that LO computations are insufficient to describe these processes (see for example [32]). Currently complete next-to-next-to-leading order (NNLO) predictions are available for the inclusive production [33].

Final states with W/Z bosons associated with quarks and gluons are of particular interest. Quarks and gluons in the final states produce cascades of particles which are observed in the detectors as *jets*, i.e. as sprays of collimated particles. Figures 2.3b, 2.3c, 2.3e

Table 2.1: Properties of the Z^0 and of the $W^\pm$ bosons [25]. The W^- decays are charge conjugate to the ones of W^+.

Z^0 boson: $m_Z = 91.1876 \pm 0.0021$ GeV; $\Gamma_Z = 2.4952 \pm 0.0023$ GeV	
Decay mode	Branching ratio (%)
e^+e^-	3.363 ± 0.004
$\mu^+\mu^-$	3.366 ± 0.007
$\tau^+\tau^-$	3.370 ± 0.008
invisible	20.00 ± 0.06
hadrons	69.91 ± 0.06
$W^\pm$ boson: $m_W = 80.385 \pm 0.015$ GeV; $\Gamma_W = 2.085 \pm 0.042$ GeV	
Decay mode	Branching ratio (%)
$e^+\nu$	10.75 ± 0.13
$\mu^+\nu$	10.57 ± 0.15
$\tau^+\nu$	11.25 ± 0.20
hadrons	67.70 ± 0.27

and 2.3f show the Feynman diagrams for the W/Z production in association with one or two final state quarks. Jets can also be originated by initial or final state radiation gluons in any of the diagrams of Figure 2.3. Next-to-leading order (NLO) perturbative QCD predictions for W+jets and Z+jets production have been developed in the last years, and experimental results are needed both to confirm these predictions and to provide input for further developments. These final states represent major backgrounds for many Standard Model and beyond Standard Model processes. An experimental determination of their cross sections and properties is crucial for a correct background estimation. These events provide also an insight on the proton content. Cross section measurements both of inclusive W/Z production and of specific W/Z+jets processes (for example $W + c$ production which is the topic of Chapter 7) provide constraints on the proton PDFs. The strange quark PDF is of particular interest due to a tension between recent experimental results and the predictions [34].

The experimental results produced by the ATLAS and CMS collaborations at the LHC on W+ jets [35, 36] and Z+ jets [36, 37, 38, 39] production are in general in good agreement with the predictions and show that LO multiparton event generators, normalised to NNLO cross section for the W inclusive production, describe the experimental data for all measured inclusive jet multiplicities within the estimated experimental and theoretical uncertainties. For W+ jets production NLO calculations from MCFM [40], studied for events with at least two jets, and from Blackhat-Sherpa [41, 42], studied for events with at least four jets, were found to be mostly in agreement with the data [35].

Events with a vector boson produced in association with heavy-flavour quark jets, i.e. bottom quark jets (b-jets) or charm quark jets (c-jets), represent a challenge for the experiments due to their cross section, which is much smaller than the one of W/Z+light-jets (jets originated by u, d, s quarks or by gluons) production. In this thesis, in Chapters 6 and 7 cross section measurements for the production of a W boson in association respectively with b-jets and with one c-jet performed by the ATLAS collaboration are documented.

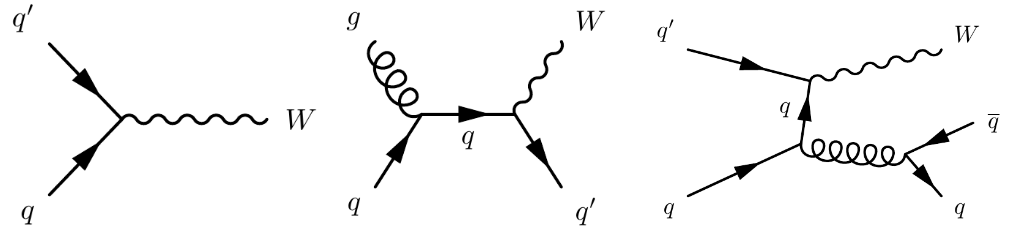

(a) W production **(b)** W+q production **(c)** W+$q\overline{q}$ production

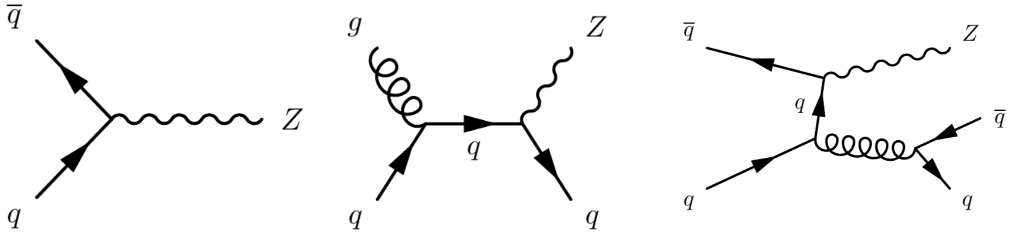

(d) Z production **(e)** Z+q production **(f)** Z+$q\overline{q}$ production

Figure 2.3: Some of the lowest order Feynman diagrams for the W(+jets) and Z(+jets) production in hadron collisions.

2.3 Monte Carlo generators

Monte Carlo simulations are of fundamental importance for most physics analyses as they provide the interface between theoretical expectations and experimental results. Simulations are used to estimate the backgrounds and to predict the signal strength as well as the event topologies, allowing for the optimisation of the signal selection criteria.

The generation of Monte Carlo events for a given process includes several steps: the simulation of the hard scattering process according to calculated *matrix elements* (ME), the propagation of the scattered partons into so-called *parton showers* (PS) under the strong interaction, the formation of hadrons from the partons (*hadronization*) and finally their decays into the final state particles. The emission of photons from particles in the initial or final state is also simulated. For proton collisions the simulation of the underlying event is additionally required. For most fundamental processes different Monte Carlo generators can be used for different applications. The following generators have been used in this thesis:

Pythia [43, 44]: a general-purpose leading order (LO) generator for particle colliders.

Herwig [45] and Herwig++ [46]: a general-purpose LO generator, complementary to Pythia. The main differences between these two generators are in the description of the parton showering (PS) and fragmentation. Herwig++ is an improved version entirely written in the C++ programming language.

Alpgen [47]: a LO generator for Standard Model (SM) multi-parton processes at hadron colliders. It has to be interfaced with another program for PS and hadronization.

Sherpa [42]: a multi-parton LO generator which describes also the showering and the hadronization of the partons.

Blackhat [41]: generator specialised in next-to-leading order (NLO) calculations for $W+$ jets and $Z+$ jets events; it can be interfaced with Sherpa.

Powheg [48]: a NLO generator of SM processes which needs to be interfaced with another program for PS and for hadronization.

MC@NLO [49]: a NLO SM generator interfaced with Herwig/Herwig++ for the parton showering.

aMC@NLO [50]: an automated calculator for production processes at NLO which is interfaced with another program for PS and for hadronization.

AcerMC [51]: a generator of Standard Model background processes for *top* quark physics at the LHC.

EvtGen [52]: a generator dedicated to b-hadron physics.

Jimmy [53]: a Herwig based generator used for the simulation of the underlying event.

MCFM [40]: a parton-level generator used for the evaluation of NLO cross sections at hadron colliders.

A description of the simulation of the detector response to the generated particles will be presented in Section 4.1.

Chapter 3

The ATLAS experiment at the Large Hadron Collider

The Large Hadron Collider (LHC) is a circular collider situated at CERN near Geneva in Switzerland [54]. Installed in the 26.7 km long tunnel previously occupied by the LEP collider [55], it is currently the world's largest particle accelerator and the one with highest centre-of-mass energy. The physics program at the LHC started end of 2009. In the first two years it was operated at $\sqrt{\mathrm{s}} = 7$ TeV. The energy was raised to $\sqrt{\mathrm{s}} = 8$ TeV in 2012. The LHC will be described in more detail in Section 3.1, followed by a description of the ATLAS experiment.

3.1 The Large Hadron Collider

The LHC is last in a chain of accelerators shown in Fig. 3.1. In this thesis the focus will be on proton-proton collisions, but the LHC is used as a lead-ion collider too. The use of hadrons in the collisions allows for high centre-of-mass energy, which by design can reach up to $\sqrt{\mathrm{s}} = 14$ TeV at the LHC. This is much higher than the energy reachable with a circular electron collider of the same size which is limited by synchrotron radiation. The composite nature of the protons is on the other hand challenging for the particle detectors at the LHC, as will be discussed in Section 3.2. The LHC has two independent vacuum pipes for the acceleration of the two particle beams crossing in four interaction points.
The LHC consists of 1232 super-conducting dipole magnets operating at 1.9 K with which magnetic fields up to 8.33 T strength can be achieved, necessary to keep the 7 TeV proton beams on their orbits. The design parameters of the LHC machine are presented in Table 3.1, as well as the records reached by the LHC for those parameters in 2012 [56].

Fig. 3.1 shows the four interaction points where the main experiments are located.
ATLAS [57] and CMS [58] are general-purpose detectors designed to study Standard Model and beyond Standard Model physics processes at the highest energies achieved so far with the main focus on the Higgs boson search. LHCb [59] and ALICE [60] are detectors with

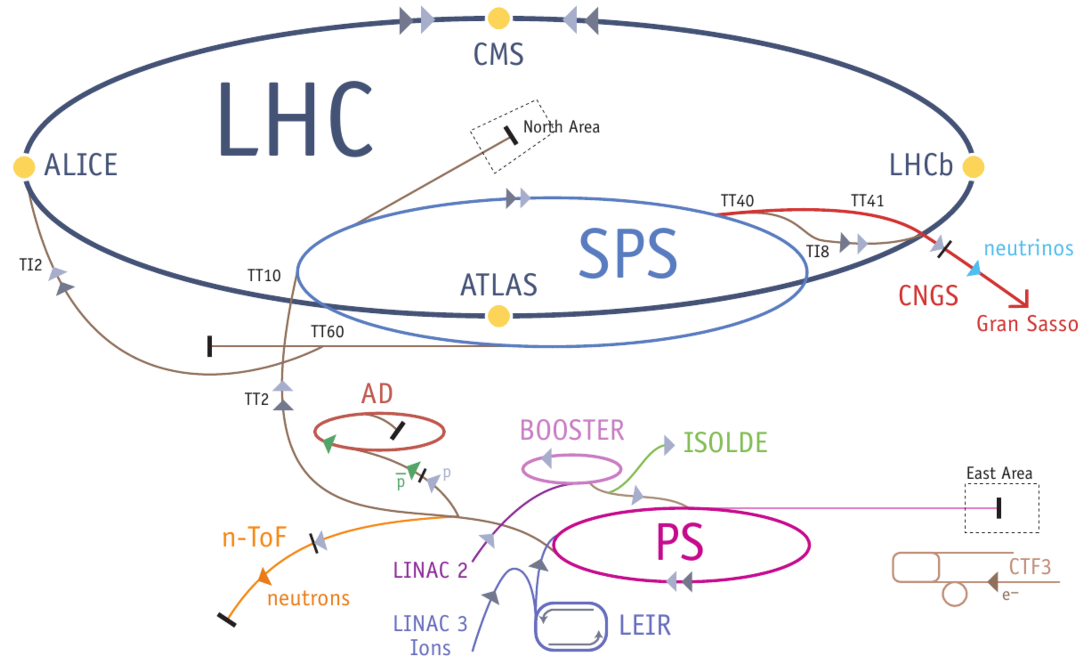

Figure 3.1: The CERN accelerator complex.

specialized physics programs: LHCb is designed to study the b-hadron physics while ALICE studies the collisions of lead-ions.

Given a generic particle interaction physics process at a collider, the corresponding event rate in the experiments can be determined from the equation

$$\frac{dN}{dt} = \mathcal{L}\sigma(\sqrt{s}) \ , \tag{3.1}$$

where $\mathcal{L}$ is the instantaneous luminosity and $\sigma(\sqrt{s})$ is the cross section of the process at the centre-of-mass energy $\sqrt{s}$. In order to study challenging rare channels, the instantaneous luminosity $\mathcal{L}$ of the collider must be as high as possible. The luminosity depends on

Table 3.1: Design parameters of the LHC [54] and achievements reached during 2012 as measured at the ATLAS interaction point [56]

Parameter	Design	Best achievement
Proton energy	7000 GeV	4000 GeV
Number of particles per bunch	$1.15 \cdot 10^{11}$	$1.66 \cdot 10^{11}$
Number of circulating bunches	2808	1380
Bunch crossing frequency	40 MHz	40 MHz
Bunch crossing time	25 ns	25 ns
Instantaneous Luminosity	10^{34} cm^{-2}s^{-1}	$0.773 \cdot 10^{34}$ cm^{-2}s^{-1}

machine parameters. It can be expressed by the equation:

$$\mathcal{L} = \frac{fnN_1N_2}{A} \ , \tag{3.2}$$

where f is the revolution frequency of the proton bunches in the collider, n the number of simultaneously circulating bunches, N_1 and N_2 the number of particles in each bunch and A is the cross section area of the colliding beams. The high number of bunches circulating in the LHC (see Table 3.1), resulting in a high frequency of bunch crossing, is meant for maximizing the luminosity.

3.2 The ATLAS detector

ATLAS [57] is one of the two main detectors at the LHC designed to study a wide range of particle physics processes at high energies. In this section the detector and its components are presented with emphasis on the performance goals that led its design. The detector is shown in Fig. 3.2.

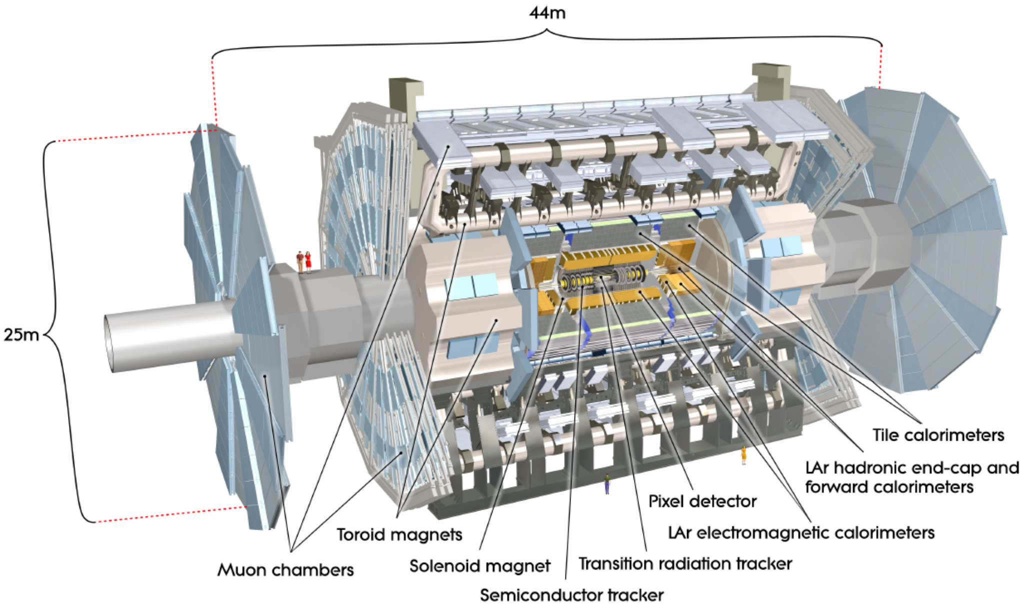

Figure 3.2: The ATLAS detector.

The characteristics of the LHC impose challenges to the experiments:

- The high luminosity of the LHC leads to very high irradiation of the detector which must have very high radiation resistance to guarantee the design performance over several years of operation.

- The high density of protons per bunch at the LHC leads to an high number of soft collisions happening in the same bunch crossing together with the hard process, the so-called "pile-up". Detectors operating at the LHC must be able to identify and reconstructs particles and jets produced in hard scatterings which take place together with several tens of such soft collisions.
- The high interaction rate and particle density produced in the collisions require fast and highly granulated detectors.

The physics goals of the ATLAS experiment lead to additional requirements on the detector:

- Precise reconstruction of the primary vertex of the hard interaction even at the high pile-up conditions.
- A highly selective trigger system ensuring sufficient reduction of the data volume with still high efficiency for the interesting processes.
- Efficient particle reconstruction and identification and a precise measurement of particle energies and of momenta.
- Large solid angle coverage which is especially important for the reconstruction of processes involving neutrinos and other new weakly interacting particles which can only be observed by measuring the energy imbalance in the events.
- Good energy resolution for electromagnetic showers in the calorimeters.

ATLAS consists of the following main elements:

- The Magnet System, providing the magnetic field needed for the momentum measurement of particle tracks is introduced in Section 3.2.2.
- The Inner Detector, a tracking system operating in a solenoidal magnetic field, is explained in Section 3.2.3.
- The Calorimeter System used for the energy measurement of electromagnetically (electrons and photons) and strongly interacting particles is described in Section 3.2.4.
- The Muon Spectrometer, operating in a toroidal magnetic field and designed to identify muons and to measure their momentum is described in detail in Section 3.2.5 as this thesis is particularly concerned with the performance of the muon reconstruction in ATLAS.
- The ATLAS Trigger System is described in Section 3.2.6.
- The Luminosity Monitoring System providing the measurement of the luminosity registered by ATLAS which is a key input for many physics analyses (see Section 3.2.7).

3.2.1 Notation and conventions

The coordinate system of ATLAS is defined in the following way (see [57]):

- The origin is at the nominal interaction point.
- The xy plane is transverse to the proton beams direction with:
  - the y axis pointing upwards and
  - the x axis pointing towards the centre of the LHC ring.
- The z axis is oriented along the beam direction forming a right-handed coordinate system.

Other important variables are defined in the following way:

- θ is the azimuthal angle measured from the z axis.
- Pseudorapidity is defined as $\eta = -ln(tan(\frac{\theta}{2}))$.
- ϕ is the polar angle in the xy plane.
- Transverse momentum p_T and transverse energy E_T are defined in the xy plane, perpendicular to the beam axis.
- Angular distance is measured by $\Delta R = \sqrt{\Delta\eta^2 + \Delta\phi^2}$.

Tracks are described by five parameters: $cot(\theta)$, ϕ, $1/p_T$, d_0 and z_0. d_0 is the transverse impact parameter, the distance of closest approach from the beam axis in the xy plane. z_0 is the longitudinal impact parameter, i.e. the z coordinate of the track at the point of closest approach to the interaction point. The detector hemispheres for $z > 0$ and $z < 0$ are defined as side A and side C, respectively.

3.2.2 The Magnet System

The ATLAS Magnet System [57] (see Fig. 3.2) consists of four superconducting magnets:

- A central solenoid with a length of 5.3 m and a diameter of 2.6 m provides a 2 T magnetic field for the momentum measurement of charged particles tracks in the Inner Detector.
- A toroidal air-core magnet system provides a bending power of $\int Bdl$ =2-8 Tm for the muon spectrometer. It consists of a barrel and two endcaps magnets.

The barrel toroid consists of eight loops surrounding the calorimeters, with a length of 26 m and inner and outer diameters of 9.4 m and 20.1 m respectively. It covers the region $0 \leq |\eta| \leq 1.3$ and provides a maximum field of 3.9 T. The endcap toroids are inserted into the central one at the ends with a length of 5 m each, an outer diameter of 10.7 m and an inner diameter of 1.7 m. They cover the regions $1.6 \leq |\eta| \leq 2.7$ and provide a maximum field of 4.1 T.

The bending power of the toroid system is reduced in the transition region between the barrel and the endcaps, for $1.3 < |\eta| < 1.6$.

3.2.3 The Inner Detector

The Inner Detector (ID) [57], shown in Fig. 3.3, is a tracking system for charged particles in a solenoidal magnetic field. It consists of three sub-detectors:

- the Pixel Detector,
- the Semiconductor Tracker (SCT) and
- the Transition Radiation Tracker (TRT).

The ID is 7 m long, has a diameter of 2.3 m, and covers the region $0 \leq |\eta| \leq 2.5$. It has a very high granularity, especially close to the interaction region where precise secondary vertex reconstruction is needed for the identification of b-hadrons.

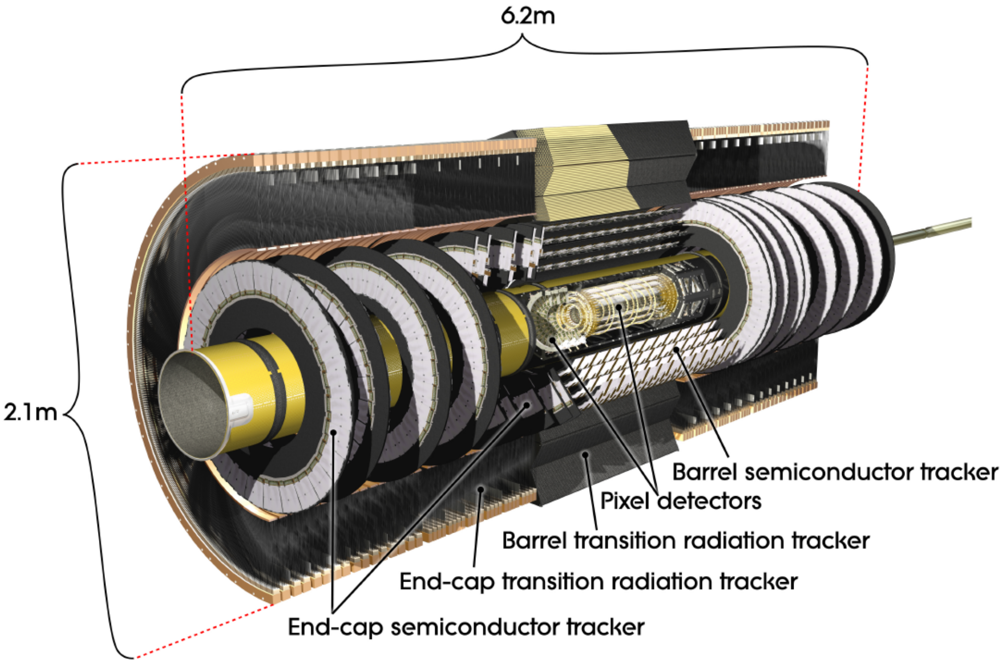

Figure 3.3: The Inner Detector.

3.2.3.1 The Pixel Detector

The Pixel detector consists of silicon pixel sensors and provides three precision position measurements along the track over the acceptance of $0 \leq |\eta| \leq 2.5$. The barrel region of the detector consists of three detector layers at radii of 5 cm, 9 cm, 12 cm from the beam axis. The endcap regions consists of five disks each. The innermost layer (the *B-layer*) is most important for the decay vertex reconstruction and is also most affected by background radiation. The mechanical design of the detector allows for a substitution of the B-layer during the 2013-14 LHC shutdown period.

The Pixel Detector provides position measurements with excellent intrinsic resolution of 10 μm in the $R\phi$ and of 115 μm in the Rz plane [61].

3.2.3.2 The Semiconductor Tracker

The Semiconductor Tracker (SCT) consists of four double layers of silicon strip detectors in the barrel and nine disk layers in the endcaps. In the barrel region the strips are oriented parallel to the beam direction while in the endcaps they are oriented radially. The detectors provide position measurements with an intrinsic resolution of 17 μm in the $R\phi$ plane and of 580 μm in the z direction in the barrel and in the radial direction for the endcaps [61], covering the region $0 \leq |\eta| \leq 2.5$.

3.2.3.3 The Transition Radiation Tracker

The Transition Radiation Tracker (TRT) consists of a large number of straw drift tubes with a diameter of 4 mm assembled in 36 layers to provide on average 30 measurements per track in the region $|\eta| \leq 2.5$. The straw tubes operate with a Xe (70%) CO_2(20%) CF_4 (10%) gas mixture. The detector measures tracks in the $R\phi$ plane with a single tube intrinsic resolution of 130 μm [61].

The TRT is also used for electron identification, especially at energies below 25 GeV. The use of a xenon gas mixture makes it possible to detect transition-radiation photons which are created in radiation sheets located between the straw tubes. The pion rejection factor varies between 20 and 100 depending on η [61].

3.2.4 The Calorimeter System

The Calorimeter System [57] provides energy and position measurements for electrons, photons and hadron jets. Furthermore it is essential for the reconstruction of hadronically decaying τ leptons and for the measurement of the missing energy via energy imbalance in the events, needed for the reconstruction of events with neutrinos or other weakly interacting particles (see Section 4.6).

The Calorimeter System consists of an Electromagnetic (EM) Calorimeter covering the region $|\eta| \leq 3.2$ and of an Hadronic Calorimeter (HCAL) covering $|\eta| \leq 4.9$.

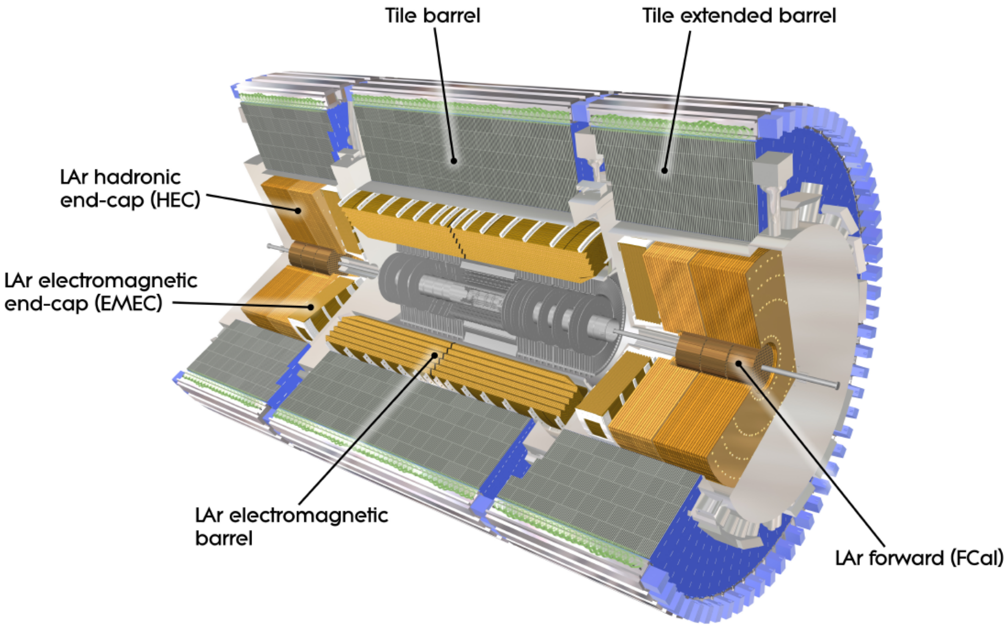

Figure 3.4: The ATLAS Calorimeter System.

3.2.4.1 The Electromagnetic Calorimeter

The EM Calorimeter consists of a barrel part in the region $|\eta| \leq 1.475$ and two endcaps for $1.375 \leq |\eta| \leq 3.2$. It is a sampling calorimeter with Liquid Argon (LAr) as active medium in between accordion-shaped lead absorber plates. The region $|\eta| \leq 2.5$ is used for precision measurements and is segmented into three longitudinal regions:

- A pre-shower layer, with a thickness of about 6 radiation lengths (X_0) and readout strips covering relative η angles between 0.003 and 0.25, depending on η itself, in order to provide a high granularity in η. The size of the segmentation of this layer is 0.1 in ϕ.

- A middle section, with a thickness of about $16X_0$ and a readout segmented into squares of $\Delta\eta \times \Delta\phi = 0.025 \times 0.025$.

- An outer layer, with an η depending thickness of 2-$12X_0$ and a readout granularity of $\Delta\eta \times \Delta\phi = 0.050 \times 0.025$.

In addition in the region $|\eta| < 1.8$ a pre-sampling layer with a $\Delta\eta \times \Delta\phi = 0.025 \times 0.1$ segmentation is used to estimate the energy loss of electrons and photons before the calorimeters. In the region $2.5 < |\eta| \leq 3.2$ where electron and photon reconstruction is not required, only two longitudinal samplings and a coarser granularity are sufficient to fulfil the required performance for jet energy and for energy imbalance measurements. In the region $3.1 \leq |\eta| \leq 4.9$, the Forward Calorimeter (FCAL), which is also using LAr as active medium, provides both electromagnetic and hadronic shower measurements.

3.2.4.2 The Hadron Calorimeter

The Hadronic Calorimeter (HCAL) is a sampling calorimeter surrounding the EM Calorimeter and covering $|\eta| \leq 4.9$. It is divided into the following regions:

- The barrel HCAL for $|\eta| \leq 1.7$.
- Two endcap HCALs for $1.5 \leq |\eta| \leq 3.2$.
- The Forward Calorimeter (FCAL) covers the region $3.1 \leq |\eta| \leq 4.9$.

The barrel HCAL uses iron as absorber and scintillating tiles as active material. The scintillation light is carried to photomultipliers by wave-length shifter (WLS) fibres. In the most part of the calorimeter the granularity is $\Delta\eta \times \Delta\phi = 0.10 \times 0.10$.

The two endcap HCALs use LAr as active material and copper plates as absorber. They are divided into two wheels, the first one with 25 mm thick copper plates and the second one with 50 mm thick plates. The 8 mm wide gap between consecutive plates is equipped with three parallel electrodes, where the central one is the readout layer and the others carry the high voltage.

The FCAL works in a very high radiation environment which represents a challenge for the detector design. It uses LAr as active medium and copper and tungsten as absorber materials. The calorimeter consists of a metal matrix with longitudinal channels in which metal rods are inserted.

An important characteristics of the HCAL is its hermeticity. Its thickness is greater than 10 hadronic interaction lengths λ over the whole acceptance ensuring a good resolution for the jet energy and for the momentum imbalance measurements and low hadron punch-through into the muon system.

3.2.5 The Muon Spectrometer

The ATLAS Muon Spectrometer (MS) [57] is designed for the reconstruction of muons and the measurement of their momentum either as a stand-alone system or in combination with the Inner Detector. Due to the importance of muons for the analyses in this thesis, the MS design is discussed in detail below.

The Muon Spectrometer shown in Fig. 3.5 covers the region $|\eta| \leq 2.7$ with a small gap at $|\eta| = 0$ used for cables and services belonging to the Inner Detector and to the Calorimeter systems. The following regions of the spectrometer can be distinguished:

- The barrel region covering $|\eta| \leq 1.05$ with the central region at $|\eta| < 0.1$.
- The endcap regions covering $1.05 < |\eta| \leq 2.7$ with the transition regions between barrel and endcaps at $1.05 < |\eta| < 1.3$ and the forward regions at $|\eta| > 2.0$.

The MS operates in the magnetic field of the toroid magnets described in Section 3.2.2. The field bending plane is the $R\eta$ plane.

The MS uses four different types of muon chambers for muon reconstruction:

- Monitored Drift Tube (MDT) chambers provide position measurement in the bending plane over most of the MS acceptance region.
- Cathode Strip Chambers (CSC) provide position measurement both in the bending and in the non-bending plane in the innermost detector layer of the forward regions.
- Resistive Plate Chambers (RPC) are used for trigger information and for non-bending plane position measurement in the barrel region.
- Thin Gap Chambers (TGC) are used for trigger information and non-bending plane position measurement in the endcap regions.

In the following the position in the bending plane will be referred to as the precision coordinate and the position in the non-bending plane as the transverse coordinate.
In the barrel region the precision MDT chambers are arranged in three layers with cylindrical symmetry around the beam axis providing the three track position measurements needed for momentum determination:

- The inner (I) layer at R=5 m.

- The middle (M) layer at R=7.5 m.

- The outer (O) layer at R=10 m.

In the endcaps chamber layers are located at 7 m (I), 14 m (M) and 21-23 m (O) from the nominal interaction point.
The chambers are arranged in polar octants, each divided into two sectors, one with larger chambers (large sector) and one with smaller chambers (small sector). The MS layout is shown in Fig. 3.5. The small and large chambers partially overlap to ensure full spatial coverage and allow for relative alignment with tracks.

The expected muon momentum resolution is shown in Fig. 3.6 as a function of the muon transverse momentum p_T. In the low and medium p_T region, the multiple scattering and

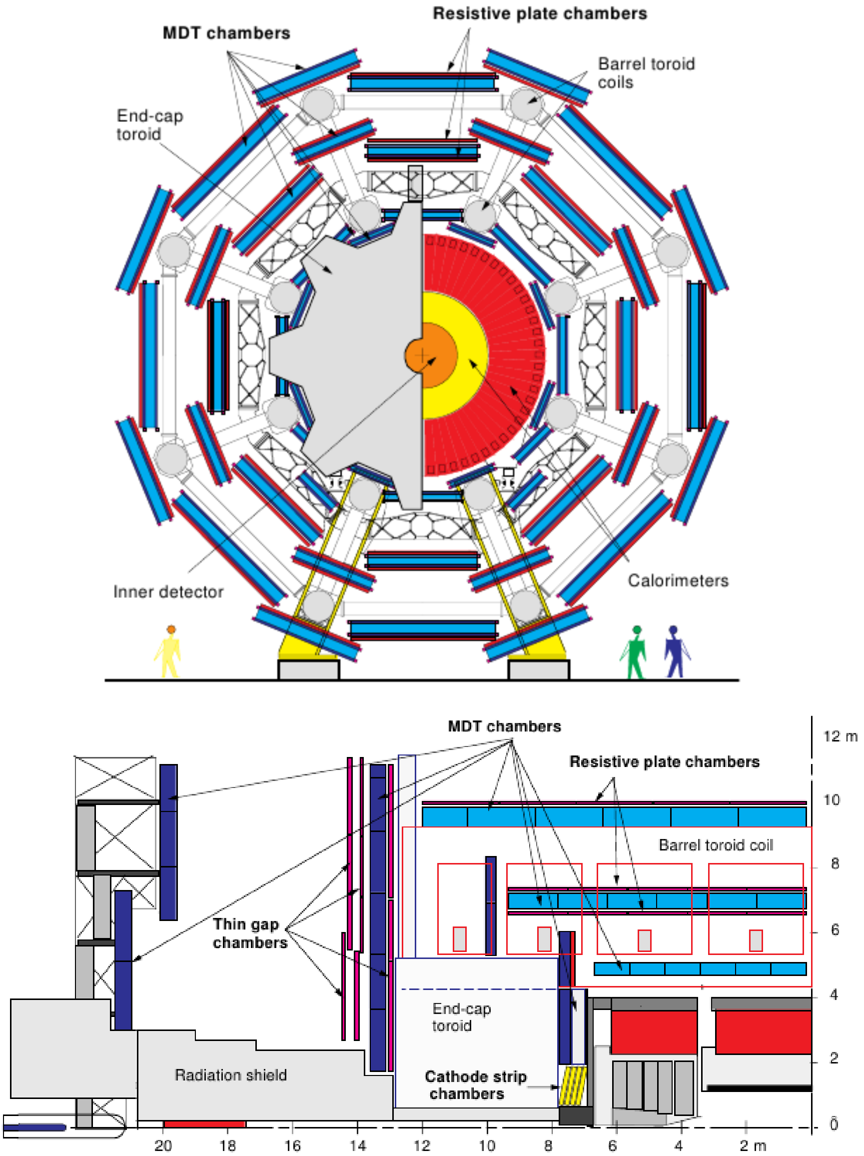

Figure 3.5: Cross section views of the ATLAS Muon Spectrometer in the non-bending plane (top) and in the bending plane (bottom).

energy loss fluctuations dominate, while in the high p_T region the chamber spatial resolution and the alignment of the chambers are the main effects determining the momentum resolution.

3.2.5.1 Monitored Drift Tube chambers

Monitored Drift Tube (MDT) chambers provide precision position measurement in the bending plane over most of the solid angle covered by the Muon Spectrometer. 1150

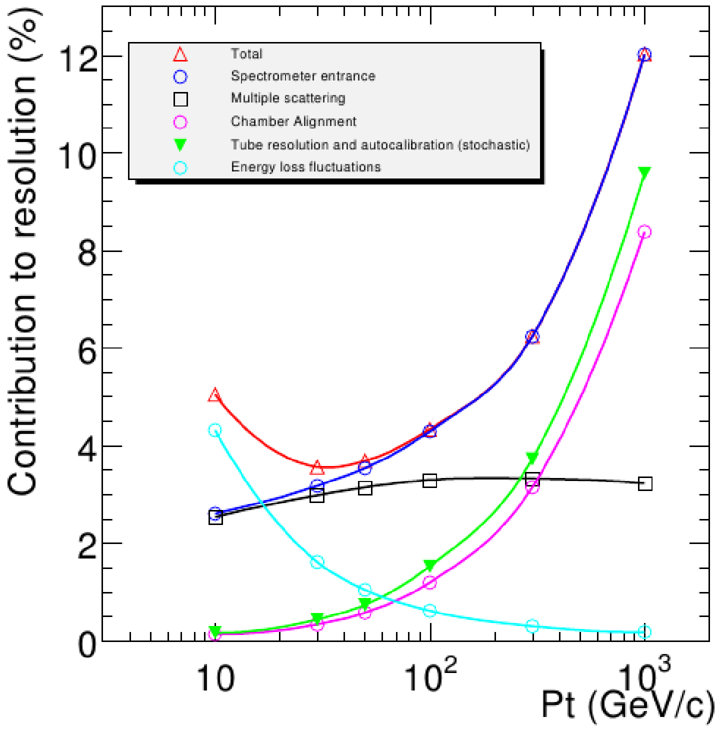

Figure 3.6: Contributions to the muon momentum resolution of the ATLAS Muon Spectrometer as a function of the muon transverse momentum [61].

chambers are operating in the spectrometer.

A MDT chamber is composed of drift tubes, with a length of 1-6 m, organized in two multilayers separated by a spacer; each multilayer is composed of 3 or 4 layers of tubes (see Fig. 3.7).

The tubes are operated with Ar/CO_2(93/7) gas at a pressure of 3 bar. The walls of the tubes are grounded. A voltage of 3080 V is applied to the central wire. In Fig. 3.7 an illustration of the operation mechanism of a drift tube is shown. When a charged particle is crossing the tube, it produces electron-ion pairs along its path (primary ionization). The electric field inside the tube causes the electrons to drift to the wire. Close to the wire the ionization electrons are sufficiently accelerated to produce new electron-ion pairs in a so-called *avalanche process* (secondary ionization). The multiplication factor (*gain*) of the device, which depends on the voltage applied, on the gas pressure and on the tube diameter, has been chosen to be $2{\cdot}10^4$, sufficiently low to prevent streamers and to avoid ageing of the drift tubes. The drift of the electrons to the wire and of the ions to the tube walls induces an electric signal on the wire. This signal is used to measure the electron drift time with respect to the time the muon passes the tube, i.e. the proton bunch crossing time corrected for the muon time of flight.

The drift time measurement is then converted into the distance of smallest approach of

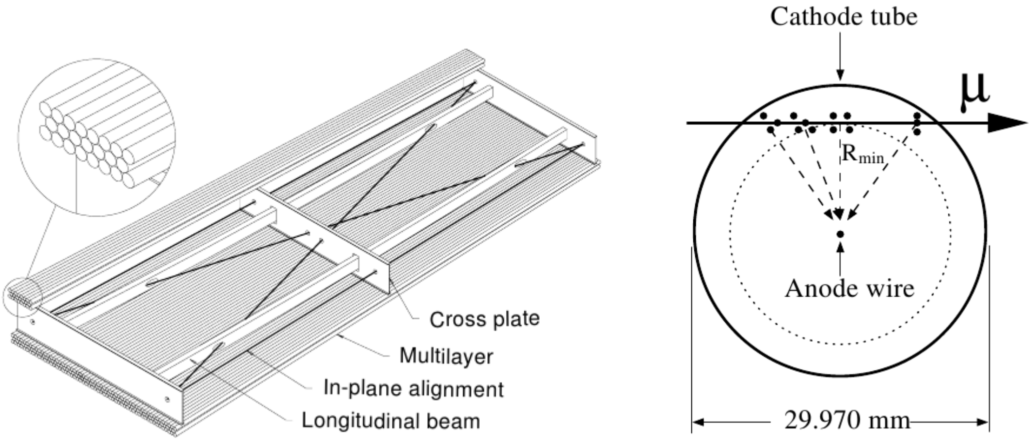

Figure 3.7: Layout of a Monitored Drift Tube chamber (left) and working principle of a drift tube (right).

the muon trajectory to the wire using the *r-t relation*, which is specific for the gas mixture and is determined depending on temperature and magnetic field strength. The muon track is fitted to the corresponding drift circles. Further details about the muon reconstruction are given in Section 4.7.

3.2.5.2 Cathode Strip Chambers

Cathode Strip Chambers (CSC) are multi-wire proportional chambers with readout cathode strips parallel and orthogonal to the wires used in the innermost layer of the $2.0 \leq |\eta| \leq 2.7$ region of the MS, where the high background radiation rate would degrade too much the performance of the MDT chambers. The layout of the CSC is shown in Fig. 3.8.

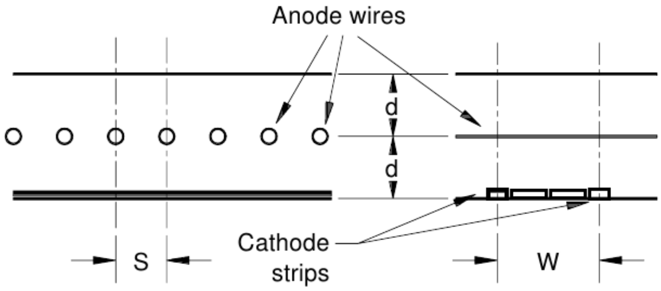

Figure 3.8: Schematic layout of a Cathode Strip Chamber.

CSC chambers operate with a $Ar/CO_2/CF_4(30/50/20)$ gas. The wires are at a potential of 2600 V. Charged particle crossing a CSC plane generate ionization charges which are multiplied by an avalanche process near the wires. The precision coordinate is determined

as the mean of the orthogonal strip cathode coordinates weighted by the charge signals induced on them, with a resolution of about 60 μm for a single CSC plane. Each chamber is composed of 4 planes. The transverse coordinate is measured with a resolution of about 5 mm by the cathode strips oriented parallel to the wires, which have larger pitch.
The CSC chambers are designed to operate with a background radiation level up to 1000 Hz/cm^2, which is sufficient to cope with the working conditions of the inner part of the forward spectrometer region.

3.2.5.3 Alignment system for the precision chambers

MDT and CSC chambers are installed with millimetre precision, but their positions must be known with a relative accuracy of 30 μm in order to reach the muon momentum resolution. To achieve this, the following strategy is used:

- Straight muon tracks are used to measure the relative chamber positions when the toroidal magnetic field is turned off.
- An optical alignment monitoring system connects the chambers in projective towers with respect to the interaction point and allows for the measurement of their relative movements with micrometer precision.

Further information can be found in [62] and [63].

3.2.5.4 Resistive Plate Chambers

Resistive Plate Chambers (RPC) are composed of two independent detector layers, each providing two-dimensional coordinate measurements. The layers consists of two Bakelite plates of 2 mm thickness separated by a 12 mm wide gap. The readout is provided by η cathode strips for the bending plane measurement and by ϕ strips for the non-bending plane measurement. They operate with $C_2H_2F_4/C_4H_{10}(97/3)$.
RPCs have a typical spatial resolution of 1 cm. Their excellent time resolution of 1 ns allows for their use as muon trigger chambers in the barrel region with identification of the bunch crossing from which the muon originates. They are arranged in three layers, two of them below and above the middle MDT layer and the third one at the outer MDT layer (see Fig. 3.5).
The first and the second RPC layers from the beam pipe are used for low-p_T muon triggers while the larger level arm between the middle and outer layers enables high p_T triggers.

3.2.5.5 Thin Gap Chambers

Thin Gap Chambers (TGC) are multi-wire proportional chambers with anode wire pitch larger than the anode-cathode distance which are operated in a CO_2/C_5H_{12} gas mixture. The wires provide the coordinate measurement in the bending direction while the

transverse coordinate measurement is provided by the cathode strips orthogonal to the wires.
Seven TGC planes are placed in the middle layer and two in the inner layer of the MS endcap regions. They are used to provide the trigger signals and the non-bending plane measurement in these regions.

3.2.6 The Trigger System

At design luminosity, the rate of proton-proton interactions is about 1 GHz. Most events are not interesting for physics analyses. The information stored for an event in ATLAS requires on averages 1.3 megabytes of disk space. Thus a trigger system with an high selective power is necessary to select the events that will be recorded at an acceptable rate. A three level trigger system [57] has been designed for the ATLAS experiment:

- The first-level (L1) trigger is completely hardware based and uses partial information of the event to reduce the data rate to 75 kHz.

- The second-level (L2) trigger uses almost complete event information to reduce the rate to 3.5 kHz.

- The event filter (EF) analyses the full event information to finally reduce the rate to 200 Hz.

The EF performs a reconstruction of the physics objects (which is different from the final, offline reconstruction) and applies kinematic requirements. Many different EF level trigger conditions are used in parallel and the ones with softer cuts may have to be prescaled to ensure that the final output rate does not exceed the sustainable 200 Hz. The final rate corresponds to 300 megabytes of data per second to be stored on disk.

3.2.6.1 The first-level muon trigger system

The first-level muon trigger uses the Resistive Plate Chambers and Thin Gap Chambers described in Sections 3.2.5.4 and 3.2.5.5. These chambers have high time resolution sufficient to unambiguously identify the bunch crossing a muon track is belonging to.

As illustrated in Fig. 3.9, the trigger algorithm is based on the concept of trigger *roads*: a first-level muon trigger results if there are hits in two, for the low-p_T trigger in the 6-9 GeV range, or three, for the high-p_T trigger in the 9-35 GeV range trigger chamber layers within roads of width depending on the p_T threshold. The muon trigger system covers the region $|\eta| \leq 2.4$.

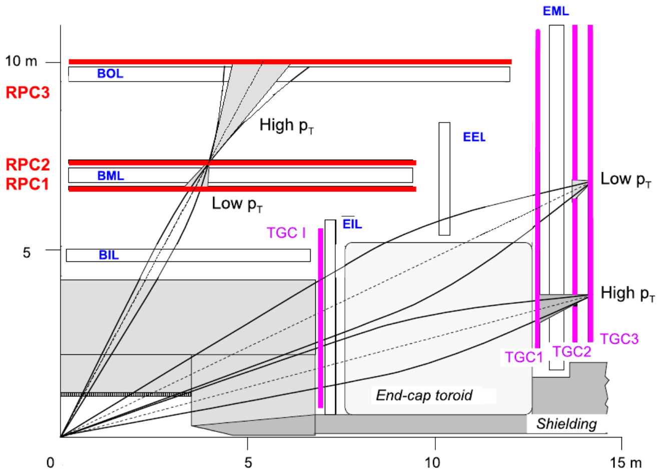

Figure 3.9: Concept and layout of the first-level muon trigger system.

3.2.7 Luminosity measurement in the ATLAS experiment

In order to determine the cross section of a physics process from the measured event rate according to Eq. 3.1 the corresponding integrated luminosity recorded by the ATLAS detector has to be measured as well. The main luminosity detector used in ATLAS is LUCID (Luminosity measurement using Čerenkov Integrating Detector) [64]. It consists of sixteen drift tubes of 15 mm diameter filled with C_4F_{10} gas and arranged around the beam pipe covering the $5.6 \leq \ |\eta| \ \leq 6.1$ angle. It is very resistant to radiation, as it has to work in a highly irradiated environment. Two LUCID detectors are symmetrically placed at $z = \ \pm$ 17 m from the interaction point.

The LUCID detector provides a measurement of the rate of inelastic collisions per bunch crossing detecting the Čerenkov photons emitted by charged particles produced in inelastic proton-proton interactions. The luminosity is calculated using this rate and the beam parameters calibrated with *van der Meer* scans as described in [64].

Chapter 4

Reconstruction of physics objects

In this chapter the algorithms used to reconstruct the trajectories and energies of different types of particles, hadron jets and other observables needed for the data analysis in this thesis are described.

4.1 Detector simulation

An introduction to Monte Carlo generators and to the simulation of physics processes has been given in Chapter 2. In order to compare data and simulation also the response of the ATLAS detector to the particle interactions has to be simulated taking into account the data taking conditions. The simulation proceeds in the following steps:

- A physics process is simulated by a Monte Carlo generator (*generator level*).
- The detector response to the generator level particles is simulated using the GEANT 4 software [65] (*detector simulation level*).
- Digitisation of the detector signals is performed providing output in the same form of the detector readout electronics. Pile-up and radiation background simulations are added in this step (*digitisation level*).
- The output of the digitisation is used to reconstruct physics objects by the same algorithms as used for data (*reconstruction level*).

The pile-up effect briefly introduced in Section 3.2 is caused by soft proton interactions recorded by the detector in the same event with a triggered hard scattering process. There are two main sources of pile-up:

- In-time pile-up is caused by multiple proton-proton interactions in a bunch crossing due to the high proton density in the bunches. Data used in this thesis are collected with up to 24 proton-proton interactions per bunch crossing [66].

- Out-of-time pile-up occurs because the readout electronics of many detectors integrates over several bunch-crossing. This effect depends on the time interval between bunches.

The main pile-up effects occur in the calorimeters where in-time pile-up increases the measured energies while out-of-time pile-up may decrease the observed energy due to the negative energy tails in the LAr pulse shaping.
In the digitisation step of the detector response simulation, pile-up events are added to the simulated physics events depending on the data taking conditions. Since simulated events are often produced before the data taking, reweightings of the Monte Carlo events according to the pile-up level measured in data is applied. The parameter used for the reweighting is the average number of interactions per bunch crossing $< \mu >$ in a given luminosity block, which usually represents a minute of data taking.

4.2 Charged particle and vertex reconstruction in the Inner Detector

The track reconstruction in the ID is performed in three steps [67]:

- In the pre-processing stage hit clusters are formed starting from the Pixel and SCT detectors. SCT clusters are transformed into space-points combining hits from the opposite sides of the SCT modules. TRT drift times are transformed into drift circles with the same technique as used for the MDT chambers (see Section 3.2.5.1).
- At the track-finding stage track-seeds are generated starting from the internal tracking layers and then extended through SCT and TRT associating clusters and hits to them. Finally, a full track fit is performed.
- In the post-processing stage the reconstruction of the primary vertex of interactions is performed, followed by secondary vertex reconstruction and photon conversion identification.

To allow for a quality assessment of reconstructed tracks, information about track *holes* (silicon sensors crossed by a track which have no hits) and *outliers* (TRT hits with large χ^2 contribution during the track-finding stage) are stored. The expected transverse momentum resolution for ID tracks is 2-5% for low p_T tracks and 4-15% for medium p_T tracks up to 100 GeV, strongly depending on $|\eta|$ (see Fig. 4.1). The measurement of the track reconstruction efficiency will be discussed in the next chapter.

Tracks are associated to common vertices, and the primary interaction vertex is identified as the vertex with highest $\sum {p_T}^2$ of the associated tracks. The tracks are then refitted using the selected primary vertex. As a figure of merit, the reconstruction efficiency for the hard scattering interaction vertex is predicted to be above 99% in simulations for $Z \to ee$ and $Z \to \mu\mu$ decays even in very high pile-up conditions [68].

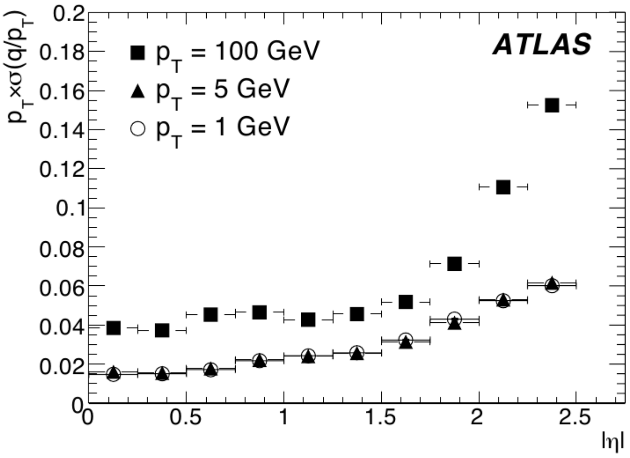

Figure 4.1: Expected 1/$\mathrm{p_T}$ resolution of ID tracks as a function of η of the tracks for simulated $\mathrm{p_T}$=1, 5, 10 GeV muon tracks [61].

4.3 Electrons and Photons

An efficient identification and reconstruction of electrons and photons as well as precise measurement of their energy is an important feature of the ATLAS detector in order to fulfil the demanding requirements of the physics program. The goal is challenging because of the working conditions of the LHC and because of the relatively large amount of material of the tracking detectors in front of the electromagnetic calorimeters.

Three algorithms are used for the reconstruction of electrons and photons [69, 70]:

- A energy cluster-seeded method is used as the standard reconstruction algorithm.
- A track-seeded algorithm is used for low-$\mathrm{p_T}$ electrons.
- A dedicated algorithm is used for electrons in the forward region ($2.5 < |\eta| < 4.9$) which is not covered by the Inner Detector.

For the purpose of this thesis only the first algorithm is described.

4.3.1 Electron reconstruction

The standard electron reconstruction is seeded by an EM calorimeter cluster consisting of energy deposits of E_T >2.5 GeV in an 3x5 group of calorimeter cells in η and ϕ. The cluster is then matched to ID tracks within a $\Delta\eta$ = 0.05 window and a $\Delta\phi$ window of 0.1 on the side of the track to which it is bending and of 0.05 on the other side [71]. This asymmetry in the $\Delta\phi$ window takes into account the effects of bremsstrahlung. EM clusters matched to ID tracks are electron candidates. The calorimeter cluster is then recomputed using 3x7 cells in the barrel and 5x5 cells in the endcaps. The energy of the electron is corrected for the estimated energy loss of the particle in the material outside the calorimeter. The energy of the electron is determined using calorimeter cluster information. For the direction of the electron, ID track information is used for tracks with silicon detectors hits and clusters information otherwise.

The reconstructed electrons are classified in three categories, *loose*, *medium* and *tight*, using several quality criteria (see [71]): among others, the agreement between ID and calorimeter measurements and the numbers of hits in the different ID subdetectors. The expected jet rejection rates in the three categories are about 500, 5000 and 50000 respectively. This classification has been improved for 2011 and 2012 data taking with the new quality categories *loose++*, *medium++*, *tight++*.

The performance of the electron reconstruction from 2011 measurements is shown in Fig. 4.2. The agreement of the measured reconstruction efficiencies in data and simulations is very good. The electron momentum resolution in the simulations is adjusted such that the simulated dielectron invariant mass distribution in simulated $Z \to ee$ events matches the data.

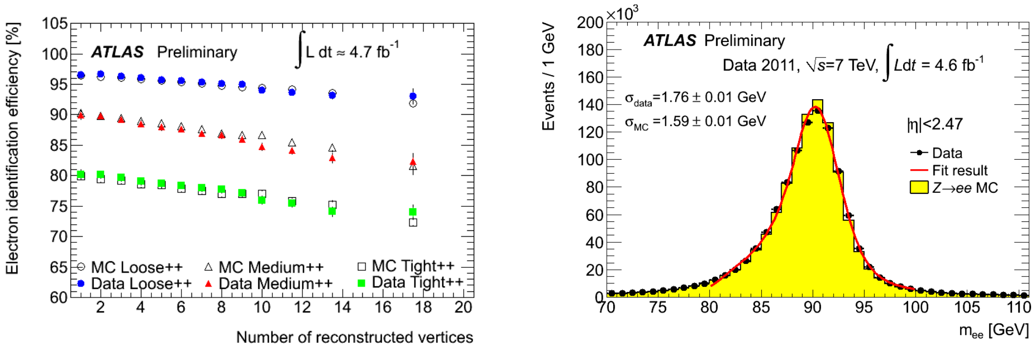

Figure 4.2: Measured electron reconstruction efficiency as a function of the number of reconstructed vertices in the events (left) and electron-positron invariant mass distribution in $Z \to ee$ decays (right) for 2011 data and Monte Carlo simulation [72].

4.3.2 Photon reconstruction

Reconstructed photons are divided into two categories: *converted photons* and *unconverted photons*.

Reconstructed unconverted photons are seeded by EM clusters like the electron candidates, but have no matching ID track. For photons converting into electron-positron pairs inside the ID, the reconstruction relies on the identification of conversion vertices, with two or even only one associated track, the latter case happening when the two conversion electrons are too close to be distinguished or when one of the two tracks, usually with very low p_T, is not reconstructed. Tracks from conversion vertices matched to calorimeter clusters like for the electron reconstruction are converted-photon candidates.

Many converted photons are also selected as electron candidates. A recovery procedure for these photons described in [69] is applied.

The photon reconstruction performance expected from simulations is shown in Fig. 4.3. After the recovery procedure on photons the predicted photon reconstruction efficiency is very high.

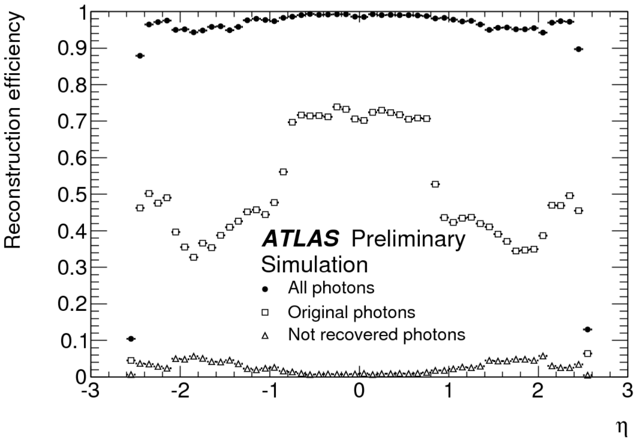

Figure 4.3: Expected photon reconstruction efficiency as a function of η [70].

4.4 Jets

Jets are collimated bunches of hadron tracks and their decay particles which at high-energy hadron colliders are by far dominating the event final states.

4.4.1 Jet Reconstruction

The baseline method for jet reconstruction in ATLAS [73] is the *anti-k_T* algorithm [74]. The reconstruction starts with a topological clustering algorithm searching for a calorimeter *seed cell* with a signal-to-noise ratio S/N > 4. Neighbouring cells with a S/N > 2 are consecutively added. Local maximums in cell energies are located and spilt off to form the seeds for separate clusters.

The iterative *anti-k_T* algorithm starts with the identification of pseudo-jets, either particle 4-momenta in Monte Carlo simulations or calorimeter clusters in data. It uses the definitions:

$$d_{ij} = min(\frac{1}{k_{Ti}^2}, \frac{1}{k_{Tj}^2})\frac{\Delta_{ij}^2}{R^2} \tag{4.1}$$

and

$$d_i = \frac{1}{k_{Ti}^2} \ , \tag{4.2}$$

where the indices i,j run over all pseudo-jets, k_T is the transverse momentum of a given pseudo-jet, $\Delta_{ij} = \sqrt{\Delta y_{ij}^2 + \Delta\phi_{ij}^2}$ the angular distance between two pseudo-jets and R a η-ϕ distance parameter with values 0.4 or 0.6 used as baseline in ATLAS.
For a given number of pseudo-jets N, the smallest of all d_{ij} and d_i variables is determined with $i, j = 1, ..., N$. The pseudo-jet i for minimum variable d_i is identified as a jet and removed from the list of pseudo-jets. Otherwise, if d_{ij} is the minimum variable, pseudo-jets i and j are recombined. The reconstruction procedure iterates until there are no pseudo-jets left. With this algorithm the hardest particles lead the merging procedure and softer particles around them will be merged with them, until the final jets are formed.
The *anti-k_T* algorithm is infrared safe [74], i.e. the eventual presence of soft particles between two hard particles does not affect their reconstruction as a single jet. It is also collinear safe [74], i.e. a jet is reconstructed without differences when a certain part of its momentum is carried by a single particle or if the same amount is carried in total by two or more collinear particles.

4.4.2 Jet quality

Jets originating from proton-proton scattering must be distinguished from non-collision background due to cosmic muons, noise, or interactions of the beam protons with residual gas molecules in the beam-pipe or with inactive detector and shielding material. For this purpose, many jet parameters are used to classify the jets in terms of cleanliness as *tight*, *medium*, *loose* jets [73] as well as jets failing even the loose requirements. A further still *looser* category has been introduced as the standard for the 2011 physics analyses [75].

4.4.3 Jet energy measurement

The jet energy calibration relates the energy deposition measured by the calorimeters to the true energy of a jet. In Monte Carlo simulations the correction factors are determined by comparison with *truth jets*, which are reconstructed from the stable particles generated using the same *anti-k_T* algorithm as for final state jets. For the real data the calibration is performed using test-beam studies.
The initial energy calibration is be performed with respect to different energy scales [73]:

- the EM scale corresponding to the response of the calorimeters to the electromagnetically interacting components of a jet and
- the local cluster weighting (LCW) scale which relies on the identification of energy clusters in a jet and their classification as hadronic or electromagnetic clusters, for which different calibration corrections are applied.

A third calibration scale, the global calorimeter cell weighting (GCW) scale is not relevant for the purpose of this thesis.

In addition to the calibration, a Jet Energy Scale (JES) correction is applied to obtain a final result as close as possible to the true energy of a jet, including corrections for pile-up effects and for the position of the primary interaction vertex of the event and simulation-based corrections.

The standard jet calibration used in this thesis is the EM+JES scheme. In Fig. 4.4 a measurement of the jet energy resolution is shown, which is performed by studying the p_T balance of events with a Z boson and one reconstructed jet, in which the jet momentum is expected to balance the one of the Z boson. The width of the distribution of the ratio of the transverse momenta of the jet and of the Z boson is used to compare the jet p_T resolution in data and in simulations, finding a good agreement.

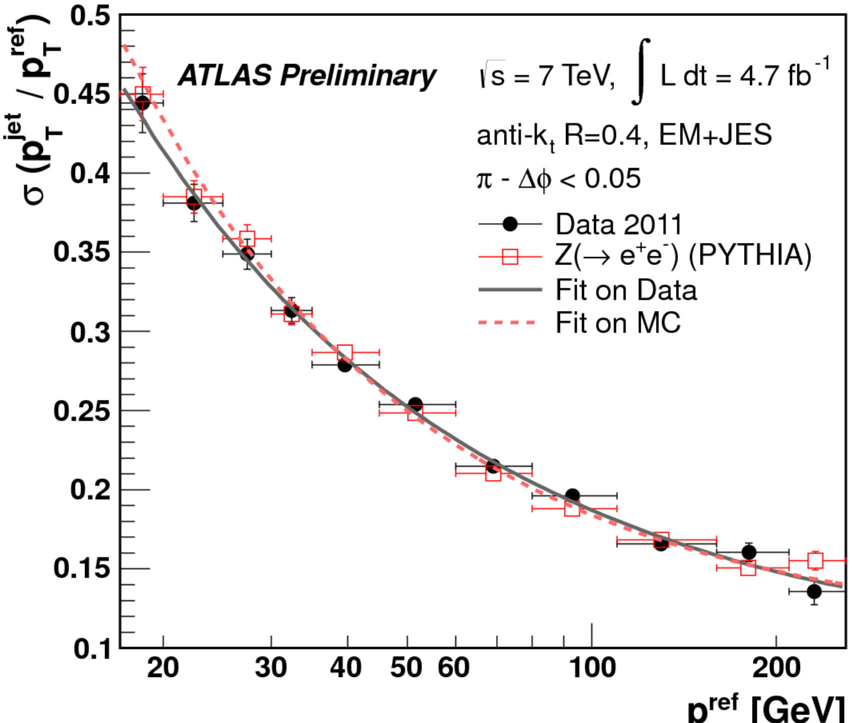

Figure 4.4: Measurement of the resolution of the jet p_T relative to $p_T{}^{ref}$ of the Z boson in Z + 1-jet events as a function of $p_T{}^{ref}$ [76].

4.4.4 Heavy flavour jet tagging

Jets originated by the hadronization of heavy flavour quarks (i.e. charm and bottom quarks) can be identified relying on the properties of b and of c hadrons. The long lifetimes and heavy masses of these hadrons produces signature that can be used to discriminate

c and b jets from light-jets. The semileptonic decays of these hadrons may also be used to identify heavy flavour jets. In this thesis two different tagging algorithms are used: *SV0* for the b-tagging in the $W+$ b-jets cross section measurement presented in Chapter 6 and the Soft Muon Tagger (SMT) used for the identification of c-jets in the $W+$ c-jet cross section measurement discussed in Chapter 7. Details on the SMT and an efficiency measurement for this tagger performed in data are given in Section 5.3.

4.4.4.1 The *SV0* b-tagging algorithm

The b-jet tagging algorithm *SV0* [77] relies on the identification of the decay vertices (*secondary vertices*) of b-hadrons in the Inner Detector exploiting the long lifetime of b-hadrons.
For each jet, tracks within ΔR <0.5 from the jet axis are used to perform a secondary vertex fit, illustrated in Fig. 4.5a. The decay length significance $L/\sigma(L)$, i.e. the distance of the reconstructed secondary vertex with respect to the primary interaction vertex of the event divided by the error on the distance itself, is used as a discriminating variable between b-jets and non-b-jets. In Fig. 4.5b $L/\sigma(L)$, is shown as evaluated in simulations for b-jets, c-jets and light-jets: this quantity is on average higher for b-jets.

The working point used in this thesis for the b-jet tagging is $L/\sigma(L) > 5.85$, with an efficiency of about 35% and a mistag rate of about 0.3% and 8% for light-jets and c-jets respectively. The calibration of the tagger has been performed in a data sample enriched in b-jets by requiring a muon reconstructed inside the jets, which is likely to be coming from b-hadron semileptonic decays, as described in [78]. The muon momentum relative to the jet axis p_T^{rel} is used to discriminate b-jets from c-jets and light-jets for this study.

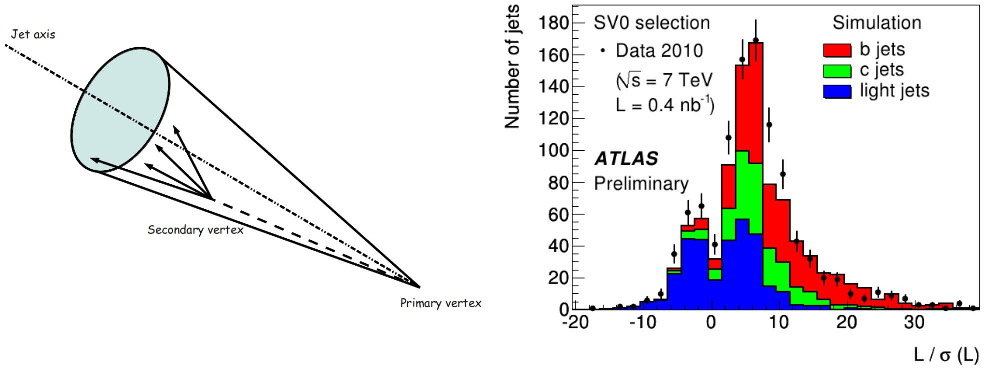

(a) Secondary vertex fit **(b)** Decay length significance

Figure 4.5: (left) Scheme of the secondary vertex fit performed by the *SV0* algorithm. (right) Decay length significance measured in data and Monte Carlo simulations for b-jets, c-jets and light-jets [77].

4.5 τ leptons

τ leptons are unstable particles decaying into hadrons with a branching ratio BR = 65% [25] and leptons with BR = 35% [25]. Due to their short lifetime, corresponding to a mean free path of about 100 μm, their leptonic decays cannot be distinguished from prompt electrons and muons. The reconstruction of hadronic τ decays and their distinction from QCD jets is challenging. It uses properties of the hadronic τ decays such as the low track multiplicity and the narrow collimation of the tracks and energy depositions in the calorimeters. A description of the hadronic τ decay reconstruction is given in [61].

4.6 Transverse missing energy

The signature of long-lived or stable weakly interacting particles like neutrinos in the detector is missing transverse energy E_T^{miss}, i.e. the energy imbalance in the transverse plane due to not detected particles. The transverse energy imbalance is used because at a hadron collider the energies of the colliding partons in the hard parton scattering are not known for each event and many soft collision products leave the detector undetected. E_T^{miss} is determined as the negative sum of the transverse energies of all final state particles E_T. The energy $E_{x,y}$ in the transverse coordinates x, y is reconstructed in ATLAS [79] by summing up the following contributions:

$$\begin{aligned} E_{x,y} =& E_{x,y}^{electrons} + E_{x,y}^{photons} + E_{x,y}^{\tau\ leptons} + E_{x,y}^{muons} + E_{x,y}^{jets} \\ &+ E_{x,y}^{soft\ jets} + E_{x,y}^{calo\ \mu} + E_{x,y}^{cell\ out} \ . \end{aligned} \tag{4.3}$$

$E_{x,y}^{jets}$ and $E_{x,y}^{soft\ jets}$ are determined from calorimeter cells in clusters associated to jets with calibrated $\mathrm{p_T} > 20$ GeV and 7 GeV $< \mathrm{p_T} <$ 20 GeV respectively. $E_{x,y}^{cell\ out}$ is the sum of calorimeter cells energies in clusters not associated to jets or particles. $E_{x,y}^{miss,calo\ \mu}$ is the energy loss of muons in the calorimeters. It is evaluated with different methods for isolated and non-isolated muons and only added in the second case to avoid double counting (see details in [79]).

Figure 4.6 shows the measured E_T^{miss} distribution in $Z \to \mu\mu$ events. Data and simulation are in good agreement with each other.

4.7 Muons

Muons are produced in many important physics processes. The detector signature for muons is very clean and therefore the misidentification rate is very low. Furthermore the Muon Spectrometer described in Section 3.2.5 detects muons with very high efficiency and momentum resolution. A detailed study of the muon spectrometer performance is presented in next chapter. In this section, the basic strategies used for muon reconstruction

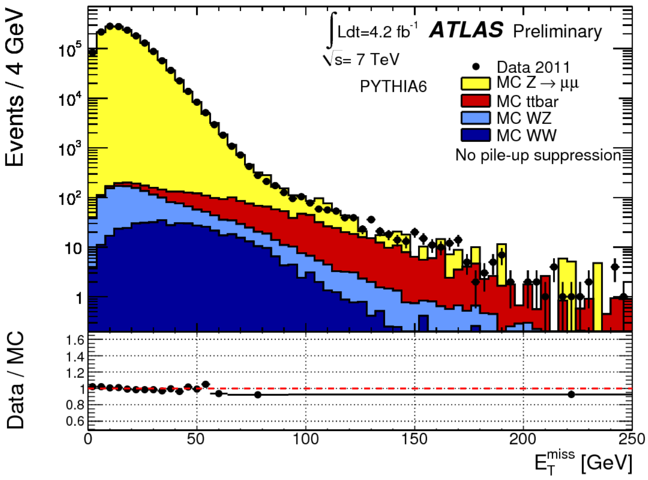

Figure 4.6: Distribution of the E_T^{miss} in $Z \to \mu\mu$ events in data and simulation [80].

are discussed.

Two groups of algorithms (*chains*) are used for muon reconstruction in ATLAS, Muid [81] and Staco [82]. Both chains include several muon reconstruction algorithms using either the muon spectrometer information only (*stand-alone reconstruction*, SA), combining ID and MS tracks (*combined reconstruction*, CB), or identifying ID tracks as muons using partial muon spectrometer information (*segment tagged reconstruction*, ST).

For the stand-alone muon reconstruction, both chains start from single hits in the precision chambers, combining them into track segments. Muon spectrometer tracks are reconstructed connecting the segments and extrapolating the track to the beam line, taking into account multiple scattering and energy loss in the detector elements. The stand-alone reconstruction covers $|\eta| \leq 2.7$, with acceptance gaps at $|\eta| < 0.1$ and $|\eta| \approx 1.2$ for the passage of services.

The combined muon reconstruction starts from an ID track and a stand-alone muon spectrometer track to produce a combined track. The Muid combined algorithm performs a refit of the total track, while the Staco algorithm combines the parameters of the two tracks statistically. The coverage of the combined reconstruction is reduced to the region $|\eta| \leq 2.5$ due to the Inner Detector acceptance, with the same gaps at $|\eta| < 0.1$ and $|\eta| \approx 1.2$ as for the stand-alone reconstruction. A measure of the quality of the track combination is provided by the parameter

$$\chi^2_{match} = (\boldsymbol{T}_{MS} - \boldsymbol{T}_{ID})^T (\boldsymbol{C}_{MS} + \boldsymbol{C}_{ID})^{-1} (\boldsymbol{T}_{MS} - \boldsymbol{T}_{ID}) \tag{4.4}$$

where $\boldsymbol{T}$ is a vector of the five track parameters defined in Section 3.2.1 and $\boldsymbol{C}$ the corresponding covariance matrix.

The segment tagged muon reconstruction identifies ID tracks as muons if they can be associated to segments in the muon spectrometer. This method is useful for low p_T muon tracks, which do not reach the layers of the muon spectrometer due to bending in the magnetic field, or in the regions $|\eta| < 0.1$ and $|\eta| \approx 1.2$ where tracks may pass through only one or two layers of chambers. This reconstruction strategy has a slightly higher fake rate but improves the muon efficiency for the reconstruction of final states with many muons, in particular from Higgs and SUSY decays.

In addition to the three muon categories, *calorimeter tagged muons* are identified as ID tracks which are associated to energy deposits in the calorimeters compatible with that of minimum ionizing particles. This type of muon candidates recovers efficiency in the $|\eta| < 0.1$ region where the MS coverage is reduced.

The muon reconstruction efficiency of the MS starts from zero at $p_T \approx 2.5$ GeV and reaches its plateau at $p_T \approx 6$ GeV [61]. In Fig. 4.7 the dimuon invariant mass resolution measured in $Z \to \mu\mu$ events using combined muon reconstruction in the 2011 data is shown for different η regions. Additional smearing of the muon momentum resolution in simulation is applied to correct for the observed disagreement with the data in the $m_{\mu\mu}$ resolution.

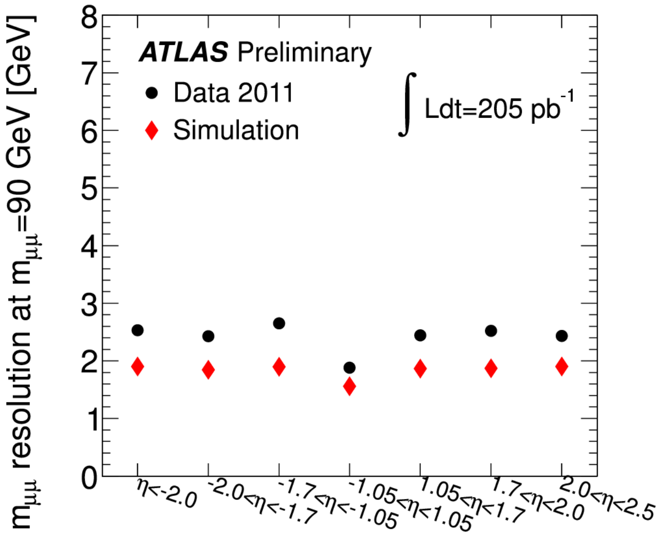

Figure 4.7: Dimuon invariant mass resolution measured in $Z \to \mu\mu$ events using combined muon reconstruction in 2011 data and simulations [83].

4.8 Track and calorimeter isolation

For many physics analyses the isolation of physics objects (e.g. muons) is a powerful discriminating variable to reject QCD background. Two kinds of variables are used to measure the isolation:

- **Track isolation** uses the sum of the p_T of all ID tracks reconstructed in a cone with a given radius ΔR with respect to an object.
- **Calorimeter isolation** uses the sum of the energy deposits in the calorimeters in a cone around the object with a radius ΔR.

Standard cone radii for the isolation requirements in ATLAS are $\Delta R = 0.1, 0.2, 0.3, 0.4$.

Chapter 5

Muon reconstruction performance

Essential for all physics analyses is the understanding of the detector performance under real data taking conditions. A tremendous effort has been put into the measurement and monitoring of the performance of the ATLAS detector in order to correct the detector response in the Monte Carlo simulations to fit the data.

Leptonic decays of W and Z bosons are natural candidates for the study of the muon system performance, since they provide clean samples of muons with high cross sections. The dimuon decays of Z bosons in particular offer a very clear signature which allows for efficient background rejection. The resulting sample of muons is used for many performance studies. In this chapter, measurements of the muon reconstruction and identification efficiencies using the so-called "Tag-and-Probe" method in $Z \rightarrow \mu\mu$ events are discussed.

5.1 Measurement of the muon reconstruction efficiency

Monitoring of the muon reconstruction efficiency during data taking is an important verification of the detector performance. Furthermore, the results are needed to correct the simulated detector response in Monte Carlo simulations to correctly reproduce the performance in data.

The correction is performed by evaluating the efficiency ϵ in data and in Monte Carlo and using the correction scale factor

$$SF = \frac{\epsilon_{DATA}}{\epsilon_{MC}} \tag{5.1}$$

to reweight the simulated events. The results of this section are for the 2011 ATLAS data set used in this thesis. In Appendix B, the results for the 2012 data set are shown.

5.1.1 Dependence on the Muon Spectrometer regions

For the efficiency measurement, the Muon Spectrometer is subdivided into ten regions according to the coverage provided and to the detector technologies and alignment system used. The SFs are determined separately for the ten regions, assuming that they are constant in each region.

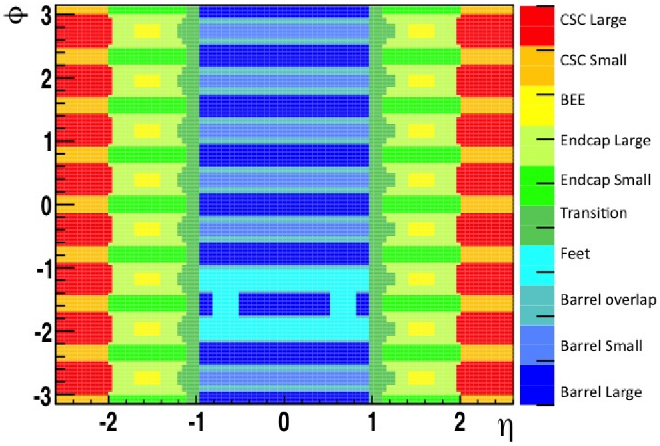

Figure 5.1: Muon Spectrometer regions in the η-ϕ plane.

The ten regions are defined in the following way (see the illustration in Fig. 5.1):

- The barrel is divided into three regions corresponding to large and small chamber sectors and the overlap between them.
- In the feet region of the barrel the geometrical acceptance of the spectrometer is degraded due to the presence of the steel feet supporting the ATLAS detector.
- The transition region between barrel and endcap is around $\eta\ = 1.1$.
- The two endcap regions, defined up to $|\eta|\ = 2.0$, are divided into large and small chamber sectors.
- The BEE region of the endcaps uses extra barrel (BEE) chambers mounted on the endcap toroid cryostat which are not connected to the optical alignment system.
- The CSC or forward region ($|\eta| > 2.0$) is covered by the CSC chambers in the inner-most endcap layer and is divided into large and small chamber sectors.

Large and small sectors are treated separately because of the different connection to the alignment system (see [62, 63]).

5.1.2 The Tag-and-Probe method

The so called Tag-and-Probe method uses $Z \rightarrow \mu\mu$ events to measure the muon reconstruction efficiency. One of the muons from the $Z \rightarrow \mu\mu$ decay fulfilling tight requirements, i.e. a well reconstructed combined muon (see Section 4.7), is used as a tag muon, while the second one, fulfilling looser requirements, is used as a probe muon. When a tag and probe muon pair is found with an invariant mass $(m_Z - 10\text{ GeV}) < \mathrm{m}_{\mu\mu} < (\mathrm{m_Z} + 10\text{ GeV})$ the event is identified as a $Z \rightarrow \mu\mu$ event. Tighter selection criteria are then applied on the probe muon and the efficiency of this tighter selection is determined as the fraction of probe muons passing the tighter cuts. The Tag-and-Probe method is applied

- to evaluate the muon reconstruction efficiency in the Muon Spectrometer (MS), by using an Inner Detector (ID) track or a calorimeter tagged muon as probe and calculating the fraction of probes matching a fully reconstructed muon and
- to evaluate the ID reconstruction efficiency by using a MS track as probe and calculating the fraction of probes matching an ID track.

Other possible applications are described later in this chapter.

The efficiency of stand-alone (SA) muon reconstruction is determined using the first method, while for combined (CB) and segment tagged (ST) muons which use both Muon Spectrometer and Inner Detector information the total reconstruction efficiency is given by

$$\epsilon_{reco} = \epsilon_{reco}^{MS} \cdot \epsilon_{combination} \cdot \epsilon_{reco}^{ID} \ . \tag{5.2}$$

Using ID tracks as probes and matching them to CB or ST muons the $\epsilon_{reco}^{MS}\epsilon_{combination}$ term can be determined. For calorimeter tagged muons, which do not use spectrometer information, the same strategy as for ID tracks is applied.

The statistical error on the measured efficiency is determined in the following way. The number k of events with unmatched probe, i.e. in which the reconstruction of the probe as muon fails, follows a Poissonian distribution. The mean value of k is $N(1-\epsilon)$ and its variance $\sigma(k) = \sqrt{k} = \sqrt{(1-\epsilon)N}$, where N is the total number of probe muons. Therefore the error on the efficiency is:

$$\sigma(\epsilon) = \sigma(1-\epsilon) = \sqrt{\frac{1-\epsilon}{N}} \ . \tag{5.3}$$

The estimate fails for $\epsilon = 1$ but is applicable in all practical cases with $\epsilon \ < 1$.

5.1.3 Data and Monte Carlo samples

For the analysis the full 2011 ATLAS data set, corresponding to 4.7 fb^{-1} of luminosity, was used. It is divided into data taking periods with uniform detector performance and with stable pile-up conditions (see Table 5.1).
The following Monte Carlo signal and background samples have been used:

- The $Z \rightarrow \mu\mu$ signal sample.

Table 5.1: 2011 data taking periods used for the Tag-and-Probe measurement. $< \mu >$ is the average number of collisions per bunch crossing. The uncertainty on the luminosity is 1.8% [84].

Period	Luminosity [pb^{-1}]	$< \mu >$
B	12.0	6.0
D	166.5	5.5
E	50.4	6.1
F	136.8	6.0
G	518.0	5.8
H	265.0	5.2
I	334.0	6.2
J	233.2	7.3
K	576.3	7.5
L	1415.9	11.2
M	1031.5	12.3
ALL	4739.1	9.5

Table 5.2: Monte Carlo simulation samples used for the 2011 Tag-and-Probe analysis. The Standard Model (SM) $t\bar{t}$ production cross section for a top quark mass of 172.5 GeV is obtained from approximate NNLO QCD calculations.

Process	Generator	Number of events	Cross section [nb]		
$Z \to \mu\mu$	Pythia	9993779	0.969	(NNLO)	[33]
$W \to \mu\nu$	Pythia	6996784	10.46	(NNLO)	[33]
$Z \to \tau\tau$	Pythia	495347	0.969	(NNLO)	[33]
$W \to \tau\nu$	Pythia	497000	10.46	(NNLO)	[33]
$c\bar{c}$(at least one $c \to \mu$, $\mathrm{p_T}^\mu > 15$ GeV)	Pythia	1499697	$42.8 \cdot 10^3$	see note [1]	
$b\bar{b}$(at least one $b \to \mu$, $\mathrm{p_T}^\mu > 15$ GeV)	Pythia	4454082	$16.4 \cdot 10^3$	see note [1]	
$t\bar{t}$(no fully hadronic decay)	MC@NLO	14958835	0.090	(app. NNLO)	[85]

- $W \to \mu\nu$ production is the most important background where the tag muon is a real muon while the probe muon candidate is either an ID track or a real muon from hadron decays in jets accompanying the W.
- $Z \to \tau\tau$ production is a small background due to the small branching ratio BR = 0.17 [25] of the $\tau \to \mu\nu\nu$ decay and because muons from this decay have low momentum.
- $W \to \tau\nu$ decays are also a very small background for the same reasons.
- $c\bar{c}$ and $b\bar{b}$ production, where one or both muons come from semi-leptonic decays of charm or bottom hadrons, is a significant background in the low momentum range due to the very high cross sections.
- $t\bar{t}$ production has a small cross section but is a source of high $\mathrm{p_T}$ muons.

---

[1] For $b\bar{b}$ and $c\bar{c}$ production cross sections predicted by Pythia have been used after scaling by a factor of 0.58 which has been determined with a data driven method [86].

The Monte Carlo samples are listed in Table 5.2.

5.1.4 Event selection

Events have only been used for the analysis if all relevant detector systems were fully operational during data taking: Inner Detector, Muon Spectrometer and the Calorimeters for studies using calorimeter information, e.g. the evaluation of the calorimeter tagged muon reconstruction efficiency.
A primary vertex with at least 3 associated tracks is required to prevent any possible contamination by cosmic muon events which have vertices with two associated tracks.

The events must pass an event filter trigger (see Section 3.2.6) with p_T threshold of 18 GeV. The simulated events are reweighted according to the average number of proton collisions per bunch crossing $<\mu>$ in each data taking period such that the $<\mu>$ distribution for data and Monte Carlo agrees (see Figure 5.2a). In addition, the events are reweighted according to the distribution of the primary interaction vertex (see Figure 5.2b) which has significative influence on the ID reconstruction efficiency at high $|\eta|$.

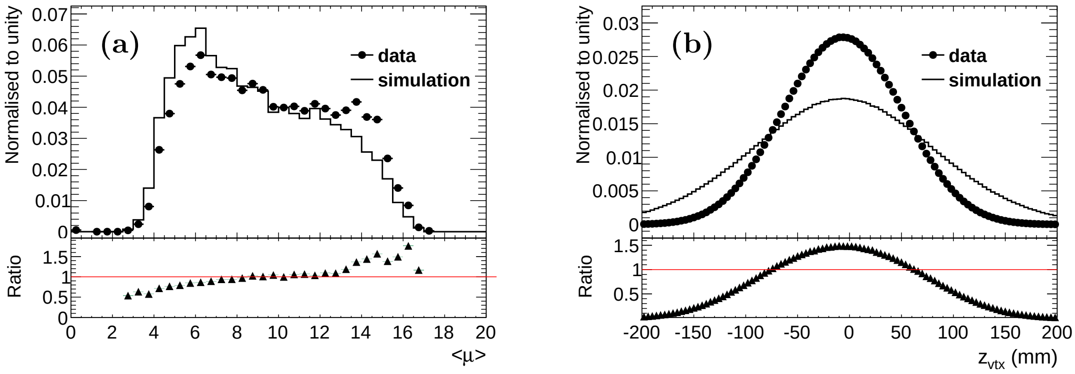

Figure 5.2: Distributions of the average number of collisions per bunch crossing (a) and of the z coordinate of the primary interaction vertex (b) for 2011 data and simulations. The bottom part of the plots shows the ratio of the data and Monte Carlo distributions which is used to reweight the simulated events.

5.1.4.1 ID track quality cuts

In order to suppress the background of non-prompt muons from π and K mesons decays, the relatively long lifetime of these particles is used. As they travel up to a few metres in the detector before decaying, it is possible to reduce the contamination due to these decays by requiring a minimum number of hits in the silicon detectors and by applying cuts on the ID track quality (see Table 5.3). The cuts can be used for ID tracks or for muon tracks reconstructed using ID information (CB, ST, calorimeter tagged muons). A qualitative study on the performance of these cuts is presented in Appendix A.

Table 5.3: ID track quality cuts. $\mathrm{N_{hits}}$ is corrected for Pixel Detector and SCT for the number of dead sensors crossed by the track. Outlier hits and missing hits (holes) are defined in Section 4.2.

B-layer	$\mathrm{N_{hits}} > 0$, excluding regions with defected modules
Pixel Detector	$\mathrm{N_{hits}} > 1$
SCT	$\mathrm{N_{hits}} > 5$
Silicon holes	$(\mathrm{N_{holes}^{pixel}} + \mathrm{N_{holes}^{SCT}}) < 2$
TRT ($\lvert\eta\rvert$ <1.9)	$(\mathrm{N_{hits}} + \mathrm{N_{outliers}}) > 5$ and $\frac{\mathrm{N_{outliers}}}{\mathrm{N_{hits}}+\mathrm{N_{outliers}}} < 0.9$
TRT ($\lvert\eta\rvert$ >1.9)	If $(\mathrm{N_{hits}} + \mathrm{N_{outliers}}) > 5 \rightarrow \frac{\mathrm{N_{outliers}}}{\mathrm{N_{hits}}+\mathrm{N_{outliers}}} < 0.9$

5.1.4.2 Tag muon selection

Tag muons are well reconstructed combined muon tracks within the acceptance of the muon trigger system ($\lvert\eta\rvert < 2.4$) and with high transverse momentum $\mathrm{p_T} > 20$ GeV. The Inner Detector track associated with the muon has to satisfy the quality criteria listed in Table 5.3. A loose cut on the muon track isolation variable is applied in order to reduce QCD background. The muon candidate is also required to match a muon reconstructed by the event filter in a $\Delta R = 0.15$ cone to ensure that the event has been selected by the event filter due to the tag muon, to avoid any bias in the measurement due to the trigger efficiency. A loose cut is also applied to the impact parameter of the muon tracks. The cuts are summarised in Table 5.4.

Table 5.4: Criteria for tag muon selection

Identification	Combined muon
Kinematic cuts	$\mathrm{p_T} > 20$ GeV, $\lvert\eta\rvert < 2.4$
Impact parameter cuts	$\lvert z_0\rvert < 10$ mm
Track isolation	$\frac{\sum^{\Delta R=0.4} p_T^{tracks}}{\mathrm{p_T}^{\mathrm{muon}}} < 0.15$
Trigger match	Match to EF muon within $\Delta R = 0.15$
ID track quality cuts	Cuts in Table 5.3

5.1.4.3 Probe muon selection

As discussed in Section 5.1.2, the definition of a probe muon is different for different efficiency measurements. The probe muon can either be an ID track (ID probe), a calorimeter tagged muon track (calorimeter probe), or a stand-alone (SA) or combined (CB) muon track (muon probe).

A $\mathrm{p_T}$ cut is applied to the probes, depending on their definition. Using muon probes already ensures a pure $Z \rightarrow \mu\mu$ sample such that the $\mathrm{p_T}$ threshold can be lower, while ID probes lead to a less pure sample requiring a harder $\mathrm{p_T}$ cut. For calorimeter and ID probes, which use the Inner Detector information, a loose impact parameter cut and the quality requirements in Table 5.3 are applied. A very loose track isolation cut is applied to enhance the purity of the sample while ensuring that the measured reconstruction efficiencies are valid also for non-isolated muons. The latter assumption has been tested with Monte Carlo simulations. The effect of the isolation cut on the selection can be judged from Fig. 5.3a: all backgrounds are reduced, in particular $t\bar{t}$ production.

For all probe definitions two additional cuts are applied:

- The invariant mass of the tag and probe pair is required to be close to the Z boson mass, $|m_{\mu\mu} - m_Z| < 10$ GeV, and
- the tag and probe are required to be approximatively back-to-back in the transverse plane as expected for $Z \to \mu\mu$ events produced nearly at rest.

The effect of these two cuts for ID Probes is shown in Figures 5.3b and 5.3c. All the backgrounds are strongly reduced, in particular $Z \to \tau\tau$, without affecting the signal significantly. The probe selection cuts are summarised in Table 5.5.

Table 5.5: Cuts applied for probe muon selection. The $\mathrm{p_T}$ cut varies depending on the application. In the table the minimum cut values are shown. For lower $\mathrm{p_T}$ thresholds, the signal to background ratio becomes too low.

Muon probe cuts	
Identification	Either SA or CB muon
Kinematic cuts	$\mathrm{p_T} > 10$ GeV, $|\eta| < 2.7$
Isolation	$\frac{\sum^{\Delta R=0.4} p_T^{tracks}}{\mathrm{p_T}^{\mathrm{muon}}} < 0.2$
ID probe cuts	
Kinematic cuts	$\mathrm{p_T} > 20$ GeV, $|\eta| < 2.5$
Impact parameter cuts	$|z_0| < 10$ mm
Isolation	$\frac{\sum^{\Delta R=0.4} p_T^{tracks}}{\mathrm{p_T}^{\mathrm{muon}}} < 0.2$
Quality requirements	From Table 5.3
Calorimeter probe cuts	
Kinematic cuts	$\mathrm{p_T} > 15$ GeV, $|\eta| < 2.5$
Impact parameter cuts	$|z_0| < 10$ mm
Isolation	$\frac{\sum^{\Delta R=0.4} p_T^{tracks}}{\mathrm{p_T}^{\mathrm{muon}}} < 0.2$
Quality requirements	From Table 5.3
Common cuts	
Invariant mass of Tag-and-Probe pair	$|m_{\mu\mu} - m_Z| < 10$ GeV
Angular distance between Tag and Probe in the transverse plane	$|\Delta\phi^{T\&P}| > 2$

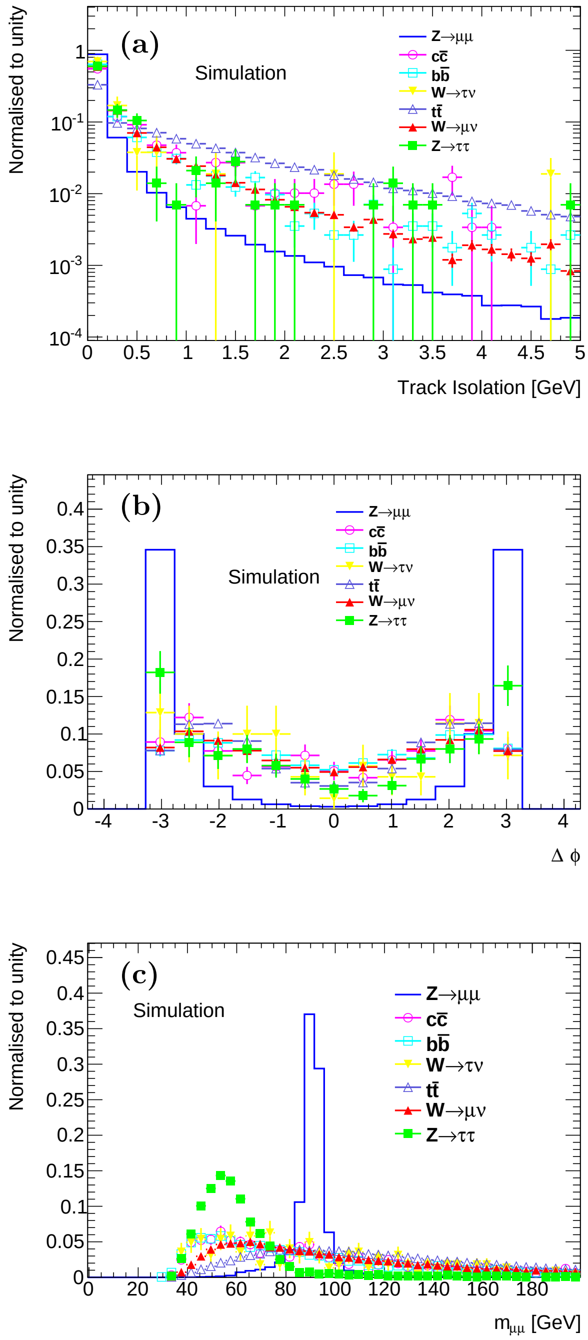

Figure 5.3: Distributions of the isolation of the ID probe (a), of the angle $\Delta\phi$ between the tag muon and the ID probe muon tracks (b) and of the invariant mass of the tag and ID probe muon pair (c) for signal and background Monte Carlo samples. All distributions are normalised to unity.

5.1.4.4 Matching

After selection of a tag and probe pair, the probe is spatially matched with a reconstructed object for which the reconstruction efficiency is determined as the fraction of successfully matched probes (see Table 5.6). For all muon objects, ID and calorimeter probes are alternatively used to evaluate the systematic error of the efficiency measurement. The main systematic uncertainty is due the background estimates. Comparing ID and calorimeter probes, where the latter select a $Z \to \mu\mu$ sample with much lower background contribution, this uncertainty can be assessed. A detailed discussion of the systematic uncertainty for the efficiency measurement is given in Section 5.1.7.

Table 5.6: Definition of probe muons and objects matched to the probes for the efficiency measurements

Measurement	**Probe**	**Object matched**
ID efficiency	Muon probe	ID track, ΔR <0.05
Calo muon efficiency	Muon probe ID track	Calo muon, ΔR <0.01
CB muon efficiency	ID track Calo muon	CB muon, ΔR <0.01
ST muon efficiency	ID track Calo muon	ST muon, ΔR <0.01
SA muon efficiency	ID track Calo muon	SA muon, ΔR <0.01

5.1.5 Inner Detector reconstruction efficiency

The measurement of the ID reconstruction efficiency is performed using a muon probe, which can be either a CB muon (which is by definition matched with an ID track) or a SA muon. SA muons which cannot be matched within $\Delta R = 0.05$ with an ID track represent cases in which the ID is inefficient. Figure 5.5 shows the p_T distribution of the muon probes in data and Monte Carlo. The selection of muon probes ensures a high background rejection. Table 5.7 gives the background contributions as predicted by the simulations.

The ID track reconstruction efficiency is shown in Fig. 5.6 as a function of η and p_T of the track. The efficiency is very close to 1 for all η covered by the ID and independent from the p_T of the track. Data is very well described by the simulations. The efficiency drop at $|\eta|$ values close to 2.5 is due to the acceptance limit of the ID. In Figure 5.7 the tracking efficiency is shown in data for different data taking periods and as a function of the average number of proton-proton interactions per event $< \mu >$. In the latter figure the comparison with the simulation is also shown. The effects of the pile-up on the tracking efficiency have been found to be negligible and the efficiency is stable during the whole year.

Table 5.7: Contributions of signal and backgrounds to the Monte Carlo muon probe sample.

Process	Contribution
$Z \to \mu\mu$	99.95%
$t\bar{t}$	0.03%
$Z \to \tau\tau$	0.01%
$W \to \mu\nu$	-
$W \to \tau\nu$	-
$c\bar{c}$	-
$b\bar{b}$	-

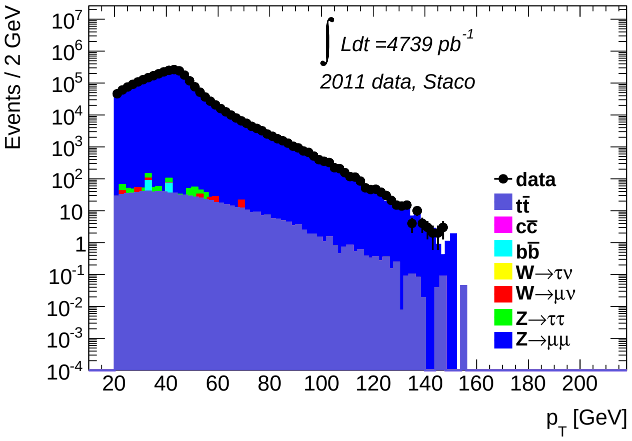

Figure 5.5: p_T distribution of muon probes selected for ID reconstruction efficiency measurement.

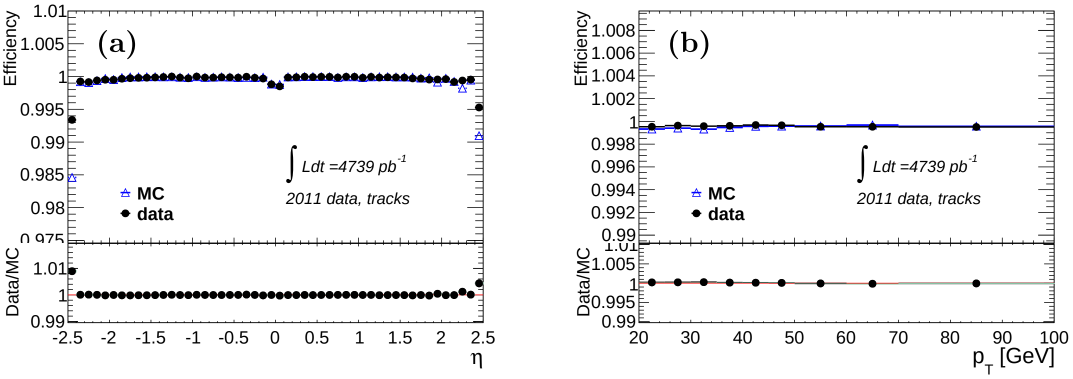

Figure 5.6: ID track reconstruction efficiency measured as a function of η (a) and p_T (b) for 2011 data and simulation with the Tag-and-Probe method. The bottom part of the plots show the correction factor SF for the Monte Carlo prediction. Only statistical errors are shown.

In Fig. 5.8 the reconstruction efficiency of ID tracks with application of the quality cuts listed in Table 5.3 is shown as a function of η and p_T. The cuts are used to reject tracks of non-prompt muons. Even with these cuts the overall efficiency is higher than 98%. The effects of the different quality cuts are shown in Fig. 5.9. Drops in efficiency are caused by reduced spatial coverage of the ID sub-detectors: TRT at $\eta = 0$, where the reduction is overestimated in simulations by 1%, and $\eta \approx 2$, where the reduction is underestimated in Monte Carlo by 1%, and SCT at $\eta \approx 1.1$. The overall level of agreement between data and simulation is excellent.

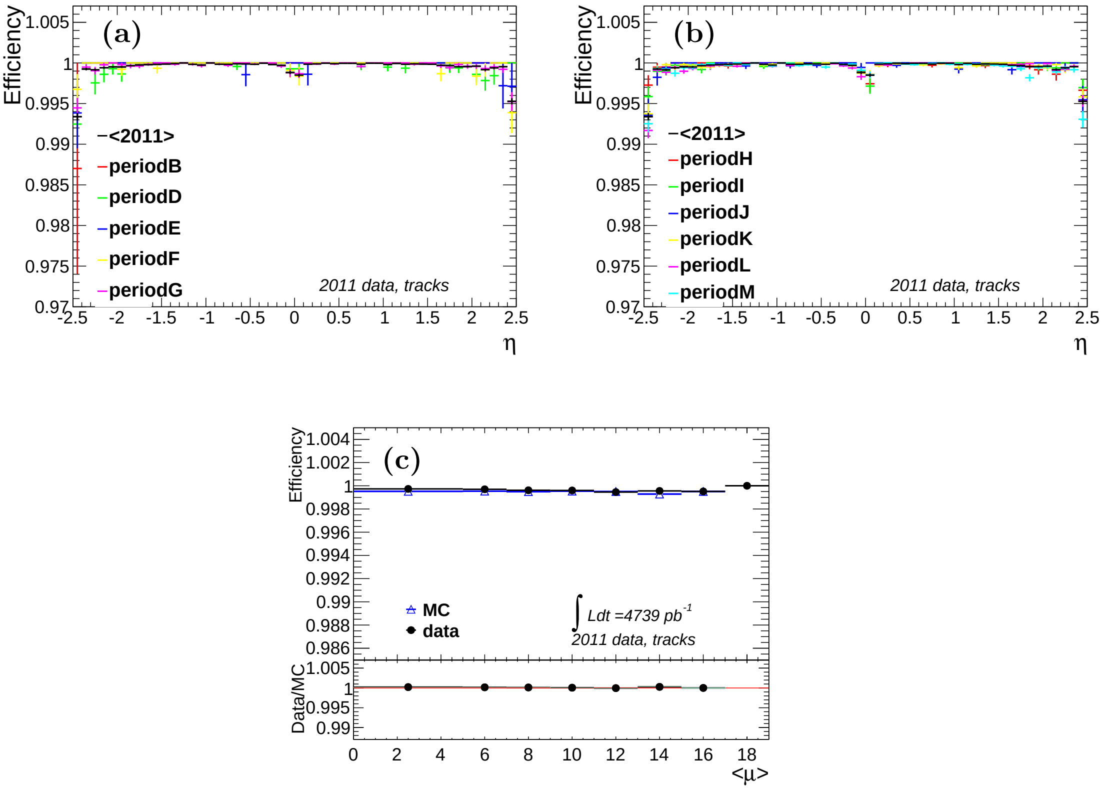

Figure 5.7: ID track reconstruction efficiency measured in early (a) and late (b) 2011 data taking periods and as a function of the average number of proton-proton interactions per event $< \mu >$ (c). In the latter case the data is compared with the simulations; the bottom part of the plot shows the SF. Only statistical errors are shown.

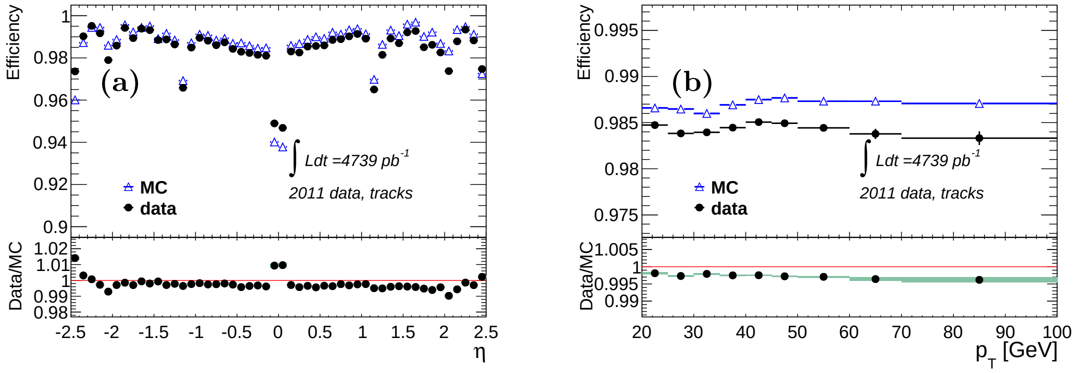

Figure 5.8: ID track reconstruction efficiency measured as a function of η (a) and p_T (b) after the application of the quality cuts in Table 5.3 for 2011 data and Monte Carlo simulations. The bottom part of the plots shows the Monte Carlo scale factors. Only statistical errors are shown.

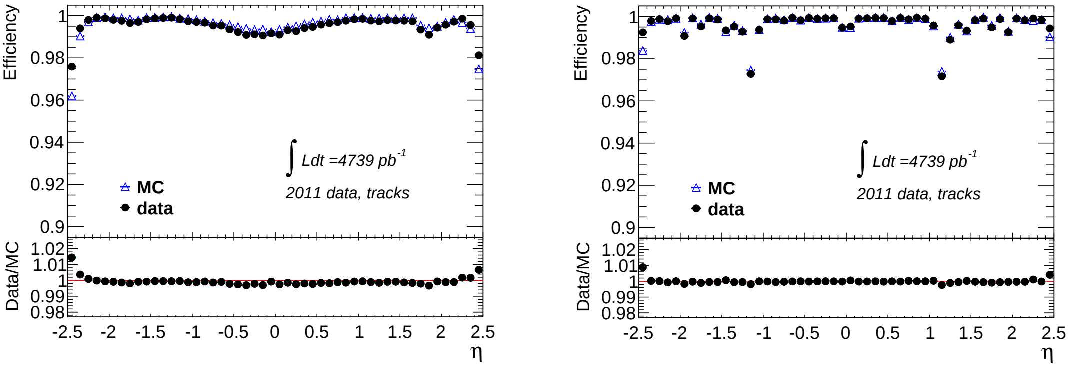

(a) Cut on the number of Pixel Detector hits

(b) Cut on the number of SCT hits

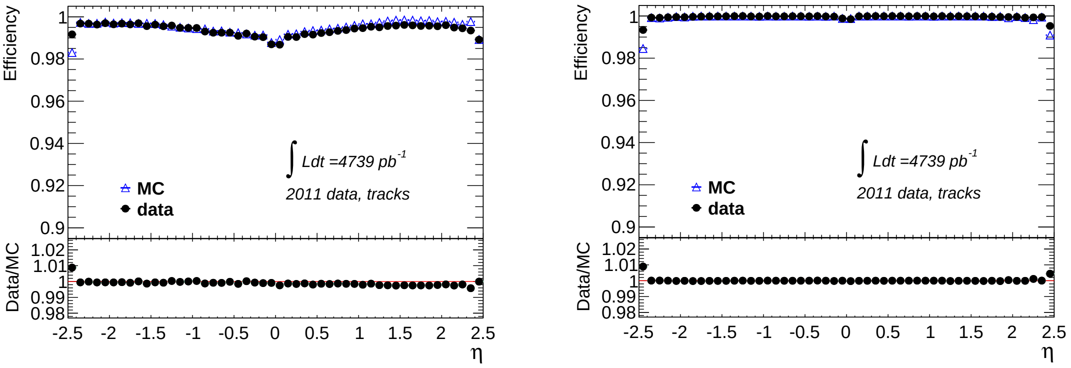

(c) Cut on the number of B-layer hits

(d) Cut on the number of missing hits (holes) in the silicon detectors

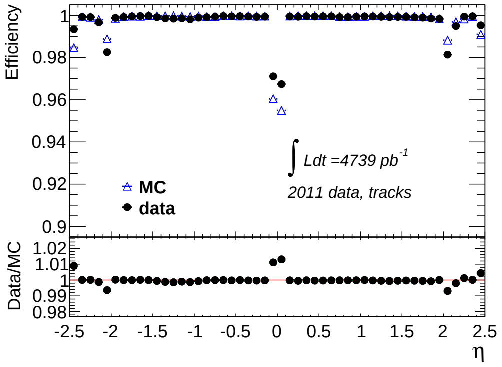

(e) Cut on the number of TRT hits

Figure 5.9: ID track reconstruction efficiency measured as a function of η for 2011 data and Monte Carlo simulations after the different quality cuts in Table 5.3. The bottom part of the plots shows the SF. Only statistical errors are shown.

5.1.6 Muon reconstruction efficiency

The measurement of the muon reconstruction efficiency is performed using ID probes and matching them to reconstructed muon tracks. In Table 5.8 the estimated contributions of signal and background to this probe sample are shown. Fig. 5.11 shows the probe p_T distribution for data and Monte Carlo. The selected sample is very pure, leading to small systematic errors.

The measured efficiency for the Muid combined reconstruction (see Section 4.7) in data and Monte Carlo and the relative SF are shown in Figure 5.12 as a function of the spectrometer regions and of η, ϕ, p_T, average number $< \mu >$ of collisions per bunch crossing. Data and simulation agree well and the SF shows little dependence on p_T and on the level of pile-up $< \mu >$. Segment tagged (ST) muons can be used in addition to the CB muons to enhance the efficiency, especially in regions with reduced geometrical acceptance of the MS. In Fig. 5.13 the total muon reconstruction efficiency, including ID track reconstruction efficiency after the quality cuts of Table 5.3, is shown for CB muons and for CB and ST muons for the two reconstruction chains Staco and Muid. Both reconstruction algorithms have similar performance, with the only significant difference in the lower CB muon efficiency of the Staco chain in the transition region. This is caused by the tighter reconstruction criteria applied by this algorithm, which ensure high momentum resolution by requiring reconstruction in all three MS layers. No variations in the reconstruction efficiency have been found during the 2011 data taking (see Figure 5.14).

The correction factors used in the cross section measurements presented in this thesis are determined separately for the 10 MS regions and for the hemispheres A ($\eta > 0$) and C ($\eta < 0$) of the spectrometer.

Table 5.8: Contributions of signal and background to the Monte Carlo ID probe sample.

Process	Contribution
$Z \to \mu\mu$	99.68%
$W \to \mu\nu$	0.19%
$t\bar{t}$	0.06%
$b\bar{b}$	0.03%
$Z \to \tau\tau$	0.02%
$W \to \tau\nu$	0.02%
$c\bar{c}$	0.01%

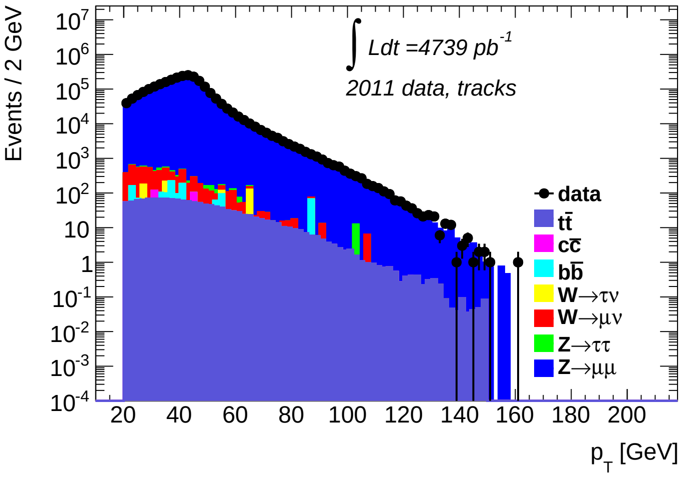

Figure 5.11: p_T distribution of ID probe muons selected for MS reconstruction efficiency measurement.

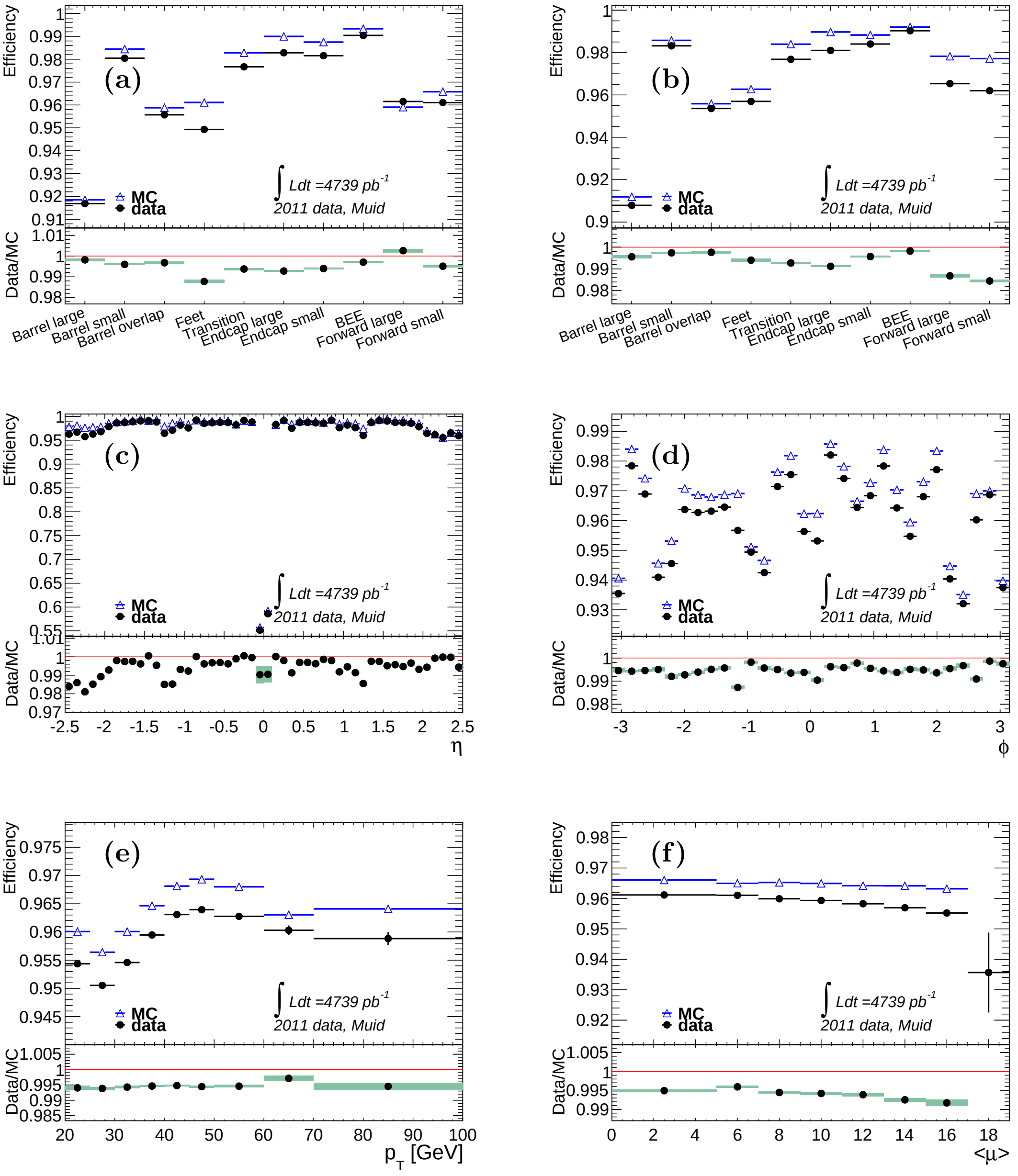

Figure 5.12: CB muon reconstruction efficiency of the Muid chain measured as a function of Muon Spectrometer regions in hemisphere A (a) and C (b), of η (c), ϕ (d), p_T (e) and of the average number of proton interactions per bunch crossing $< \mu >$ (f). The bottom part of the plots shows the SF. Only statistical errors are shown.

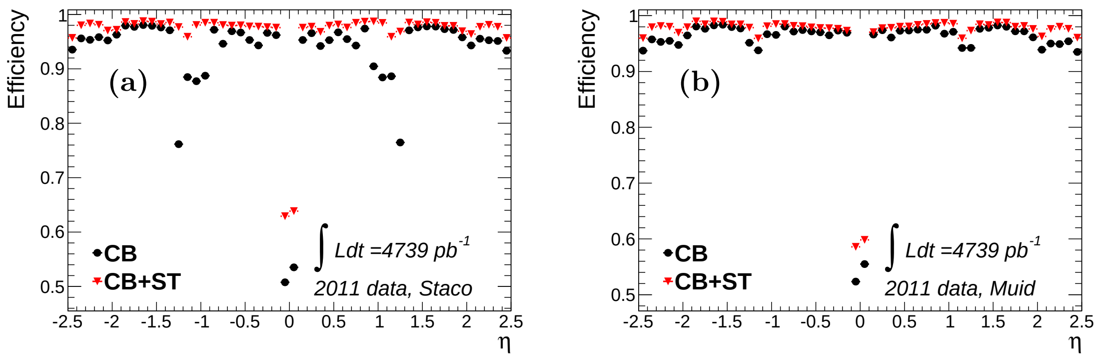

Figure 5.13: Efficiency of CB muons only (black circles) and of CB and ST muons (red triangles) reconstructed by the Staco (a) and the Muid (b) chains measured as a function of η for 2011 data. Only statistical errors are shown.

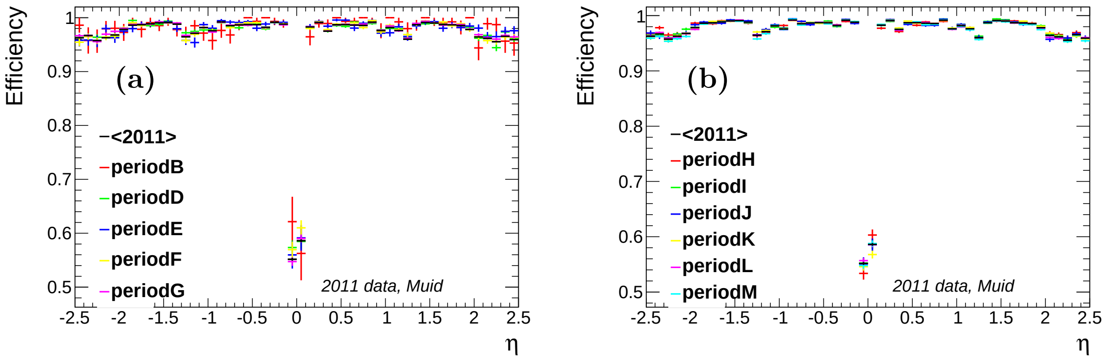

Figure 5.14: CB muon reconstruction efficiency measured during the early (a) and late (b) 2011 data taking periods for the Muid chain. The black points represent the average over the whole year. Only statistical errors are shown.

5.1.7 Systematic errors of the muon efficiency scale factors

The muon reconstruction efficiency scale factors are defined as a ratio, therefore most systematic errors cancel. The reweighting of the z_{vtx} and $< \mu >$ distributions (see Section 5.1.4) ensures agreement in the description of the beam spot and of the pile-up between data and Monte Carlo simulation. The dependence of the SF on the muon p_T is found to be negligible, as discussed in Section 5.1.6, therefore no correction of the muon momentum resolution is taken into account for the simulated events. The main source of systematic error is the background contribution to the measurement, which is entirely estimated from simulation. The purity of the selected samples is however so high that the uncertainties in the background estimation have small effects on the determination of the scale factors.

To assess the impact of the background uncertainties the muon reconstruction efficiency scale factors evaluated with the ID probe sample, which has an estimated background contribution of about 0.3%, and with the calorimeter muon probe sample, which has a background contribution below 0.1%, are compared. The results are shown in Figure 5.17 for the Muid chain: the two measurements are in very good agreement. The systematic uncertainty on the SFs is defined as the difference

$$\sigma^{syst}(SF) = \left|SF_{ID\ probe} - SF_{calo\ probe}\right| \ , \tag{5.4}$$

evaluated separately for the 10 MS regions defined in Section 5.1.6 and for the two hemispheres of the detector. A minimum systematic uncertainty per region of 0.1% is assumed, which is increased to

- 0.5 % for muons with 10 GeV $< \mathrm{p_T} <$ 15 GeV,
- 1.0 % for muons with 6 GeV $< \mathrm{p_T} <$ 10 GeV and
- 2.0 % for muons with 3 GeV $< \mathrm{p_T} <$ 6 GeV

for the reasons discussed in Section 5.1.8.

The total error on the SFs is determined as the linear sum of the statistical and systematic errors $\sigma(SF) = \sigma^{stat}(SF) + \sigma^{syst}(SF)$. The systematic variations are performed with the same data and simulation samples used for the SF measurements themselves. Statistical and the systematic errors are therefore considered conservatively totally correlated.

Table 5.9: Contributions of signal and background to the Monte Carlo calorimeter probe sample.

Process	Contribution
$Z \to \mu\mu$	99.94%
$t\bar{t}$	0.03%
$W \to \mu\nu$	0.01%
$Z \to \tau\tau$	0.01%
$W \to \tau\nu$	-
$c\bar{c}$	-
$b\bar{b}$	-

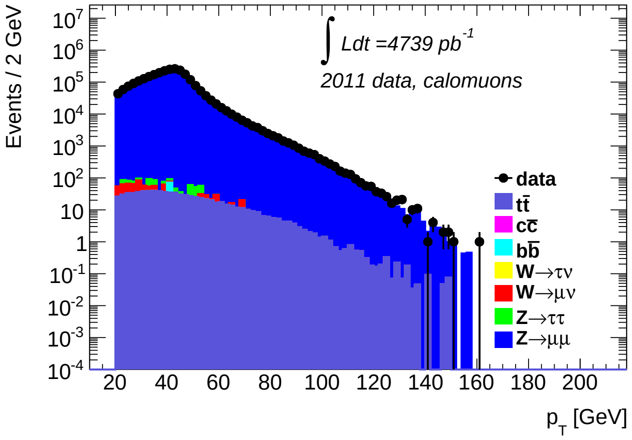

Figure 5.16: $\mathrm{p_T}$ distribution of calorimeter probe muons selected for the MS reconstruction efficiency measurement.

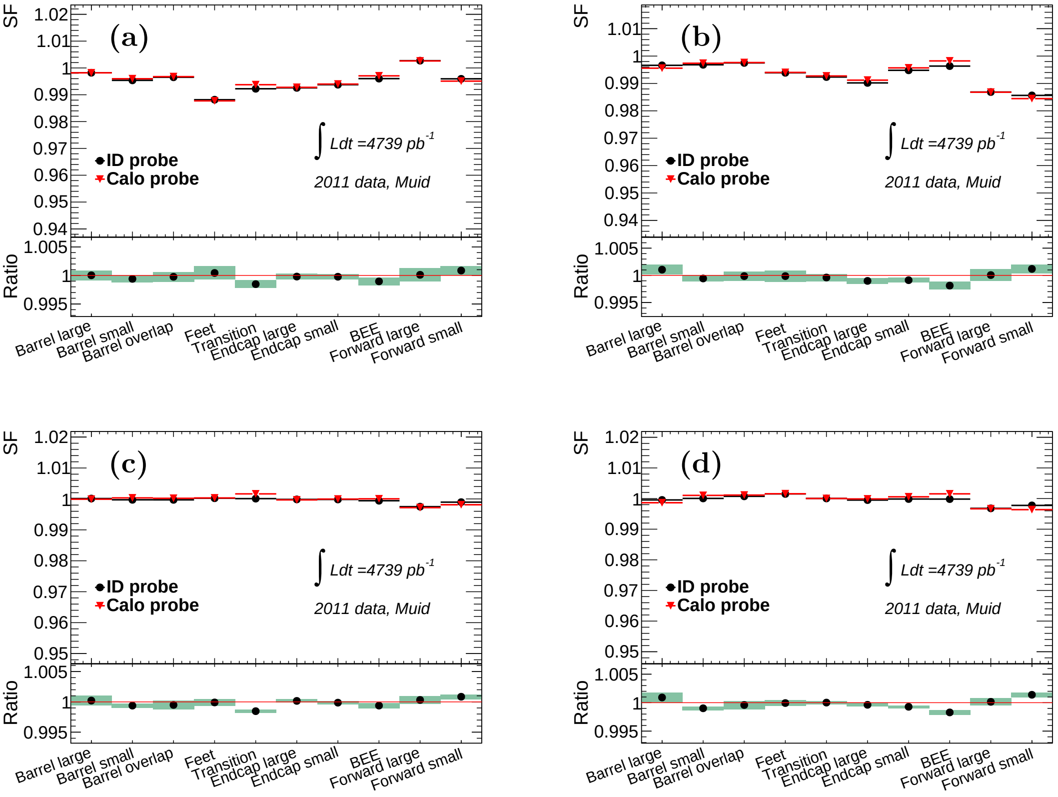

Figure 5.17: Comparison of the SF evaluated with ID probes (black circles) and with calorimeter probes (red circles) for CB (a, b) and CB and ST muons (c, d) reconstructed by the Muid chain in side A (a, c) and C (b, d) of the spectrometer in 2011 data and simulation. The errors shown are statistical.

5.1.8 Muon reconstruction efficiency for low-p_T muons

The measurement of the reconstruction efficiency and of the SF using the Tag-and-Probe method in $Z \to \mu\mu$ events is possible only above a certain p_T threshold. Below $p_T \approx 20$ GeV the background contribution is not negligible any more. The SF determination with ID probes has been extended down to $p_T = 15$ GeV by using the calorimeter probe method which is less affected by background. Both methods agree for $p_T > 20$ GeV. Below 15 GeV even the calorimeter probe samples starts to be affected by the background. In order to evaluate the efficiencies for low-p_T muons, a Tag-and-Probe analysis has been performed on $J/\Psi \to \mu\mu$ events [87] which confirmed the SF measurements in $Z \to \mu\mu$ events even for low-p_T muons, although with large uncertainty. For this reason, the SFs measured in $Z \to \mu\mu$ events are used for the whole muon p_T range but with increased systematic errors in the low p_T region (see Sec .5.1.7) which are determined by a comparison with the central value of the $J/\Psi \to \mu\mu$ measurement.

5.2 Measurement of the muon trigger and isolation efficiency

In this section the efficiency of the muon isolation requirements applied in many analyses to reduce the QCD multi-jet background contribution and of the muon trigger system is studied using the Tag-and-Probe method. For the trigger efficiency measurement the muon probes must be either combined or stand-alone muons. No isolation cut is applied to the probes to avoid bias in the measurement, since the use of muon probes already selects a very pure sample of $Z \to \mu\mu$ events. The efficiency of a trigger requirement is given by the fraction of probes matched with muons reconstructed by the event filter (EF) within $\Delta R = 0.15$. In the 2011 data set, the lowest threshold unprescaled muon triggers are EF_mu18 [88], requiring a single muon with $\mathrm{p_T} > 18$ GeV, for the early data taking periods (B-I) at lower instantaneous luminosity, and EF_mu18_medium [88] with the same $\mathrm{p_T}$ cut but tighter selection of the seeding first-level muons for the late periods (J-M). The efficiency measurements shown in Fig. 5.18 have been performed for $\mathrm{p_T} > 20$ GeV, in the plateau region of the trigger efficiency. In the endcap regions the trigger efficiency is about 85%. In the barrel region a stronger η dependency is found and the average efficiency is about 75%.

The same method is used to measure the efficiency of the muon isolation requirements The efficiency is defined as the fraction of muon probes which are isolated. The $Z \to \mu\mu$ selected sample consists mainly of isolated muons, but $Z+$ jets events also contribute. The resulting efficiencies for a track isolation cut of $\sum^{\Delta R=0.3} p_T^{tracks} < 2.5$ GeV and calorimeter isolation cut of $\sum^{\Delta R=0.2} E_T^{calo} < 4$ GeV are shown in Fig. 5.19. There is an excellent agreement between data and simulations and no dependence on the muon $\mathrm{p_T}$ and on the pile-up conditions.

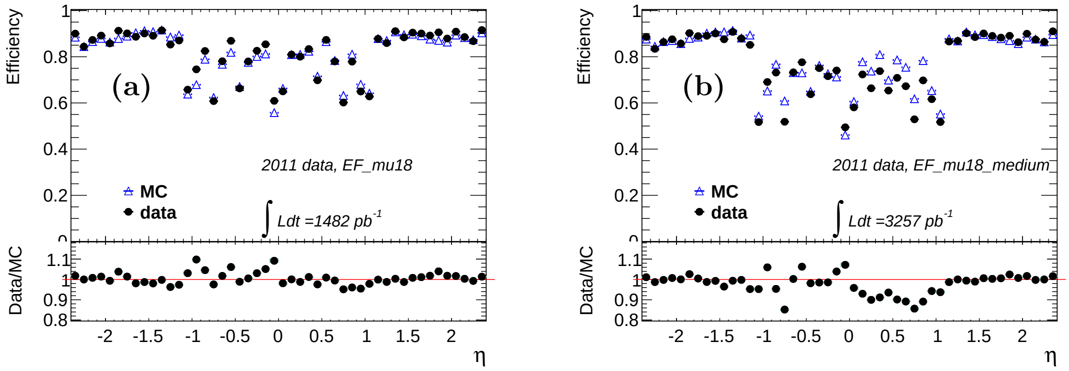

Figure 5.18: Muon trigger efficiency measurement for 2011 data and simulation and SF for EF_mu18 (a) and EF_mu18_medium (b) trigger requirements. Statistical error only is shown.

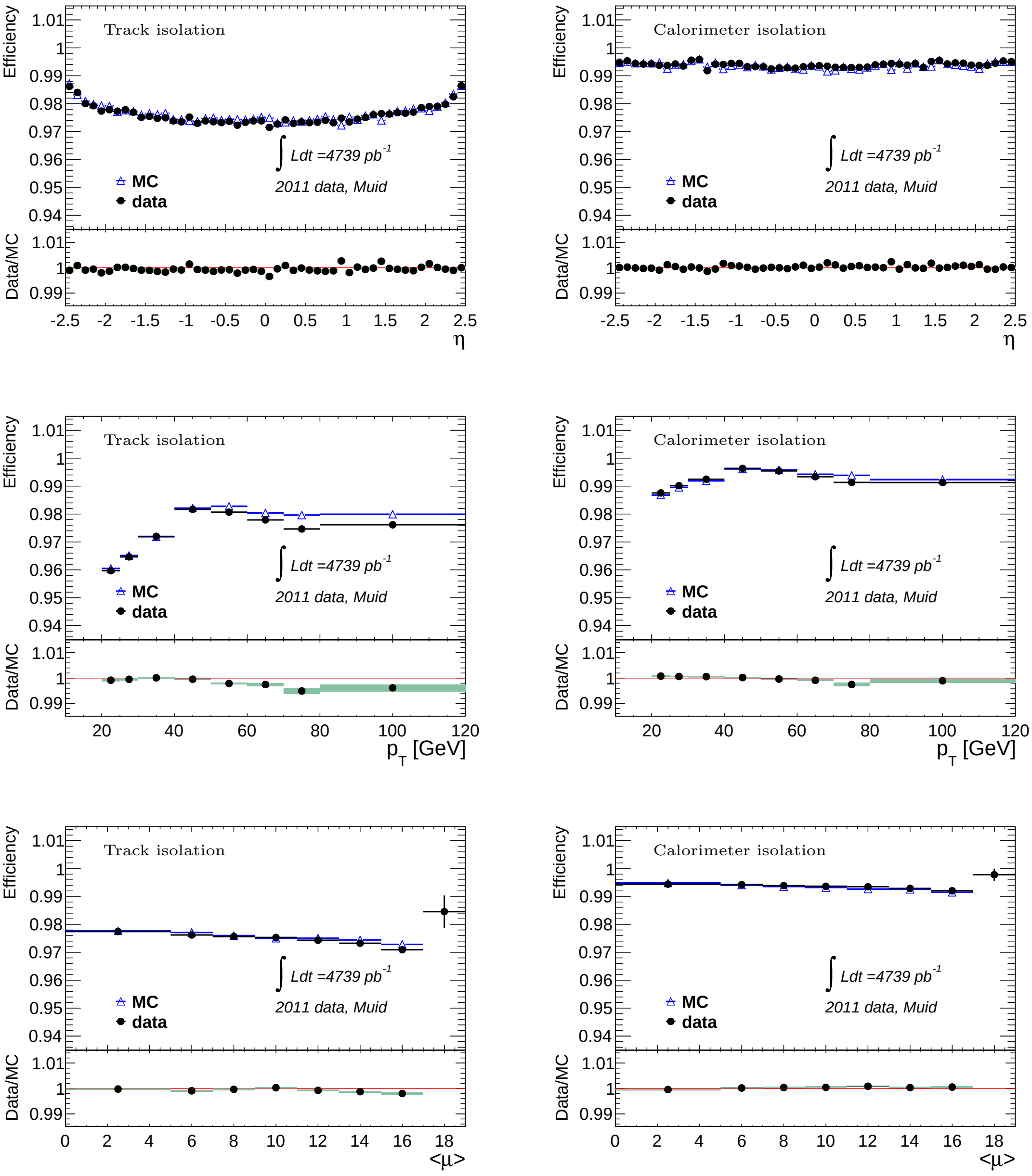

Figure 5.19: Muon isolation efficiency measurement for 2011 data and simulation for a track isolation cut of $\sum^{\Delta R=0.3} p_T^{tracks} < 2.5$ GeV (left plots) and a calorimeter isolation cut of $\sum^{\Delta R=0.2} E_T^{calo} < 4$ GeV (right plots). Only statistical errors are shown.

5.3 Heavy flavour jet tagging efficiency

The Soft Muon Tagger (SMT) is an algorithm designed to discriminate heavy flavour jets (c and b jets) from light-quark jets. The semileptonic decays of c and b hadrons are exploited, in particular the muonic decays which provide a very clean signature. The efficiency reduction due to the semileptonic branching ratios of the heavy flavour hadrons, of order 10%, is compensated by a high rejection factor for light-quark jets which rarely contain muons, mostly non-prompt muons from pion and kaon decays which can be further rejected with dedicated muon selection.

The SMT selects jets matched to a reconstructed muon within $\Delta R = 0.5$, requiring

- combined muons by the Staco chain (see Section 4.7) with $\mathrm{p_T}$>4 GeV, $|d_0| < 3$ mm and $|z_0 \sin\theta| < 3$ mm,
- ID track associated to the muon fulfilling the quality requirements of Table 5.3 and
- a combination of the ID and the spectrometer track with $\chi^2_{match} < 3.2$ (see Section 4.7).

The use of combined muons ensures an strong fake rejection at high muon efficiency. The track quality cuts of Table 5.3 and the cuts on the impact parameter of the muon track reduce the contamination from non-prompt muon. The χ^2_{match} cut also reduces the non-prompt muons contributions since pions and kaons have rather long lifetimes and on average decay after flight distance of the order of a metre in the ID leading to a bias in the ID track and to a higher χ^2_{match} value. The mistag rate of the tagger, i.e. the fraction of light-quark jets which are wrongly tagged as heavy-flavour jets, has been measured in a data sample on QCD multi-jet events to be 0.2%-0.5% depending on the η and $\mathrm{p_T}$ of the jet.

The efficiency of the soft muon tagger measured in Monte Carlo simulation is corrected with data-driven techniques to match the efficiency in the data. The tagging efficiency depends on the branching ratio of the semimuonic heavy-flavour decays, on their kinematics and on the final state selection applied. An example of such effects is given in Section 7.9.3 in the context of the $W+$ c-jets cross section measurement. However, the efficiency of the muon selection applied by the SMT only depends on the muon kinematics and can thus be measured using the Tag-and-Probe method as described below.

The measurement of the efficiency of the muon selection criteria applied by the SMT has been performed with $J/\Psi \rightarrow \mu\mu$ and $Z \rightarrow \mu\mu$ events. In this section the latter are discussed. The tag definition of Section 5.1.4 is used, and CB muons with $\mathrm{p_T} > 10$ GeV are used as muon probes. The efficiency is the fraction of muon probes satisfying the SMT requirements. The χ^2_{match} distribution of the selected muon probes is shown in Fig. 5.20 The results are shown in Fig. 5.21. The SF decrease with increasing $\mathrm{p_T}$ due to the ideal MS alignment which is assumed as a standard in the Monte Carlo simulation. In the region $\eta > 2$, corresponding to the detector region in which Cathode Strip Chambers are used in the hemisphere A of the muon spectrometer, a strong drop of the efficiency in the simulation is visible, which is due to an error in the simulation of the detector response resulting in a χ^2_{match} distribution with much bigger tails than in the corresponding region $\eta <$ -2 of the hemisphere C, as shown in Fig. 5.22f. Fig. 5.23 shows the comparison of the efficiencies and SF for simulations with ideal alignment and with realistic misalignment. In the latter case, the $\mathrm{p_T}$ dependence of the SF is significantly reduced. The $\mathrm{p_T}$ dependence is not too relevant for the practical applications of the SMT: muon resulting from b and c hadrons decays have low transverse momentum, usually below 30 GeV, a region where the $\mathrm{p_T}$ dependence is less significant.

The possible bias introduced by the efficiency measurement performed in a $Z \rightarrow \mu\mu$ sample, with mostly isolated muons, while the SMT selection criteria are applied to muons inside jets has been studied in a sample of probe muons selected without the usual isolation cut adopted for the Tag-and-Probe method. It is shown in Fig. 5.24 that the efficiency measurement does not depend significantly on the isolation of the muons.

The systematic error of the SF in this case cannot be determined by changing the probe definition as it was done for the reconstruction efficiency measurement. To study the impact of uncertainties in the background contribution to the sample of muon probes the cut on tag-and-probe invariant mass has been varied from the nominal cut of $|m_{\mu\mu} - m_Z| < 10$ GeV to 7.5 GeV and 15 GeV. Similarly the probe track isolation cut has been varied from $\frac{\sum^{\Delta R=0.4} p_T^{tracks}}{\mathrm{p_T}^{\mathrm{muon}}} < 0.2$ to 0.1 and 0.3.
The total systematic error is determined as the quadratic sum of both contributions (see Fig. 5.25) and found to be small. The total error on the SF is the linear sum of the statistical and systematic error (see Section 5.1.6).

The SMT SFs used for the $W+$ c-jet cross section measurement described in Chapter 7 are determined as a function of η and $\mathrm{p_T}$ in the low-$\mathrm{p_T}$ region, where the measurement has been performed in $J/\Psi \rightarrow \mu\mu$ events, and as a function of $\mathrm{p_T}$ and MS region for muon $\mathrm{p_T}$>12 GeV, where the measurement has been performed with $Z \rightarrow \mu\mu$ events.

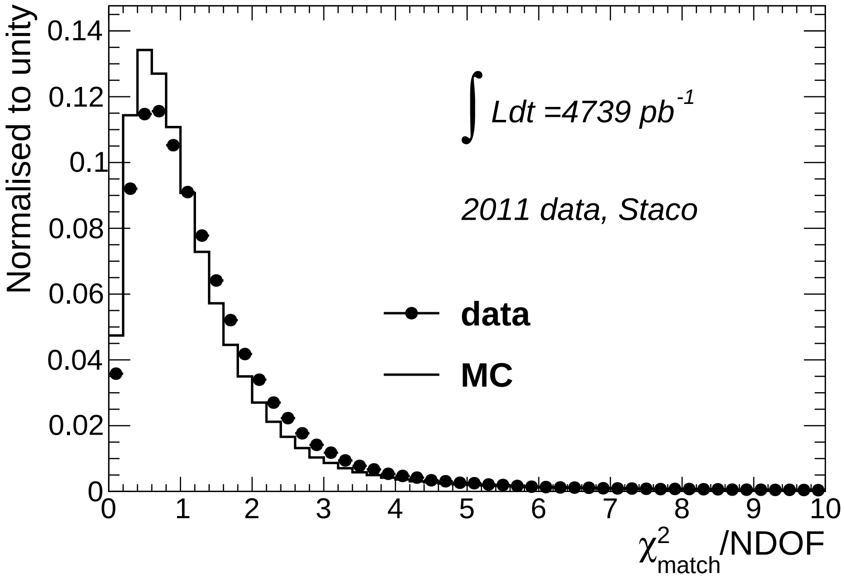

Figure 5.20: χ^2_{match} distribution of muon probes from $Z \to \mu\mu$ events in 2011 data and simulation normalised to unity.

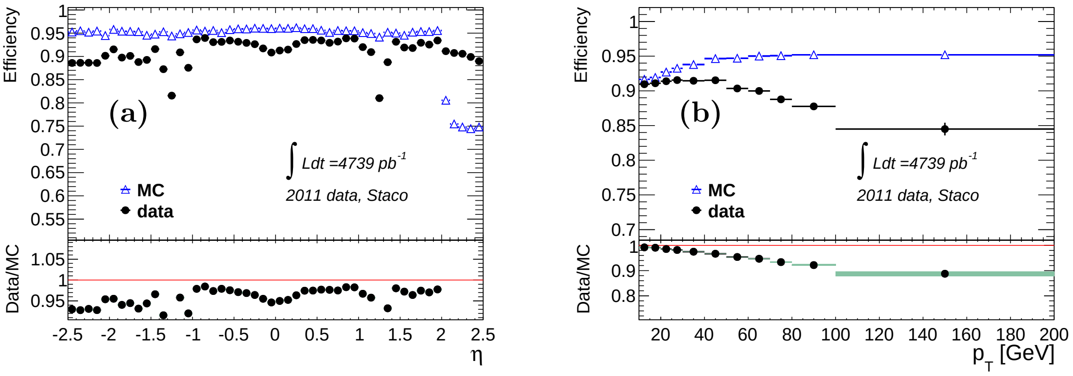

Figure 5.21: SMT muon selection efficiency and scale factor as a function of η (a) and p_T (b) for 2011 data and simulation.

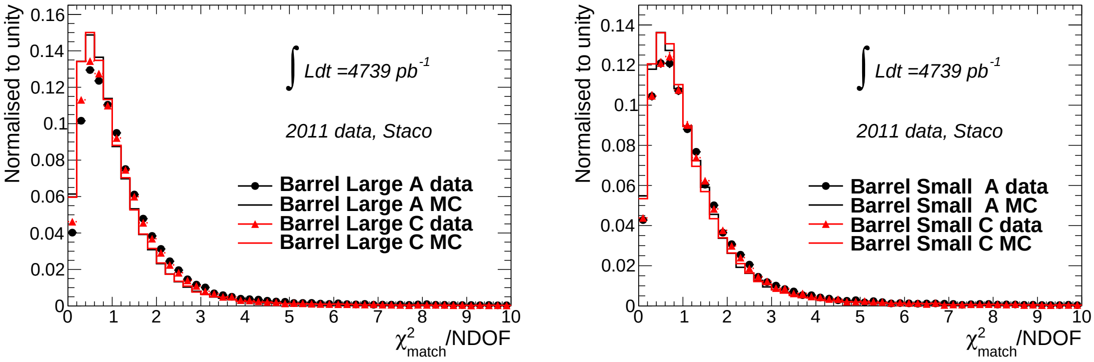

(a) Large barrel region **(b)** Small barrel region

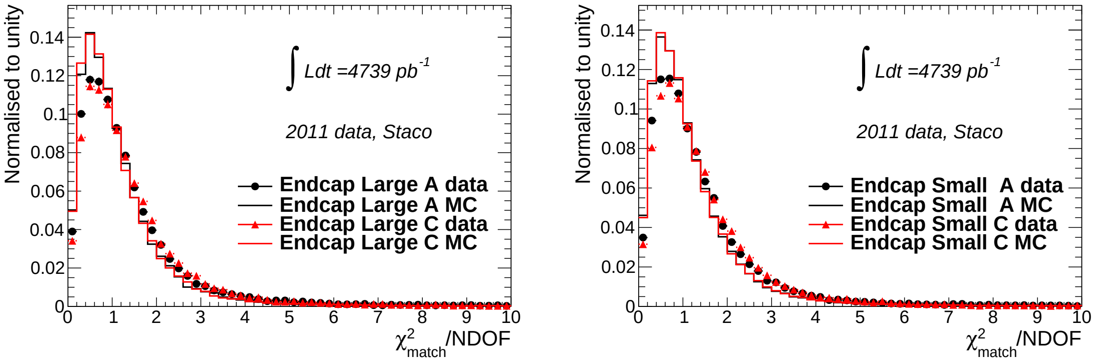

(c) Large endcap region **(d)** Small endcap region

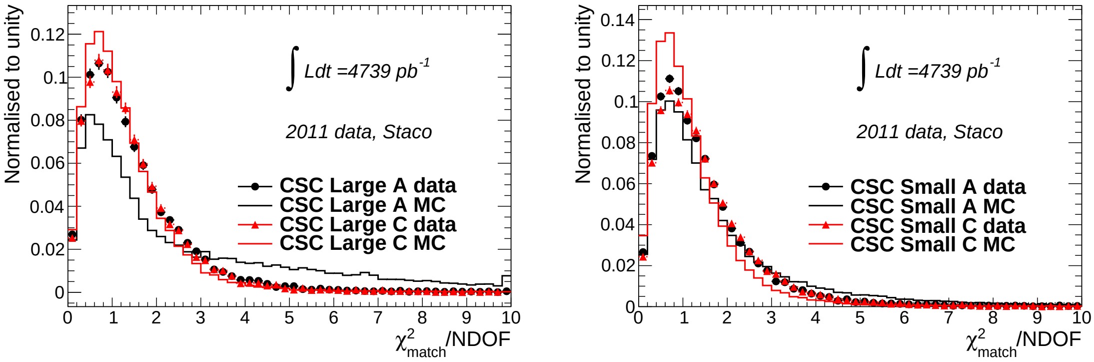

(e) Large CSC region **(f)** Small CSC region

Figure 5.22: χ^2_{match} distributions for muon probes with 10 GeV $< p_T <$ 30 GeV normalised to unity area evaluated in 2011 data and simulations for different MS regions. Regions in side A ($\eta > 0$) are drawn in black, regions in side C ($\eta < 0$) in red (see Section 5.1.1).

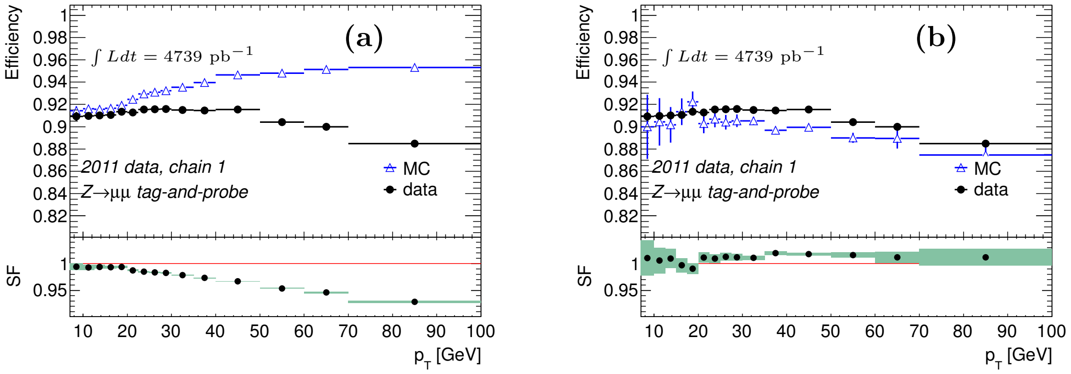

Figure 5.23: SMT muon selection efficiency in 2011 data and simulation and the SF as a function of p_T for simulation with ideal MS alignment (a) and with realistic misalignment (b).

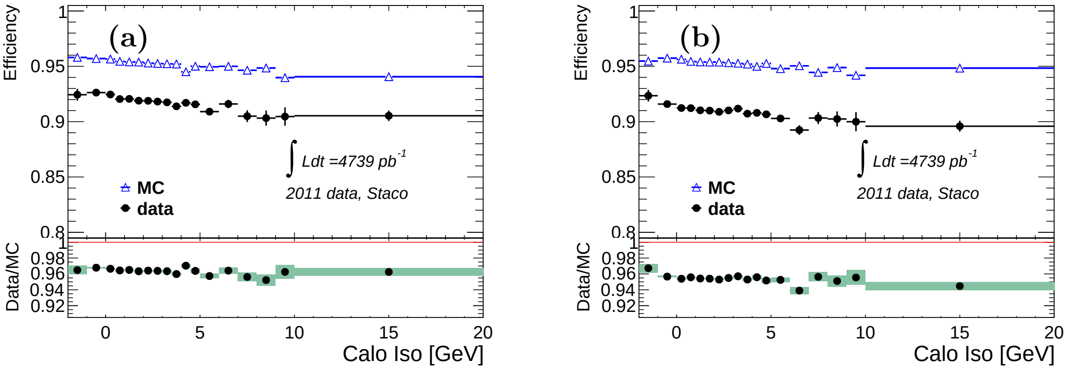

Figure 5.24: SMT muon selection efficiency in 2011 data and simulation and SF as a function of the calorimeter isolation cut on the probe in side A (a) and C (b) of the muon spectrometer.

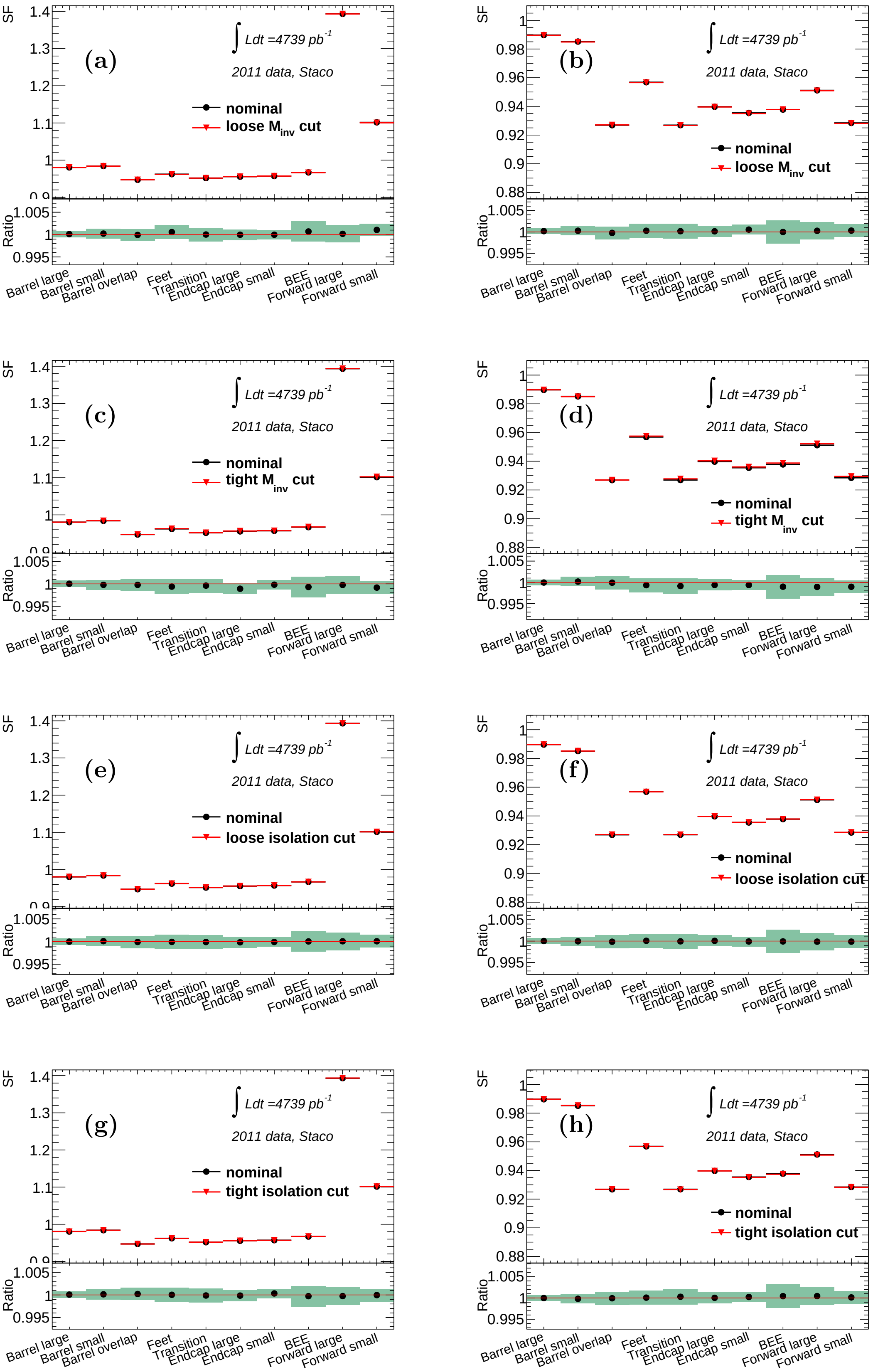

Figure 5.25: Systematic errors of the SMT muon selection efficiency SF determined as a function of the MS region for side A (left plots) and C (right plots) of the spectrometer by varying the tag and probe invariant mass cut applied in the selection of the sample to looser (a,b) and tighter (c,d) values and varying the isolation cut on the probe to looser (e,f) and tighter (g,h) values. The SF determined with the nominal (black circles) and modified (red triangles) cuts are shown. The bottom part of the plots shows the ratio between the two determinations, the green band represents the statistical error on the ratio.

5.4 Conclusion

The performance of the ATLAS Inner Detector and Muon Spectrometer have been studied in data collected in 2011 and in Monte Carlo simulation using the Tag-and-Probe method in $Z \to \mu\mu$ events.

The Inner Detector reconstruction efficiency for muon tracks is found to be nearly 1 in the data and simulation. The inefficiency introduced for muon ID tracks by the quality criteria applied to reject the contribution of non-prompt muons is measured in data to be about 1.6%, slightly higher than the expectation in simulations of 1.4%. The muon reconstruction efficiency for the combined reconstruction of ID and MS tracks is found to be higher than 95% in data, in good agreement with the simulations. Corrections factors of the order of 1% have been derived for the Monte Carlo events. No dependence is found on the $\mathrm{p_T}$ of the muon and on the pile-up conditions for the muon reconstruction. The systematic uncertainties of the correction factors for the simulations have been assessed to be at 0.1% level.

The efficiency of the cuts on muon isolation variables applied in physics analyses to reject mainly the QCD multi-jet background is found to be perfectly described by simulation. The trigger efficiency is found to be about 80% for the even filter algorithms used for the 2011 data set.

The efficiency of the muon selection criteria applied by the Soft Muon Tagger which identifies heavy-flavour jets is found to about 90% in data. In this case larger corrections scale factors are needed for Monte Carlo events since no misalignment is considered by default in the simulations. These corrections are anyway below 5% in the low $\mathrm{p_T}$ region of the semimuonic decays of heavy-flavour hadrons.

In conclusion, excellent performance are found for the ATLAS muon reconstruction and identification in the data set collected during 2011 in agreement with the expectations, a result confirmed by the measurements performed for the 2012 data set reported in Appendix B.

Chapter 6

Measurement of the $W+$ b-jet production cross section

The production of W bosons associated with jets ($W+$ jets) is a process predicted by the Standard Model (see Section 2.2). In second order perturbation theory, bottom quark-antiquark pairs are produced in association with a W boson according to the Feynman diagrams shown in Figure 6.1. Final states with a single b quark are suppressed because of the small values of the CKM matrix elements V_{ub} and V_{cb}.
The study of $W+$ b-jets production is an important test of perturbative QCD predictions. A measurement of the $W+$ b-jets production cross section performed by the CDF experiment [89] shows an excess over theoretical predictions, although with large uncertainties. $W+$ b-jets events are also an important background for the search for $H \to b\bar{b}$ decays in the process $pp \to WH + X \to Wb\bar{b} + X$, for single top quark and top quark $t\bar{t}$ pair production, and for processes predicted by theories beyond the Standard Model.

In this chapter, a measurement of the $W+$ b-jets production cross section with the ATLAS detector [1], which is the result of the efforts of a small analysis team, is described. The main contributions of this work are the signal event selection including measurement of the selection efficiency and the cross section determination with the assessment of the systematic uncertainties.

6.1 Data samples used for the analysis

The study of $W+$ b-jets production presented here uses an integrated luminosity of 35.5 pb^{-1} of proton-proton collisions data at $\sqrt{\text{s}}$=7 TeV, collected by the ATLAS detector during 2010. Only $W \to e\nu$ and $W \to \mu\nu$ decays are considered in the analysis.

The background processes taken into account for the measurement are listed in Table 6.1. $W+$ b-jets production via $t \to W + b$ decays is not included in the signal definition and

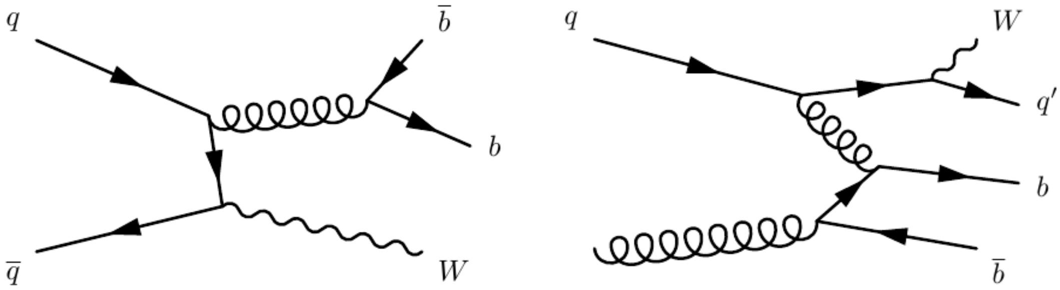

(a) LO diagram

(b) NLO diagram

Figure 6.1: Feynman diagrams for $W+$ b-jets production in proton-proton collisions: (a) leading order (LO) and (b) next-to-leading order (NLO).

therefore taken into account as a background. The contributions of $Z+$ jets events and of diboson and single-top productions are small and therefore estimated by Monte Carlo simulation. The largest background contributions are due to $t\bar{t}$ and $W+$ jets events which are determined by data-driven techniques using Monte Carlo simulations for the shapes of discriminating variables used for event selection. The QCD multi-jet background is entirely estimated from data.

$W+$ jets processes are generated using ALPGEN [47], interfaced with HERWIG [45] for the parton shower and with JIMMY [53] for the underlying event simulation. The production processes W+0-5 partons ($W+$ light-jets), $W + c$+0-4 partons, $W + c\bar{c}$+0-3 partons and $W + b\bar{b}$+0-3 partons are separately generated by ALPGEN: the matrix element is therefore calculated for each process with a fixed number of outgoing partons, and the resulting 19 simulated sample are combined to completely describe $W+$ jets production. The procedures for the removal of overlap between the samples are described in Section 6.1.1.

ALPGEN+HERWIG samples are used to simulate the $Z+$ jets background. The $t\bar{t}$ background sample was generated using MC@NLO [49]. The single-top background is simulated with ACERMC [51] for the t-channel and for the Wt-channel, while the s-channel is simulated with MC@NLO. HERWIG has been used for the simulation of the WW, WZ, ZZ diboson production. The different Monte Carlo generators have been introduced in Section 2.3.

6.1.1 Overlap removal for the Alpgen $W+$ jets samples

The ALPGEN $W+$ jets samples are generated with a given fixed number of hard partons. Partons are considered hard if they have $p_T > 15$ GeV. Hard partons must also be separated by $\Delta R > 0.7$. For the analysis, a maximum of five hard partons is considered.

Table 6.1: Monte Carlo event signal and background samples used for the W+ b-jets cross section measurement. The total cross section of the four W+ jets samples is normalised to the NNLO W inclusive production cross section calculated in [33].

Physics process	Generator	$\sigma \cdot$ BR [nb]		
$W \rightarrow l\nu$ $+b\bar{b}$	Alpgen[47]			
$W \rightarrow l\nu$ +jets	Alpgen[47]			
$W \rightarrow l\nu$ $+c\bar{c}$	Alpgen[47]			
$W \rightarrow l\nu$ $+c$	Alpgen[47]			
Total $W \rightarrow l\nu$ + jets		10.46	NNLO	[33]
$t\bar{t}$	MC@NLO[49]	89.7	approx. NNLO	[85]
QCD multi-jet	-	contribution estimated in data		
single-top (s-channel)	MC@NLO[49]	4.3×10^{-4}	NLO	[40]
single-top (t-channel)	AcerMC[51]	6.34×10^{-3}	NLO	[40]
single-top (Wt)	AcerMC[51]	13.1×10^{-3}	NLO	[40]
$Z \rightarrow \ell\ell$ + jets ($m_{\ell\ell} > 40$ GeV)	Alpgen[47]	1.07	NNLO	[33]
WW	Herwig [45]	44.9×10^{-3}	NLO	[40]
WZ	Herwig [45]	18.5×10^{-3}	NLO	[40]
ZZ	Herwig [45]	5.7×10^{-3}	NLO	[40]

The Alpgen generator describes the hard scattering process (see Section 2.3) while the evolution of the partons via soft QCD interactions, i.e. the parton shower (PS), is simulated with a second generator, Herwig in this case. The PS algorithm can generate jets at small relative angle. Some collinear jets are also produced according to the matrix elements (ME) of the Alpgen generator. In order to avoid double counting of these jets, an overlap removal procedure is applied using the MLM matching scheme[90] for the interface of the ME and PS algorithms. After the showering performed by Herwig, jets are formed from the generated particles using a clustering algorithm. These jets are required to have $p_T > 20$ GeV. The hard parton with the highest p_T is associated to the jet closets within ΔR <0.7 which is removed from the list of jets. The procedure is repeated for the remaining partons. Events are kept only if each hard parton is matched with a jet and if there are no unmatched jets. Events with unmatched jets are kept only in the sample with the highest multiplicity of hard partons.

Alpgen samples with heavy flavour quark production at ME level are also produced separately. The Alpgen samples used are W (+ 0-5 partons), $W + c\bar{c}$ (+ 0-3 partons), $W + b\bar{b}$ (+ 0-3 partons), $W + c$ (+ 0-4 partons). A second kind of overlap must be taken into account when the samples for the different quark flavours are combined. For example, a final state with W, u quark and a $b\bar{b}$ pair can arise either from the $W + b\bar{b}$ + 1-parton Alpgen sample or from the W+1-parton sample with a $b\bar{b}$ pair produced by the PS algorithm. The solution applied relies on the assumption that the ME describes $b\bar{b}$ final states with a large angle between the two b quarks, while the PS algorithm describe the final states with more collinear b quarks. Therefore events containing a $b\bar{b}$ pair are kept in the $W+$ light-jets sample, where they only originate from PS, only if the angle between the two b quarks is ΔR <0.4. Similarly, in the $W + b\bar{b}$ sample events are kept only if the b quarks are separated by ΔR >0.4.

For the c quarks, the situation is slightly different. While in the $W+$ light-jets sample there are no b quarks in the initial state partons at ME level, massless c quarks are taken into account[1]. When combining the samples all events with c quarks at ME level are therefore removed from the $W+$ light-jets sample, as this process is completely described by the dedicated $W + c$ sample. The same overlap removal procedure as for $b\bar{b}$ pairs is applied also to $c\bar{c}$ pairs.

This second overlap removal procedure is referred to as *Heavy Flavour Overlap Removal* (HFOR).

6.2 Event selection

The event selection criteria for the cross section measurement are summarized in Table 6.2.

6.2.1 Preselection

Events used for the analysis were collected with the ATLAS detector subsystems fully operational. The primary vertex of the event is required to be associated to at least 3 ID tracks in order to reject cosmic muon events which have a vertex with two associated tracks.

In the Monte Carlo simulations, two general corrections similar to the ones described in Section 5.1.4 are applied. Events are reweighted according to the pile-up conditions and the longitudinal size of the beam spot observed in the data. The first correction is performed by weighting with the ratio of the numbers of reconstructed vertices with at least 3 associated tracks in data and Monte Carlo events (which is a measure of the pile-up level). The second correction is performed by reweighting such that the distribution of the z coordinate of the primary vertex in simulations matches the one in the data.

6.2.2 Trigger requirements

The least stringent unprescaled trigger requirements are used. For the electron channel this is EF_e15_medium trigger which requires an electron with $p_T > 15$ GeV. For the

---

[1] This modellization is known as 4-flavours numbering scheme (4FNS). u, d, s, c quarks (and corresponding antiparticles) are considered to be present in the proton with their own PDF, while b and t quarks (and corresponding antiparticles) are produced only via gluon splitting. In the 5-flavours numbering scheme (5FNS) b quarks have their own PDF and are considered also in the initial state.

muon channel, three different algorithms have been used in different data taking periods in 2010:

- EF_MU10_MSonly, requiring a muon track reconstructed in the MS with $p_T > 10$ GeV, in the early periods,
- EF_MU13, requiring a combined muon track with $p_T > 13$ GeV for intermediate luminosities in the middle period and
- EF_MU13_tight, requiring a combined muon track with $p_T > 13$ GeV with tighter cuts on the p_T of the seeding muon selected at the first trigger level (see Section 3.2.6.1), for the late data taking period with the highest instantaneous luminosities.

The lepton candidates selected by the trigger algorithms are required by the analysis selection to match within ΔR <0.15 the leptons reconstructed offline, to ensure that no bias is introduced by the trigger.

6.2.3 Lepton selection

The p_T cut of 20 GeV applied to the reconstructed electrons and muons ensures that the trigger algorithms are working in the efficiency plateau region. An η cut is applied, corresponding to the detector acceptance for the electrons and to the acceptance of the trigger chambers for the muons. Electrons in the transition region between barrel and endcap, corresponding to $1.37 < |\eta| < 1.52$, are removed because of gaps in the calorimeter coverage in this region. Electrons are selected using the *tight* identification criteria (see Section 4.3). Combined (CB) muon tracks are used (see Section 4.7) applying the quality cuts of Table 5.3 on the ID track associated to the muon. Corrections for the muon reconstruction and identification efficiencies, for the electron energy resolution and for the muon momentum resolution are applied to the simulated events to match the performance measured in the data (see [71] for the electron and [91, 92] for the muon corrections).

In order to reject the QCD multi-jet background, the leptons are required to be isolated. In the electron channel, a combination of track and calorimeter isolation requirements with an expected signal efficiency of 95% is applied (see [69]). An η-dependent correction is applied to the isolation efficiency in simulations to match the performance measured in data [71]. Muons are required to have an angular distance with respect to the nearest jet of $\Delta R(\mu, jet)$ >0.4. A 4 GeV cut on the track and calorimeter isolation variables, in both cases for a cone radius $\Delta R = 0.3$, is also applied. More details on the isolation criteria are given in Section 4.8.

For the electron channel, events with exactly one electron and no muons are selected. For the muon channel, exactly one muon and no electrons are required. The dilepton veto

Table 6.2: Events selection criteria used for the $W+$ b-jets cross section measurement

Cut	$W \rightarrow e\nu$ **channel**	$W \rightarrow \mu\nu$ **channel**
Preselection		
Data taking conditions Primary vertex	All sub-detectors and systems in optimal working conditions $n^{PV}_{tracks} \geq 3$	
Trigger algorithm	EF_e15_medium	EF_MU10_MSonly (early data) EF_MU13 (middle period) EF_MU13_tight (late data)
Trigger matching	offline selected lepton within $\Delta R < 0.15$ to trigger object	
W selection		
Lepton identification	*tight* (see Section 4.3)	CB muon (see Section 4.7), quality cuts in Table 5.3
Kinematic cuts	E_T >20 GeV $\lvert\eta\rvert$ <2.47 $\lvert\eta\rvert$ <1.37 or $\lvert\eta\rvert$ >1.52	$\mathrm{p_T} > 20$ GeV $\lvert\eta\rvert$ <2.4
Lepton isolation	iso95 (see text and [69])	$\Delta R(\mu, jet) > 0.4$ $\sum^{\Delta R=0.3} p_T^{tracks} < 4$ GeV $\sum^{\Delta R=0.3} E_T^{calo} < 4$ GeV
Selected leptons	1 electron, no muons	1 muon, no electrons
Missing energy W transverse mass	$E_T^{\mathrm{miss}} > 25$ GeV $m_{\mathrm{T}}^{W} > 40$ GeV	
Jet selection		
Kinematic cuts Quality cuts Pile-up cleaning Jets multiplicity	$\mathrm{p_T} > 25$ GeV $\lvert y\rvert < 2.1$ *Loose* criteria (see Section 4.4 and [73]) Jet vertex fraction JVF > 0.75 (see text) n_{jets}=1 or 2	
b-jet selection		
SV0 b-tagger b-jet multiplicity	$L/\sigma(L) > 5.85$ $n^{SV0}_{tagged\ jets}$=1	

rejects $Z+$ jets and $t\bar{t}$ backgrounds.

6.2.4 *W* boson selection

The events are required to have a transverse momentum imbalance of $E_T^{\mathrm{miss}} > 25$ GeV to account for the presence of a neutrino in the W decay. The E_T^{miss} reconstruction is described in Section 4.6. In the Monte Carlo simulations, all corrections applied to the momenta of the different reconstructed objects are propagated to the E_T^{miss}.

The transverse mass of the W is determined from the momentum of the selected lepton and E_T^{miss} according to:

$$m_{\mathrm{T}}^{W} = \sqrt{2 \mathrm{p_T}^{\mathrm{lep}} \mathrm{p_T}^{\nu} (1 - \cos(\phi^{\mathrm{lep}} - \phi^{\nu}))} \ . \tag{6.1}$$

A $m_{\mathrm{T}}^{W} > 40$ GeV cut is applied.

6.2.5 Jet selection and b-jet tagging

Jets are reconstructed using the *anti-k_T* algorithm with a distance parameter $R = 0.4$. They are reconstructed from energy clusters in the calorimeters at the EM scale and are then recalibrated to the hadronic scale (see Section 4.4). The jets are required to have $\mathrm{p_T} > 25$ GeV and $|y| < 2.1$, in the fiducial region of the b-tagging algorithm used in the measurement. The *loose* quality cuts [73] are applied to the jets. In order to reject jets from pile-up interactions a cut of JVF > 0.75 is applied on the jet vertex fraction. This variable is defined as the fraction of the sum of transverse momenta of the tracks in the jet which belongs to tracks associated to the primary vertex. Events are classified in two categories with exactly one and exactly two selected jets respectively.

In the one-jet category the jet is required to be tagged as a b-jet by the *SV0* tagging algorithm [77] described in Section 4.4.4.1. The *SV0* tagger is used at a working point which ensures a selection efficiency for b-jets of about 35%. Simulated events are reweighted to reproduce the *SV0* performance measured in data. In the two-jets category only one of the jets is required to be tagged as a b-jet, while events with both jets tagged as b-jets are vetoed: the fraction of $W + b\bar{b}$ events in which two true b-jets are reconstructed and tagged is about 2%, due to detector acceptance effects, the kinematic cuts applied and the b-tagging efficiency and because the two b quarks may not be resolved in separated jets. Furthermore, the two-jets category with both jets tagged as a b-jets has a very high background contribution from $t\bar{t}$ production.

The efficiency of the b-jet tagging and the rate of c and light-jets passing the *SV0* selection are corrected in the simulations to match the efficiency and mistag rate measured in data [78].

6.3 Background estimation

The contributions of $W + c\bar{c}$, $W + c$ and $W+$ light-jets, $t\bar{t}$ and QCD multi-jet production processes are estimated with data-driven techniques explained in this section. All other backgrounds are estimated from Monte Carlo simulations.

6.3.1 The $W+$ jets background

The b-jet tagging requirement reduces the background due to the production of a W boson in association with charm or with light-quark jets, but the cross sections of these processes are much higher than the signal cross section leading to a non-negligible contribution of these backgrounds. Final states including c quarks are most problematic, since the mistag rate of the b-tagger is much higher for c-jets than for light-jets due to the relatively long lifetime of charm hadrons.

In order to determine the contributions of these processes the higher mass of the b-hadrons compared to others is exploited. The invariant mass m_{SV} of the tracks emerging from a secondary vertex reconstructed inside a b-jet serves as discriminating variable.
The fractions of events with b-jets, c-jets and light-jets in the selected data sample are determined by a fit of a linear superposition of the m_{SV} distributions for all contributing processes to the m_{SV} distribution measured in data. In this fit, the fractions of $W+$ b-jets, $W+$ c-jets and $W+$ light-jets events are used as free parameters, while the distributions for all other background processes are normalised to the predictions obtained as described below. The m_{SV} template shapes for $W+$ b-jets, $W+$ c-jets and $W+$ light-jets events are determined from Monte Carlo simulations. The m_{SV} distribution for $t\bar{t}$ events is taken from simulation and normalised to the number of $t\bar{t}$ events passing the selection, which is estimated from data as described in Section 6.3.2. The m_{SV} distribution for QCD multi-jet events and its normalisation are determined using a data control region as discussed in Section 6.3.3.

The results of the fit in each of the two event categories in the two lepton channels are shown in Fig. 6.2. The results of the fit to the data agree with the simulations, especially in bins dominated by background. This means that the modelling of the background processes is correct. The numerical results are given in Table 6.3.

6.3.2 The $t\bar{t}$ background

$t\bar{t}$ production contributes to the background because of the $t \to W + b$ decays, which have a BR of almost 100%. The resulting final states have W bosons and b-jets with similar properties as for the signal one but with a much higher average number of jets.

The $t\bar{t}$ contribution is first determined from a control data set defined by events with at least four jets including one or more b-tagged jets. This control data sample is dominated by $t\bar{t}$ events and has contributions from $W+$ b-jets and QCD multi-jet events. A fit of a superposition of the m_{SV} templates for $t\bar{t}$, $W+$ b-jets and multi-jet events is used to determine the number of $t\bar{t}$ events in the control sample. The m_{SV} templates for $t\bar{t}$ and for $W+$ b-jets events are determined by Monte Carlo simulations while the shape for QCD multi-jet events is determined in a control data sample defined in Section 6.3.3. The normalisation of the $W+$ b-jets contribution is fixed to the Monte Carlo prediction, with an assigned uncertainty of 100%. In the electron channel, the QCD multi-jet m_{SV} template is normalised with the same data-driven technique as described in Section 6.3.3. The normalisation of the $t\bar{t}$ template is therefore the only free parameter of the m_{SV} fit

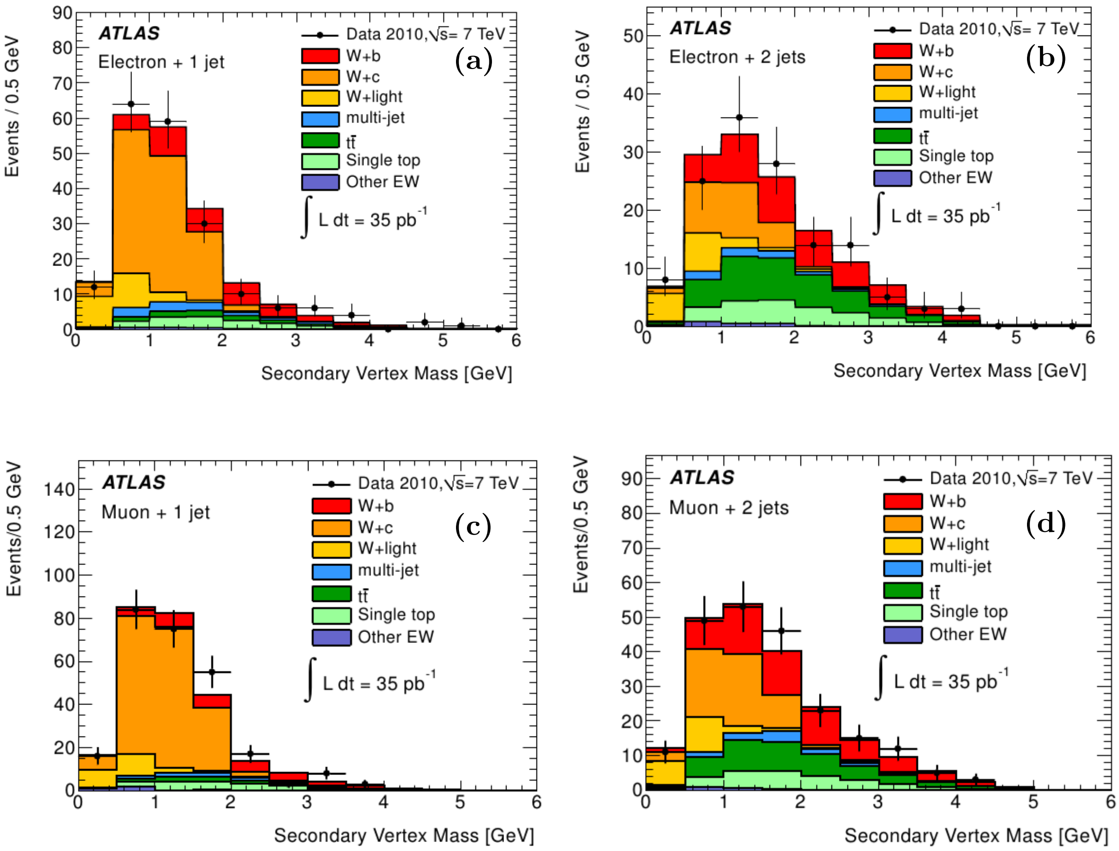

Figure 6.2: m_{SV} distributions for the b-tagged jets in data and Monte Carlo simulations in the 1-jet (a and c) and 2-jet (b and d) event category for the electron (a and b) and the muon channels (c and d) [1]. The Monte Carlo distributions for $W+$ b-jet(s), $W+$ c-jet(s) and $W+$ light-jets events are normalised to their fitted contribution in data. The normalisation of the $t\bar{t}$ and the QCD multi-jet background are determined with data driven techniques. Other backgrounds are from Monte Carlo simulations.

in the control region. In the muon channel, the fit of the m_{SV} distribution is performed simultaneously with a fit to the track-based muon isolation variable which fixes the normalisation of the QCD multi-jet contribution.

The number of $t\bar{t}$ background events in the selected $W+$ b-jets data sample is determined as the number of $t\bar{t}$ events measured in the control sample multiplied by the ratio of $t\bar{t}$ events in signal and control regions predicted by Monte Carlo simulation. The advantage of this approach is that the the uncertainty in the b-tagging efficiency and mistag rate, which are the biggest systematic errors for the measurement, mostly cancels in the ratio. The main source of uncertainty for the $t\bar{t}$ background estimation is the error in the jet energy scale. Other systematic uncertainties are negligible. The error on the $t\bar{t}$ background normalisation is 20-25% in the 1-jet and 2-jet categories for both lepton channels. The $t\bar{t}$ background prediction is shown in Table 6.3.

6.3.3 The QCD multi-jet background

QCD multi-jet productions contribute to the background mostly due to the limited detector resolution and to misreconstructed events. In the electron channel, jets and photons may be misidentified as electrons. Electrons and muons from heavy-flavour hadrons decays may wrongly be classified as isolated. Non-prompt muons from pion and kaon decays may be wrongly attributed to W boson decays. QCD multi-jet cross sections have large theoretical uncertainties and these processes are not modelled well enough and with sufficient statistics by Monte Carlo simulations after the very strong rejection by the analysis cuts. But even with high rejection, QCD multi-jet final states contribute significantly because of their high cross sections. The QCD multi-jet background is therefore determined exclusively by using data-driven techniques. The results are presented in Table 6.3.

6.3.3.1 Electron channel

In the electron channel, the data E_T^{miss} distribution is fitted in the 0-100 GeV range using two templates, one for QCD multi-jet events and the other one for the signal and all the other backgrounds. The normalisation of the multi-jet background is determined by the fit.

The multi-jet E_T^{miss} template is obtained from a data control sample dominated by multi-jet events and obtained applying a modified event selection with no E_T^{miss} cut and with an electron selection which requires passing the *loose* electron identification (see Section 4.3) but failing *medium* and *tight* requirements. An electron trigger condition based on loose electron identification has been used to avoid bias. The multi-jet E_T^{miss} distribution has been studied in Monte Carlo simulations and shows no distortion due to the inverted electron identification compared to the nominal one. The E_T^{miss} template for signal and all other backgrounds is determined from Monte Carlo simulations. The E_T^{miss} distribution in the signal region (without any cut on the E_T^{miss}) is shown in Fig. 6.3 with the multi-jet component from the fit. The low E_T^{miss} region with significant contribution from multi-jet events is well described.
The multi-jet background normalisation has a 50% uncertainty due to the statistical error of the E_T^{miss} data distribution and of the templates, which is the dominant error. Systematic studies have been performed by changing the definition of the control region used to define the multi-jet E_T^{miss} template.

6.3.3.2 Muon channel

In the muon channel, the multi-jet background is estimated using the so-called *matrix method* described in [93]. Two data samples with *loose* and *tight* muon selection are defined, where the second one is a subset of the first, differing only by the muon selection

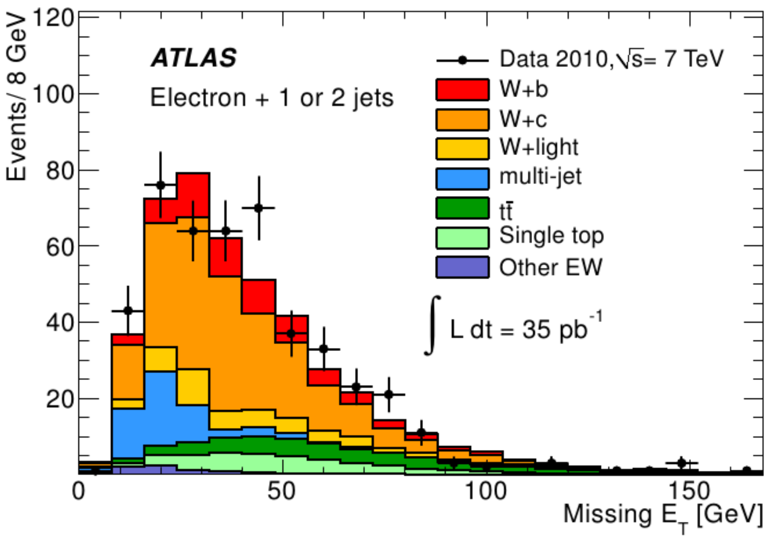

Figure 6.3: E_T^{miss} distribution in the $W+$ b-jets signal region for the electron channel without E_T^{miss} cut [1]. The multi-jet contribution is normalised to the data-driven prediction while all other contributions are from to Monte Carlo simulations.

used. The tight selection is the nominal selection while for the loose selection the muon isolation requirements are removed, requiring only that the selected muon is separated from selected jets by ΔR >0.4. Both samples contains contributions of *fake* non-prompt muons, produced in QCD multi-jet events, and of *real* prompt muons:

$$\begin{aligned} N^{loose} &= N^{loose}_{real} + N^{loose}_{fake}\,, \\ N^{tight} &= N^{tight}_{real} + N^{tight}_{fake} = \epsilon_{real} N^{loose}_{real} + \epsilon_{fake} N^{loose}_{fake} \end{aligned} \tag{6.2}$$

where ϵ_{real} and ϵ_{fake} are the probabilities for a real loose muon and a fake loose muon, respectively, to pass the tight requirements.

$$\epsilon_{real} = \frac{N^{tight}_{real}}{N^{loose}_{real}},\ \epsilon_{fake} = \frac{N^{tight}_{fake}}{N^{loose}_{fake}}\ . \tag{6.3}$$

N^{tight}_{fake} is therefore the contribution of non-prompt muons generated in QCD multi-jet events to the selected data sample and can be evaluated as

$$N^{tight}_{fake} = \frac{\epsilon_{fake}}{\epsilon_{real} - \epsilon_{fake}} (N^{loose}\epsilon_{real} - N^{tight})\ . \tag{6.4}$$

ϵ_{real} is measured using the Tag-and-Probe method in a $Z \to \mu\mu$ data sample (see Chapter 5). ϵ_{fake} is measured in a data control region enriched with QCD multi-jet events using the same selection as in Section 6.2 but reverting the cut on the transverse mass of the W to m_{T}^{W} < 20 GeV. The small $W+$ jets and $Z+$ jets contributions in this control

region are estimated with Monte Carlo simulations and subtracted.
A 30% uncertainty is assigned to the resulting QCD normalisation from Monte Carlo studies. In Fig. 6.4 the m_{T}^{W} distribution in the signal region (without cut on the m_{T}^{W}) is shown with the estimated multi-jet component. The low-m_{T}^{W} region in data, which is dominated by multi-jet background, is well described.

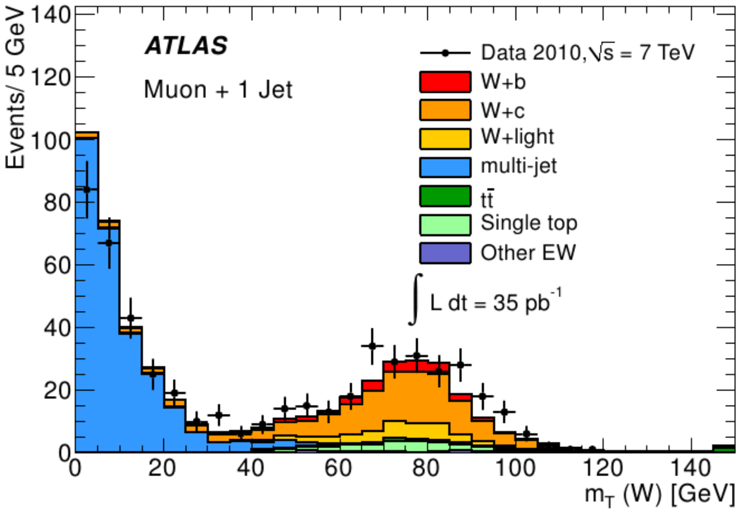

Figure 6.4: W transverse mass distribution in the $W+$ b-jets signal region for the muon channel in the 1-jet category without cut on m_{T}^{W} [1]. The multi-jet contribution is normalised using the data-driven technique while all other contributions are from Monte Carlo simulations.

6.3.3.3 QCD multi-jet m_{SV} templates

The multi-jet m_{SV} templates used for the $W+$ jets and $t\bar{t}$ background estimations of Sections 6.3.1 and 6.3.2 are determined from data control samples. In the electron channel, the same control region as for the evaluation of the multi-jet normalisation is used. In the muon channel, the control region dominated by multi-jet events obtained by applying the full signal selection but without cut on m_{T}^{W} and with reversed cut $E_T^{\mathrm{miss}} < 10$ GeV on the transverse missing energy is used. Systematic uncertainties in these templates are obtained by varying the control region definitions.

6.4 Cross section determination

The signal and background event yields for the $W+$ b-jets selection are shown in Table 6.3. The cross section measurement is defined for a *fiducial phase space* with kinematic cuts listed in Table 6.4. The definition of the fiducial region follows the cuts applied for the selection of the $W+$ b-jets data sample, in order to avoid model-dependent phase space extrapolations of the cross section measurement which would introduce theoretical uncertainties. In the analysis selection events with two b-tagged jets are vetoed, but the fiducial

Table 6.3: Event yields in the 1 and 2-jet categories of the electron and muon channels [1]. For the W+b, W+c, W+light-quark jets contributions, the Monte Carlo predictions are compared to the m_{SV} fit results with statistical errors only. The $t\bar{t}$ and multi-jet contributions are normalised using data-driven techniques. All other background contributions are estimated from simulations.

	$W \to \mu\nu$, 1-jet		$W \to \mu\nu$, 2-jet		$W \to e\nu$, 1-jet		$W \to e\nu$, 2-jet	
	Pred.	Fit result	Pred.	Fit result	Pred.	Fit result	Pred.	Fit result
W+b-jets	25	28 ± 13	26	62 ± 18	18	33 ± 12	19	38 ± 14
W+c-jets	108	170 ± 20	45	54 ± 19	84	105 ± 18	36	24 ± 15
W+ light-jets	38	21.2 ± 9.9	20	21 ± 10	30	22 ± 10	17	14.4 ± 7.7
multi-jet	8	-	10	-	10	-	5.8	-
$t\bar{t}$	11	-	44	-	8.1	-	33	-
single-top	17	-	23	-	14	-	18	-
Other backgrounds	3.9	-	2.5	-	1.9	-	2.1	-
Total Predicted	212	-	170	-	167	-	131	-
Data	261		217		194		136	

region for the cross section is defined for events with at least one b-jet. This means that the fiducial cross section measurement for the 2-jet category is defined for events with a b-jet and a second jet that can either be a b-jet (which in the data sample is not tagged due to the inefficiency of the *SV0* tagger) or a c or light-jet.

Table 6.4: Fiducial phase space for the W+ b-jets analysis. A jet is identified as a b-jet if it is matched to a b-hadron quark with $\mathrm{p_T} > 5$ GeV within $\Delta R = 0.3$.

Variable	Cut
$W \to e\nu / W \to \mu\nu$ selection	
$W \to \tau\nu \to e/\mu\nu\nu\nu$ decays	Excluded
Lepton momentum	$\mathrm{p_T} >$ 20 GeV
Lepton pseudo-rapidity	$\lvert\eta\rvert <2.5$
Neutrino	$\mathrm{p_T} >$ 25 GeV
W transverse mass	$m_\mathrm{T}^W >$ 40 GeV
Jets	
Jet momentum	$\mathrm{p_T} >$ 25 GeV
Jet rapidity	$\lvert y\rvert <2.1$
Jet multiplicity	$1 \leq n \leq 2$
b-jet multiplicity	$n \geq 1$
Jet-lepton isolation	$\Delta R(jet, l) > 0.5$

The W+ b-jets cross section is determined separately for the electron and the muon channels and in the 1 and 2-jet categories according to

$$\sigma^{fid}_{W+\ b\text{-}jet} \times BR(W \to \ell\nu) = \frac{N_{W+\ b\text{-}jets}}{\mathcal{U}^{fid} \cdot \int \mathcal{L} dt} \tag{6.5}$$

where $N_{W+\ b\text{-}jets}$ is the W+ b-jets events yield measured in data (see Table 6.3), $\mathcal{U}^{fid}$ the signal selection efficiency in the fiducial phase space and $\int \mathcal{L}dt$ the integrated luminosity of the data set.

The selection efficiency $\mathcal{U}^{fid}$ is determined in Alpgen+Herwig $W+$ jets simulated events with the equation

$$\mathcal{U}^{fid} = \frac{n_{MC,reco}}{n_{MC,true}^{W+\ b\text{-}jets,fid}} \ . \tag{6.6}$$

where $n_{MC,reco}$ is the number of reconstruction level events (i.e. Monte Carlo events after full simulation of the detector response) passing the analysis selection and $n_{MC,true}^{W+\ b\text{-}jets,fid}$ the number of generated $W+$ b-jets events which are in the fiducial region of the measurement.

The jets at generator level are built using the *anti-k_T* algorithm with a distance parameter of R = 0.4 on the 4-momenta of generated stable particles (see Section 4.4). A generator level jet is identified as a true b-jet if matched to a b-hadron with $p_T > 5$ GeV within $\Delta R = 0.3$. The same b-hadron matching is also applied to the jets at reconstruction level, to ensure that $\mathcal{U}^{fid}$ is evaluated only for signal events. The possible bias introduced by this convention has been studied by using b quarks instead of the hadrons for the matching and found to be negligible.

At generator level the momentum of the electron/muon produced in the $W \to e/\mu\nu$ decay is evaluated including the momenta of all final state radiation photons within a $\Delta R = 0.1$ cone (*dressed momentum*).

The $W \to \tau\nu \to e/\mu\nu\nu$ decays, which are explicitly vetoed in the denominator of $\mathcal{U}^{fid}$ since they are not included in the fiducial region, give a small contribution at reconstruction level. They are included in the numerator of $\mathcal{U}^{fid}$ to correct for the small contribution of these decays in the data sample. The numerator is therefore defined as

$$n_{MC,reco} = n_{MC,reco}^{W\to e/\mu\nu} + n_{MC,reco}^{W\to\tau\nu\to e/\mu\nu\nu} \ .$$

The final results on the selection efficiency are presented in Table 6.5.

Table 6.5: Selection efficiency within the fiducial region for the cross section measurement. Only statistical uncertainties are shown.

	Jet category	$n_{MC,reco}^{W\to e/\mu\nu}$	$n_{MC,reco}^{W\to\tau\nu\to e/\mu\nu\nu}$	$n_{MC,true}^{W+\ b\text{-}jets,fid}$	$\mathcal{U}^{fid}$ [%]
Electrons	1	17.64±0.84	0.276±0.078	108.1±2.2	16.57±0.85
	2	18.15±0.69	0.73 ±0.15	91.1±1.6	20.72±0.86
Muons	1	24.2 ±1.0	0.61 ±0.16	107.0±2.1	23.2 ±1.1
	2	25.53±0.84	0.374±0.091	91.7±1.6	28.2 ±1.0

6.5 Systematic uncertainties

In this section the systematic error estimation is described, which has the following contributions.

b-tagging efficiency

The uncertainty in the efficiency of the *SV0* b-jet tagging algorithm represents one of the biggest systematic uncertainties for the measurement. It has been measured to be between 6% and 13% depending on the jet p_T [78].

m_{SV} templates

The uncertainty in the m_{SV} templates used for the data-driven background normalisation described in Section 6.3.1 is another important source of systematic error. The systematic errors in the m_{SV} templates for b-jets, c-jets and light-quark jets obtained from Monte Carlo events are determined comparing data and simulation in control regions enriched with the respective quark flavours.

$t\bar{t}$ background

There are two sources of uncertainty in the $t\bar{t}$ background estimation described in Section 6.3.2, the uncertainty in the $t\bar{t}$ yield in the control region and the uncertainty in the extrapolation of this yield from the control to the signal region. The first one is dominated by limited data statistics, the second one has a significant contribution from the jet energy scale uncertainty. Uncertainties due to the Monte Carlo modelling of the $t\bar{t}$ production process are also considered, in particular the uncertainties on the PDFs and in the description of the initial and final state radiation and on the differences in the description of $t\bar{t}$ events from different Monte Carlo generators.

Single-top background

The single-top background is estimated from Monte Carlo simulation. A 10% uncertainty is attributed to the theoretical uncertainties on the cross section, determined by varying the factorization and renormalisation scales by a factor 2 and considering the PDF uncertainties. Another source of error in the normalisation of the single-top background is the description of the initial and final state radiation in the Monte Carlo simulation. Uncertainties on the estimated single-top contribution due to detector effects are also taken into account.

Signal modelling

The uncertainties in the description of the signal process in the Monte Carlo simulation are determined studying the effects of variations of the shapes of the b-jet spectrum and of the $b\bar{b}$ pair opening angle distribution on the selection efficiency. Two extreme cases are considered: distributions fully modelled by the matrix elements and distributions obtained from the parton shower description.

Multi-jet background estimation

As described in Section 6.3.3, in the electron channel the uncertainty in the measurement of the QCD background normalisation is 50%, mostly due to limited data statistics. Systematic variations of the normalisation and of the multi-jet m_{SV} template have been studied modifying the definition of the control region used for the background estimation. In the muon channel the uncertainty in the normalisation is 30%, which has been determined studying the matrix method used for the background estimation in simulated samples. Uncertainties in the m_{SV} template have been studied by varying the control region definition in the muon channel as well.

Jet energy uncertainties

Uncertainties in the jet energy scale and the jet energy resolution assessed in [73] affect the signal selection efficiency.

Lepton reconstruction uncertainties

The measured uncertainties in the lepton trigger, reconstruction and isolation cut efficiencies as well as the lepton momentum scales and resolutions [71, 92] affect the signal selection efficiency.

E_T^{miss} uncertainty

Variations in the lepton and jet momenta are propagated to the measured missing transverse energy. An additional uncertainty is attributed to the contribution of soft jets, with $\mathrm{p_T} < 20$ GeV to the E_T^{miss} [79].

Luminosity error

The 35.5 pb^{-1} dataset used for the analysis has an uncertainty in the luminosity measurement of 3.4% [94].

Pile-up effects

The uncertainty due to the presence of jets generated by pile-up collisions is estimated from the variation of the yields when the cut on the jet vertex fraction described in Section 6.2 is removed.

6.6 Results of the fiducial cross section measurement

The cross section measured in the fiducial phase space region defined in Table 6.4 for the production of a leptonically decaying W in association with one b-jet and a maximum of one additional jet of any flavour are given in Table 6.6 separately for the $W \to e\nu$ and $W \to \mu\nu$ channels for the 1-jet and 2-jet event categories. The cross section are determined for the combination of the two leptonic channels by averaging the individual results and for the combination of the two jet categories summing linearly the individual measurements. Most of the systematic uncertainties are correlated between the channels and the event categories.

Table 6.6: Fiducial cross section for the production of a leptonically decaying W boson in association with at least one b-jet for events with 1 and 2 jets and their combination and breakdown of the contributions to the systematic error [1]. The fiducial region of the measurement is given in Table 6.4.

Fiducial cross section [pb]									
Event category	1 jet			2 jet			1+2 jet		
Lepton channel	μ	e	μ & e	μ	e	μ & e	μ	e	μ & e
Measured cross section	3.5	5.5	4.5	6.2	5.1	5.7	9.7	10.7	10.2
Statistical uncertainty	1.6	2.1	1.3	1.8	1.9	1.3	2.4	2.8	1.9
Systematic uncertainty	1.1	1.7	1.3	1.5	1.5	1.4	2.4	3.0	2.6
Breakdown of systematic uncertainty [%]									
b-tagging efficiency	15	14	14	10	10	10	11	12	12
Template shapes	16	13	12	10	12	10	11	11	10
$t\bar{t}$	9	6	7	12	16	13	11	11	11
single-top	10	6	8	4	6	5	7	6	6
Signal modelling	9	8	9	10	10	10	9	9	9
Multi-jet	7	18	11	4	8	4	5	13	7
Jet uncertainties	9	6	7	7	10	8	7	7	7
Lepton uncertainties	3	5	3	2	5	3	2	5	3
E_T^{miss}	1	1	1	2	2	1	1	1	1
Luminosity	5	5	5	4	5	5	5	5	5
Multiple interactions	5	4	5	3	3	3	3	4	3

The theoretical predictions for the fiducial cross section [95] are shown in Table 6.7 and compared to the measurements in this thesis in Figure 6.5. The theoretical predictions have been performed at next-to-leading order (NLO) in the 5 flavours number scheme (5FNS), i.e. considering production diagrams with b quarks in the initial state. The population of b quarks in the initial state is described by a parton density function (PDF). The experimental results are in agreement with the theoretical predictions within the uncertainties. The results in the 2-jet category indicate an excess of the measurement of

5.7±1.9 pb above the prediction $1.9^{+0.8}_{-0.4}$ pb. The results of a subsequent ATLAS measurement of the $W+$ b-jets cross section with the larger 2011 dataset [96] do not confirm this discrepancy. The 2011 measurement for the 2-jet category of 2.2±0.5 pb, in a fiducial region slightly different from the one adopted for the 2010 analysis presented in this thesis, is in good agreement with the NLO prediction of $1.7^{+0.5}_{-0.3}$ pb [96] calculated with the Monte Carlo software MCFM [40] in the 5FNS.

Table 6.7: [95] NLO QCD predictions for the $W+$ b-jets cross section in the fiducial phase region of the measurement (see Table 6.4) [95]. Theoretical errors are due to the uncertainty in the renormalisation and factorization scale (SC), in the parton density functions estimates (PDF), in the uncertainty in the b mass (m_b) and in the non-perturbative corrections (NP).

Category	Fiducial cross section (NLO) [pb]
1-jet	$2.9^{+0.4}_{-0.4}$ (SC) $^{+0.2}_{-0.0}$ (PDF) $^{+0.2}_{-0.1}$ (m_b) $\pm$ 0.2 (NP)
2-jet	$1.9^{+0.8}_{-0.4}$ (SC) $^{+0.1}_{-0.0}$ (PDF) $^{+0.1}_{-0.1}$ (m_b) $\pm$ 0.1 (NP)
1+2-jet	$4.8^{+1.2}_{-0.7}$ (SC) $^{+0.3}_{-0.0}$ (PDF) $^{+0.3}_{-0.2}$ (m_b) $\pm$ 0.3 (NP)

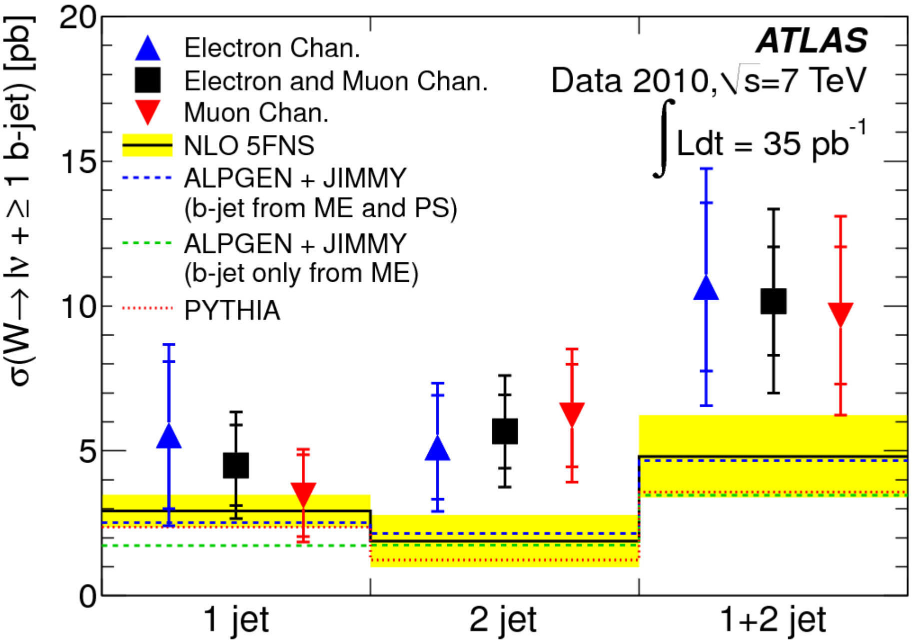

Figure 6.5: Measured cross sections with statistical and total errors [1] in comparison with the theoretical prediction evaluated in the 5 flavour number scheme [95], where the yellow band represents the total uncertainty. The cross sections predicted by the ALPGEN+HERWIG+JIMMY Monte Carlo generator using ME+PS and ME only (see Sections 2.1 and 6.1.1), and by PYTHIA are also shown.

Chapter 7

Measurement of the $W+$ c-jet production cross section

In this chapter a measurement of the production cross section of a W boson in association with a single c quark jet ($W+$ c-jet) with the ATLAS detector is presented [2]. This process is sensitive to the s quark content of the proton. Measurements of the cross section can be used to constrain the s quark PDF. Such measurements have already been performed at the Tevatron [97] and at the LHC [98], but with uncertainties too large for using them for PDF determination. Recently preliminary cross section measurements of $W + c$ production have been published by ATLAS [99] and CMS [100].

The measurement presented in this chapter is the result of the efforts of a very small analysis team. The main contribution of this work is the calibration of the c-jet tagger and the measurement of the muon reconstruction efficiency, the signal event selection including measurement of the selection efficiency and the cross section determination with the assessment of the systematic uncertainties.

7.1 Motivation

An introduction to $W+$ jets production at the LHC has been given in Chapter 2. The Feynman diagrams of the dominant processes for the $W+$ c-jet production at the LHC are shown in Figure 7.1. Due to the small values of the CKM matrix elements V_{ub} and V_{cb}, the process with a s quark in the initial state dominates. Therefore the $W+$ c-jet cross section measurement is sensitive to the s quark content of the proton.

It was introduced in Section 2.1 that the quantum numbers of the proton are determined by its valence quarks, two u and one d quarks, while quark pairs of all flavours (sea quarks) are produced inside the proton by the gluons exchanged between the valence quarks. The contributions of the gluons and of the different quark flavours to the proton momentum are described by parton density functions (PDFs). The densities of $s/\overline{s}$ and of $\overline{u}$ and $\overline{d}$ quarks

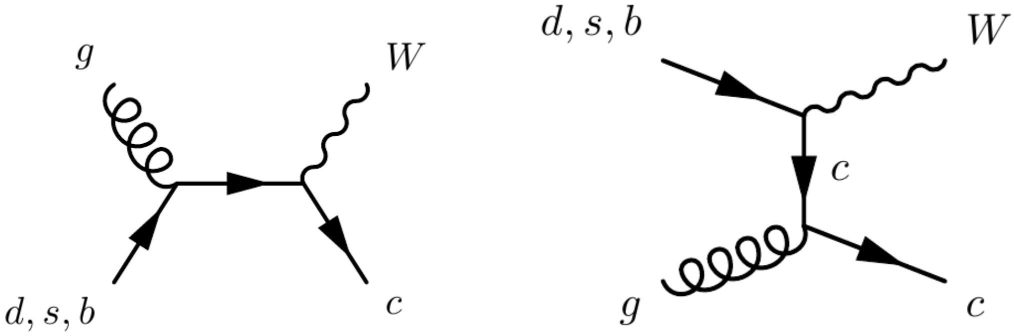

(a) LO diagram **(b)** LO diagram

Figure 7.1: The most relevant Feynman diagrams for the $W + c$ production in proton-proton collisions.

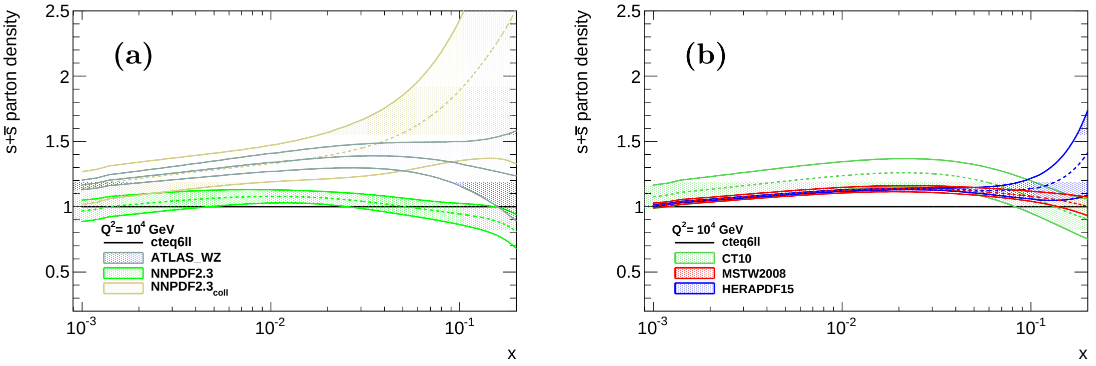

Figure 7.2: $(s + \overline{s})$ quark densities as a function of the fraction x of the proton momentum carried by the quark predicted by different PDF sets. The distributions are estimated at a scale $Q^2 = 10^4$ GeV^2 and normalised to the `cteq6ll` PDF [101]. (a) `ATLAS_WZ` [34], `NNPDF 2.3` [102] and `NNPDF 2.3`$_{\text{coll}}$ [102] and (b) `MSTW 2008` [103], `HERAPDF 1.5` [104, 105] and `CT10` [106]. The plots have been produced using the LHAPDF software [107]. The error bands corresponds to a 68% confidence level.

in the proton sea are predicted to be the same by flavour symmetry. Differences may raise from non-perturbative QCD effects [108] and are experimentally confirmed for the $\overline{u}$ and $\overline{d}$ quarks densities (see for example [109]). This difference is due to non-perturbative QCD effects [108]. The higher mass of the strange quark may also lead to a suppression of its contribution. In Figure 7.2 the $(s + \overline{s})$ quark density distributions derived from different predictions for the s quark PDF at the LHC are shown. The distributions are normalised to the `cteq6ll` leading order PDF [101] which is used to generate the $W + c$ Monte Carlo sample used for the present analysis. Figure 7.3 shows the ratio between the s and the $\overline{d}$ quark PDF predicted by different PDF sets. The `ATLAS_WZ` set is obtained from the

ATLAS measurement of the W and Z production cross section and from HERA electron-proton deep inelastic scattering data [34]. The resulting s quark PDF, still with large uncertainty, shows a negligible suppression of the s quark content of the proton compared to the $\overline{d}$ quarks (see [34]). The `CT10` [106] PDF set predicts a small suppression of the s quark PDF compared to the $\overline{d}$ quark PDF, while the suppression is predicted to be larger by the `MSTW 2008` [103], `NNPDF 2.3` [102] and `HERAPDF 1.5` [104, 105] PDFs. These four PDF sets use neutrino-nucleon deep inelastic scattering data [110, 111] to constrain the s quark PDF. This procedure is subject to large uncertainties due to the nuclear corrections and requires a large extrapolation from the phase space covered by the fixed-target experiments to the case of proton collisions at the LHC which cover the lower x and much higher Q^2 region. The `NNPDF 2.3`$_{\text{coll}}$ [102] s quark PDF is only based on HERA, LHC and Tevatron collider data. In this case an enhancement of the s quark PDF with respect to the $\overline{d}$ quark density is predicted.

Another motivation for the $W + c$ cross section measurement is the study of a possible difference between the s and $\overline{s}$ momentum distributions. Since strange quarks are sea components in the proton, the PDFs of s and $\overline{s}$ quarks must have the same integral over the momentum fraction phase space

$$\int f^s(Q^2, x)dx = \int f^{\overline{s}}(Q^2, x)dx \ , \tag{7.1}$$

but their momentum distributions $xf^s(Q^2, x)$ and $xf^{\overline{s}}(Q^2, x)$ can in principle be different, for example due to the different virtual bound states formed by s and $\overline{s}$ with the valence quarks of the proton [112]. Several analyses interpret the results of the neutrino-nucleon deep inelastic scattering experiments introducing an asymmetry between the s and $\overline{s}$ distributions [110, 113, 114]. No $s/\overline{s}$ asymmetry is assumed in the `ATLAS_WZ`, `CT10` and `HERAPDF 1.5` PDF sets, while small differences are taken into account in the `NNPDF 2.3`, `NNPDF 2.3`$_{\text{coll}}$ and `MSTW 2008` PDF sets. The ratio of $W^+ + \overline{c}$ and $W^- + c$ production cross sections is sensitive to the $s/\overline{s}$ asymmetry.

7.2 Measurement strategy

For the selection of the $W+$ c-jet sample, only $W \rightarrow e\nu$ and $W \rightarrow \mu\nu$ decays are used. The identification of the c-jet relies on the selection of the semileptonic decays of the c-hadrons produced by the hadronization of the final state c quark. Only c-hadron$\rightarrow \mu + X$ decays are used. Muons produced in these decays are referred to as *soft muons* in the following. At most one additional jet due to higher order radiative processes is allowed. The additional jet is required not to be associated with a soft muon.

An important property of $W + c$ production are the opposite charges of the W boson and

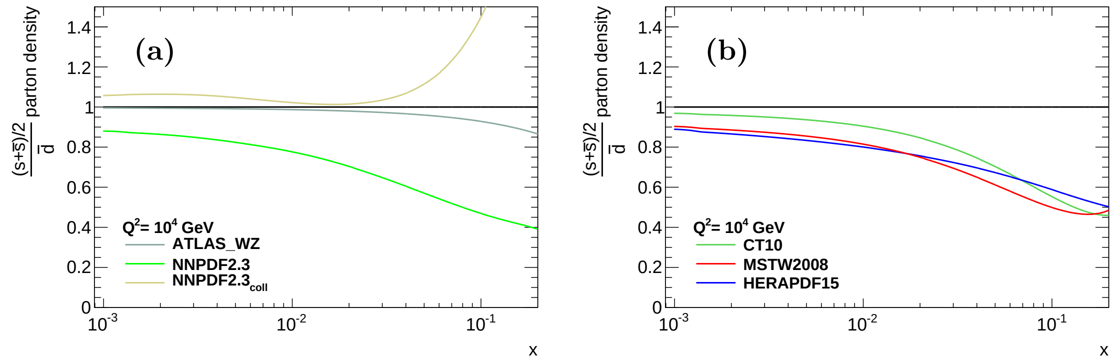

Figure 7.3: Average of the s and $\bar{s}$ parton densities divided by the $\bar{d}$ quark PDF as a function of the fraction x of the proton momentum carried by the quark predicted by different PDF sets. The distributions are estimated at a scale $Q^2 = 10^4$ GeV^2. (a) `ATLAS_WZ` [34], `NNPDF 2.3` [102] and `NNPDF 2.3`$_{\text{coll}}$ [102] and (b) `MSTW 2008` [103], `HERAPDF 1.5` [104, 105] and `CT10` [106]. The plots have been produced using the LHAPDF software [107]. The uncertainties are not shown.

the c quark. The charge of the c quark is identified by the charge $q^{soft-\mu}$ of the soft muon while the charge of the W boson is identified by the charge q^{W-lep} of its decay lepton as illustrated in Figure 7.4. The selected events are classified into the same sign (SS) or opposite sign (OS) categories if $q^{W-lep}q^{soft-\mu} = 1$ or $q^{W-lep}q^{soft-\mu} = -1$, respectively.

Signal events contribute only to the OS category by definition while background events are almost equally divided between the SS and OS categories. For this reason, the numbers of OS and SS events selected as discussed in Section 7.4 are subtracted from each other defining the difference

$$N^{OS-SS} \equiv N^{OS} - N^{SS} = N^{OS}_{signal} + N^{OS}_{background} - N^{SS}_{background} \ . \tag{7.2}$$

in which most background contributions cancel and the signal contribution is enhanced, since $N^{OS}_{background} \approx N^{SS}_{background}$. Simulation predicts about 80% signal contribution to N^{OS-SS}. The following background processes are considered:

- $W+$ light-jets production, where soft muons inside jets are mostly non-prompt muons from pion and kaon decays. This process gives a higher contribution to the OS than to the SS category due to the production diagrams with u/d-gluon fusion which also result in opposite charges for the hard lepton and the soft muon. Therefore this background is still sizeable after the $N^{OS} - N^{SS}$ subtraction.

- QCD multi-jet background also has a larger OS than SS component, since both the selected hard lepton and the soft muon in $b\bar{b}$ and $c\bar{c}$ events likely originate from the two heavy flavour particles in the final state which have opposite charges.

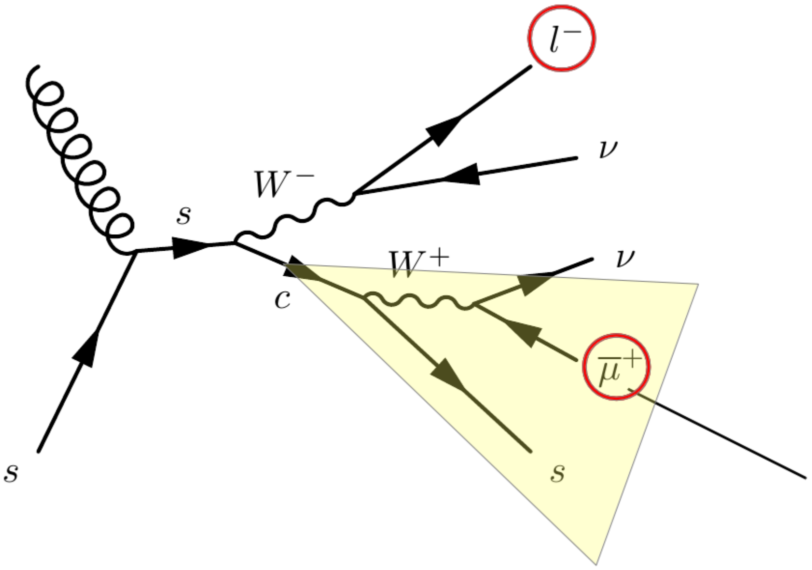

Figure 7.4: Diagram of $W + c$ production and decay. The lepton from the W decay and the soft muon from c quark decay, which have opposite charge, are indicated as well as the jet (yellow cone) containing the soft muon.

- The $Z+$ jets production background is very small in the electron channel but it is significant in the muon channel where the muon pairs from $Z \to \mu\mu$ decay may be misidentified as a lepton from a W and a soft muon. $Z+$ jets background contribute mostly to the OS category and the $N^{OS} - N^{SS}$ subtraction does not neglect its contribution. Fortunately, most muons of this kind are isolated, and therefore not matched with a jet.

- $W + b\bar{b}$ and $W + c\bar{c}$ events may produce a signature similar to the signal one, with a leptonically decaying W and a soft muon produced by an heavy-flavour hadron, but these events are evenly divided between the OS and SS categories, thus their contribution is negligible after the $N^{OS} - N^{SS}$ subtraction.

- The $t\bar{t}$ and single-top backgrounds have relatively small cross sections and their contribution is expected to be small after the $N^{OS} - N^{SS}$ subtraction.

- Diboson production (WW, WZ, ZZ) has a larger OS than SS component, but the low cross sections, the leptonic branching ratios of the bosons and the isolation of the leptons result in a very small background contribution.

7.3 Samples used for the analysis

The analysis is performed for 4.64 fb^{-1} of proton-proton collision at $\sqrt{s} = 7$ TeV data collected by the ATLAS detector during 2011.

A Monte Carlo simulated sample of the $W + c$ signal events is used to determine the selection efficiency for the determination of the fiducial cross section (see Section 7.9). The small contributions of $t\bar{t}$, single-top, diboson and $Z+$ jets (in the electron channel) are estimated with Monte Carlo simulation as well. $W + b\bar{b}$ and $W + c\bar{c}$ contributions are predicted by Monte Carlo simulations to be negligible after the $N^{OS} - N^{SS}$ subtraction. The contribution of $Z+$ jets events in the muon channel and of $W+$ light-jets production do not vanish after the subtraction and are therefore evaluated with data-driven methods. The QCD multi-jet background is completely estimated from data.

The simulated event samples and the cross section calculations used for their normalisation are listed in Table 7.1. The Alpgen [47] generator was used for the simulation of the signal and of the $W + c\bar{c}$, $W + b\bar{b}$ and $W+$ light-jets background processes. Pythia [43] was used for the parton shower (PS) simulation in the signal sample because it was found to describe better the c hadronization than Herwig. For $W + c\bar{c}$, $W + b\bar{b}$ and $W+$ light-jets events Herwig [45] was used as PS algorithm, since higher statistics samples were available. MC@NLO [49] was used for the $t\bar{t}$ background simulation, Herwig [45] for the WW, WZ and ZZ production. The single-top background in the t and Wt-channels was simulated with AcerMC [51] while the s-channel was simulated with MC@NLO. For the $Z+$ jets background, Alpgen+Herwig samples were used.

The MLM [90] and HFOR overlap removal procedures described in Section 6.1.1 were used for the $W+$ jets sample.

Table 7.1: Monte Carlo event samples used for the $W+$ c-jet cross section measurement. The total cross section of the four $W+$ jets samples is normalised to the NNLO inclusive W production cross section calculated in [33].

Physics process	Generators	PDF set		σ·BR (nb)		
$W(\to l\nu)$ $+c$	Alpgen [47]+Pythia [43]	cteq6ll	[101]			
$W(\to l\nu)$ +jets	Alpgen [47]+Herwig [45]	cteq6ll	[101]			
$W(\to l\nu)$ $+b\bar{b}$	Alpgen [47]+Herwig [45]	cteq6ll	[101]			
$W(\to l\nu)$ $+c\bar{c}$	Alpgen [47]+Herwig [45]	cteq6ll	[101]			
Total $W\to l\nu$ + jets				10.46	NNLO	[33]
$Z(\to ll)$ +jets	Alpgen [47]+Herwig [45]	cteq6ll	[101]	1.07	NNLO	[33]
WW	Herwig [45]	MRSTMCal	[115]	44.9×10^{-3}	NLO	[40]
WZ	Herwig [45]	MRSTMCal	[115]	18.5×10^{-3}	NLO	[40]
ZZ	Herwig [45]	MRSTMCal	[115]	5.96×10^{-3}	NLO	[40]
$t\bar{t}$	MC@NLO [49]+Herwig [45]	CT10	[106]	90.5×10^{-3}	approx.NNLO	[85]
single-top (t-channel)	AcerMC[51]+Pythia [43]	CT10	[106]	64.6×10^{-3}	NNLO	[116]
single-top (s-channel)	MC@NLO [49]+Herwig [45]	MRSTMCal	[115]	4.6×10^{-3}	NNLO	[117]
single-top (Wt)	MC@NLO [49]+Herwig [45]	CT10	[106]	15.7×10^{-3}	NNLO	[118]

7.4 Event selection

The event selection criteria are summarised in Table 7.2. The selection is analogous to the one used for the $W+$ b-jets cross section measurement discussed in Section 6.2, with cuts updated for the 2011 data taking conditions and optimized for the background rejection. For the c-jets a different tagging technique is used based on soft muons reconstructed inside the jets.

7.4.1 Preselection

Only data have been used where all ATLAS detector subsystems were fully operational. The primary vertex of the event is required to have at least 3 associated ID tracks in order to avoid contamination by cosmic muon events.

A reweighting procedure is applied to the Monte Carlo events such that the distributions of the average number of interactions per bunch crossing $< \mu >$ and of the z coordinate of the primary vertex match the data. The procedures are analogous to the ones applied in Section 5.1.4 for the muon reconstruction efficiency measurement.

7.4.2 Trigger requirements

The least stringent unprescaled trigger requirements were used. They varied from the early data taking period, with relatively low instantaneous luminosity, to the late period with higher instantaneous luminosity and pile-up levels. For the electron channel the following trigger conditions are applied [119]:

- EF_e20_medium in the early data taking period requiring an electron with $\mathrm{p_T} > 20$ GeV of *medium* quality (see Section 4.3).
- EF_e22_medium in the intermediate period requiring an electron of *medium* quality with $\mathrm{p_T} > 22$ GeV.
- EF_e22vh_medium in the late data taking period requiring an electron with $\mathrm{p_T} > 22$ GeV of *medium* quality and with a veto on energy deposits higher than 1 GeV in the hadronic calorimeter in a $\Delta\eta \times \Delta\phi = 0.2 \times 0.2$ window around the electron.

For the muon channel, the following trigger requirements are used [88]:

- EF_mu18 in the early data taking period requiring a muon with $\mathrm{p_T} > 18$ GeV seeded by a level-1 trigger muon candidate with $\mathrm{p_T} > 10$ GeV (see Section 3.2.6.1).
- EF_mu18_medium in the late data taking period requiring a muon with $\mathrm{p_T} > 18$ GeV seeded by a level-1 trigger muon candidate with $\mathrm{p_T} > 11$ GeV.

The leptons selected by the trigger algorithms are required to match within $\Delta R = 0.15$ the leptons reconstructed offline to ensure that no bias is introduced by the trigger.
The Monte Carlo simulations are reweighted to correctly describe the varying trigger conditions in data [88, 119].

7.4.3 Lepton selection

Different $\mathrm{p_T}$ cuts are applied for electrons ($\mathrm{p_T} > 25$ GeV) and muons ($\mathrm{p_T} > 20$ GeV) because of the different trigger conditions. The values are chosen to lie in the plateau region of the trigger efficiency. All leptons are required to be inside the trigger acceptance: $|\eta| <2.47$ (without $1.37 < |\eta| < 1.52$) for electrons and $|\eta| < 2.4$ for muons.

In order to reject the QCD multi-jet background, the leptons are required to be isolated. A multi-lepton veto is applied in both channels to reject background processes.

7.4.3.1 Electron channel

The *tight++* electron identification (see Section 4.3) is used for electron selection. A loose cut on the transverse impact parameter of the electron is applied to ensure that it is coming from the reconstructed primary vertex. The calorimeter energy in a $\Delta R = 0.3$ cone around the electron is required to be less than 3 GeV.

A veto is applied against additional electrons fulfilling a looser selection criteria: *medium++* identification and $\mathrm{p_T} > 20$ GeV within $|\eta| <2.47$ (without $1.37 < |\eta| < 1.52$). To reject diboson and $t\bar{t}$ backgrounds, a veto is applied against combined muons reconstructed with Staco (see Section 4.7) and with $\mathrm{p_T} > 20$ GeV, $|\eta| < 2.5$ and $z_0 < 10$ mm, satisfying the quality requirements in Table 5.3 and passing a track isolation cut of $\sum^{\Delta R=0.2} p_T^{tracks}/\mathrm{p_T} < 0.1$.

7.4.3.2 Muon channel

Combined muons reconstructed with Muid (see Section 4.7) passing the kinematic cuts mentioned above are selected. The quality cuts of Table 5.3 are applied to the Inner Detector (ID) tracks associated to the muons. Track and calorimeter isolation criteria $\sum^{\Delta R=0.3} p_T^{tracks} < 2.5$ GeV and $\sum^{\Delta R=0.2} E_T^{calo} < 4$ GeV, respectively, are applied.

Events with more than one selected muon are rejected. To reject diboson and $t\bar{t}$ backgrounds a veto is applied against *tight++* electrons with $E_T > 25$ GeV, $|\eta| < 2.47$ (without $1.37 < |\eta| < 1.52$) fulfilling η and $\mathrm{p_T}$ dependent ID and calorimeter isolation requirements with 90% efficiency.

7.4.3.3 Lepton-jet overlap removal

The jet closest to the signal lepton within $\Delta R = 0.2$ is removed as it may be a fake jet reconstructed due to the calorimeter activity from the signal lepton. Furthermore, electrons within $\Delta R = 0.5$ of a jet with $\mathrm{p_T} > 25$ GeV and muons within ΔR =0.4 of a jet with $\mathrm{p_T} > 25$ GeV and JVF > 0.75 (see section 7.4.5) are rejected.

7.4.3.4 Lepton efficiency corrections

Corrections are applied to the lepton trigger, reconstruction and isolation efficiencies in the simulations to fit the data. The corrections presented in Chapter 5 are used for the muon reconstruction efficiency. Corrections for the the muon isolation and trigger efficiencies are evaluated with a Tag-and-Probe method analogous to the one used in Section 5.2. The electron reconstruction and identification efficiency measurements are described in [72]. Corrections for the electron isolation and impact parameter cut efficiencies are evaluated with a Tag-and-Probe method analogous to the one described for the muons.

The muon momentum and electron energy scales and resolutions are also corrected in the simulations to match the data (see [72, 83]).

7.4.4 *W* boson selection

Only events with a reliable evaluation of the missing transverse energy E_T^{miss} are kept (so-called E_T^{miss} *cleaning*). Events with a jet with $\mathrm{p_T} > 20$ GeV failing the *looser* reconstruction quality criteria (see Section 4.4) and events with jets falling into the calorimeter region damaged in 2011 or containing noise bursts in the LAr calorimeter are rejected. An $E_T^{\mathrm{miss}} > 25$ GeV cut is applied in the electron channel which is lowered to 20 GeV in the muon channel. The lepton and the reconstructed E_T^{miss} are used to determine the transverse mass m_{T}^W of the W boson using Eq. 6.1. A $m_{\mathrm{T}}^W > 40$ GeV cut is applied in the electron channel which is raised to 60 GeV in the muon channel. The difference between the cuts applied in the two channels is justified by the different backgrounds contamination especially due to QCD multi-jet events. The cuts are optimized for maximum background rejection.

7.4.5 Jet selection

The *anti-k_T* algorithm (see Section 4.4) with a distance parameter $R = 0.4$ is used for jet reconstruction. Jets are reconstructed from calorimeter clusters at the electromagnetic energy scale and then recalibrated to the hadronic energy scale and corrected for pile-up effects [73]. A jet $\mathrm{p_T}$ cut of 25 GeV is applied. The jets are required to be in the fiducial region of the c-jet tagger of $|\eta| < 2.5$. A $JVF > 0.75$ cut (see Section 6.2.5) is applied on the jet vertex fraction to remove jets produced by pile-up interactions. Events are required to contain one or two jets and are classified in the 1 and 2-jet categories, respectively.

Table 7.2: Event selection criteria for the $W+$ c-jet cross section measurement

Cut	$W \rightarrow e\nu$ **channel**	$W \rightarrow \mu\nu$ **channel**
Preselection		
Data taking conditions	All sub-detectors working	
Primary vertex	$n_{tracks}^{PV} \geq 3$	
Trigger conditions	EF_e20_medium[119] (early) EF_e22_medium[119] (medium) EF_e22vh_medium[119] (late)	EF_mu18[88] (early) EF_mu18_medium[88] (late)
Trigger matching	Offline reconstructed lepton within $\Delta R = 0.15$ to trigger lepton	
W selection		
Lepton identification	*Tight++*	CB muon, quality cuts in Table 5.3
Kinematic cuts	$E_T > 25$ GeV $\lvert\eta\rvert < 2.47$ $\lvert\eta\rvert < 1.37$ or $\lvert\eta\rvert > 1.52$	$\mathrm{p_T} > 20$ GeV $\lvert\eta\rvert < 2.4$
Impact parameter cuts	$d_0/\sigma_{d_0} < 10$	
Lepton isolation	$\sum^{\Delta R=0.3} E_T^{calo} < 3$ GeV	$\sum^{\Delta R=0.2} E_T^{calo} < 4$ GeV $\sum^{\Delta R=0.3} p_T^{tracks} < 2.5$ GeV
Lepton-jet overlap removal	See text	
Lepton-jet isolation	See text	
Electron veto	Veto events with add. *medium++ e* with E_T >20 GeV, $\lvert\eta\rvert$ <2.47, 1.37< $\lvert\eta\rvert$ <1.52 excluded	Veto events with *tight++ e* with $E_T > 25$ GeV, $\lvert\eta\rvert < 2.47$, 1.37< $\lvert\eta\rvert$ <1.52 excluded, $\sum^{\Delta R=0.3} E_T^{calo}$ cut @90% eff. $\sum^{\Delta R=0.3} p_T^{tracks}$ cut @90% eff.
Muon veto	Veto events with CB μ, with $\mathrm{p_T} > 20$ GeV, $\lvert\eta\rvert < 2.5$, $z_0 < 10$ mm, quality cuts in Table 5.3, $\sum^{\Delta R=0.2} p_T^{tracks}/\mathrm{p_T} < 0.1$	Exactly one μ
E_T^{miss} cleaning	*Looser* jet cleaning, no jets in LAr hole (see text), LAr noise cleaning	
Missing energy	$E_T^{\mathrm{miss}} > 25$ GeV	$E_T^{\mathrm{miss}} > 20$ GeV
W transverse mass	$m_{\mathrm{T}}^{W} > 40$ GeV	$m_{\mathrm{T}}^{W} > 60$ GeV
Jets selection		
Kinematic cuts	$\mathrm{p_T} > 25$ GeV, $\lvert\eta\rvert$ <2.5	
Quality cuts	*Loose* criteria (see Section 4.4 and [73])	
Pile-up cleaning	Jet vertex fraction JVF > 0.75 (see text)	
Jet multiplicity	n_{jets}=1 or 2	
c-jet selection		
SMT tagger	Exactly one jet within $\Delta R = 0.5$, exactly one muon satisfying SMT cuts (see Section 5.3)	
c-jet cuts		#tracks > 3 or EMF >0.8 (see text)
Lepton cuts		8 GeV $< m(\mu, soft\ \mu) <$ 11 GeV rejected 80 GeV $< m(\mu, soft\ \mu) <$ 100 GeV rejected

7.4.6 *c*-jet selection

The Soft Muon Tagger (SMT) is used to select c-jets. It relies on the muonic decays of the c-hadrons. Combined muons with $\mathrm{p_T} > 4$ GeV and $\Delta R = 0.5$ from the axis of the jet are selected. They are referred to as *soft muons.* Further details on the cuts applied by the SMT and a detailed study of its performance in the data are given in Section 5.3. The corrections evaluated there are applied to the simulations to match the data. The tagged jet is required to be associated to only one soft muon, and events with more than one tagged jet are rejected.

In the muon channel, $Z+$ jets production is a non-negligible background. A significant fraction of this background is due to Z dimuon decays in which one of the muons emits a final state radiation photon which is wrongly reconstructed as a jet and then selected by the SMT. An additional cut for the jets tagged by the SMT is, therefore, applied in the muon channel. They are required to either contain at least 3 ID tracks or that the fraction of their total energy which is measured in the electromagnetic calorimeter (EMF) is less than 80%. Furthermore, the invariant mass of the hard and the soft muons is required to differ from the Υ and Z masses by rejecting events with 8 GeV $< m(\mu, \textit{soft-}\mu) <$ 11 GeV or 80 GeV $< m(\mu, \textit{soft-}\mu) <$ 100 GeV.

In the Monte Carlo $W + c$ sample additional corrections are applied concerning properties of the c-hadron. The events are reweighted to take into account most recent measurements of the fractions of different c-hadron species (*fragmentation fraction*), the fraction of c-jet momentum carried by the first c-hadron in the jet (*fragmentation function*) and the semimuonic branching ratios of the different c-hadron species. More details are given in Section 7.9.3.

7.5 Background estimation

In the electron channel, QCD multi-jet and $W+$ light-jets productions are the most important backgrounds, since these processes give higher contributions to the number N^{OS} of selected events in the opposite sign category than to the same sign N^{SS} one. Their residual contribution after the $N^{OS} - N^{SS}$ subtraction is therefore significant and it is estimated with data-driven techniques. In the muon channel, in addition to these two processes, $Z+$ jets production is also an important background and its contribution is determined from data. All other backgrounds are estimated from Monte Carlo simulations.

7.5.1 QCD multi-jet background

QCD multi-jet events pass the event selection for the following reasons:

- The selected isolated high-$\mathrm{p_T}$ electron or muon can come from a hadron decay.
- Jets and photons may be misreconstructred as electrons.
- Soft muons from hadron decays inside a jet may be selected by the Soft Muon Tagger in QCD multi-jet events.

The cuts on the lepton $\mathrm{p_T}$ and isolation variables and the E_T^{miss} and m_{T}^{W} cuts ensure high rejection of multi-jet events, but their production cross section is several orders of magnitude higher than for the signal one. The influence of QCD multi-jet background on the cross section measurement is reduced by the $N^{OS} - N^{SS}$ subtraction but not negligible.

Because of the high production cross section and the strong rejection it is impossible to simulate enough events for a reliable prediction of the impact of QCD multi-jet production on the measurement. Therefore this contribution has to be entirely determined with data-driven techniques.

7.5.1.1 Electron channel

The contribution of QCD multi-jet events in the electron channel is estimated with a technique analogous to the one described for the $W+$ b-jets cross section measurement in Section 6.3.3. The E_T^{miss} distribution is measured in data applying the selection cuts of Section 7.4 apart from the cut on E_T^{miss}. Two E_T^{miss} distributions, one for QCD multi-jet events and one for all other processes, are used in a template fit to the data E_T^{miss} distribution to get the size of the multi-jet contribution.

The multi-jet E_T^{miss} template is obtained from a data control sample enriched with QCD multi-jet events by applying the selection cuts without the cut on E_T^{miss} and inverting part of the electron quality requirements and the nominal isolation variable cut, which is therefore required to be higher than 3 GeV. The *medium++* quality cuts (see Section 4.3) are still applied for the electron identification as well as *tight++* cuts which are used for the electron trigger and, therefore, have to be applied also to the reconstructed electrons to avoid bias in the selection of the control sample. The *tight++* requirements which are not used by the trigger algorithms, namely a cut on the number of hits of the electron track in the TRT detector and a cut discriminating electrons from photon conversions, are inverted in the control sample selection.
Small contributions from other processes than QCD multi-jet in the control region are estimated with Monte Carlo simulations and subtracted.
The E_T^{miss} distributions obtained separately for OS and SS multi-jet events are found to be in agreement within the uncertainties. A common multi-jet template for both categories is therefore used in order to reduce the statistical error.

The non-multi-jet E_T^{miss} template includes contributions from the $W + c$ signal and from all other backgrounds and is determined from Monte Carlo simulations.
The fit to the data E_T^{miss} distribution is performed in the $10 < E_T^{\text{miss}} < 90$ GeV range separately for OS and SS events to determine the QCD multi-jet contribution separately for the two event categories. The charge-asymmetry

$$\alpha^{QCD} = \frac{N_{OS}^{QCD} - N_{SS}^{QCD}}{N_{OS}^{QCD} + N_{SS}^{QCD}} \tag{7.3}$$

of the QCD multi-jet background is evaluated using the fit results. α^{QCD} has a smaller uncertainty than the individual event numbers because part of the uncertainties cancels. The fit result for N_{SS}^{QCD} is also used as input to the fitting procedure described in Section 7.5.3 which gives the final estimate of the QCD multi-jet background in the electron channel.

The variation of α^{QCD} under the following variations is taken as the uncertainty on this parameter:

- The E_T^{miss} range in the fit, changing the lower bound between 5-20 GeV and the higher one between 70-120 GeV.
- The multi-jet template is varied by changing the inverted isolation cut between 1-7 GeV and varying the quality criteria for the electron selection.
- The non-multi-jet template is varied by changing the fraction of each contributing process by 20%.

The effect of the statistical uncertainties in the templates is evaluated using toy Monte Carlo simulations. The final results for the charge-asymmetry of QCD multi-jet events with one or two selected jets are

$$\alpha^{QCD}_{1-jet,e} = 0.025 \pm 0.06 \tag{7.4}$$

and

$$\alpha^{QCD}_{2-jet,e} = 0.04 \pm 0.09 \ . \tag{7.5}$$

7.5.1.2 Muon channel

In the muon channel, the QCD multi-jet contribution is estimated as

$$N^{QCD}_{OS-SS} = N^{QCD}_{pre-tag} \cdot R^{QCD}_{SMT} \cdot \alpha^{QCD} \tag{7.6}$$

where $N^{QCD}_{pre-tag}$ is the number of events passing the selection cuts without the Soft Muon Tagger cuts and R^{QCD}_{SMT} the tagging rate of the SMT measured for QCD multi-jet events.

$N^{QCD}_{pre-tag}$ is measured with a method analogous to the one presented for the $W+$ b-jets cross section measurement in Section 6.3.3. A *loose* selection is performed by dropping the muon isolation requirements, the *tight* selection uses the nominal isolation cuts. The tight and loose samples both contains contributions of *fake* non-prompt muons, produced in QCD multi-jet events, and of *real* prompt muons. Measuring the selection efficiency of the tight isolation cut for these two components, $N^{QCD}_{pre-tag}$ can be determined applying Eq. 6.4. The efficiency ϵ_{real} of the isolation cuts for prompt muons is determined in a data sample enriched with $Z \to \mu\mu$ events by measuring the fraction of muons passing these cuts, in analogy with the measurement described in Section 5.2. The efficiency ϵ_{fake} of the isolation cuts for non-prompt muons is measured in a data control sample enriched with QCD multi-jet events selected using inverted E_T^{miss} and m_{T}^W cuts. To quantify the uncertainty of ϵ_{fake} an alternative estimation of ϵ_{fake} is performed evaluating the isolation efficiency as a function of the impact parameter significance d_0/σ_{d_0} of the muons, since at high d_0/σ_{d_0} values muons from c and b decays are dominating. The two methods give different results for ϵ_{fake} as the second method is more sensitive to heavy flavour production in QCD multi-jet events which results in muons with higher d_0/σ_{d_0} values. ϵ_{fake} is, therefore, taken as the average of the two results and their difference is used as systematic uncertainty.

R^{QCD}_{SMT} and α^{QCD} are measured in two different data control samples enriched with QCD multi-jet events (see Figure 7.5). The first sample is selected by inverting the muon isolation cuts, i.e. by requiring $\sum^{\Delta R=0.2} E_T^{calo} > 5$ GeV and $\sum^{\Delta R=0.3} p_T^{tracks} > 3.5$ GeV. For the second sample $m^W_{\mathrm{T}} < 30$ GeV is required. The contributions of $W+$ jets and $Z+$ jets events in the control regions are estimated from Monte Carlo simulations and subtracted. A 25% uncertainty including cross section and detector related errors is assigned to this estimation. All other processes give very small contributions and are thus neglected.

In the two control data samples, R^{QCD}_{SMT} and α^{QCD} are evaluated from the numbers of events $N^{pre-tag}$ and N^{SMT} before and after the Soft Muon Tagger cuts as

$$R^{QCD}_{SMT} = \frac{N^{SMT}_{data} - N^{SMT}_{W/Z+jets,MC}}{N^{pre-tag}_{data} - N^{pre-tag}_{W/Z+jets,MC}} \tag{7.7}$$

and

$$\alpha^{QCD} = \frac{(N^{SMT}_{data} - N^{SMT}_{W/Z+jets,MC})^{OS} - (N^{SMT}_{data} - N^{SMT}_{W/Z+jets,MC})^{SS}}{(N^{SMT}_{data} - N^{SMT}_{W/Z+jets,MC})^{OS} + (N^{SMT}_{data} - N^{SMT}_{W/Z+jets,MC})^{SS}} \; . \tag{7.8}$$

The R^{QCD}_{SMT} and α^{QCD} results obtained in the two control data samples are averaged. The uncertainty in R^{QCD}_{SMT} is defined as the difference between the two estimates divided by $\sqrt{2}$, which is larger than the uncertainty on the individual measurements. The largest one of the errors of the two measurements is used as the uncertainty on the average α^{QCD} since it is larger than the difference between the two measurements.
To refine the estimate of R^{QCD}_{SMT}, a second method has been developed:. In the control region with inverted isolation cuts, R^{QCD}_{SMT} is found to increase linearly with decreasing muon isolation cuts, i.e. for less isolated muons. A linear extrapolation of the R^{QCD}_{SMT} values from the control to the signal region provide results in agreement with the previously determined values but with smaller uncertainties.

The results of the multi-jet background estimation in the muon channel are summarized in Table 7.3.

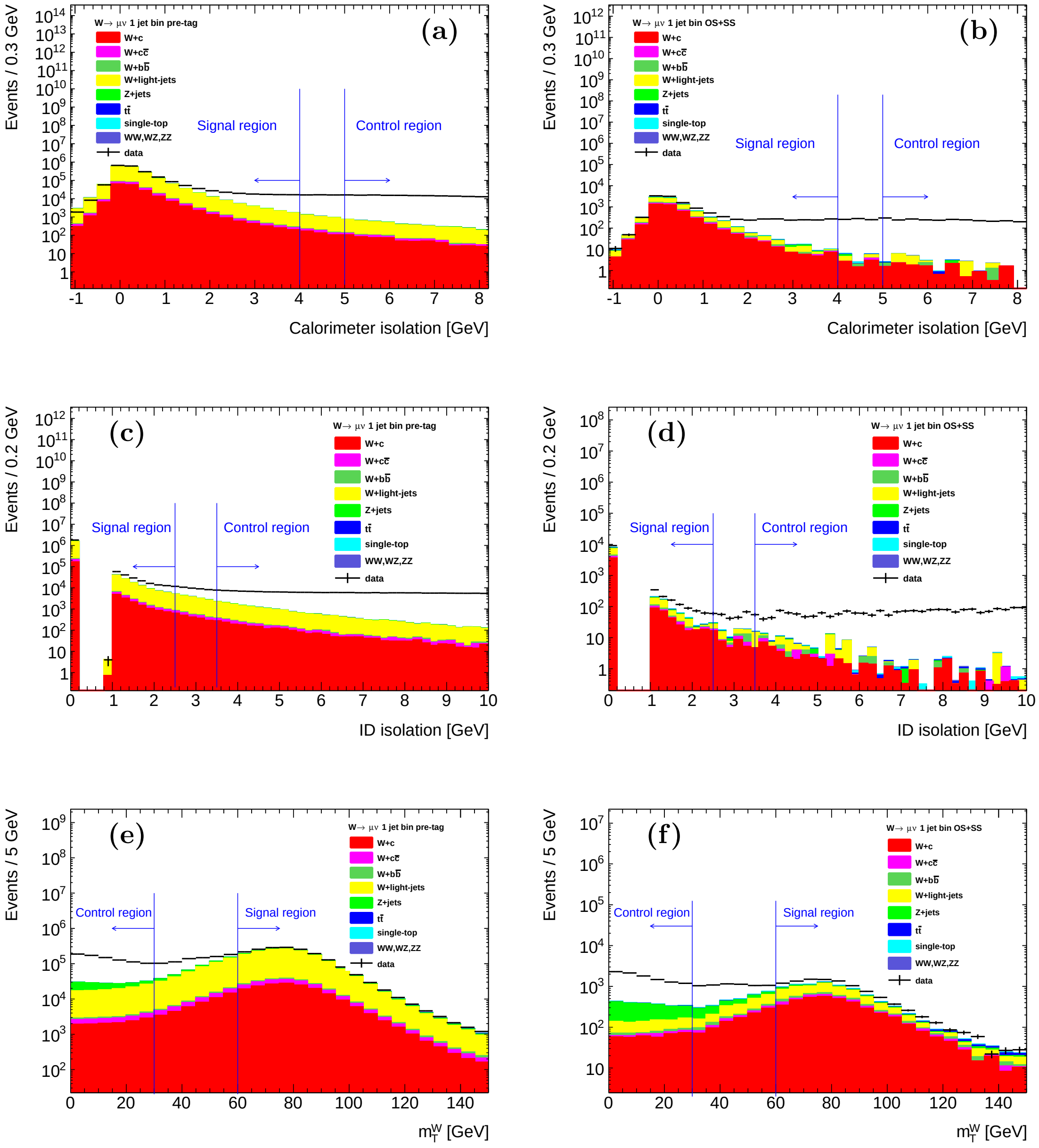

Figure 7.5: Selection of two QCD multi-jet enriched control samples for the muon channel using inverted isolation cuts (a, b, c, d) and an inverted m_{T}^{W} cut (e, f. The left plots are before SMT cuts, the right plots are after the full selection for the combination of the OS and SS samples. Simulated distributions for the $W + c$ signal and all backgrounds, except QCD multi-jet, are shown in the plots and normalised to the Monte Carlo predictions. Data exceeding the Monte Carlo estimated contributions is assumed to correspond to QCD multi-jet events which are the dominating component in the control regions.

Table 7.3: Variables used for the QCD multi-jet background prediction in the muon channel

	1-jet events	2-jet events
$N^{QCD}_{pre-tag,\mu}$	21955 ± 3011	6254 ± 1519
$R^{QCD}_{SMT,\mu}$	0.0144 ± 0.0048	0.035 ± 0.010
α^{QCD}_{μ}	0.226 ± 0.038	0.237 ± 0.044

7.5.2 $W+$ light-jets background

$W+$ light-jets events contribute to the background due to mistagged light-jets. Soft muons inside light-jets likely are from semileptonic decays of π or K mesons which make up almost all of the tracks inside a jet. Despite the strong rejection of the SMT against light-jets, $W+$ light-jets background is important due to the high production cross section. This process gives a higher contribution to the OS sample than to the SS one and is therefore not negligible in the $N^{OS} - N^{SS}$ subtraction. Its contribution is determined with a data-driven method.

7.5.2.1 Electron channel

In the selected data sample without application of the Soft Muon Tagger cuts (pre-tag data sample) the number of combinations of the electron with tracks in the selected jets with OS and SS charges are determined in order to measure the OS/SS charge-asymmetry $\alpha^{W+\ light\text{-}jets}_{tracks}$ (defined as for Eq. 7.3) for the $W+$ jets background, which is the dominating contribution to the pre-tag sample. The QCD multi-jet contribution to this sample is estimated with the same technique as discussed in Section 7.5.1, all other background contributions are determined by simulations. The background contributions are then subtracted from the data. The $W + c$ background for the $\alpha^{W+\ light\text{-}jets}_{tracks}$ measurement is also estimated in simulations.

The ratio of the charge-asymmetry for tracks and for the nominal selection in Monte Carlo events $\alpha^{W+\ light\text{-}jets}_{MC}/\alpha^{W+\ light\text{-}jets}_{MC,tracks}$ is then used to rescale the value of $\alpha^{W+\ light\text{-}jets}_{tracks}$ measured in data to determine $\alpha^{W+\ light\text{-}jets}$. The results for events with one and two selected jets are

$$\alpha^{W+\ light\text{-}jets}_{1-jet,e} = 0.09 \pm 0.03 \tag{7.9}$$

and

$$\alpha^{W+\ light\text{-}jets}_{2-jet,e} = 0.07 \pm 0.03 \ , \tag{7.10}$$

respectively. The asymmetry parameters are used together with the results of the fitting technique described in Sec. 7.5.3 to determine the $W+$ light-jets contribution after the $N^{OS} - N^{SS}$ subtraction in the electron channel.

7.5.2.2 Muon channel

In the muon channel, the $W+$ light-jets contribution is estimated with a strategy similar to the one used for the QCD multi-jet background. The $W+$ light-jets contributions after the $N^{OS} - N^{SS}$ subtraction is

$$N_{OS-SS}^{W+\ light\text{-}jets} = N_{pre-tag}^{W+\ jets} \cdot f^{W+\ light\text{-}jets} \cdot R_{SMT}^{W+\ light\text{-}jets} \cdot \alpha^{W+\ light\text{-}jets} \tag{7.11}$$

where $N_{pre-tag}^{W+\ jets}$ is the number of $W+$ jets events before the Soft Muon Tagger cuts, $f^{W+\ light\text{-}jets}$ the fraction of $W+$ light-jets events in the pre-tag $W+$ jets sample, $R_{SMT}^{W+\ light\text{-}jets}$ the SMT tagging rate in $W+$ light-jets events and $\alpha^{W+\ light\text{-}jets}$ the OS/SS charge-asymmetry of $W+$ light-jets events (defined as for Eq. 7.3).

The number of pre-tag $W+$ jets events is determined from data assuming that after subtraction of the backgrounds only $W+$ jets events remain. Diboson, $t\bar{t}$ and single-top backgrounds are estimated with Monte Carlo simulations and the QCD multi-jet and $Z+$ jets contributions with the methods described in Section 7.5.1 and 7.5.4, respectively.

$f^{W+\ light\text{-}jets}$ is evaluated using a heavy-flavour jet tagger based on the long lifetime of c-hadrons and b-hadrons, *MV1* [120]. The number of pre-tag $W+$ jets events which are tagged by MV1 can be expressed as the sum of the $W+$ light-jets, $W+b\bar{b}$, $W+c\bar{c}$ and $W+c$ pre-tag contributions, each one multiplied by the corresponding tagging rate R:

$$\begin{aligned} N_{MV1,pre-tag}^{W+\ jets,\pm} = N_{pre-tag}^{W+\ jets,\pm}(& f^{W+b\bar{b}} R_{MV1}^{W+b\bar{b}} + f^{W+c\bar{c}} R_{MV1}^{W+c\bar{c}} \\ & + f^{W+c} R_{MV1}^{W+c} + f^{W+\ light\text{-}jets} R_{MV1}^{W+\ light\text{-}jets}) \ , \end{aligned} \tag{7.12}$$

$$f^{W+b\bar{b}} + f^{W+c\bar{c}} + f^{W+c} + f^{W+\ light\text{-}jets} = 1 \ . \tag{7.13}$$

The tagging rates of MV1 for $W+$ light-jets, $W+b\bar{b}$, $W+c\bar{c}$ and $W+c$ events are determined using simulated event samples, with the jet-$\mathrm{p_T}$ dependent data-driven corrections to the tagging efficiency evaluated in [120] applied. The fraction of $W+b\bar{b}/W+c\bar{c}$ events is also evaluated in simulations. Considering separately W^+ and W^- events the equations can be finally solved to find $f^{W+\ light\text{-}jets}$.

The SMT tagging rate $R_{SMT}^{W+\ light\text{-}jets}$ is estimated from Monte Carlo simulations with data-driven correction factors applied (see Section 5.3). The asymmetry $\alpha^{W+\ light\text{-}jets}$ is determined as for the electron channel. The final results on the $W+$ light-jets background estimation in the muon channel are given in Table 7.4

Table 7.4: Parameters used for the $W+$ light-jets background estimation in the muon channel

	1-jet events	2-jet events
$N^{W+\ jets}_{pre-tag,\mu}$	1746273 ± 5438	365518 ± 2538
$f_{\mu}^{W+\ light\text{-}jets}$	0.848 ± 0.068	0.762 ± 0.061
$R^{W+\ light\text{-}jets}_{SMT,\mu}$	0.00211 ± 0.00030	0.00578 ± 0.00082
$\alpha_{\mu}^{W+\ light\text{-}jets}$	0.069 ± 0.022	0.023 ± 0.025

7.5.3 Refinement of the QCD multi-jet and $W+$ light-jets background determination in the electron channel

In the electron channel the estimations of the QCD multi-jet and $W+$ light-jets contributions, discussed in Sections 7.5.1.1 and 7.5.2.1, are the dominating sources of background uncertainties. The estimate of the size of their contributions is refined using a fitting technique in the SS sample, after subtraction of all other processes which are estimated from Monte Carlo, assuming that the difference between prediction and data for SS events can be totally attributed to QCD multi-jet and $W+$ light-jets events. The following quantity is minimized:

$$\chi^2 = \frac{(N_{QCD}^{fit,SS} - N_{QCD})^2}{\sigma^2_{QCD,SS}} + \frac{(N^{fit,SS}_{W+\ light\text{-}jets} - N^{SS}_{W+\ light\text{-}jets})^2}{\sigma^2_{W+\ light\text{-}jets,SS}}, \tag{7.14}$$

with N^{SS}_{QCD} and $N^{SS}_{W+\ light\text{-}jets}$ being the data driven estimates of the QCD multi-jet and $W+$ light-jets SS contributions and $N^{fit,SS}_{QCD}$ and $N^{fit,SS}_{W+\ light\text{-}jets}$ being the refined estimate of their SS contributions which are constrained by

$$N^{fit,SS}_{W+\ light\text{-}jets} = N^{SS}_{data} - N^{fit,SS}_{QCD} - N^{MC,SS}_{other\ processes}\ . \tag{7.15}$$

The uncertainties $\sigma_{QCD,SS}$ and $\sigma_{W+\ light\text{-}jets,SS}$ on the estimates of the SS contributions are determined in simulations as 50% and 30%, respectively.

The $N^{fit,SS}_{QCD}$ and $N^{fit,SS}_{W+\ light\text{-}jets}$ resulting from the minimization are used together with the charge-asymmetries $\alpha_{QCD,W+\ light\text{-}jets}$ estimated in Sections 7.5.1 and 7.5.2 to compute the contributions of QCD multi-jet and $W+$ light-jets backgrounds after the $N^{OS} - N^{SS}$ subtraction by using the equation

$$N^{OS-SS}_{QCD,W+\ light\text{-}jets} = \frac{2 \cdot \alpha_{QCD,W+\ light\text{-}jets} \cdot N^{SS}_{QCD,W+\ light\text{-}jets}}{1 - \alpha_{QCD,W+\ light\text{-}jets}}\ . \tag{7.16}$$

The lower impact of the uncertainties in the QCD multi-jet background estimation and the higher relevance of the $Z+$ jets background in the muon channel would greatly reduce the benefits of this method, which is therefore used in the electron channel only.

7.5.4 $Z+$ jets background

$Z+$ jets production is a small background in the electron channel, where it is estimated from simulations, but is important in the muon channel. The analysis selection defines a dimuon data sample with an isolated hard muon and a soft muon inside a jet. Most $Z+$ jets events with a $Z \to \mu\mu$ decay are rejected by the dilepton veto applied, which discards events with two isolated muons. $Z+$ jets events in which one of the two Z-muons is not reconstructed by the detector and with a soft muon produced inside one of the jets contribute equally to the OS and SS sample and their contribution is therefore negligible after the $N^{OS} - N^{SS}$ subtraction.

On the other hand, events in which one of the Z muons is not isolated, mostly because it radiates a photon which is misreconstructed as a jet, represent an important background because they only contribute to the OS sample like the signal events. An additional cut is applied in the muon channel to the jet tagged by the SMT in order to reduce the contribution of these events. The jet is required either to be associated with at least 3 ID tracks or to have an electromagnetic fraction (EMF), i.e. the fraction of its total energy which is reconstructed in the electromagnetic calorimeter, below 80%. As shown in Figure 7.6 $Z+$ jets events are characterised on average by a lower track multiplicity $nTracks$ and and a higher electromagnetic fraction EMF with respect to signal events.

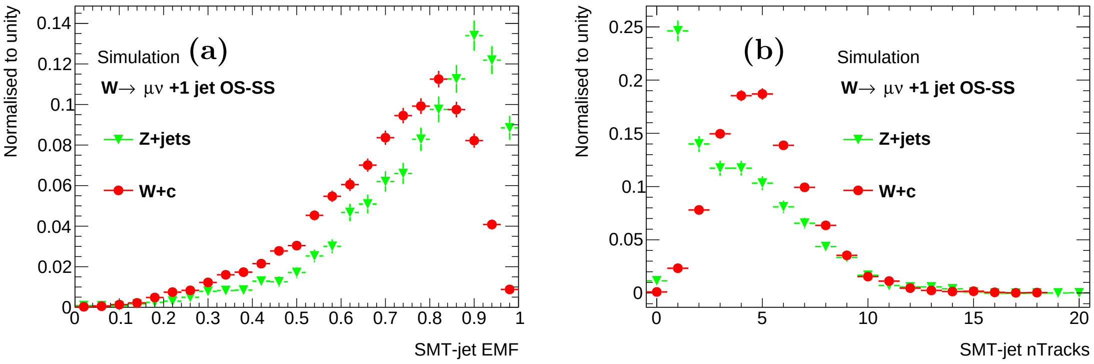

Figure 7.6: Electromagnetic energy fraction EMF (a) and track multiplicity $nTracks$ (b) distributions normalised to unity for SMT tagged jet in Monte Carlo $Z+$ jets (green) and $W+c$ (red) muon channel events No dilepton invariant mass cut is applied to the events in the plots. is not applied. Only statistical errors are shown.

To further reduce the $Z+$ jets contribution the difference between the invariant mass of the hard and soft muons $m(\mu, soft\text{-}\mu)$ and the Z mass is required to be at least 10 GeV in the muon channel. The 80 GeV $<$ $m(\mu, soft\text{-}\mu)$ $<$100 GeV region defines a control sample dominated by $Z+$ jets production (see Figure 7.7a) which is used to determine the

$Z+$ jets background with a data driven technique.

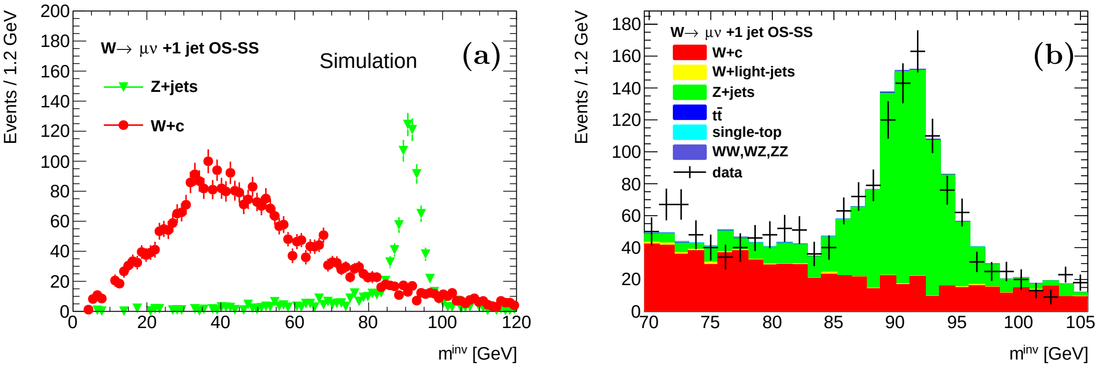

Figure 7.7: (a) Distributions of the invariant mass $m(\mu, \textit{soft-}\mu)$ of hard and soft muons in Monte Carlo $Z+$ jets and $W + c$ events after the selection. (b) data $m(\mu, \textit{soft-}\mu)$ distribution near the Z peak with the estimated background contributions. The $W + c$ normalisation from simulations is increased by 27% as determined by the procedure described in the text, the $Z+$ jets simulated distributions is corrected for the results of the data-driven estimation discussed in this section. The QCD multi-jet contribution is expected to be negligible and is therefore not considered in the plot, the $t\bar{t}$, single-top and diboson contributions are predicted to be small.

The number of $Z+$ jets events is evaluated in the data control region after subtraction of $W + c$, $W+$ light-jets and diboson Monte Carlo events, while all other contributions are negligible. Uncertainties of 25% and 50% for $W+$ light-jets and diboson production, respectively, cover cross section uncertainties and detector effects. A 25% uncertainty is assigned also to the $W + c$ Monte Carlo prediction, but this prediction is constrained by data using the following strategy: the $W + c$ Monte Carlo contribution in the control region is used to obtain a first estimate of the $Z+$ jets component in the control sample and a correction factor is determined for the $Z+$ jets simulation to match the data. This correction factor is applied to $Z+$ jets simulation in the signal region to determine a preliminary $W + c$ event yield, which is found to be 27% higher than the Monte Carlo predictions. The $W+c$ Monte Carlo contribution in the control region is therefore increased by 27% providing a final estimate of the correction to the normalisation of the simulated $Z+$ jets events

$$SF^{Z+\ jets} = \frac{N^{Z+\ jets}_{CR,data}}{N^{Z+\ jets}_{CR,MonteCarlo}} = 1.066 \pm 0.067 \ . \tag{7.17}$$

The estimated contribution of $Z+$ jets events in the signal region is therefore multiplied by this scale factor. The $m(\mu, \textit{soft-}\mu)$ distribution in the control data sample is found to be well described simulated data after the data-driven background normalisation as shown in Figure 7.7b.

7.6 Signal and background yields

In Tables 7.5, 7.6 the contributions of the background processes in the electron channel are shown respectively for the 1-jet and 2-jet event categories. Tables 7.7, 7.8 are relative to the muon channel. The yields in the OS and SS samples are reported for illustrative purpose, while the results after the $N^{OS} - N^{SS}$ subtraction are used for the cross section determination as discussed in Section 7.9. $W + b\bar{b}$ and $W + c\bar{c}$ contributions are compatible with zero after the subtraction and are therefore neglected. $t\bar{t}$ production is a very small background for events with one selected jet, while its contribution to events with two selected jets is larger. QCD multi-jet, $W+$ light-jets and $Z+$ jets (the latter in the muon channel only) are important backgrounds even after the $N^{OS} - N^{SS}$ subtraction and are estimated in data as discussed in last section. The Monte Carlo predictions for $W+$ light-jets and $Z+$ jets are also shown in the tables.

Table 7.5: Background contributions in the electron channel for 1-jet events

e channel - 1-jet	N^{OS}	N^{SS}	N^{OS-SS}
$W + b\bar{b}$	183 ± 12(stat)	181 ± 12(stat)	2 ± 18(stat)
$W + c\bar{c}$	217 ± 14(stat)	237 ± 14(stat)	-20 ± 20(stat)
$t\bar{t}$	94 ± 2(stat)	81 ± 2(stat)	12 ± 3(stat)
Single-top	178 ± 3(stat)	115 ± 2(stat)	63 ± 3(stat)
Diboson	51 ± 1(stat)	15 ± 0(stat)	36 ± 1(stat)
$Z+$ jets	62 ± 5(stat)	54 ± 5(stat)	7 ± 7(stat)
$W+$ light-jets (Monte Carlo)	1498 ± 61(stat)	1189 ± 54(stat)	309 ± 82(stat)
$W+$ light-jets (measured)	1448 ± 360(syst)	1199 ± 289(syst)	248 ± 106(syst)
QCD multi-jet (measured)	1067 ± 330(syst)	1014 ± 289(syst)	52 ± 128(syst)

Table 7.6: Background contributions in the electron channel for 2-jet events

e channel - 2-jet	N^{OS}	N^{SS}	N^{OS-SS}
$W + b\bar{b}$	226 ± 13(stat)	241 ± 13(stat)	-15 ± 19(stat)
$W + c\bar{c}$	238 ± 12(stat)	245 ± 13(stat)	-7 ± 18(stat)
$t\bar{t}$	562 ± 5(stat)	484 ± 5(stat)	77 ± 7(stat)
Single-top	314 ± 4(stat)	234 ± 3(stat)	80 ± 5(stat)
Diboson	59 ± 1(stat)	23 ± 0(stat)	35 ± 1(stat)
$Z+$ jets	71 ± 5(stat)	56 ± 4(stat)	14 ± 6(stat)
$W+$ light-jets (Monte Carlo)	788 ± 40(stat)	663 ± 36(stat)	125 ± 54(stat)
$W+$ light-jets (measured)	765 ± 188(syst)	662 ± 157(syst)	102 ± 56(syst)
QCD multi-jet (measured)	558 ± 198(syst)	515 ± 157(syst)	42 ± 101(syst)

The data yields and the sum of the estimated background contributions are summarised in Table 7.9, as well as the $W + c$ yield measurement determined as the excess of data over backgrounds, which is compared with the Monte Carlo predictions. The yields are also measured in the combination of the 1 and 2-jet event samples (see Table 7.10). The backgrounds are redetermined in the combined sample to exploit the higher statistics available, therefore the combined 1+2-jet yield is not the direct sum of the two individual yields.

Table 7.7: Background contributions in the muon channel for 1-jet events

μ channel - 1-jet	N^{OS}	N^{SS}	$N^{\text{OS}-\text{SS}}$
$W+b\bar{b}$	233 ± 15(stat)	268 ± 15(stat)	-35 ± 21(stat)
$W+c\bar{c}$	220 ± 14(stat)	243 ± 15(stat)	-23 ± 21(stat)
$t\bar{t}$	91 ± 22	69 ± 17	23 ± 4
Single-top	175 ± 28	117 ± 20	57 ± 10
Diboson	51 ± 15	14 ± 5	36 ± 10
$Z+$ jets (Monte Carlo)	293 ± 12(stat)	93 ± 6(stat)	200 ± 14(stat)
$Z+$ jets (measured)	312 ± 24	99 ± 9	214 ± 20
$W+$ light-jets (Monte Carlo)	1559 ± 60(stat)	1289 ± 59(stat)	270 ± 84(stat)
$W+$ light-jets (measured)	1667 ± 271	1451 ± 237	216 ± 78
QCD multi-jet (measured)	194 ± 70	122 ± 44	71 ± 28

Table 7.8: Background contributions in the muon channel for 2-jet events

μ channel - 2-jet	N^{OS}	N^{SS}	$N^{\text{OS}-\text{SS}}$
$W+b\bar{b}$	268 ± 15(stat)	238 ± 13(stat)	30 ± 20(stat)
$W+c\bar{c}$	245 ± 13(stat)	256 ± 13(stat)	-11 ± 18(stat)
$t\bar{t}$	549 ± 109	430 ± 89	119 ± 24
Single-top	299 ± 38	217 ± 31	82 ± 14
Diboson	58 ± 19	19 ± 6	39 ± 13
$W+$ light-jets (Monte Carlo)	773 ± 32(stat)	727 ± 35(stat)	46 ± 47(stat)
$W+$ light-jets (measured)	824 ± 135	786 ± 129	38 ± 40
$Z+$ jets (Monte Carlo)	243 ± 11(stat)	72 ± 6(stat)	172 ± 12(stat)
$Z+$ jets (measured)	215 ± 16	61 ± 5	154 ± 13
QCD multi-jet (measured)	135 ± 51	83 ± 32	52 ± 22

In Figure 7.8 the distributions of the electron, soft muon and tagged jet transverse momentum, of the tagged jet η, of E_T^{miss} and m_{T}^{W} are shown. The data distributions in the plots are the difference between the distributions measured in OS and SS events, the signal and background distributions are normalised to their respective estimated contributions after the $N^{OS}-N^{SS}$ subtraction. The QCD multi-jet distributions are determined in QCD enriched control data samples defined in Section 7.5.1. The distributions relative to all other processes are evaluated from simulations. The corresponding plots for the muon channel are shown in Figure 7.9. The transverse momentum of the electron and of the tagged jet and the E_T^{miss} in 2-jet events are shown for both channels in Figure 7.10.

Data and Monte Carlo are in good agreement in all the plots. In Figures 7.8d and 7.9d the drop at $\eta\approx0$ is caused by the reduced acceptance of the muon spectrometer which leads to a lower tagging rate for the SMT in that region.

Table 7.9: Summary of the yields measured in data, of the background estimations, and of the measured and predicted $W + c$ yields for 1-jet and 2-jet events for the electron and muon channels. The errors are the sum of the statistical and the systematic uncertainties where not differently stated.

	1-jet events		2-jet events	
	e channel	μ channel	e channel	μ channel
Data	4321 ± 102(stat)	4961 ± 103(stat)	1574 ± 82(stat)	1897 ± 83(stat)
Estimated background	420 ± 162	617 ± 87	354 ± 114	484 ± 56
$W + c$ measured	3900 ± 191	4344 ± 134	1219 ± 140	1413 ± 100
$W + c$ predicted	3351 ± 43(stat)	3393 ± 44(stat)	1190 ± 27(stat)	1154 ± 27(stat)

Table 7.10: Summary of the yields measured in data, of the background estimations, and of the measured and predicted $W + c$ yields for 1+2-jet events for the electron and muon channels. The errors are the sum of the statistical and the systematic uncertainties where not differently stated.

	1+2-jet events	
	e channel	μ channel
Data	5895 ± 131(stat)	6858 ± 132(stat)
Estimated background	810 ± 206	1097 ± 107
$W + c$ measured	5084 ± 244	5761 ± 170
$W + c$ predicted	4541 ± 52(stat)	4547 ± 52(stat)

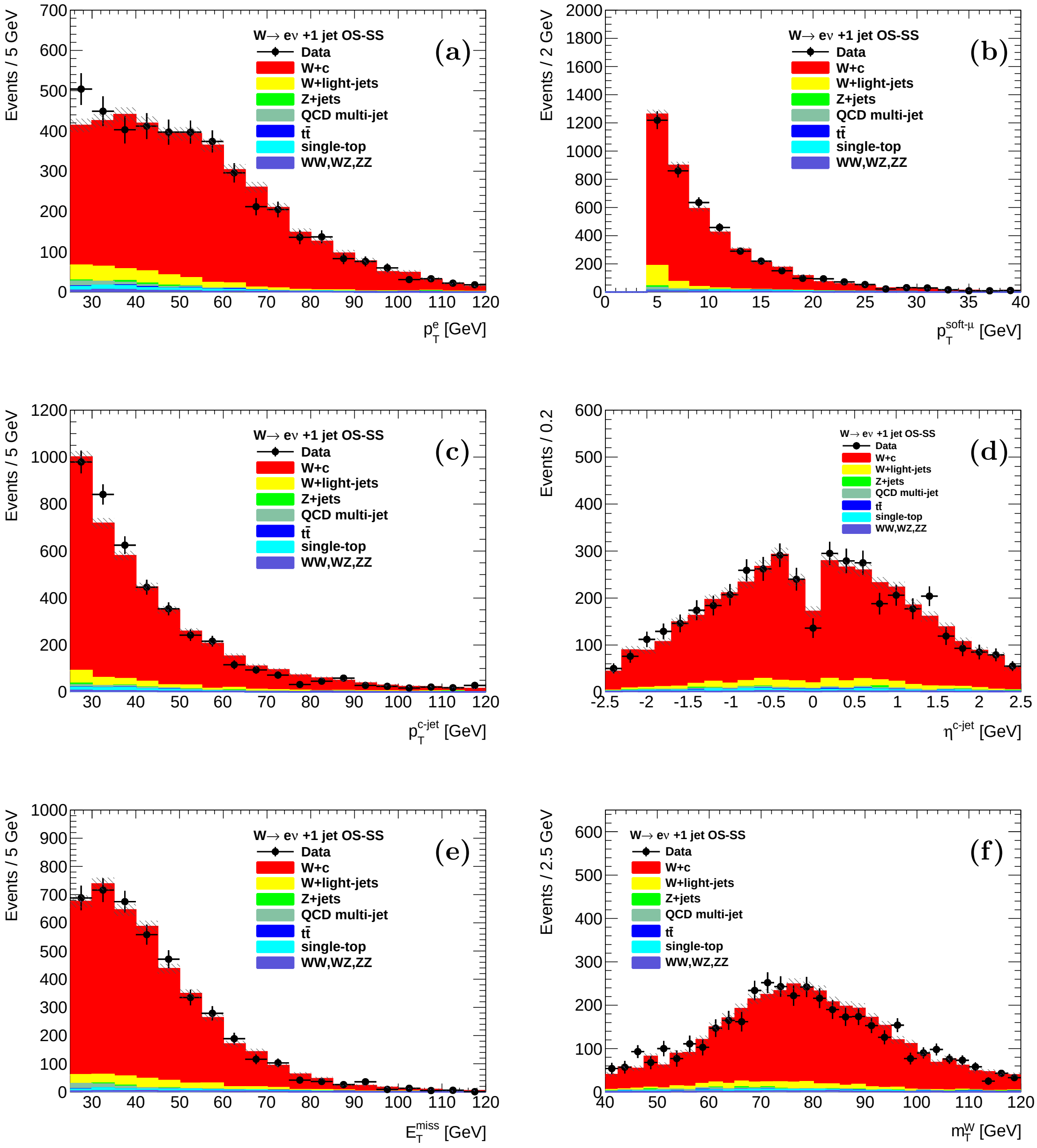

Figure 7.8: Distributions of the electron (a), soft muon (b) and tagged jet (c) $\mathrm{p_T}$, of the tagged jet η (d) and of E_T^{miss} (e) and m_{T}^{W} (f) for 1-jet events in the electron channel. The data distributions are obtained in OS events and subtracted of the SS distribution. Signal and background distributions are normalised to the estimated contribution after the $N^{OS} - N^{SS}$ subtraction. The Monte Carlo statistical errors are shown as a dashed area. Statistical errors are shown for data.

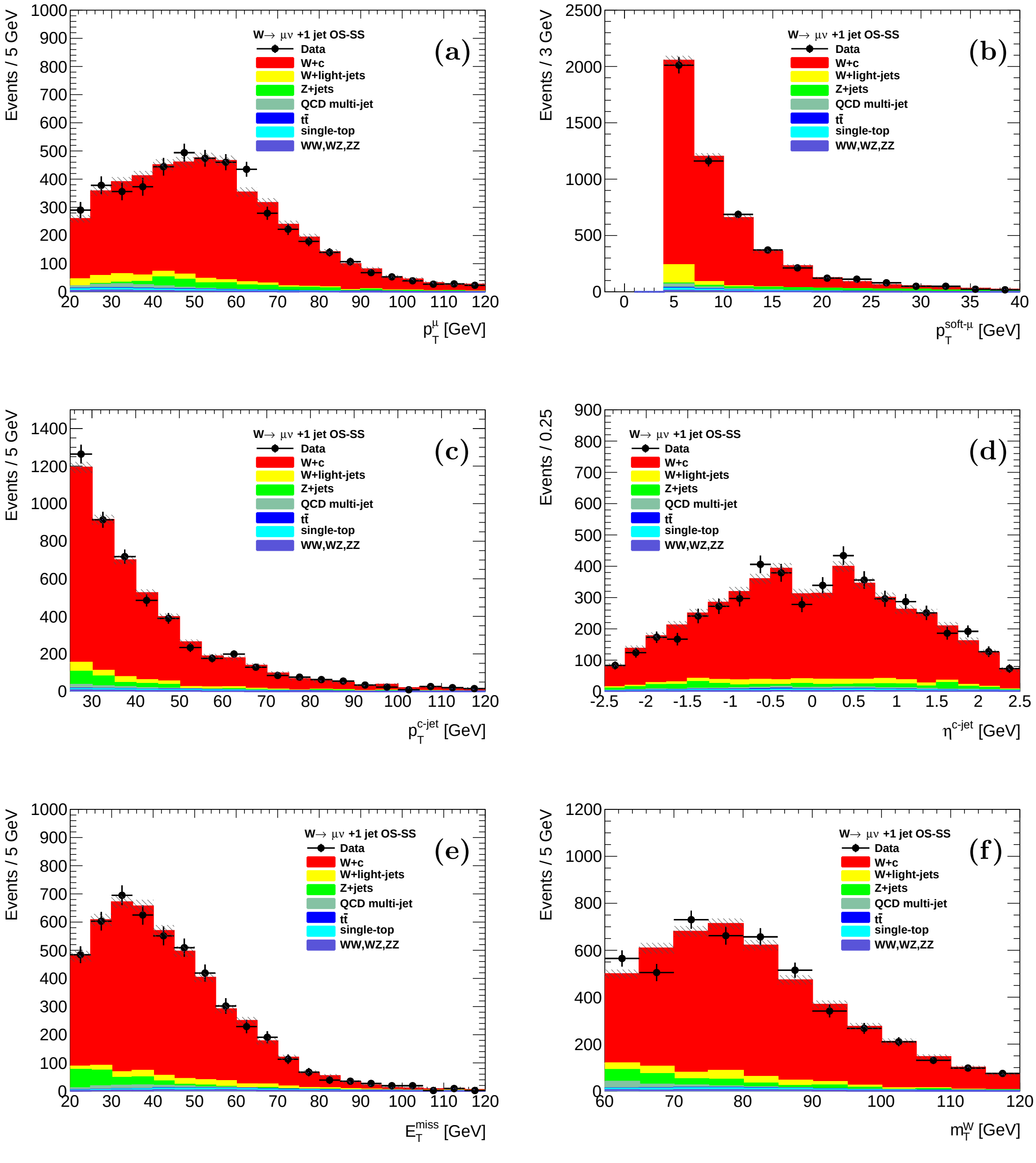

Figure 7.9: Distributions of the muon (a), soft muon (b) and tagged jet (c) $\mathrm{p_T}$, of the tagged jet η (d) and of E_T^{miss} (e) and m_{T}^{W} (f) for 1-jet events in the muon channel. The data distributions are obtained in OS events and subtracted of the SS distribution. Signal and background distributions are normalised to the estimated contribution after the $N^{OS} - N^{SS}$ subtraction. The Monte Carlo statistical errors are shown as a dashed area. Statistical errors are shown for data.

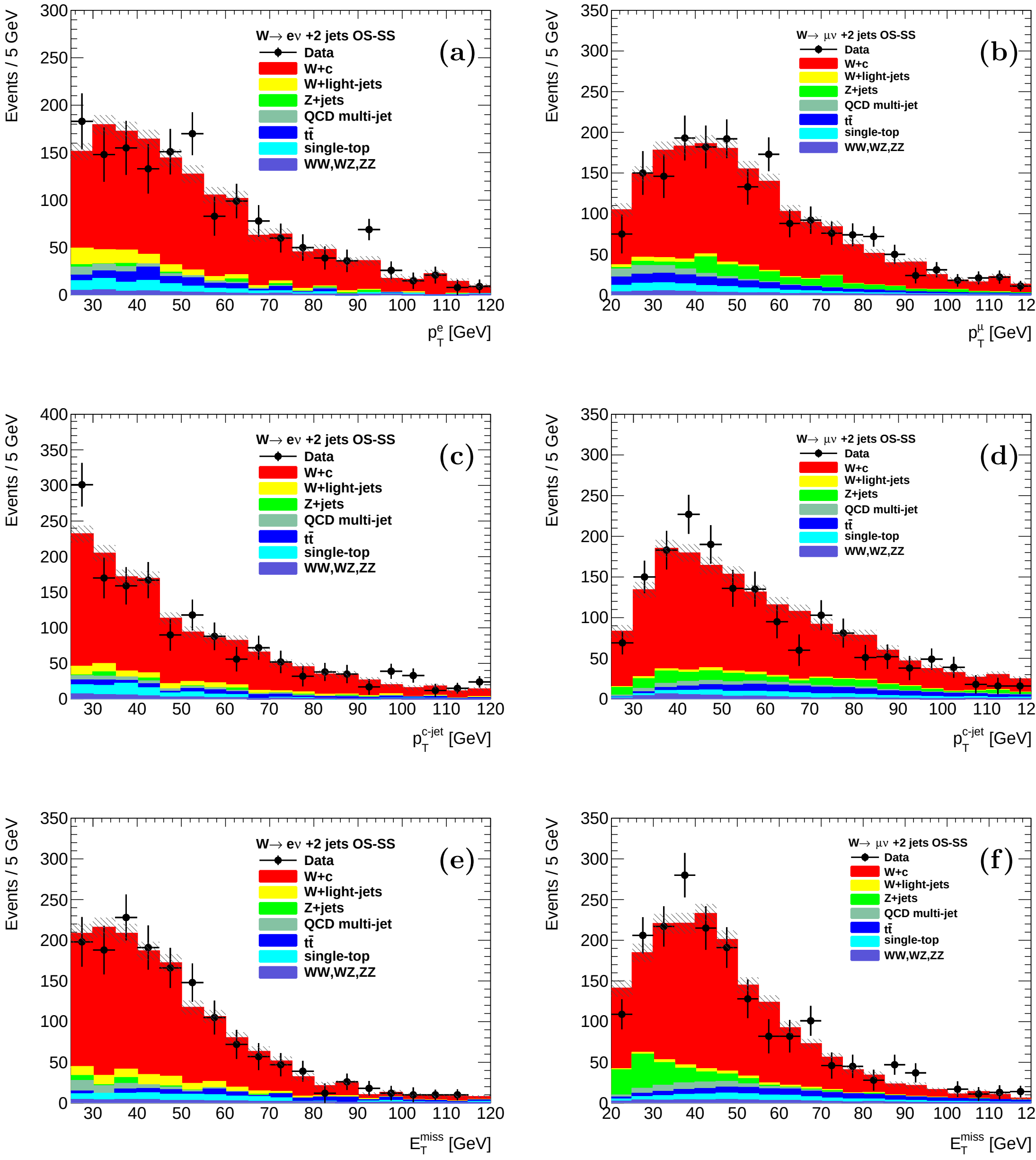

Figure 7.10: Distributions of the $\mathrm{p_T}$ of the lepton from the W decay (a and b), and of the tagged jet (c and d) and of E_T^{miss} (e and f) for 2-jet events in the electron (left plots) and muon (right plots) channels. The data distributions are obtained in OS events and subtracted of the SS distribution. Signal and background distributions are normalised to the estimated contribution after the $N^{OS} - N^{SS}$ subtraction. The Monte Carlo statistical errors are shown as a dashed area. Statistical errors are shown for data.

7.7 W^++ c-jet and W^-+ c-jet production

The yields of W^++ c-jet and W^-+ c-jet events are measured separately. The ratio of the yields after background subtraction is given by

$$R^{+/-}_{yields} = \frac{N^{OS-SS}_{\mathrm{data}^+} - N^{OS-SS}_{\mathrm{bkg}^+}}{N^{OS-SS}_{\mathrm{data}^-} - N^{OS-SS}_{\mathrm{bkg}^-}} \, . \tag{7.18}$$

For each background contribution j, the ratio $R^{+/-}_{\mathrm{bkg,j}}$ is evaluated separately.
$R^{+/-}_{\mathrm{bkg,j}}$ is determined from simulations of the $t\bar{t}$, diboson, single-top and $Z+$ jets backgrounds. In the muon channel, where the $Z+$ jets contribution is important, the value of $R^{+/-}_{\mathrm{bkg},Z+\text{ jets}}$ obtained in simulations is found in agreement with a data-driven estimation performed with the method described in Section 7.5.4.
For the QCD multi-jet events, $R^{+/-}_{\mathrm{bkg,QCD}}$ is evaluated in the electron channel using the same template fit on the E_T^{miss} distribution described in Section 7.5.1.1. In the muon channel $R^{+/-}_{\mathrm{bkg,QCD}}$ is evaluated separately in the two data control samples dominated by QCD multi-jet events defined for the asymmetry measurement in Section 7.5.1. In both control regions $W+$ jets and $Z+$ jets contributions are estimated from Monte Carlo simulations and subtracted, assigning an uncertainty by varying this contamination by 25%. The values of $R^{+/-}_{\mathrm{bkg,QCD}}$ measured in the two control samples are averaged.

For the $W+$ light-jets background, $R^{+/-}_{\mathrm{bkg},W+\text{ light-jets}}$ is evaluated in both channels at pre-tag level as the ratio of positive and negative events selected without applying the SMT cuts (pre-tag selection). This data sample is dominated by $W+$ jets events; the estimated contributions of other processes are subtracted. A correction factor for the extrapolation of the ratio from pre-tag to tagged events is evaluated on Monte Carlo simulations and found to be compatible with 1.
Using the values of the ratio of the yields for the different background processes determined as described above, the yields for the $W^+ + \bar{c}$ and $W^- + c$ productions and their ratio can be evaluated with the following equations:

$$\begin{aligned} N^{OS-SS}_{W^{+}+\ c\text{-}jet} &= N^{OS-SS}_{data^+} - \sum_{\mathrm{j}} \frac{R^{+/-}_{\mathrm{bkg,j}}}{1 + R^{+/-}_{\mathrm{bkg,j}}} \times N^{OS-SS}_{\mathrm{bkg,j}} \ , \\ N^{OS-SS}_{W^{-}+\ c\text{-}jet} &= N^{OS-SS}_{data^-} - \sum_{\mathrm{j}} \frac{1}{1 + R^{+/-}_{\mathrm{bkg,j}}} \times N^{OS-SS}_{\mathrm{bkg,j}} \ , \\ R^{yields}_{+/-} &= \frac{N^{OS-SS}_{W^{+}+\bar{c}}}{N^{OS-SS}_{W^{-}+c}} \ , \end{aligned} \tag{7.19}$$

where the index j is running over all background processes. The results are shown in Tab. 7.11 for the electron channel, in Tab. 7.12 for the muon channel.

Table 7.11: $W^{+}+$ c-jet and $W^{-}+$ c-jet event yields and their ratio in the electron channel

		$W^{+}+\bar{c}$	$W^{-}+c$	$R_{+/-}^{yields}$
1-jet	Monte Carlo	1632 ± 30(stat)	1718 ± 31(stat)	0.949 ± 0.024(stat)
	Measured	1815 ± 75(stat) $\pm$ 88(syst)	2084 ± 69(stat) $\pm$ 75(syst)	0.87 ± 0.046(stat) $\pm$ 0.013(syst)
2-jet	Monte Carlo	529 ± 18(stat)	660 ± 20(stat)	0.801 ± 0.037(stat)
	Measured	593 ± 60(stat) $\pm$ 62(syst)	626 ± 55(stat) $\pm$ 52(syst)	0.946 ± 0.128(stat) $\pm$ 0.025(syst)
1+2-jet	Monte Carlo	2162 ± 36(stat)	2379 ± 37(stat)	0.908 ± 0.02(stat)
	Measured	2390 ± 96(stat) $\pm$ 112(syst)	2694 ± 89(stat) $\pm$ 94(syst)	0.887 ± 0.046(stat) $\pm$ 0.013(syst)

Table 7.12: $W^{+}+$ c-jet and $W^{-}+$ c-jet event yields and their ratio in the muon channel

		$W^{+}+\bar{c}$	$W^{-}+c$	$R_{+/-}^{yields}$
1-jet	Monte Carlo	1593 ± 30(stat)	1800 ± 32(stat)	0.885 ± 0.023(stat)
	Measured	2143 ± 76(stat) $\pm$ 54(syst)	2201 ± 69(stat) $\pm$ 40(syst)	0.973 ± 0.046(stat) $\pm$ 0.018(syst)
2-jet	Monte Carlo	539 ± 19(stat)	615 ± 20(stat)	0.876 ± 0.042(stat)
	Measured	626 ± 62(stat) $\pm$ 33(syst)	787 ± 55(stat) $\pm$ 24.11(syst)	0.80 ± 0.096(stat) $\pm$ 0.021(syst)
1+2-jet	Monte Carlo	2132 ± 35(stat)	2415 ± 38(stat)	0.883 ± 0.020(stat)
	Measured	2768 ± 97(stat) $\pm$ 66(syst)	2993 ± 89(stat) $\pm$ 48(syst)	0.925 ± 0.043(stat) $\pm$ 0.015(syst)

7.8 Yields as a function of the $|\eta^{\ell}|$ of the lepton from the W decay

The $W+$ c-jet production cross section is also measured as a function of $|\eta^{\ell}|$ of the lepton from the W decay in the 11 $|\eta^{\ell}|$ bins of variable size listed in Tab. 7.13. The region $1.37 < |\eta| < 1.52$ is excluded from the geometrical acceptance for the electrons: in the corresponding bin the measurement is performed in the muon channel only. The yields are evaluated separately for $W^{+}+$ c-jet and $W^{-}+$ c-jet events.

Table 7.13: $|\eta^{\ell}|$ intervals used for the differential measurement

Number	1	2	3	4	5	6	7	8	9	10	11
Interval	0.00-0.21	0.21-0.42	0.42-0.63	0.63-0.84	0.84-1.05	1.05-1.37	1.37-1.52	1.52-1.74	1.74-1.95	1.95-2.18	2.18-2.50

The background $|\eta^{\ell}|$ distributions are obtained from simulations and normalised to the estimated contributions after the $N^{OS} - N^{SS}$ subtraction (see Section 7.7). A data-driven estimation of the $|\eta^{\ell}|$ shape is used for the QCD multi-jet contribution only. In the electron channel, the E_{T}^{miss} template fit described in Section 7.5.1 is applied separately in each $|\eta^{\ell}|$ bin to determine the QCD shape. OS and SS samples are combined in this case to reduce the statistical error of this measurement. A 50% uncorrelated uncertainty is considered in each bin covering the fit uncertainties. In the muon channel the $|\eta^{\ell}|$ shape is evaluated in the two control regions defined in Section 7.5.1 for the asymmetry measurement and averaged, after the subtraction of the estimated $W+$ jets and $Z+$ jets contributions. The difference between the two shapes is used as systematic uncertainty.

Uncertainties on the background $|\eta^{\ell}|$ shapes due to detector effects are found to be negligible, while the shapes are significantly varied by different PDF descriptions. The biggest effect is due to the gluon PDF, which is very differently described by the LO PDF sets used by default for the simulations (see Table 7.1) and by higher order computations. A PDF uncertainty on the $|\eta^{\ell}|$ shape is determined for each background process as the difference between the shape obtained in the nominal simulations and the ones reweighted with the `HERAPDF 1.5` PDF set [105] using the LHAPDF software [107].

The results are shown in Figure 7.11 for data and backgrounds after the $N^{OS} - N^{SS}$ subtraction.

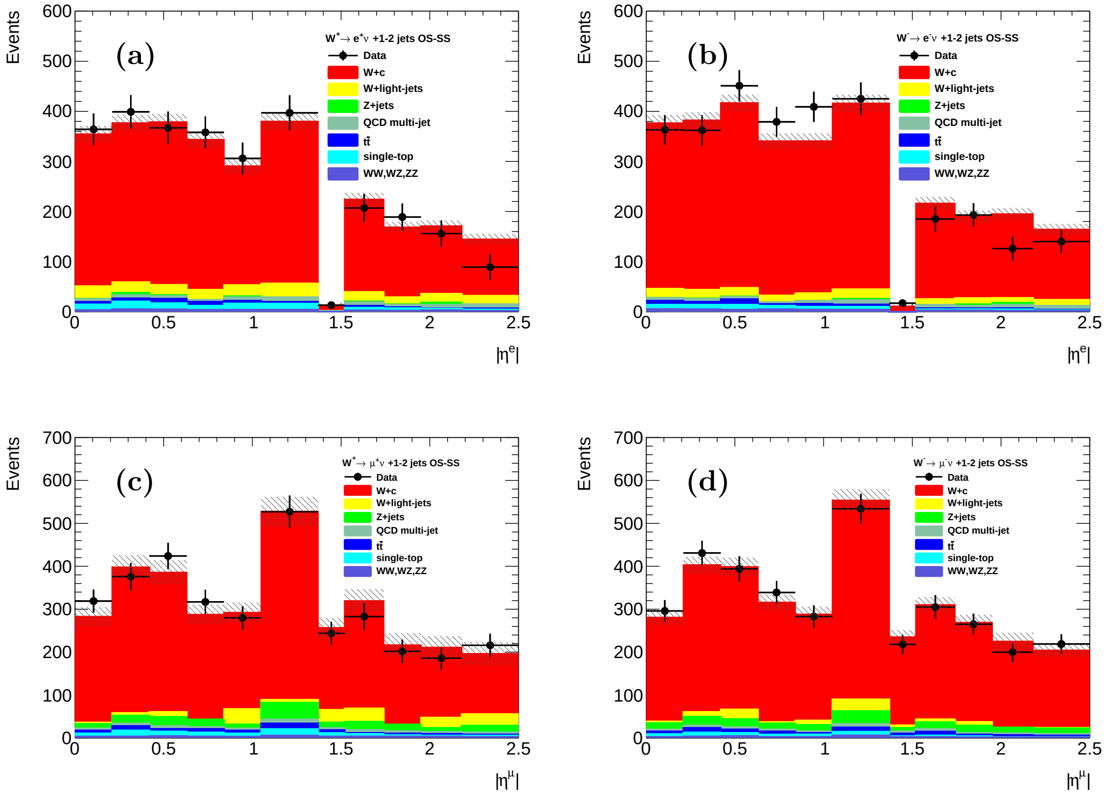

Figure 7.11: W^{+}+ c-jet (a, c) and W^{-}+ c-jet (b, d) event yields as a function of $|\eta^{\ell}|$ of the lepton from the W decay in the electron (a, b) and muon (c, d) channels for the combined 1+2-jet sample. The signal and background contributions are described in the text.

7.9 Cross section determination

The cross section is measured in a *fiducial* phase space region (see Table 7.14) with cuts following the ones applied for the selection of the $W+$ c-jet data sample in order to avoid a model-dependent phase space extrapolation of the experimental result. A small phase space extrapolation from the kinematic regions defined by the different electron and muon selection cuts to a common phase space is performed to facilitate the comparison of the results in the two leptonic channels and to combine them to a fiducial cross section measurement for events with a $W \to \ell\nu$ decay. This phase space extrapolation does not introduce a significant systematic error in the cross section measurement since the relevant kinematic variables are found to be well described in simulation.

Table 7.14: Fiducial phase space region for the $W+$ c-jet cross section measurement. The fiducial cuts on the soft muon are applied only for the $W+$ c-jet cross section measured for events with a $c \to \mu + X$ decay.

$W \to e\nu / W \to \mu\nu$ selection	
$W \to \tau\nu \to e/\mu\nu\nu\nu$ decays	Excluded
Lepton momentum	$\mathrm{p_T} > 20$ GeV
Lepton pseudo-rapidity	$\lvert\eta\rvert < 2.5$
Neutrino	$\mathrm{p_T} > 25$ GeV
Wtransverse mass	$m_{\mathrm{T}}^{W} > 40$ GeV
Jet selection	
Jet momentum	$\mathrm{p_T} > 25$ GeV
Jet pseudo-rapidity	$\lvert\eta\rvert < 2.5$
Jet multiplicity	$1 \leq n_{jet} \leq 2$
c-jet selection	
c-hadron momentum	$\mathrm{p_T} > 5$ GeV
c-hadron-jet matching	$\Delta R(hadron, jet) < 0.3$
c-jet multiplicity	$n_{c\text{-}jet} = 1$
Soft muon (from c-hadron-decay)	
Soft muon momentum	$\mathrm{p_T} > 4$ GeV
Soft muon pseudo-rapidity	$\lvert\eta\rvert < 2.5$
Soft muon-jet matching	$\Delta R(soft\ \mu, jet) < 0.5$

The fiducial cross section for the production of a leptonically decaying W boson in association with a charm hadron jet, with the c-hadron decaying semileptonically into a muon, is determined using the equation

$$\sigma^{fid}_{W+\ c\text{-}jet(c\to\mu)} \times BR(W \to \ell\nu) = \frac{N^{OS-SS}_{data} - N^{OS-SS}_{bkg}}{\mathcal{U}^{fid} \cdot \int \mathcal{L}dt} \,, \tag{7.20}$$

where N^{OS-SS}_{data} and N^{OS-SS}_{bkg} are the signal and background yields after the $N^{OS} - N^{SS}$ subtraction, respectively, $\mathcal{U}^{fid}$ is the signal selection efficiency in the fiducial phase space region and $\int \mathcal{L}dt$ the integrated luminosity. The selection efficiency is separately evaluated for events with exactly one and exactly two jets and for the two leptonic channels. The fiducial cross section for $W+$ c-jet events, without requiring a semimuonic decay of the c-hadron, is evaluated as

$$\sigma^{fid}_{W+\ c\text{-}jet} \times BR(W \to \ell\nu) = \frac{\sigma^{fid}_{W+\ c\text{-}jet(c\to\mu)} \times BR(W \to\ \ell\nu)}{\mathcal{B}^{fid}} \tag{7.21}$$

where $\mathcal{B}^{fid}$ corrects for the average branching ratio of the semileptonic decays of c-hadrons and for the efficiency on signal of the fiducial cuts applied to the soft muon (see Table 7.14). The cross section is also measured separately for $W^{+}+$ c-jet and $W^{-}+$ c-jet productions and as a function of $|\eta^{\ell}|$ of the lepton from the W decay.

7.9.1 Determination of the selection efficiency

The signal selection efficiency is defined as

$$\mathcal{U}^{fid} = \frac{N^{W+\ c\text{-}jet(c\to\mu),OS-SS}_{MC,reco}}{N^{W+\ c\text{-}jet(c\to\mu),OS-SS}_{MC,truth}}\ , \tag{7.22}$$

and determined in $W + c$ simulated events.

The numerator of Eq. 7.22 is evaluated at reconstruction level, i.e. after full simulation of the detector response, using the analysis selection (see Section 7.4). Several corrections are applied to the simulated events to ensure a realistic simulation of the data taking conditions and of the performance of the detector: the pile-up conditions, the distribution of the z coordinate of the primary interaction vertex, the energy scale and resolution of leptons, jets and E_T^{miss}, the lepton trigger and reconstruction efficiencies and the tagging efficiency and the mistag rate of the Soft Muon Tagger are corrected in Monte Carlo to match the data measurements. A further correction is applied to the description of the charm quark fragmentation and to the modelling of the decays of the charm hadrons (see Section 7.9.3).

In the denominator of Eq. 7.22 Monte Carlo $W+c$ events in the fiducial phase space region of Table 7.14 at generator level are selected. The *truth* jets are reconstructed using the *anti-*k_T algorithm with a distance parameter of R = 0.4 for stable particles. A truth jet is identified as a c-jet if a c-hadron with $\text{p}_\text{T} > 5$ GeV is found within $\Delta R = 0.3$ of the jet axis. c-hadrons originating from b-hadron decays are excluded. The potential bias introduced by this procedure has been studied using quarks instead of hadrons and changing the p_T and ΔR cuts. These variations lead only to per-mill level differences.
The momenta of the W-leptons are evaluated before the emission of final state radiation photons. Three corrections are applied at generator level: the pile-up conditions and the distribution of the z coordinate of the primary interaction vertex are reweighted to reproduce the data, and the charm quark fragmentation modelling and the description of the

semimuonic decays of c-hadrons are corrected as described in Section 7.9.3.
The $N^{OS} - N^{SS}$ subtraction is applied at generator level as well in order to correct for the small fraction of events, about 1%, which are either produced by double parton interactions or in which the soft muon inside the c-hadron jet is not produced by the c-hadron.

$W \to \tau\nu \to e/\mu\nu\nu\nu$ decays are an irreducible background on the order of 2% for the measurement which is corrected for by the selection efficiency by keeping these events in the numerator, at reconstruction level, but removing them from the denominator.

The results for the selection efficiency are shown in Table 7.15.

7.9.2 Determination of the extrapolation factor

$\mathcal{B}^{fid}$ is the extrapolation factor from the $\sigma^{fid}_{W+\ c\text{-}jet(c\to\mu)}$ to the $\sigma^{fid}_{W+\ c\text{-}jet}$ cross section and it is evaluated from Monte Carlo signal events at generator level as

$$\mathcal{B}^{fid} = \frac{N^{W+\ c\text{-}jet(c\to\mu),OS-SS}_{MC,truth}}{N^{W+\ c\text{-}jet,OS-SS}_{MC,truth}} \, . \tag{7.23}$$

The numerator is identical with the denominator of $\mathcal{U}^{fid}$, while for the denominator the requirement of a soft muon associated with the c-jet is dropped. The corrections used at generator level for the determination of $\mathcal{U}^{fid}$ (see Section 7.9.1) are applied also in this case. $\mathcal{B}^{fid}$ is expected to be identical for the two lepton channels. Using Equations 7.22 and 7.23,

$$\mathcal{U}^{fid} \cdot \mathcal{B}^{fid} = \frac{N^{W+\ c\text{-}jet(c\to\mu),OS-SS}_{MC,reco}}{N^{W+\ c\text{-}jet,OS-SS}_{MC,truth}} \tag{7.24}$$

and the $W+$ c-jet cross section can be directly determined from the event yields with the equation

$$\sigma^{fid}_{W+\ c\text{-}jet} \times BR(W \to \ell\nu) = \frac{N^{OS-SS}_{data} - N^{OS-SS}_{bkg}}{\mathcal{U}^{fid} \cdot \mathcal{B}^{fid} \cdot \int \mathcal{L}dt} \, . \tag{7.25}$$

The results for $\mathcal{B}^{fid}$ and $\mathcal{U}^{fid} \cdot \mathcal{B}^{fid}$ are shown in Table 7.15.

7.9.3 c-hadron fragmentation and decay

The description of the c quark fragmentation and of the semileptonic decays of c-hadrons in Monte Carlo simulations is essential to the correct description of the properties of the c-jets and of the soft muons. For this reason the following parameters of the simulation have been tuned to the most recent measurements:

- the c quark fragmentation fractions for D^0, $D^{\pm}$, $D^{\pm}_s$ and $\Lambda^{\pm}_c$ hadrons,

Table 7.15: Correction factors $\mathcal{U}^{fid}$ and $\mathcal{B}^{fid}$ and their product for the electron and muon channels. The uncertainties are statistical only.

Channel	Jet multiplicity	$\mathcal{U}^{fid}$	$\mathcal{B}^{fid}$	$\mathcal{U}^{fid} \cdot \mathcal{B}^{fid}$
Electron	1-jet	0.3605 ± 0.0037	0.0486 ± 0.0004	0.0175 ± 0.0002
	2-jet	0.4315 ± 0.0070	0.0514 ± 0.0007	0.0222 ± 0.0005
	1+2-jet	0.3767 ± 0.0033	0.0492 ± 0.0003	0.0185 ± 0.0002
Muon	1-jet	0.3687 ± 0.0037	0.0481 ± 0.0004	0.0177 ± 0.0002
	2-jet	0.4102 ± 0.0070	0.0519 ± 0.0007	0.0213 ± 0.0005
	1+2-jet	0.3784 ± 0.0033	0.0489 ± 0.0003	0.0185 ± 0.0002

- the c quark fragmentation function,
- the semimuonic decay branching ratios of the different c-hadron species and
- the soft muon momentum (p^*) spectrum in the rest frame of the c-hadron.

The reweighting is applied both at reconstruction and at generator level.

The c quark fragmentation fractions are the fractions of different c-hadron species produced in the hadronization of the c quark. They are reweighted in the $W+c$ signal sample according to the most recent average of results obtained at e^+e^- and ep colliders [121] (see Table 7.16). The uncertainty in these measurements is included in the systematic uncertainty of the $W+$ c-jet cross section.

Table 7.16: Fragmentation fractions of the c quark from HERA [121]

	D^0	$D^\pm$	$D_s^\pm$	$\Lambda_c^\pm$
Fraction	0.5643±0.0151	0.2256±0.0077	0.0797±0.0045	0.1080±0.0091

The c quark fragmentation function describes the fraction of transverse momentum of the c-jet carried by the first c-hadron in the jet. No correction is applied to the fragmentation function used by Pythia [43]. A systematic uncertainty arises from the comparison of the Pythia and Herwig [45] charm fragmentation description. The different fragmentation function used by the two programs, which are both used for the parton shower simulation together with the Alpgen generator [47], leads to different predictions for the $\frac{p_T^{c-hadron}}{p_T^{c\text{-}jet}}$ distribution shown in Figure 7.12 for $D^\pm$ and $\Lambda_c^\pm$.

The branching ratios of the semimuonic decays of the different c-hadrons species into muons are corrected for according to the measurements in [25] (see Table 7.17). For D^0, $D^\pm$ and $\Lambda_c^\pm$ the more precise measurements of the decays into electrons are used assuming lepton universality. For $D_s^\pm$, the semimuonic decay branching ratio includes $\tau \to \mu\nu\nu$ decays. To evaluate the branching ratios of Ω_c^0, Ξ_c^0, $\Xi_c^\pm$ decays into muons the $\Lambda_c^\pm \to \mu + X$ semimuonic branching ratio is scaled with the lifetime ratio:

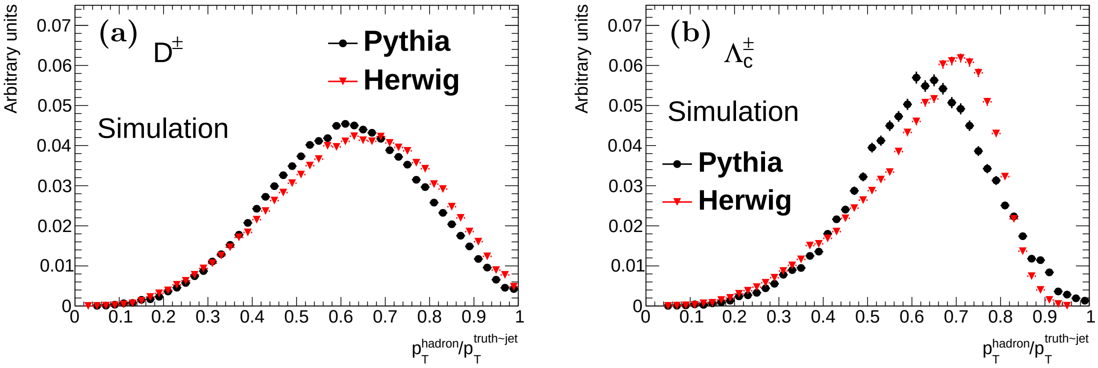

Figure 7.12: Normalised distributions of $\frac{p_T^{c-hadron}}{p_T^{c\text{-}jet}}$ as predicted by Pythia (black) and Herwig (red) for $D^{\pm}$ mesons (a) and $\Lambda_c^{\pm}$ barions (b).

$$BR_{\Omega_c^0,\Xi_c^0,\Xi_c^{\pm}} = \frac{\tau_{\Omega_c^0,\Xi_c^0,\Xi_c^{\pm}}}{\tau_{\Lambda_c^{\pm}}} \cdot BR_{\Lambda_c^{\pm}} \ . \tag{7.26}$$

Table 7.17: Branching ratios of the c-hadron decays into muons [25]

	D^0	$D^{\pm}$	$D_s^{\pm}$	$\Lambda_c^{\pm}$	Ω_c^0	Ξ_c^0	$\Xi_c^{\pm}$
BR[%]	6.49±0.11	16.07±0.30	7.4±0.4	4.5±1.7	2.5±1.0	9.9±3.8	1.6±0.6

The distribution of the momentum p^* of the soft muons from the c-hadron decay in the rest frame of the c-hadron has direct impact on the efficiency of the Soft Muon Tagger. Different Monte Carlo generators make different predictions, as shown in Figure 7.13 for $D^{\pm}$ and $\Lambda_c^{\pm}$ decays. The Alpgen+Pythia Monte Carlo sample is reweighted to fit the predictions by EvtGen [52] which is expected to give the best description of the data. The difference between EvtGen and Pythia is used as systematic uncertainty.

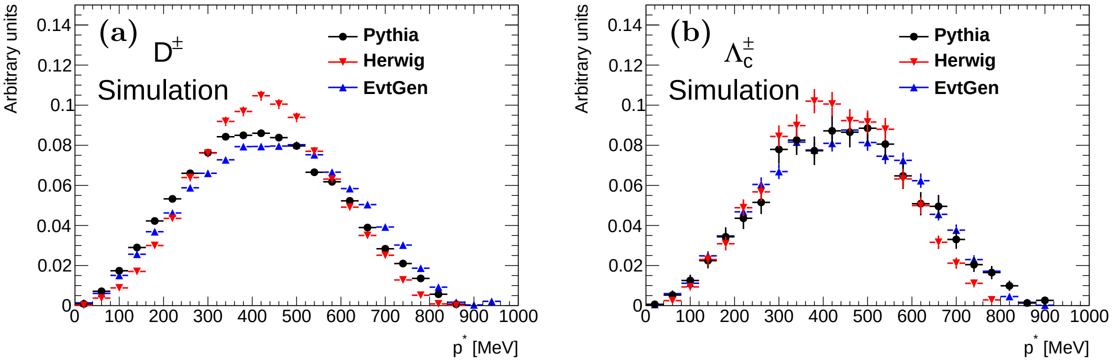

Figure 7.13: Normalised distributions of the momentum p^* of the soft muons from decays of c-hadrons $D^{\pm}$ (a) and $\Lambda_c^{\pm}$ (b) at rest, as predicted by Pythia (black), Herwig (red) and EvtGen (blue).

7.10 Measurement of the W^++ c-jet and W^-+ c-jet production cross sections

The ratio of the W^++ c-jet and W^-+ c-jet production cross sections is given by

$$R^{fid}_{+/-} = \frac{N^{OS-SS}_{W^+ + \; c\text{-}jet} / N^{OS-SS}_{W^- + \; c\text{-}jet}}{(\mathcal{U}^{fid} \cdot \mathcal{B}^{fid})^+ / (\mathcal{U}^{fid} \cdot \mathcal{B}^{fid})^-} \,, \tag{7.27}$$

where $N^{OS-SS}_{W^+ + \; c\text{-}jet}$ and $N^{OS-SS}_{W^- + \; c\text{-}jet}$ are the numbers of selected W^++ c-jet and W^-+ c-jet events after OS-SS subtraction and $(\mathcal{U}^{fid} \cdot \mathcal{B}^{fid})^+$ and $(\mathcal{U}^{fid} \cdot \mathcal{B}^{fid})^-$ are the selection efficiency times the extrapolation factor for W^++ c-jet and W^-+ c-jet channels, respectively. $R^{corr}_{+/-} = (\mathcal{U}^{fid} \cdot \mathcal{B}^{fid})^+ / (\mathcal{U}^{fid} \cdot \mathcal{B}^{fid})^-$ correct the ratio of the event yields for possible charge-dependent detector effects. It is expected to be close to 1.

$(\mathcal{U}^{fid} \cdot \mathcal{B}^{fid})^+$ and $(\mathcal{U}^{fid} \cdot \mathcal{B}^{fid})^-$ could be evaluated separately with the same procedure described in the previous section for the average of $W^+ + \bar{c}$ and $W^- + c$ simulated events. This approach results in a too large uncertainty on the determination of $R^{corr}_{+/-}$ due to Monte Carlo statistics, that would be the dominant uncertainty in the cross section ratio measurement since most other systematic effects cancel. In order to increase the precision on $R^{corr}_{+/-}$, it is evaluated without requiring a semimuonic c-hadron decay. One of the selected jets at reconstruction level is required to be matched with a generator level c-hadron with $\mathrm{p_T} > 5$ GeV within $\Delta R = 0.3$ (so-called *truth labelling*). The charge of the c-hadron is used for the classification of the events in the OS and SS categories.
Charge-dependent detector effects from soft muon reconstruction or the Soft Muon Tagger cuts have been studied with the Tag-and-Probe method described in Chapter 5. They were found to be at the 0.1% level and therefore are neglected. The selection efficiency for the ratio measurement determined before the SMT is therefore valid also for the nominal selection.

Bias in the efficiency evaluation can be introduced due to the fact that a reconstructed c-jet with $\mathrm{p_T} \approx 25$ GeV and an associated soft muon corresponds on average to a generator level jet with $\mathrm{p_T} \approx$ 35-40 GeV. This bias in the c-jet phase space is compensated by adjusting the c-jet $\mathrm{p_T}$ cut as described in the following. In Figure 7.14 the generator level W and c-jet $\mathrm{p_T}$ distributions for W^++ c-jet and W^-+ c-jet events are shown for the nominal selection (i.e. with SMT cuts) and without SMT cuts but with reconstructed c-jet $\mathrm{p_T}$ cuts of 32 and 40 GeV. The nominal $\mathrm{p_T}$ spectrum is between the other two. $R^{corr}_{+/-}$ is therefore determined (see Table 7.18) as the average of the values obtained without SMT cuts for c-jet $\mathrm{p_T}$ cuts of 32 and 40 GeV. Half of the difference between the two values is taken as additional systematic error on $R^{corr}_{+/-}$ of about 0.5%.

For the W^++ c-jet and W^-+ c-jet fiducial cross section measurements the correction factors $(\mathcal{U}^{fid} \cdot \mathcal{B}^{fid})^+$ and $(\mathcal{U}^{fid} \cdot \mathcal{B}^{fid})^-$ are evaluated using the $R^{corr}_{+/-}$ value determined with the procedure described above using the equation

$$
\begin{aligned}
(\mathcal{U}^{fid} \cdot \mathcal{B}^{fid})^{+} &= \frac{N_{MC,reco}^{W^{+}+\ c\text{-}jet(c\rightarrow\mu),OS-SS}}{N_{MC,truth}^{W^{+}+\ c\text{-}jet,OS-SS}} \\
&= \frac{N_{MC,reco}^{W^{+}+\ c\text{-}jet(c\rightarrow\mu),OS-SS}}{N_{MC,truth}^{W^{+}+\ c\text{-}jet,OS-SS}} \cdot \frac{N_{MC,reco}^{W^{+}+\ c\text{-}jet(c\rightarrow\mu),OS-SS} + N_{MC,reco}^{W^{-}+\ c\text{-}jet(c\rightarrow\mu),OS-SS}}{N_{MC,reco}^{W^{+}+\ c\text{-}jet(c\rightarrow\mu),OS-SS} + N_{MC,reco}^{W^{-}+\ c\text{-}jet(c\rightarrow\mu),OS-SS}} \\
&= \frac{N_{MC,reco}^{W^{+}+\ c\text{-}jet(c\rightarrow\mu),OS-SS} + N_{MC,reco}^{W^{-}+\ c\text{-}jet(c\rightarrow\mu),OS-SS}}{N_{MC,truth}^{W^{+}+\ c\text{-}jet,OS-SS} + N_{MC,reco}^{W^{-}+\ c\text{-}jet(c\rightarrow\mu),OS-SS} \cdot N_{MC,truth}^{W^{+}+\ c\text{-}jet,OS-SS} / N_{MC,reco}^{W^{+}+\ c\text{-}jet(c\rightarrow\mu),OS-SS}} \\
&= \frac{N_{MC,reco}^{W^{+}+\ c\text{-}jet(c\rightarrow\mu),OS-SS} + N_{MC,reco}^{W^{-}+\ c\text{-}jet(c\rightarrow\mu),OS-SS}}{N_{MC,truth}^{W^{+}+\ c\text{-}jet,OS-SS} + N_{MC,truth}^{W^{-}+\ c\text{-}jet,OS-SS} / R_{+/-}^{corr}}
\end{aligned}
$$

and similarly

$$
(\mathcal{U}^{fid} \cdot \mathcal{B}^{fid})^{-} = \frac{(N_{MC,reco}^{W^{+}+\ c\text{-}jet(c\rightarrow\mu),OS-SS} + N_{MC,reco}^{W^{-}+\ c\text{-}jet(c\rightarrow\mu),OS-SS})}{R_{+/-}^{corr} N_{MC,truth}^{W^{+}+\ c\text{-}jet,OS-SS} + N_{MC,truth}^{W^{-}+\ c\text{-}jet,OS-SS}} \; .
$$

Table 7.18: Correction factors $(\mathcal{U}^{fid} \cdot \mathcal{B}^{fid})^{+}/(\mathcal{U}^{fid} \cdot \mathcal{B}^{fid})^{-}$ for the electron and the muon channel. The uncertainties are statistical only.

Channel	1-jet	2-jet	1+2-jet
Electron	0.999 ± 0.006	0.997 ± 0.009	0.998 ± 0.005
Muon	1.011 ± 0.005	0.986 ± 0.008	1.004 ± 0.004

7.11 Systematic uncertainties

Systematic uncertainties due to background estimation, detector effects and signal simulation are taken into account.

7.11.1 Background estimation

The assessment of the uncertainties in the background contributions to $W+$ c-jet events is discussed in Section 7.5 while the additional background uncertainties for $W^{+} + \bar{c}$ and $W^{-} + c$ event yields are evaluated as described in Section 7.7. The resulting uncertainties in the measured yields are shown for the combination of the 1 and 2-jet samples separately for $W^{+} + \bar{c}$ and $W^{-} + c$ events in Tables 7.19 and 7.20 for the electron and muon channel, respectively. The uncertainties in the OS/SS asymmetry and in the normalisation of the background contributions are treated separately in the the electron channel due

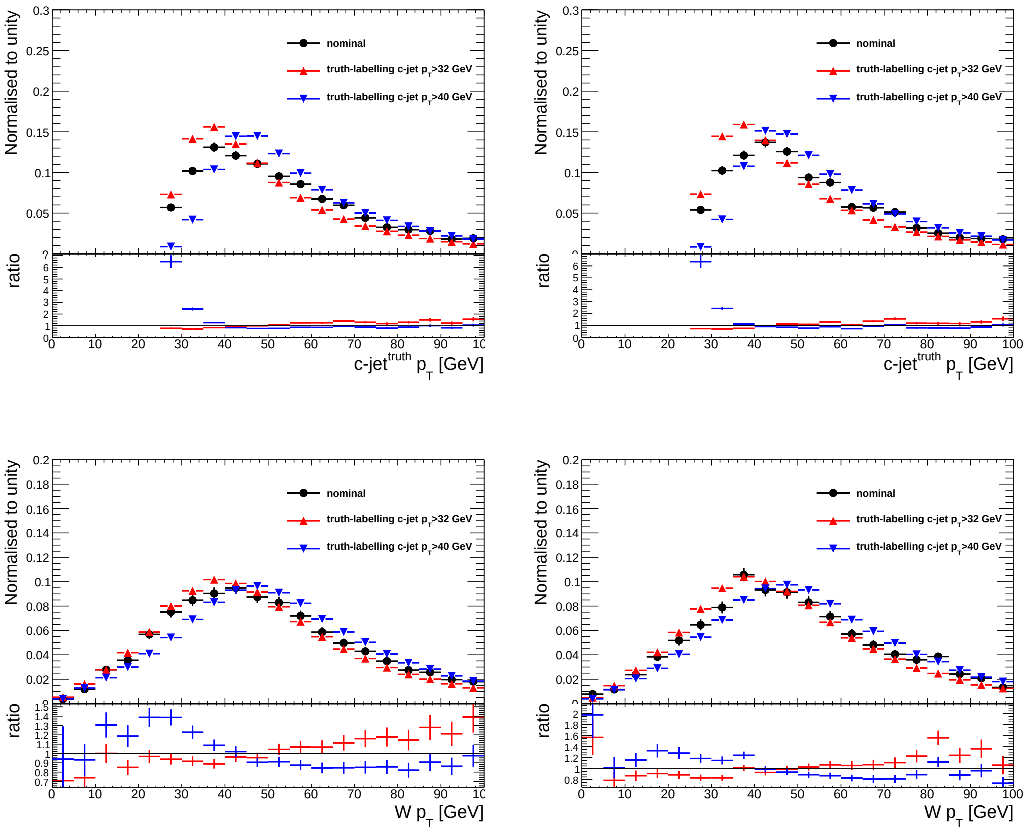

Figure 7.14: Distributions of the generator level c-jet (top) and W (bottom) transverse momentum in $W^{-}+$ c-jet (left) and $W^{+}+$ c-jet (right) simulated events selected at reconstruction level with the nominal selection (black curves), i.e. after the Soft Muon Tagger cuts, and for pre-tag events with a jet spatially matched with a generator level c-hadron (truth labelling) passing a jet p_{T} cut at reconstruction level of 32 GeV (red curves) and 40 GeV (blue curves). Only statistical errors are shown.

to the fitting procedure described in Section 7.5.3. In that channel the uncertainties on the normalizations of the QCD multi-jet and $W+$ light-jets backgrounds arise from the uncertainty in the fit of these contributions described in Section 7.5.3.

The limited statistics of the data sample is the largest source of uncertainty. The uncertainty in the OS/SS asymmetry measurement for $W+$ light-jets production are significant in both channels, and this uncertainty for the QCD multi-jet production is the largest systematic error in the electron channel.

Uncertainties in the background contributions determined in simulations due to limited Monte Carlo statistics, the PDFs used in the simulations, theoretical uncertainties in the cross sections and detector effects are taken into account but were found to be small.

For the differential cross section measurement as a function of $|\eta^{\ell}|$ of the lepton from the W decay additional uncertainties in the $|\eta^{\ell}|$ dependence of the backgrounds have to be taken into account (see Section 7.8).

Table 7.19: Uncertainties in the $W^{+}+$ c-jet and $W^{-}+$ c-jet yields N^{+} and N^{-} and their ratio $R^{W^{+}+\ c\text{-}jet/W^{-}+\ c\text{-}jet}$ in the electron channel for events with one or two selected jets. *Other backgrounds* are $t\bar{t}$, single-top, diboson and $Z+$ jets events.

Uncertainty [%]	N^{+}	N^{-}	$R^{W^{+}+\ c\text{-}jet/W^{-}+\ c\text{-}jet}$
Data statistics	4	3.3	5.2
QCD (or $W+$ light-jets) background normalisation	1.2	0.6	0.6
QCD background asymmetry	3.5	2.9	0.5
$W+$ light-jets background asymmetry	2.7	1.6	1
QCD background ratio	0.1	0.1	0.2
$W+$ light-jets background ratio	0.2	0.1	0.4
Other backgrounds normalisations	0.3	0.2	0.1
Other backgrounds asymmetries	0.5	0.4	0.1
Other backgrounds ratios	0	0	0.1
Total	6.2	4.8	5.4

Table 7.20: Uncertainties in the $W^{+}+$ c-jet and $W^{-}+$ c-jet yields N^{+} and N^{-} and their ratio $R^{W^{+}+\ c\text{-}jet/W^{-}+\ c\text{-}jet}$ in the muon channel for events with one or two selected jets. *Other backgrounds* are $t\bar{t}$, single-top, and diboson events.

Uncertainty [%]	N^{+}	N^{-}	$R^{W^{+}+\ c\text{-}jet/W^{-}+\ c\text{-}jet}$
Data statistics	3.5	3.0	4.6
QCD background normalisation	0.7	0.6	0.1
$W+$ light-jets background normalisation	2.0	1.2	0.8
$Z+$ jets background normalisation	0.6	0.5	0.1
QCD background ratio	0.1	0.1	0.1
$W+$ light-jets background ratio	0.7	0.6	1.3
$Z+$ jets background ratio	0.2	0.1	0.3
Other backgrounds normalisations	0.6	0.5	0.2
Other backgrounds ratio	0	0	0.1
Total	4.2	3.4	4.9

7.11.2 Detector effects

The impact of the uncertainties in reconstruction efficiencies and in energy/momentum scales and resolutions is evaluated by varying these parameters within their measurement errors. Uncertainties in the lepton trigger, reconstruction and isolation efficiencies, the lepton energy/momentum scales and resolutions, the SMT efficiency and mistag rate, the jet energy scale (see [73]), the jet energy resolution (see [122]) and the E_{T}^{miss} determination are taken into account. The uncertainty in the jet energy resolution is determined as the average of the uncertainties in the two leptonic channels to reduce the impact of the limited Monte Carlo statistics on its estimation. All corrections applied to particle and jet momenta are propagated to E_T^{miss} measurement, therefore most E_T^{miss} uncertainties are already included in the previously discussed uncertainties. Uncertainties in the energy scale and resolution due to the soft E_T^{miss} contributions (see Section 4.6) evaluated in [80] are additionally taken into account.

The results are presented in Table 7.21 and Table 7.22 for the electron and muon channels, respectively. Uncertainties from the determination of the lepton reconstruction efficiency and of the jet energy scale are the by far largest contributions.

Table 7.21: Systematic uncertainties due to detector effects in the electron channel

Uncertainty [%]	1-jet	2-jet	1+2-jet
Electron Charge Flip	0.3	< 0.1	0.2
Electron efficiency	1.9	1.9	1.9
Electron energy scale	0.9	0.3	0.8
Electron energy resolution	0.2	< 0.1	0.1
Muon efficiency	1.2	1.1	1.1
Muon energy scale	< 0.1	< 0.1	< 0.1
Muon energy resolution	< 0.1	< 0.1	< 0.1
SMT efficiency	0.5	0.5	0.5
SMT fake rate	0.2	0.4	0.3
Jet energy Resolution	0.5	< 0.1	0.3
Jet Energy Scale	1.5	7.5	3.1
Soft E_T^{miss} resolution	0.2	0.6	< 0.1
Soft E_T^{miss} scale	0.6	0.6	0.6
Total	3.0	7.9	4.0

Table 7.22: Systematic uncertainties due to detector effects in the muon channel

Uncertainty [%]	1-jet	2-jet	1+2-jet
Muon efficiency	2.8	2.7	2.8
Muon energy scale	0.8	0.7	0.8
Muon energy resolution	< 0.1	0.4	0.1
SMT efficiency	0.5	0.5	0.5
SMT fake rate	0.1	< 0.1	0.1
Jet energy resolution	0.5	< 0.1	0.3
Jet energy scale	1.5	6.4	2.7
Soft E_T^{miss} resolution	< 0.1	0.3	< 0.1
Soft E_T^{miss} scale	0.2	0.6	0.1
Total	3.4	7.0	4.0

7.11.3 Uncertainties in $W + c$ signal modelling

The Monte Carlo description of the fragmentation and semileptonic decays of the c-hadrons is a significant source of systematic error for the W+ c-jet cross section measurement which is assessed as discussed in Section 7.9.3.

The uncertainty due to non-perturbative effects in the simulation of parton showers is estimated by comparing the selection efficiency determined using ALPGEN Monte Carlo simulations of $W + c$ production showered alternatively with PYTHIA and HERWIG programs. Effects estimated in the two leptonic channels are averaged to reduce the impact of the limited Monte Carlo statistics.

Another source of uncertainty is the modelling of the kinematics of the $W \to l\nu$ decay. The lepton $\mathrm{p_T}$, E_T^{miss} and m_{T}^W distributions agree very well between data and simulations, therefore no additional systematic uncertainties are assigned to them.

Uncertainties in the selection efficiency due to the PDFs used in the simulations have been evaluated by reweighting the simulated $W + c$ events for different PDF sets using the LHAPDF software [107]. The impact of this effect is slightly higher in the electron than in the muon channel because of the different selection kinematic cuts. The biggest difference in the selection efficiency is between the nominal `cteq6ll` PDF set and the `HERAPDF 1.5` set which is therefore used as the uncertainty due to the PDF description in the simulation.

The results are shown in Table 7.23 for the electron channel and in Table 7.24 for the muon channel.

Table 7.23: Systematic uncertainties due to Monte Carlo modelling in the electron channel

	1-jet		2-jet		1+2-jet	
Uncertainty [%]	U	$U \times B$	U	$U \times B$	U	$U \times B$
D^0 fraction	< 0.1	0.7	< 0.1	0.6	< 0.1	0.7
D^+ fraction	< 0.1	1.3	< 0.1	1.2	< 0.1	1.3
D_s fraction	< 0.1	< 0.1	< 0.1	0.1	< 0.1	< 0.1
Baryon fraction	< 0.1	1.4	0.3	1.1	0.1	1.3
Fragmentation function	1.6	0.3	1.1	0.6	1.5	0.4
Non-perturbative	0.8	1.7	6.5	4.6	1.0	0.3
D^0 decay BR	< 0.1	0.7	< 0.1	0.7	< 0.1	0.7
D^+ decay BR	< 0.1	0.8	< 0.1	0.8	< 0.1	0.8
D_s decay BR	< 0.1	0.4	< 0.1	0.4	< 0.1	0.4
Baryon decay BR	< 0.1	2.1	0.3	2.3	0.1	2.2
p^*	1.4	1.6	1.3	1.3	1.4	1.5
PDF	0.9	1.7	0.3	1.2	0.8	1.7
Total	2.4	4.3	6.7	5.9	2.4	3.9

Table 7.24: Systematic uncertainties due to Monte Carlo modelling in the muon channel

	1-jet		2-jet		1+2-jet	
Uncertainty [%]	U	$U \times B$	U	$U \times B$	U	$U \times B$
D^0 fraction	< 0.1	0.3	< 0.1	0.3	< 0.1	0.3
D^+ fraction	< 0.1	1.0	< 0.1	1.0	< 0.1	1.0
D_s fraction	< 0.1	< 0.1	0.1	0.2	< 0.1	0.1
Baryon fraction	< 0.1	1.3	0.3	0.9	< 0.1	1.2
Fragmentation function	1.7	0.7	1.4	0.7	1.7	0.7
Non-perturbative	0.8	1.7	6.5	4.6	1.0	0.3
D^0 decay BR	< 0.1	0.7	< 0.1	0.8	< 0.1	0.7
D^+ decay BR	< 0.1	0.8	< 0.1	0.8	< 0.1	0.8
D_s decay BR	< 0.1	0.4	< 0.1	0.3	< 0.1	0.4
Baryon decay BR	< 0.1	2.0	0.3	2.5	0.1	2.1
p^*	1.3	1.5	1.4	0.6	1.4	1.3
PDF	0.3	0.5	0.3	0.4	0.3	0.5
Total	2.3	3.7	6.8	5.6	2.4	3.3

7.12 $W+$ c-jet fiducial cross section results

The fiducial cross section results for a leptonically decaying W boson produced in association with one c-jet are shown in Table 7.25 separately for the electron and muon channels and for the W^++ c-jet, W^-+ c-jet productions. Results are given separately for events with exactly one jet and exactly two jets. The result for the combination of the jet categories (1+2-jet) is not the direct sum of the two individual cross sections, since for its determination the background estimation and the systematic uncertainty assessment are performed directly in the combined sample.

The cross section measured in the muon channel is higher than the one in the electron channel with a significance of less than 2σ (see Table 7.26) when taking into account the correlation between the systematic uncertainties in the two leptonic channels. The results obtained in the electron and muon channels are therefore in agreement and can be combined as discussed in Section 7.13.

The results for the ratio of the W^++ c-jet and W^-+ c-jet production cross sections in the fiducial phase space of the measurement are given in Table 7.27.

A breakdown of the uncertainties for the $\sigma^{fid}_{W+\ c\text{-}jet} \times BR(W \to \ell\nu)$ measurement is shown in Table 7.28 for the two leptonic channels. The results for the fiducial cross section measurement as a function of $|\eta^\ell|$ of the lepton from the W decay are given in Section 7.13.

Table 7.25: Fiducial cross sections measured in the electron and muon channels in the 1-jet and 2-jet data sets and in their combination

Jet category	Electron channel	Muon channel
	$\sigma^{fid}_{W+\ c\text{-}jet} \times BR(W \to \ell\nu)$ [pb]	
1-jet	47.97 ± 1.26(stat.) ± 3.39(syst.)	52.76 ± 1.25(stat.) ± 3.08(syst.)
2-jet	11.85 ± 0.80(stat.) ± 1.65(syst.)	14.28 ± 0.84(stat.) ± 1.47(syst.)
1+2-jet	59.09 ± 1.53(stat.) ± 4.27(syst.)	66.98 ± 1.53(stat.) ± 3.96(syst.)
	$\sigma^{fid}_{W^{+}+\ c\text{-}jet} \times BR(W \to\ \ell\nu)$ [pb]	
1-jet	22.33±0.93(stat)±1.66(syst) [pb]	25.86±0.92(stat)±1.58(syst) [pb]
2-jet	5.77±0.59(stat)±0.86(syst) [pb]	6.38±0.63(stat)±0.67(syst) [pb]
1+2-jet	27.81±1.13(stat)±2.14(syst) [pb]	32.14±1.13(stat)±2.01(syst) [pb]
	$\sigma^{fid}_{W^{-}+\ c\text{-}jet} \times BR(W \to\ \ell\nu)$ [pb]	
1-jet	25.62±0.86(stat)±1.77(syst) [pb]	26.87±0.84(stat)±1.60(syst) [pb]
2-jet	6.08±0.54(stat)±0.80(syst) [pb]	7.90±0.55(stat)±0.84(syst) [pb]
1+2-jet	31.28±1.04(stat)±2.17(syst) [pb]	34.87±1.04(stat)±2.05(syst) [pb]

Table 7.26: Difference between the measured fiducial cross section $\sigma^{fid}_{W+\ c\text{-}jet} \times BR(W \to \ell\nu)$ in the electron and muon channels. The statistical and the total significance and the correlation of the systematic uncertainties between the two leptonic channels are given.

	$\sigma^{fid}_{W+\ c\text{-}jet} \times BR(W \to \ell\nu)$			
Jet channel	Difference [pb]	Stat. sign.[σ]	Tot. sign.[σ]	Correlation
1-jet	-4.78 ± 1.78(stat.) ± 2.94(syst.)	2.7	1.4	0.51
2-jet	-2.42 ± 1.16(stat.) ± 1.39(syst.)	2.1	1.3	0.47
1+2-jet	-7.88 ± 2.16(stat.) ± 3.51(syst.)	3.6	1.9	0.56

Table 7.27: $R^{fid}_{+/-}$ measured in the electron and muon channels in the 1-jet and 2-jet data sets and in their combination

	$R^{fid}_{+/-}$	
Jet category	Electron channel	Muon channel
1-jet	0.87 ± 0.05(stat.) ± 0.02(syst.)	0.96 ± 0.05(stat.) ± 0.03(syst.)
2-jet	0.95 ± 0.13(stat.) ± 0.04(syst.)	0.81 ± 0.10(stat.) ± 0.03(syst.)
1+2-jet	0.89 ± 0.05(stat.) ± 0.02(syst.)	0.92 ± 0.04(stat.) ± 0.02(syst.)

Table 7.28: Systematic uncertainties in the $\sigma^{fid}_{W+\ c\text{-}jet}\times BR(W \to \ell\nu)$ measurement in the electron and muon channels. The semi-leptonic decay uncertainty includes uncertainties on the p^* and on the c-hadron semimuonic branching ratio.

Systematic uncertainty [%]	Electron channel			Muon channel		
	1-jet	2-jet	1+2-jet	1-jet	2-jet	1+2-jet
Background yields	4.2	9.4	4.1	2.0	4.0	1.9
Monte Carlo statistics	1.3	2.3	1.1	1.3	2.3	1.1
Object reconstruction	3.0	7.9	4.0	3.4	7.0	4.0
Semi-leptonic decay	2.9	2.9	2.9	2.8	2.8	2.7
c-fragmentation	2.0	1.9	2.0	1.8	1.5	1.7
Non-perturbative	1.7	4.6	0.3	1.7	4.6	0.3
PDF	1.7	1.2	1.7	0.5	0.4	0.5
Luminosity	1.8	1.8	1.8	1.8	1.8	1.8
Total	7.1	13.9	7.2	5.8	10.3	5.9

7.13 Combination of the electron and muon channels

The results in the electron and muon channels are combined, assuming lepton universality, using an averaging technique developed by the HERA experiments [123, 124, 125].

Since the measurements in the electron and muon channels are statistically independent, the average fiducial cross section σ can be obtained from the individual fiducial cross sections σ_e and σ_μ by minimising

$$\chi^2(\sigma) = \sum_{k=e,\mu} \frac{(\sigma_k - \sigma)^2}{(\Delta_k^{stat})^2}\ , \tag{7.28}$$

where Δ_k^{stat} are the statistical uncertainties for in the two channels and systematic errors are disregarded. Taking into account the dependence of the measured cross sections on the systematic uncertainties, which are estimated independently for the two channels, the minimisation procedure can also be used to improve the estimates of these uncertainties. Let j label a given systematic uncertainty which has a correlated influence on σ_e and σ_μ and $\gamma_j^{e,\mu}$ be the estimated impact of this uncertainty on $\sigma_{e,\mu}$ assessed as described in Section 7.11. Assuming that a refined estimation $\gamma_j'^{e,\mu}$ of the uncertainty can be determined and defining the relative correction to the estimation $b_j \equiv (\gamma_j'^{e,\mu} - \gamma_j^{e,\mu})/\gamma_j^{e,\mu}$, a modified χ^2 [124] can be written as

$$\chi^2(\sigma, b_1...b_N) = \sum_{k=e,\mu} \frac{[\sigma - \sum_{j=1}^{N} \gamma_j^k \sigma b_j - \sigma_k]^2}{(\Delta_k^{stat})^2 + (\Delta_k^{uncorr})^2} + \sum_{j=1}^{N} b_j^2\ , \tag{7.29}$$

with Δ_k^{uncorr} being the sum of the systematic uncertainties which have no correlated effects on σ_e and σ_μ. The χ^2 minimisation can be used to simultaneously determine the average

σ and the corrections b_j $(j = 1...N)$.

The systematic uncertainties related to detector effects and the theoretical uncertainties are fully correlated between the electron and muon channels. The background contribution uncertainties, which are estimated in statistically independent control samples for the different measurements, are uncorrelated between the channels.

The $W+$ c-jet fiducial cross section in the electron and muon channel and the $W^{+}+$ c-jet and $W^{-}+$ c-jet cross sections, together, are averaged simultaneously for the 1-jet and 2-jet event categories taking into account the correlations between the uncertainties in these samples (see Tables 7.29 and 7.30). The averaging for the combined 1+2-jet sample is performed separately with the result

$$\sigma^{\mathrm{1+2-jet,fid}}_{\mathrm{W+\ c\text{-}jet}} \times \mathrm{BR(W} \to \ \ell\nu) = \ 64.6 \ \pm \ 1.1 \ (\mathrm{stat}) \ \pm \ 3.7 \ (\mathrm{syst}) \ \mathrm{pb} \ ,$$

corresponding to the minimum χ^2/n_{dof} $= 3.4/1$. The results of the separate combination of the $W^{+}+$ c-jet and $W^{-}+$ c-jet for the 1+2-jet sample are shown in Table 7.31.

Table 7.29: $W+$ c-jet fiducial cross section times $W \to \ell\nu$ branching ratio for the 1-jet and 2-jet categories. The χ^2/n_{dof} value shows that the results for the different data samples are consistent with each other.

$\sigma^{fid}_{W+\ c\text{-}jet} \times BR(W \to \ell\nu)$	1-jet	2-jet
Cross section [pb]	51.2	13.6
Statistical uncertainty [pb]	0.9	0.6
Systematic uncertainty [pb]	2.9	1.4
Total uncertainty [pb]	3.0	1.5
Minimum χ^2/n_{dof}	3.1/2	
Correlation coefficient	0.34	

Table 7.30: Averaged $W^{+}+$ c-jet and $W^{-}+$ c-jet fiducial cross sections times $W \to \ell\nu$ branching ratio for the 1-jet and 2-jet categories. The correlation matrix of the combined χ^2 minimization is also shown.

	$W^{+}+$ c-jet 1-jet	$W^{-}+$ c-jet 1-jet	$W^{+}+$ c-jet 2-jet	$W^{-}+$ c-jet 2-jet
Cross section [pb]	24.5	26.5	6.2	7.1
Statistical uncertainty [pb]	0.7	0.6	0.4	0.4
Systematic uncertainty [pb]	1.4	1.5	0.7	0.7
Total uncertainty [pb]	1.6	1.6	0.8	0.8
Minimum χ^2/n_{dof}	5.6/4			
	Correlation matrix			
$W^{+}+$ c-jet 1-jet	1.00	0.78	0.34	0.34
$W^{-}+$ c-jet 1-jet	0.78	1.00	0.28	0.26
$W^{+}+$ c-jet 2-jet	0.34	0.28	1.00	0.68
$W^{-}+$ c-jet 2-jet	0.34	0.26	0.68	1.00

Table 7.31: Averaged W^++ c-jet and W^-+ c-jet fiducial cross sections times $W \to \ell\nu$ branching ratio in the 1+2-jet category

	W^++ c-jet	W^-+ c-jet
Cross section [pb]	30.8	33.8
Statistical uncertainty [pb]	0.8	0.7
Systematic uncertainty [pb]	1.9	1.9
Total uncertainty [pb]	2.0	2.1
Minimum χ^2/n_{dof}	3.5/2	
Correlation coefficient	0.81	

The averaged ratio $R^{fid}_{+/-}$ of the fiducial W^++ c-jet and W^-+ c-jet cross sections for the 1-jet and 2-jet categories are in Table 7.32 and the result for the combined 1+2-jet category is

$$R^{fid,1+2-jet}_{+/-} \;=\; 0.91 \;\pm\; 0.03 \text{ (stat)} \;\pm\; 0.01 \text{ (syst)} \;,$$

with a minimum $\chi^2/n_{dof} \; = 0.2/1$.

Table 7.32: $R^{fid}_{+/-}$ measurement in 1-jet and 2-jet categories

$R^{fid}_{+/-}$	1-jet	2-jet
Ratio	0.92	0.87
Statistical uncertainty	0.03	0.08
Systematic uncertainty	0.02	0.03
Total uncertainty	0.04	0.08
Fit $\chi^2/ndof$	2.3/2	
Correlation coefficient	-0.02	

Finally, the same combination is performed for the differential cross section measurements in 11 $|\eta^\ell|$ bins. In order to increase the statistical precision, the 1 and 2 jets categories are combined. The W^++ c-jet and W^-+ c-jet measurements are simultaneously averaged with a minimum $\chi^2/n_{dof} \; = 18.4/22$. The latter fit has 20 degrees of freedom, 10 for W^++ c-jet and 10 for W^-+ c-jet events, as in the bin corresponding to $1.37 \; < |\eta^\ell| \; < 1.52$ there is only a cross section measurement in the muon channel. The results of the combination are shown in Tables 7.33 and 7.34 and in Figure 7.15 in comparison with the individual measurements for the two channels.

7.14 Comparison with theoretical predictions

The results presented in the last section are compared with leading order (LO) and next-to-leading (NLO) order predictions obtained with the ALPGEN [47] and aMC@NLO [50] Monte Carlo generators, respectively. The ALPGEN generator has been proved to pro-

Table 7.33: $W^{+}+$ c-jet cross section times $W \to \ell\nu$ branching ratio as function of the $|\eta^{\ell}|$ of the lepton from the W decay in the 1+2-jet sample. The $|\eta^{\ell}|$ bins are defined in Table 7.13.

$\lvert\eta^{\ell}\rvert$ bin	1	2	3	4	5	6	7	8	9	10	11
Cross section [pb]	3.80	3.56	3.54	3.40	3.13	4.31	1.93	2.33	1.86	1.67	2.04
Stat. error [pb]	0.26	0.24	0.23	0.25	0.25	0.28	0.26	0.23	0.22	0.22	0.29
Syst. error [pb]	0.41	0.22	0.28	0.20	0.27	0.29	0.40	0.30	0.15	0.19	0.25
Total. error [pb]	0.48	0.33	0.36	0.32	0.37	0.40	0.48	0.38	0.27	0.28	0.38

Table 7.34: $W^{-}+$ c-jet cross section times $W \to \ell\nu$ branching ratio as function of the $|\eta^{\ell}|$ of the lepton from the W decay in the 1+2-jet sample. The $|\eta^{\ell}|$ bins are defined in Table 7.13.

$\lvert\eta^{\ell}\rvert$ bin	1	2	3	4	5	6	7	8	9	10	11
Cross section [pb]	3.75	3.82	3.84	3.77	3.82	4.70	1.81	2.45	2.26	1.65	2.38
Stat. error [pb]	0.25	0.22	0.22	0.23	0.24	0.26	0.22	0.21	0.19	0.19	0.23
Syst. error [pb]	0.25	0.28	0.23	0.21	0.21	0.30	0.40	0.19	0.20	0.17	0.28
Total error [pb]	0.35	0.35	0.31	0.31	0.32	0.39	0.46	0.29	0.27	0.26	0.37

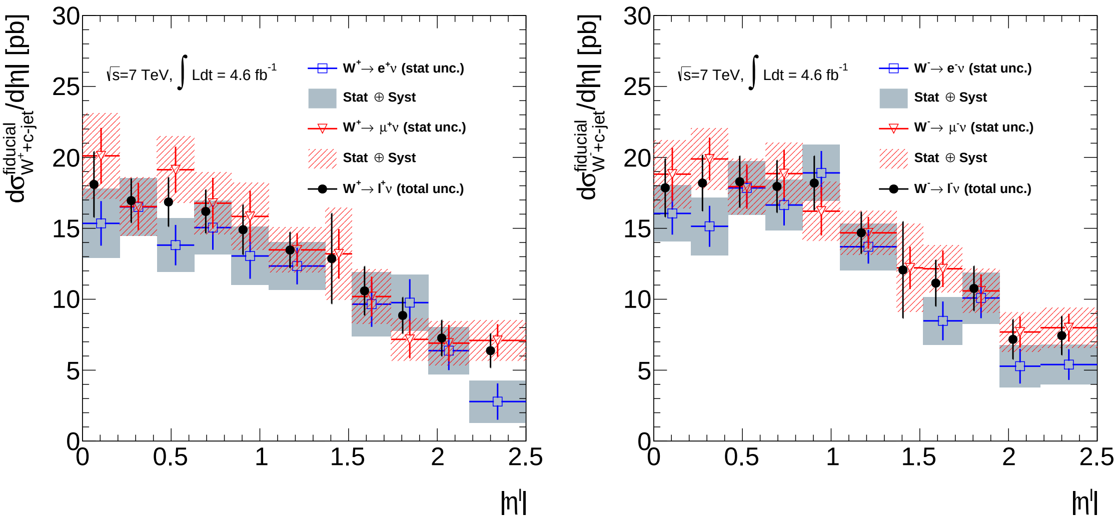

Figure 7.15: Differential cross sections for $W^{+}+$ c-jet (left) and $W^{-}+$ c-jet (right) production with zero and one additional jet as a function of $|\eta^{\ell}|$ of the lepton $\ell = e, \mu$ from the W decay for the electron and muon channels and their combination.

vide a reliable description of the kinematics and jet multiplicities of $W+$ jets events [35]. aMC@NLO is a new NLO Monte Carlo generator which is used for the first time in ATLAS in the context of $W+$ jets analyses for the $W + c$ measurements in this thesis and in [99].

The Alpgen predictions in this section are multiplied by a 1.195 scale factor to correct the Alpgen W inclusive production cross section to the next-to-next-to-leading order

(NNLO) calculation [33].
The comparison is performed for the different PDF sets introduced in Section 7.1. The results are shown in Tables 7.35 and 7.36 for the aMC@NLO and Alpgen predictions, respectively. The uncertainties on the predictions include Monte Carlo statistical errors and the PDF uncertainties. Uncertainties due to renormalisation and factorization scales, expected to be at 5% level (see [100]) are not taken into account. Figure 7.16 shows the comparison of the measured $W+$ c-jet fiducial cross section with the aMC@NLO and Alpgen predictions for events with zero or one additional jet. The measurement agrees best with PDF predictions with small or no suppression of the s quark compared to the $\overline{d}$ sea quark content as `CT10` [106] and `ATLAS_WZ` [34]. The predictions of the two Monte Carlo generators are significantly different. The jet multiplicity of $W+$ c-jet events in the fiducial phase space of the measurements is better described by Alpgen. The ratios of the cross sections of $W+$ c-jet events with one additional jet and with no further jet $\sigma^{fid,2-jet}_{W+\ c\text{-}jet}/\sigma^{fid,1-jet}_{W+\ c\text{-}jet}$ predicted by Alpgen and aMC@NLO are 0.28 ± 0.04 and 0.41 ± 0.07, respectively, with the first in better agreement with the result obtained in data 0.27 ± 0.03.

In order to be able to compare the results with the ones recently published by ATLAS for the associated production of a W and a D meson [99] the experimental results are compared with the aMC@NLO predictions from now on.

The $R^{fid}_{+/-}$ ratio between the $W^{+}+$ c-jet and $W^{-}+$ c-jet fiducial cross sections is sensitive to a possible asymmetry between the PDF of s and $\overline{s}$ quarks. It is expected to be smaller than 1 even in absence of such asymmetry due to the contribution of Feynman diagrams with a d or $\overline{d}$ quark in the initial state to the $W+$ c-jet production (see Figure 7.1). d quarks are in the valence component of the proton, resulting in a higher contribution with respect to $\overline{d}$ quarks. The measured value of $R^{fid}_{+/-}$ is compared with the aMC@NLO predictions in Table 7.37 and in Figure 7.17. All the PDF sets used for the comparison take into account small or no $s/\overline{s}$ asymmetry (see Section 7.1) and their predictions are in agreement with the result in data within uncertainties.

In Figure 7.18 the fiducial cross section measured as a function of $|\eta^{\ell}|$ of the lepton from the W decay for $W^{+}+$ c-jet and $W^{-}+$ c-jet productions is compared with the predictions for the 1+2-jet category. The cross section shape appears well described by all PDF set apart from `NNPDF 2.3`$_{\text{coll}}$ which predicts a distribution flatter than measured in experimental data.

The results shown in this thesis are therefore in favour of small or no s quark suppression in the proton sea with respect to the contributions of lighter quarks, with uncertainties too high to rule out PDF models taking into account higher strange suppression. This is in agreement with the results obtained by ATLAS for the inclusive W and Z productions [34] and with the preliminary ATLAS results for the associated production of a W boson and a D meson [99], both best consistent with no strange suppression. The preliminary results published by CMS [100] for the W+ c-jet cross section are best in agreement with the `CT10` set description, i.e. with small suppression. These results cannot be directly compared with the ones presented in this thesis due to the different fiducial phase space of the ATLAS and CMS measurements. The W^++ c-jet/W^-+ c-jet ratio measurements presented in this thesis and in [99, 100] are limited by high statistical uncertainties and are therefore not sensitive enough to prove or disprove a small asymmetry between the s and $\overline{s}$ quark PDFs.

The new results of this thesis and of [99, 100] provide new and more precise experimental constraints for the s quark PDF determination.

Table 7.35: Comparison of the measured $\sigma^{fid}_{W+\ c\text{-}jet} \times BR(W \to \ell\nu)$ fiducial cross section with the aMC@NLO predictions for different PDF sets

	1-jet [pb]	2-jet [pb]	1+2-jet [pb]
Measured	51.2±3.0	13.6±1.5	64.6±3.9
`CT10` [106]	40.4±4.8	16.4±1.9	56.8±6.6
`MSTW 2008` [103]	38.4±0.7	15.6±0.3	54.0±1.0
`NNPDF 2.3` [102]	36.9±1.3	15.1±0.5	51.9±1.8
`HERAPDF 1.5` [104, 105]	39.4±4.5	15.9±1.7	55.2±6.2
`ATLAS_WZ` [34]	44.7±3.8	18.0±1.4	62.7±5.2
`NNPDF 2.3`$_{\text{coll}}$ [102]	49.4±5.3	19.7±2.0	69.1±7.3

Table 7.36: Comparison of the measured $\sigma^{fid}_{W+\ c\text{-}jet} \times BR(W \to \ell\nu)$ fiducial cross section with the Alpgen predictions for different PDF sets

	1-jet [pb]	2-jet [pb]	1+2-jet [pb]
Measured	51.2±3.0	13.6±1.5	64.6±3.9
`CT10` [106]	48.4±5.6	13.7±1.4	62.1±7.0
`MSTW 2008` [103]	46.0±0.8	13.4±0.2	59.3±1.0
`NNPDF 2.3` [102]	43.9±1.6	12.8±0.5	56.7±2.1
`HERAPDF 1.5` [104, 105]	46.7±5.3	13.6±1.5	60.3±6.7
`ATLAS_WZ` [34]	53.4±4.5	15.0±1.2	68.4±5.6
`NNPDF 2.3`$_{\text{coll}}$ [102]	59.5±7.1	17.7±2.4	77.2±9.4

Table 7.37: Comparison of the measured ratio of the $W^{+}+$ c-jet and $W^{-}+$ c-jet fiducial cross sections with the aMC@NLO predictions for different PDF sets

	1-jet	2-jet	1+2-jet
Measured	0.92±0.04	0.87±0.08	0.91±0.03
`CT10` [106]	0.92±0.01	0.90±0.02	0.92±0.01
`MSTW 2008` [103]	0.89±0.03	0.87±0.03	0.89±0.03
`NNPDF 2.3` [102]	0.90±0.02	0.88±0.02	0.89±0.02
`HERAPDF 1.5` [104, 105]	0.92±0.01	0.90±0.02	0.91±0.01
`ATLAS_WZ` [34]	0.93±0.01	0.91±0.02	0.92±0.01
`NNPDF 2.3`$_{\mathrm{coll}}$ [102]	0.93±0.03	0.91±0.03	0.92±0.02

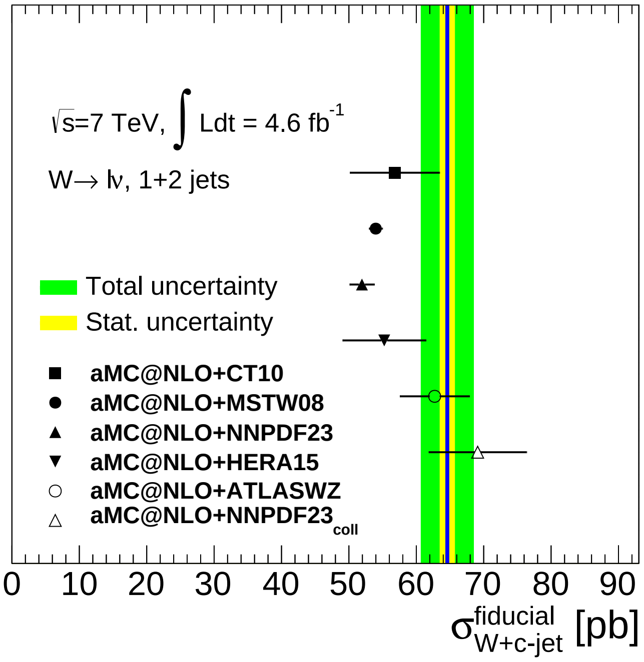

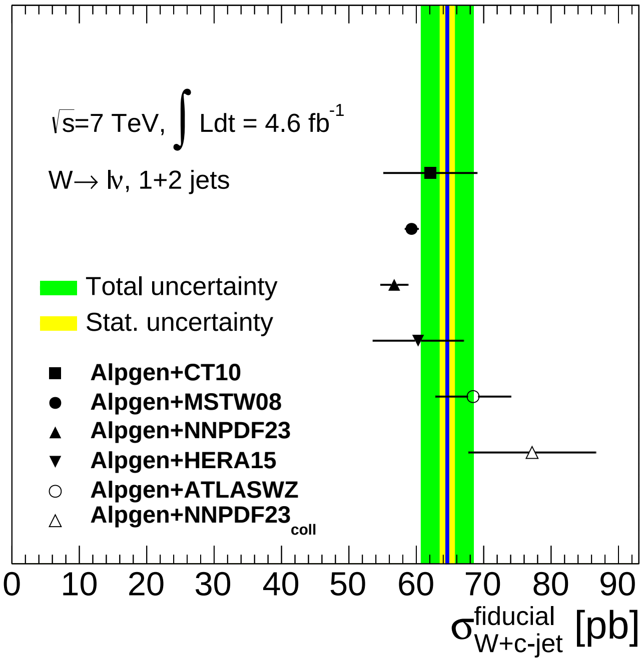

Figure 7.16: Fiducial cross section measurement for $W+$ c-jet production for events with zero and one additional jet compared with aMC@NLO (top) and ALPGEN (bottom) predictions obtained for different PDF sets. The ALPGEN leading order predictions shown in the plots are corrected by a scale factor 1.195 evaluated comparing the ALPGEN W inclusive production cross section with NNLO calculations [33]. The uncertainties on the predictions include the statistical error and the uncertainties in the PDF description.

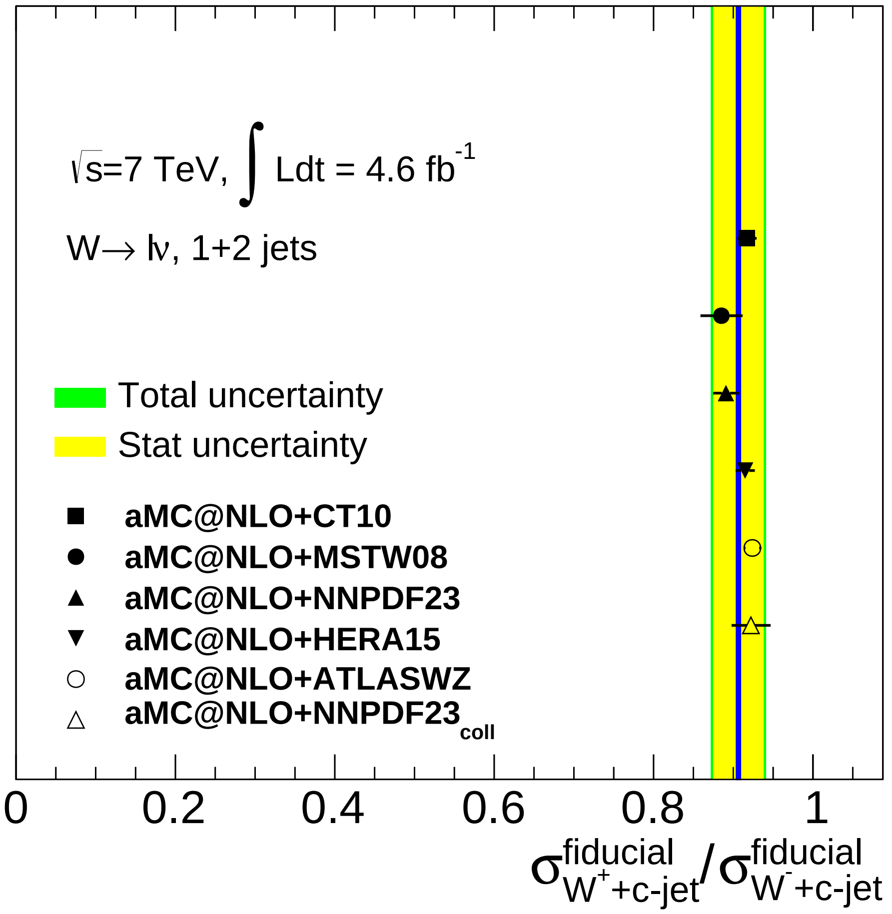

Figure 7.17: Ratio of the fiducial cross section measurements for W^{+}+ c-jet and W^{-}+ c-jet productions for events with zero and one additional jet compared with aMC@NLO predictions obtained for different PDF sets. The uncertainties on the predictions include the statistical error and the uncertainties in the PDF description.

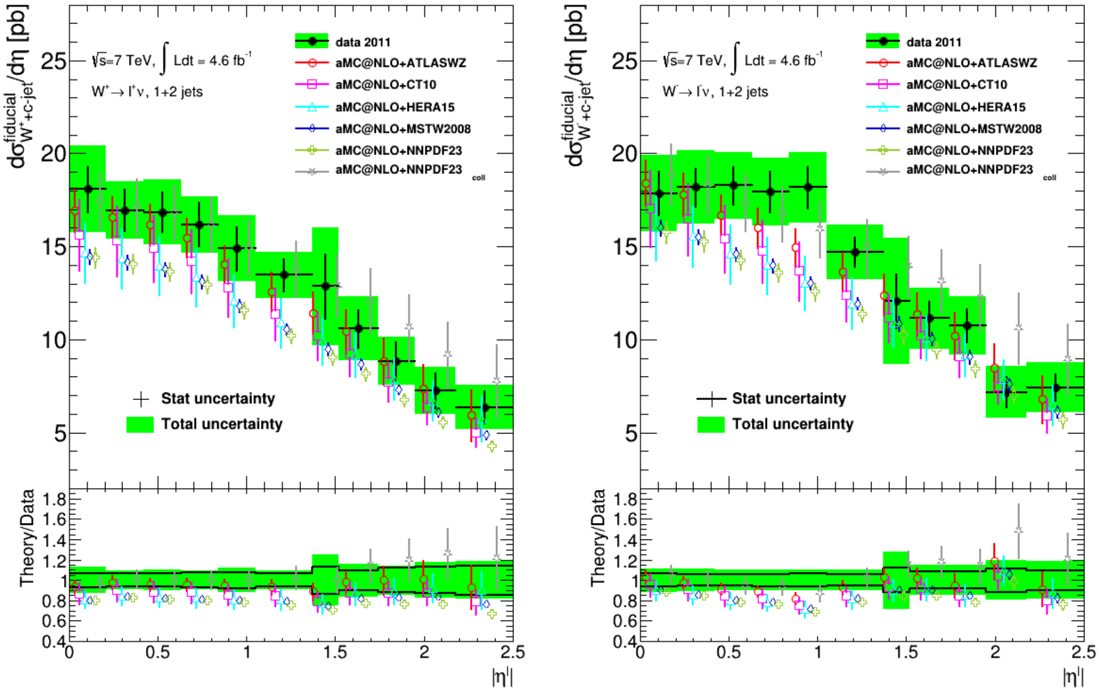

Figure 7.18: $W^{+}+$ c-jet (left) and $W^{-}+$ c-jet (right) fiducial production cross sections for events with zero and one additional jet as a function of $|\eta^{\ell}|$ of the lepton form the W decay compared to aMC@NLO predictions obtained for different PDF sets. The uncertainties on the predictions include the statistical error and the uncertainties in the PDF description.

Conclusions

After three years of operation, the Large Hadron Collider (LHC) was shut down at the beginning of 2013 for an upgrade in order to pursue a new ambitious physics program at increased centre-of-mass energy of $\sqrt{s} = 13$ TeV starting in 2015. During the last three years the ATLAS detector at the LHC recorded more than 25 fb^{-1} of proton-proton collision data at $\sqrt{s} = 7$ and 8 TeV. With these data, the Standard Model predictions for the new energy regime have been confirmed and a new particle with the properties of the Standard Model Higgs boson has been discovered.

In this thesis, the cross sections for W boson production in association with charm and bottom quark jets have been measured in proton-proton collisions at $\sqrt{s} = 7$ TeV with the ATLAS detector. The muon reconstruction efficiency of the ATLAS detector has been determined from data, not only for the above cross section measurements but also for use in all ATLAS analyses involving muons.

The measurement of W boson production in association with b quark jets is an important test of perturbative QCD predictions. The process $pp \to W + b\bar{b} \; + \; X$ is an important background for many physics studies at the LHC such as the search for the Higgs boson in decays $H \to W^+W^-$ and $H \to b\bar{b}$. The analysis presented in this thesis has been performed by a small analysis team with a data set corresponding to an integrated luminosity of 35 pb^{-1} of proton-proton collisions at $\sqrt{s} = 7$ TeV collected by ATLAS in 2010. For the identification of the W bosons, their leptonic decays have been used. b-jets have been identified by requiring a reconstructed b-hadron decay vertex belonging to the jet. Data-driven methods have been used to evaluate the dominant background contributions from $t\bar{t}$, QCD multi-jet, $W+$ c-jets and $W+$ light-quark jets production. The main focus of this work was on the development of the signal selection criteria, the determination of the selection efficiency from data and the evaluation of the cross sections for W production with a b-jet and zero or one additional jet together with their systematic uncertainties. The measurement has been published in [1].

The results in a predefined kinematic fiducial region (see Table 6.4),

$$\sigma^{fid}(pp \to W + b\text{-}jet) \; \times \; BR(W \to \; \ell\nu) = 4.5 \; \pm \; 1.3 \; \pm \; 1.3 \text{ pb}$$

and

$$\sigma^{fid}(pp \to W + b\text{-}jet + jet) \ \times \ BR(W \to \ \ell\nu) = 5.7 \ \pm \ 1.3 \ \pm \ 1.4 \text{ pb} \ ,$$

where $BR(W \to \ \ell\nu)$ is the average leptonic branching ratio of the W boson, are consistent with the next-to-leading order QCD predictions [95] for the fiducial cross sections, 2.9 ± 0.5 pb and $1.9^{+0.8}_{-0.4}$ pb, respectively, in the two jet categories. The latter measurement is 1.8 σ above the expectation. The subsequent measurement with 2011 ATLAS data [96] agrees even better with the predictions.

The $W+$ c-jet cross section measurement presented in this thesis is of particular interest because of the sensitivity of this process to the strange quark content of the proton, which has large uncertainties, especially in the kinematic region of parton interactions at the LHC. For exact flavour symmetry, up, down and strange quarks are expected to give the same contributions to the proton sea quarks. But due to their higher mass and non-perturbative QCD effects, the strange quark content of the proton is suppressed compared to up and down by amounts depending on the analysis of the available data. The $W+$ c-jet measurement has been performed by a very small analysis team with 4.6 fb^{-1} of proton-proton collision data at $\sqrt{\text{s}}$=7 TeV collected by ATLAS in 2011. W bosons have been selected via their leptonic decays into electrons and muons. The associated c-jets have been identified by the semileptonic decays of c-hadrons into muons. The uncertainties of the contributions of QCD multi-jet, $W+$ light-quark jets and $Z+$ jets background events to the $W+$ c-jet sample are minimised by using data driven background determination techniques. A detailed study of the muon reconstruction and c-jet identification efficiencies needed for measurements in this thesis has been performed. In addition, the focus of this work has been on the optimization of the event selection criteria in the two leptonic decay channels, on the determination of signal selection efficiency from data, on the evaluation of the systematic uncertainties and on the evaluation of the cross sections for W boson production in association with a c-jet and zero or one additional jet and their combination.

The combined result

$$\sigma^{fid}(pp \to W + c\text{-}jet + 0 - 1 \ jet) \ \times \ BR(W \to \ \ell\nu) = 64.6 \ \pm \ 1.1 \ \pm \ 3.7 \text{ pb} \ ,$$

in a predefined kinematic fiducial region (see Table 7.14), is compared to the predictions of the Alpgen [47] and aMC@NLO [50] Monte Carlo generators with different sets of parton density functions (PDF). For Alpgen the best agreement is found using the `CT10` PDF set [106], which involves a small suppression of the s quark density, with a predicted cross section of 62.1 ± 7.0 pb. aMC@NLO gives the best prediction of 62.7 ± 5.2 pb for the `ATLAS_WZ` PDF set [34], which contains no s quark suppression. The results favour models of the strange quark content of the proton with small or no suppression compared to up and down sea quarks, but still does not exclude strange quark suppression.

The ratio of the fiducial cross sections for W^++ c-jet and W^-+ c-jet events with a maximum of one additional jet has been measured to be

$$R^{fid}_{+/-} = 0.91 \ \pm \ 0.03 \ \pm \ 0.01$$

in agreement with the aMC@NLO prediction of 0.92 ± 0.01 for `CT10` PDF set and similar for the other PDF sets.

These results, together with other recent measurements by the CMS [98] and ATLAS [99] experiments, are an important input for a more precise determination of the strange quark density function in the proton.

Appendix A

Rejection of non-prompt muons

In Section 5.1.4.1 the quality cuts applied to Inner Detector tracks used for the muon reconstruction in order to reject non-prompt muons coming from pions and kaons decays have been presented. A qualitative test of the effects of these cuts is presented in this appendix. The cuts have been tested in data collected by the ATLAS detector in 2011 selecting a data sample of non-prompt muons using $K_s^0 \to \pi^+\pi^- \to \mu + X$ decays which is compared with prompt muons produced by $J/\Psi \to \mu\mu$ decays. The relevant properties of these particles are listed in Table A.1.

Table A.1: Properties of the $\pi^\pm$, K_s^0, J/Ψ mesons [25]

Particle	Mass [MeV]	$c\tau$ [mm]	Relevant decay	Branching ratio
$\pi^\pm$	139.57018±0.00035	$7.8 \cdot 10^3$	$\mu\nu$	99.9%
K_s^0	497.614±0.024	26.8	$\pi^+\pi^-$	69.2%
J/Ψ	3096.916±0.011	$< 10^{-3}$	$\mu^+\mu^-$	5.9%

Events collected with all ATLAS sub-systems operational are used for the analysis. A primary vertex with at least three associated ID tracks is required to be reconstructed in the event to avoid contamination from cosmic muon events. $J/\Psi \to \mu\mu$ decays are selected requiring two combined muons in the event with an invariant mass $2.9 < m_{\mu\mu} < 3.25$ GeV. The ID tracks associated to the combined muons are used to evaluate the efficiency of the track quality cuts on prompt muons.

$K_s \to \pi^+\pi^- \to \mu + X$ decays are selected choosing pairs of opposite charged ID tracks and reconstructing the decay vertices with a fit. The two tracks associated to the vertex must have an invariant mass of $0.45 < m_{tracks} < 0.55$ GeV. A cut is applied on the transverse decay lent λ of the fitted vertex with respect to the primary vertex reconstructed in the event, requiring $\lambda > 20$ mm. At least one of the two tracks must be matched to a fully reconstructed combined muon.

The efficiency of the track quality cuts of Table 5.3 has been measured to be about 60% and 98% for prompt and non-prompt muons respectively The latter measurement is compatible with the one performed at higher energies on $Z \rightarrow \mu\mu$ events presented in Section 5.1.5.

Appendix B

Muon reconstruction performance in 2012 data

In 2012 more than 20 fb^{-1} of proton-proton collisions at $\sqrt{\mathrm{s}} = 8$ TeV have been recorded by the ATLAS detector. In this section a brief overview of the performance of the ATLAS Inner Detector (ID) and Muon Spectrometer (MS) in 2012 is given. The reconstruction efficiency is measured in 16.9 fb^{-1} of 2012 data with the Tag-and-Probe method presented in Chap. 5, with small changes in the selection due to the different data taking conditions. A signal Powheg+Pythia $Z \to \mu\mu$ Monte Carlo sample only has been used for this measurement: for this reason the muon reconstruction has been determined using calorimeter tagged probes which ensure a background contamination in data below 0.1%.

In Figure B.1 the ID reconstruction efficiency is shown. The efficiency of the quality cuts of Table 5.3 is included in the measurement. The efficiency in data is measured to be about 98.5%, about 0.5% lower than the Monte Carlo prediction. The effects of the single cuts are shown in Fig. B.2: the main source of this small discrepancy is the cut on the number of hits in the B-layer ($\mathrm{N}_{\mathrm{hits}}^{\mathrm{B-layer}} > 0$. This has been found to be due to dead modules which are not taken into account in the simulation.

In Fig. B.3 a comparison of the muon reconstruction efficiency of the Staco and the Muid chain for 2011 and 2012 data is shown for the combined (CB) muons and combined and segment tagged (ST) muons. The only significant difference found is an increase of the reconstruction efficiency for CB muons at $\eta \approx -1.1$ as a consequence of the installation of new tracking chambers in that region that improved the geometrical acceptance of the detector. This gain is particularly relevant for the Staco CB reconstruction due to the tight cuts applied by this algorithm. Small increases can be observed also in the forward regions ($|\eta| > 2$).

A third algorithm chain, (*Muons*), has been introduced for the 2012 data set, combining characteristics and algorithms of the two other chains. In Figure B.4 an overview of the

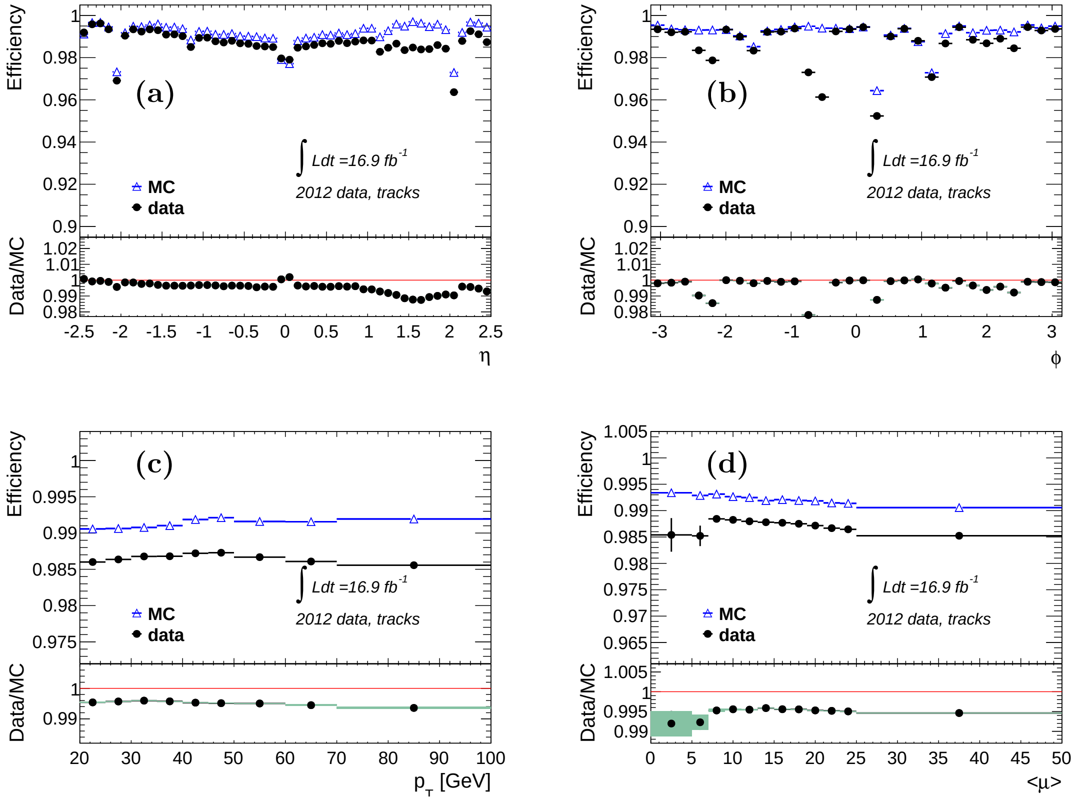

Figure B.1: ID track reconstruction efficiency including the track quality criteria in Table 5.3 measured as a function of η (a), ϕ (b), $\mathrm{p_T}$ (c) and of the average number of collisions per bunch crossing $< \mu >$ (d) for 2012 data and simulations. The bottom part of the plots shows the SF. Only statistical errors are shown.

performance this new chain is given, with a combined reconstruction efficiency in data of about 98% well in agreement with the simulations.

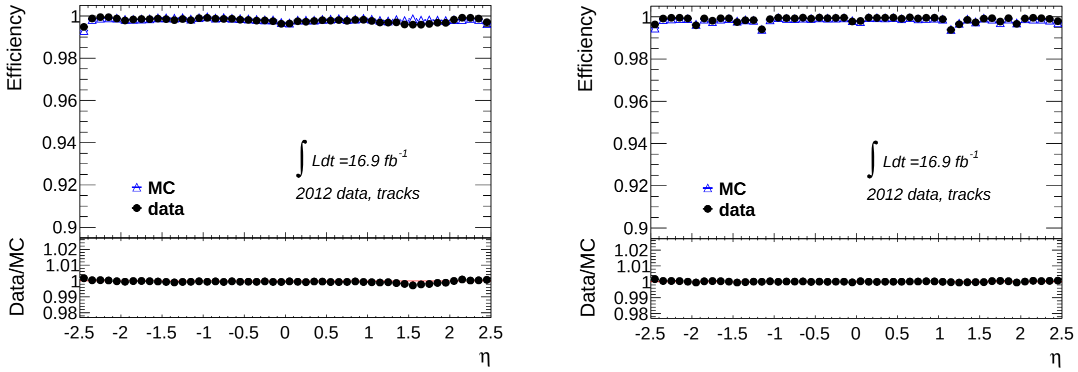

(a) Cut on the number of Pixel Detector hits

(b) Cut on the number of SCT hits

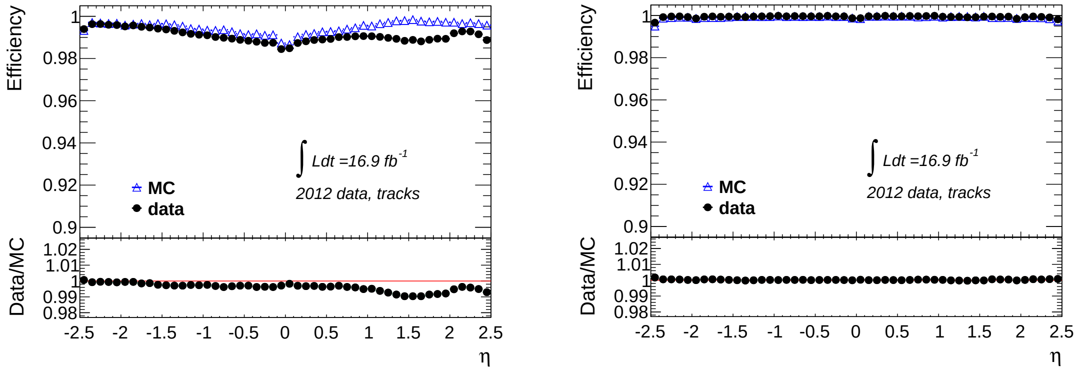

(c) Cut on the number of B-layer hits

(d) Cut on the number of missing hits (holes) in the silicon detectors

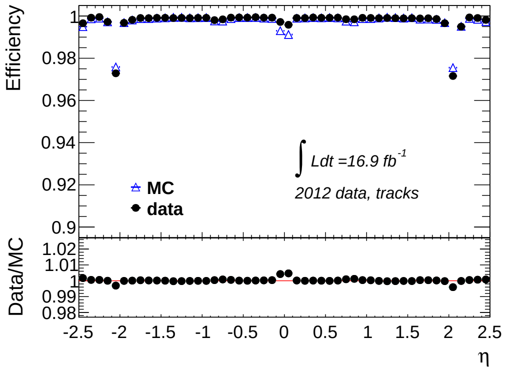

(e) Cut on the number of TRT hits

Figure B.2: ID track reconstruction efficiency measured as a function of η for 2012 data and Monte Carlo simulations after the different quality cuts in Table 5.3. The bottom part of the plots shows the SF. Only statistical errors are shown.

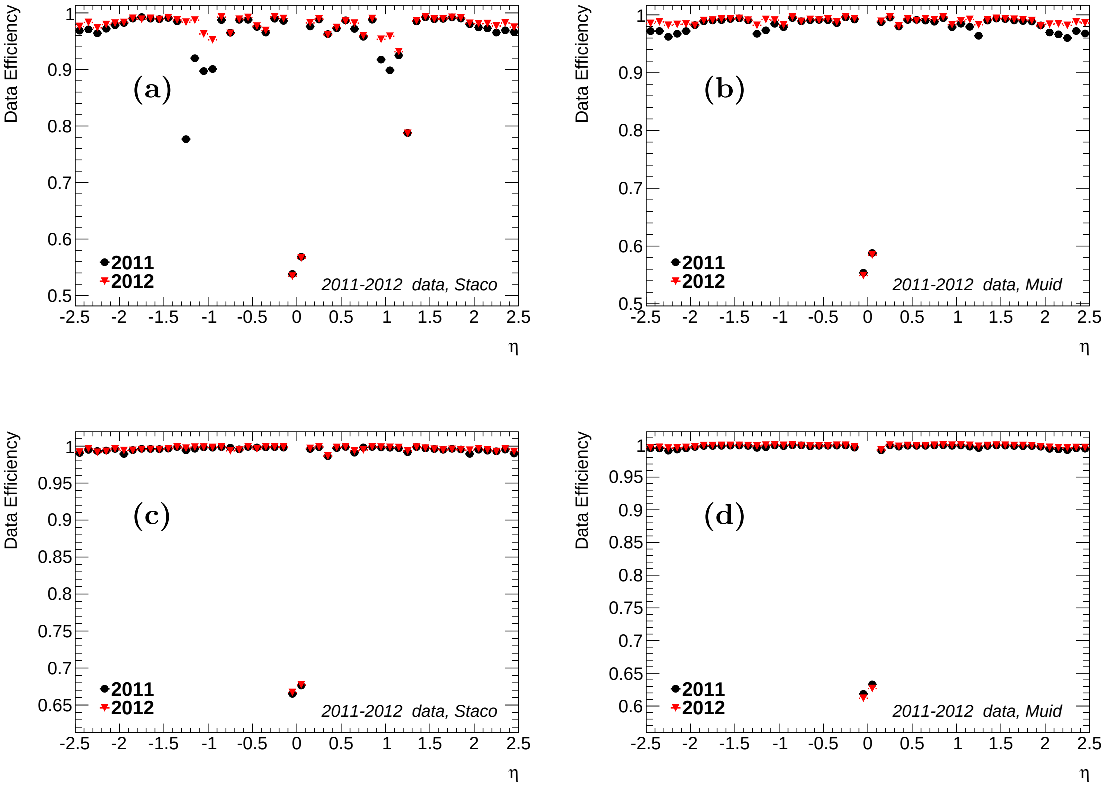

Figure B.3: Comparison of the muon reconstruction efficiency measured in 2011 (black circles) and 2012 (red triangles) data for the Staco (left plots) and Muid (right plots) combined (a, b) and combined and segment tagged (c, d) muons.

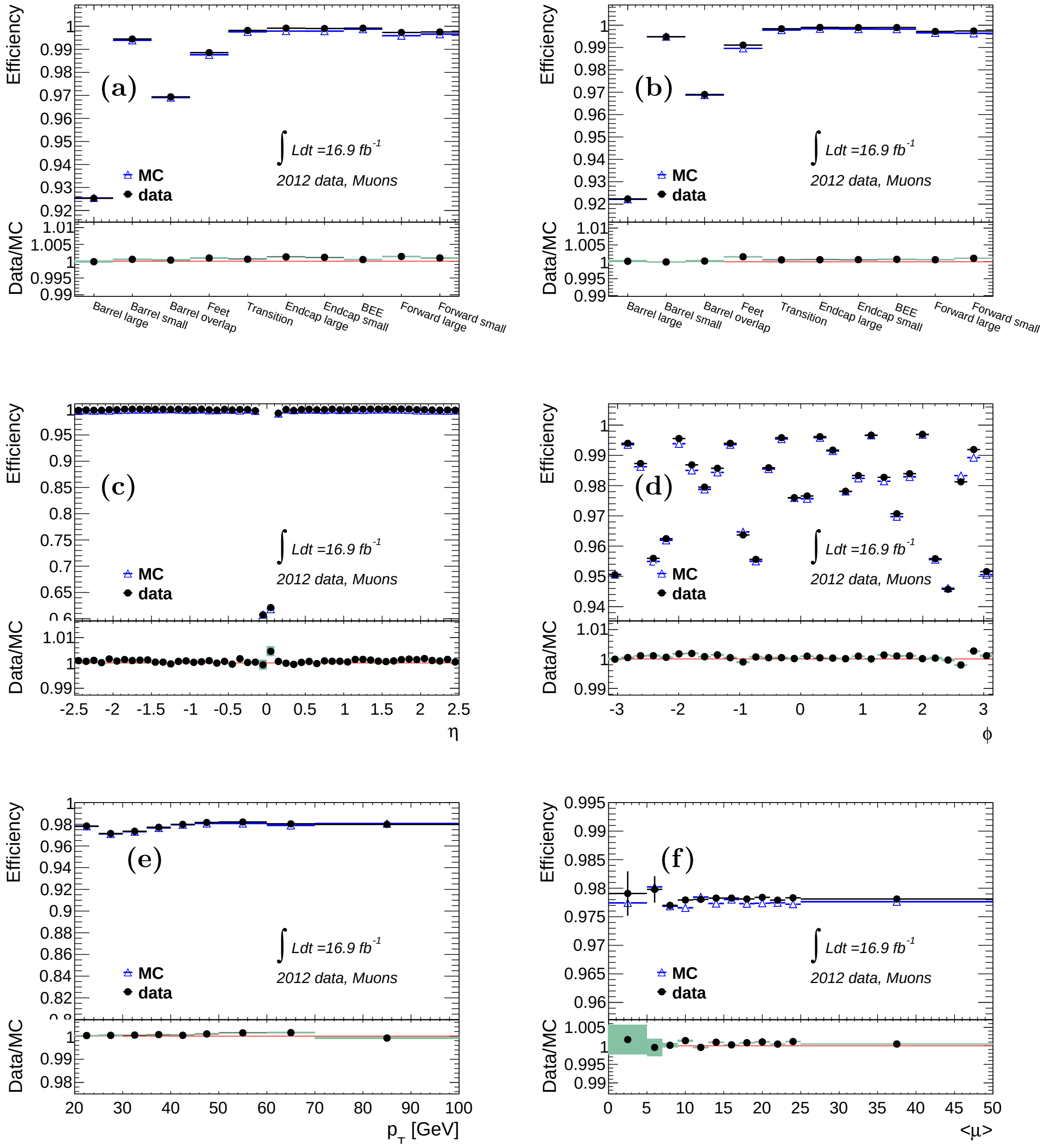

Figure B.4: Combined muon reconstruction efficiency for the Muons chain measured as a function of the MS region in side A (a) and C (b), of η (c), ϕ (d), p_T (e) and of the average number of collisions in a bunch crossing $< \mu >$ (f) for 2012 data and simulation. Only statistical error shown.

Bibliography

[1] ATLAS Collaboration, G. Aad et al., *Measurement of the cross section for the production of a W boson in association with b-jets in pp collisions at* $\sqrt{s} = 7$ *TeV with the ATLAS detector*, Phys. Lett. **B 707** (2012) 418.

[2] ATLAS Collaboration, G. Aad et al., *Measurement of the cross section for the production of a W boson in association with a single c-jet in pp collisions at* $\sqrt{s} = 7$ *TeV with the ATLAS detector*, internal reference, to be submitted to JHEP.

[3] *The International System of Units (SI)*, NIST Special Publication 330 (USGPO, Washington DC), 1991.

[4] *Guide for the Use of the International System of Units (SI)*, NIST Special Publication 811 (USGPO, Washington DC), 1995.

[5] S. Glashow, *Partial Symmetries of Weak Interactions*, Nucl. Phys. **22** (1961) 579.

[6] S. Weinberg, *A Model of Leptons*, Phys. Rev. Lett. **19** (1967) 1264.

[7] A. Salam, *Weak and Electromagnetic Interactions*, originally printed in "Svartholm: Elementary Particle Theory, Proceedings of the Nobel Symposium held 1968 at Lerum, Sweden" Stockholm (1968) 367.

[8] G. 't Hooft and M. Veltman, *Regularization and Renormalization of Gauge Fields*, Nucl. Phys. **B44** (1972) 189.

[9] G. Lüders, *On the Equivalence of Invariance under Time Reversal and under Particle-Antiparticle Conjugation for Relativistic Field Theories*, Kong. Dan. Vid. Sel. Mat. Fys. Med. **28N5** (1954) 5.

[10] W. Pauli, *Exclusion Principle, Lorentz Group and Reflection of Space-Time and Charge. In Niels Bohr and the Development of Physics*, ed. by W. Pauli, Pergamon Press, New York, 1955, p. 30.

[11] J. S. Bell, *Time reversal in field theory*, Proceedings of the Royal Society of London A vol. 231 no. 1187, 1955, p. 479.

[12] R. Jost, *Eine Bemerkung zum CPT-Theorem*, Helv. Phys. Acta **30** (1957) 409.

[13] A. Djouadi, *The anatomy of electro-weak symmetry breaking, I: The Higgs boson in the standard model*, Phys. Rep. **457** (2008) 1.

[14] A. Pich, *The Standard model of electroweak interactions*, arXiv:hep-ph/0705.4264, 2007.

[15] W. Burcham and M. Jobes, *Nuclear and Particle Physics*, Prentice-Hall, 1995.

[16] S. Weinberg, *Mixing Angle in Renormalizable Theories of Weak and Electromagnetic Interactions*, Phys. Rev. D **5** (1972) 1962.

[17] F. Englert and R. Brout, *Broken Symmetry and the Mass of Gauge Vector Mesons*, Phys. Rev. Lett. **13** (1964) 321.

[18] P. W. Higgs, *Broken symmetries, massless particles and gauge fields*, Phys. Lett. **12** (1964) 132.

[19] P. W. Higgs, *Broken Symmetries and the Masses of Gauge Bosons*, Phys. Rev. Lett. **13** (1964) 508.

[20] G. S. Guralnik, C. R. Hagen, and T. W. B. Kibble, *Global Conservation Laws and Massless Particles*, Phys. Rev. Lett. **13** (1964) 585.

[21] P. W. Higgs, *Spontaneous Symmetry Breakdown without Massless Bosons*, Phys. Rev. **145** (1966) 1156.

[22] T. Kibble, *Symmetry breaking in nonAbelian gauge theories*, Phys. Rev. **155** (1967) 1554.

[23] J. Goldstone, *Field Theories with Superconductor Solutions*, Nuovo Cim. **19** (1961) 154.

[24] J. Goldstone, A. Salam, and S. Weinberg, *Broken Symmetries*, Phys. Rev. **127** (1962) 965.

[25] Particle Data Group Collaboration, J. Beringer et al., *Review of Particle Physics (RPP)*, Phys. Rev. **D86** (2012) 010001.

[26] R. Hofstadter and R. McAllister, *Electron scattering from the proton*, Phys. Rev. **98** (1955) 217.

[27] A. Martin, W. Stirling, R. Thorne, and G. Watt, *Parton distributions for the LHC*, Eur. Phys. J. **C63** (2009) 189.

[28] UA1 Collaboration, G. Arnison et al., *Experimental Observation of Lepton Pairs of Invariant Mass Around 95 GeV/*c^2 *at the CERN SPS Collider*, Phys. Lett. **B126** (1983) 398.

[29] UA1 Collaboration, G. Arnison et al., *Experimental Observation of Isolated Large Transverse Energy Electrons with Associated Missing Energy at $\sqrt{s} = 540$ GeV*, Phys. Lett. **B122** (1983) 103.

[30] UA2 Collaboration, M. Banner et al., *Observation of Single Isolated Electrons of High Transverse Momentum in Events with Missing Transverse Energy at the CERN $p\overline{p}$ Collider*, Phys. Lett. **B122** (1983) 476.

[31] UA2 Collaboration, P. Bagnaia et al., *Evidence for $Z^0 \rightarrow e^+e^-$ at the CERN $p\overline{p}$ Collider*, Phys. Lett. **B129** (1983) 130.

[32] G. Altarelli, R. K. Ellis, and G. Martinelli, *Large Perturbative Corrections to the Drell-Yan Process in QCD*, Nucl. Phys. **B157** (1979) 461.

[33] K. Melnikov and F. Petriello, *Electroweak gauge boson production at hadron colliders through $O(\alpha^2(s))$*, Phys. Rev. **D74** (2006) 114017.

[34] ATLAS Collaboration, G. Aad et al., *Determination of the strange quark density of the proton from ATLAS measurements of the $W \rightarrow l\nu$ and $Z \rightarrow ll$ cross sections*, Phys. Rev. Lett. **109** (2012) 012001.

[35] ATLAS Collaboration, G. Aad et al., *Study of jets produced in association with a W boson in pp collisions at $\sqrt{s} = 7$ TeV with the ATLAS detector*, Phys. Rev. **D85** (2012) 092002.

[36] CMS Collaboration, S. Chatrchyan et al., *Jet Production Rates in Association with W and Z Bosons in pp Collisions at $\sqrt{s} = 7$ TeV*, JHEP **1201** (2012) 010.

[37] CMS Collaboration, S. Chatrchyan et al., *Measurement of Rapidity Distributions for a Z Boson or a Photon in Association with a Single Jet in pp Collisions at $\sqrt{s}$= 7 TeV*, CMS-PAS-SMP-12-004, 2012.

[38] CMS Collaboration, S. Chatrchyan et al., *Event shapes and azimuthal correlations in Z + jets events in pp collisions at $\sqrt{s} = 7$ TeV*, Phys. Lett. **B722** (2013) 238.

[39] ATLAS Collaboration, G. Aad et al., *Measurement of the production cross section for Z/gamma* in association with jets in pp collisions at $\sqrt{s} = 7$ TeV with the ATLAS detector*, Phys. Rev. **D85** (2012) 032009.

[40] J. M. Campbell and R. Ellis, *MCFM for the Tevatron and the LHC*, Nucl. Phys. Proc. Suppl. **205-206** (2010) 10.

[41] C. Berger, Z. Bern, L. Dixon, F. Febres Cordero, D. Forde, et al., *An Automated Implementation of On-Shell Methods for One-Loop Amplitudes*, Phys. Rev. **D78** (2008) 036003.

[42] T. Gleisberg, S. Hoeche, F. Krauss, M. Schonherr, S. Schumann, et al., *Event generation with SHERPA 1.1*, JHEP **0902** (2009) 007.

[43] T. Sjostrand, S. Mrenna, and P. Z. Skands, *PYTHIA 6.4 Physics and Manual*, JHEP **0605** (2006) 026.

[44] T. Sjostrand, S. Mrenna, and P. Z. Skands, *A Brief Introduction to PYTHIA 8.1*, Comp. Phys. Comm. **178** (2008) 852.

[45] G. Corcella, I. Knowles, G. Marchesini, S. Moretti, K. Odagiri, et al., *HERWIG 6: An Event generator for hadron emission reactions with interfering gluons (including supersymmetric processes)*, JHEP **0101** (2001) 010.

[46] M. Bahr, S. Gieseke, M. Gigg, D. Grellscheid, K. Hamilton, et al., *Herwig++ Physics and Manual*, Eur. Phys. J. **C58** (2008) 639.

[47] M. L. Mangano, M. Moretti, F. Piccinini, R. Pittau, and A. D. Polosa, *ALPGEN, a generator for hard multiparton processes in hadronic collisions*, JHEP **0307** (2003) 001.

[48] P. Nason, *A New method for combining NLO QCD with shower Monte Carlo algorithms*, JHEP **0411** (2004) 040.

[49] S. Frixione and B. R. Webber, *Matching NLO QCD computations and parton shower simulations*, JHEP **0206** (2002) 029.

[50] R. Frederix, S. Frixione, V. Hirschi, F. Maltoni, R. Pittau, et al., *Scalar and pseudoscalar Higgs production in association with a top-antitop pair*, Phys. Lett. **B701** (2011) 427.

[51] B. P. Kersevan and E. Richter-Was, *The Monte Carlo event generator AcerMC version 2.0 with interfaces to PYTHIA 6.2 and HERWIG 6.5*, arXiv:hep-ph/0405247v2, 2004.

[52] A. Ryd, D. Lange, N. Kuznetsova, S. Versille, M. Rotondo, et al., *EvtGen: A Monte Carlo Generator for B-Physics*, EVTGEN-V00-11-07, 2005.

[53] J. Butterworth, J. R. Forshaw, and M. Seymour, *Multiparton interactions in photoproduction at HERA*, Z.Phys. **C72** (1996) 637.

[54] e. Evans, Lyndon and e. Bryant, Philip, *LHC Machine*, JINST **3** (2008) S08001.

[55] S. Myers, *The LEP collider, from design to approval and commissioning*, CERN-91-08, 1991.

[56] LHC Collaboration, *LHC Performance and Statistics*, `https://lhc-statistics.web.cern.ch/LHC-Statistics/index.php`, 2013.

[57] ATLAS Collaboration, G. Aad et al., *The ATLAS Experiment at the CERN Large Hadron Collider*, JINST **3** (2008) S08003.

[58] CMS Collaboration, S. Chatrchyan et al., *The CMS experiment at the CERN LHC*, JINST **3** (2008) S08004.

[59] LHCb Collaboration, J. Alves, A. Augusto et al., *The LHCb Detector at the LHC*, JINST **3** (2008) S08005.

[60] ALICE Collaboration, K. Aamodt et al., *The ALICE experiment at the CERN LHC*, JINST **3** (2008) S08002.

[61] ATLAS Collaboration, G. Aad et al., *Expected Performance of the ATLAS Experiment - Detector, Trigger and Physics*, arXiv:hep-ex/0901.0512, 2009.

[62] J. Barriere, F. Bauer, M. Fontaine, A. Formica, V. Gautard, et al., *The alignment system of the ATLAS barrel muon spectrometer*, ATL-MUON-PUB-2008-007, 2008.

[63] S. Aefsky, C. Amelung, J. Bensinger, C. Blocker, A. Dushkin, et al., *The optical alignment system of the ATLAS muon spectrometer endcaps*, JINST **3** (2008) P11005.

[64] ATLAS Collaboration, G. Aad et al., *Improved luminosity determination in pp collisions at* $\sqrt{s} = 7$ *TeV using the ATLAS detector at the LHC*, arXiv:hep-ex/1302.4393, 2013.

[65] GEANT4 Collaboration, S. Agostinelli et al., *GEANT4: A Simulation toolkit*, Nucl. Instrum. Meth. **A506** (2003) 250.

[66] ATLAS Collaboration, G. Aad et al., *ATLAS Luminosity public plots*, `https://twiki.cern.ch/twiki/bin/view/AtlasPublic/LuminosityPublicResults`, 2013.

[67] ATLAS Collaboration, T. Cornelissen et al., *Concepts, design and implementation of the ATLAS new tracking*, ATL-SOFT-PUB-2007-007, 2007.

[68] ATLAS Collaboration, G. Aad et al., *ATLAS Inner Detector Tracking Combined Performance group public plots*, `https://twiki.cern.ch/twiki/bin/view/AtlasPublic/InDetTrackingPerformanceApprovedPlots`, 2013.

[69] ATLAS Collaboration, G. Aad et al., *Expected electron performance in the ATLAS experiment*, ATLAS-PHYS-PUB-2011-006, 2011.

[70] ATLAS Collaboration, G. Aad et al., *Expected photon performance in the ATLAS experiment*, ATLAS-PHYS-PUB-2011-007, 2011.

[71] ATLAS Collaboration, G. Aad et al., *Electron performance measurements with the ATLAS detector using the 2010 LHC proton-proton collision data*, Eur. Phys. J. **C72** (2012) 1909.

[72] ATLAS Collaboration, G. Aad et al., *ATLAS Egamma group public plots*, `https://twiki.cern.ch/twiki/bin/view/AtlasPublic/ElectronGammaPublicCollisionResults`, 2013.

[73] ATLAS Collaboration, G. Aad et al., *Jet energy measurement with the ATLAS detector in proton-proton collisions at* $\sqrt{s} = 7$ *TeV*, arXiv:hep-ex/1112.6426v1, 2011.

[74] M. Cacciari, G. P. Salam, and G. Soyez, *The Anti-*k_t *jet clustering algorithm*, JHEP **0804** (2008) 063.

[75] ATLAS Collaboration, G. Aad et al., *Selection of jets produced in proton-proton collisions with the ATLAS detector using 2011 data*, ATLAS-CONF-2012-020, 2012.

[76] ATLAS Collaboration, G. Aad et al., *Probing the measurement of jet energies with the ATLAS detector using Z+jet events from proton-proton collisions at* $\sqrt{s} = 7$ *TeV*, ATLAS-CONF-2012-053, 2012.

[77] ATLAS Collaboration, G. Aad et al., *Performance of the ATLAS Secondary Vertex b-tagging Algorithm in 7 TeV Collision Data*, ATLAS-CONF-2010-042, 2010.

[78] ATLAS Collaboration, G. Aad et al., *Calibrating the b-Tag Efficiency and Mistag Rate in 35* pb^{-1} *of Data with the ATLAS Detector*, ATLAS-CONF-2011-089, 2011.

[79] ATLAS Collaboration, G. Aad et al., *Performance of Missing Transverse Momentum Reconstruction in Proton-Proton Collisions at 7 TeV with ATLAS*, Eur. Phys. J. **C72** (2012) 1844.

[80] ATLAS Collaboration, G. Aad et al., *Performance of Missing Transverse Momentum Reconstruction in ATLAS with 2011 Proton-Proton Collisions at* $\sqrt{s} = 7$ *TeV*, ATLAS-CONF-2012-101, 2012.

[81] T. Lagouri et al., *A Muon Identification and Combined Reconstruction Procedure for the ATLAS Detector at the LHC at CERN*, IEEE Trans. Nucl. Sci. (2004) 3030.

[82] S. Hassani et al., *A muon identification and combined reconstruction procedure for the ATLAS detector at the LHC using the (MUONBOY, STACO, MuTag) reconstruction packages*, Physics Research **A572** (2007) 77.

[83] ATLAS Collaboration, G. Aad et al., *ATLAS Muon Combine Performance group public plots*, `https://twiki.cern.ch/twiki/bin/view/AtlasPublic/MuonPerformancePublicPlots`, 2013.

[84] ATLAS Collaboration, G. Aad et al., *Improved Luminosity Determination in pp Collisions at* $\sqrt{s}$ *= 7 TeV using the ATLAS Detector at the LHC*, ATLAS-CONF-2012-080, 2012.

[85] M. Aliev, H. Lacker, U. Langenfeld, S. Moch, P. Uwer, et al., *HATHOR: HAdronic Top and Heavy quarks crOss section calculatoR*, Comp. Phys. Comm. **182** (2011) 1034.

[86] ATLAS Collaboration, G. Aad et al., *Measurement of the* $W \to \ell\nu$ *production cross-section and observation of* $Z \to \ell\ell$ *production in proton-proton collisions at* $\sqrt{s}$*=7 TeV with the ATLAS detector*, ATLAS-CONF-2010-051, 2010.

[87] G. Aad et al., *A measurement of the muon reconstruction efficiency in 2010 ATLAS data using* J/Ψ *decays*, ATLAS-CONF-2012-125, 2012.

[88] ATLAS Collaboration, G. Aad et al., *Performance of the ATLAS muon trigger in 2011*, ATLAS-CONF-2012-099, 2012.

[89] CDF Collaboration, T. Aaltonen et al., *First Measurement of the b-jet Cross Section in Events with a W Boson in* $p\overline{p}$ *Collisions at* $\sqrt{s}$ *= 1.96 TeV*, Phys. Rev. Lett. **104** (2010) 131801.

[90] M. L. Mangano, M. Moretti, and R. Pittau, *Multijet matrix elements and shower evolution in hadronic collisions:* $Wb\bar{b} + n$ *jets as a case study*, Nucl. Phys. **B632** (2002) 343.

[91] ATLAS Collaboration, G. Aad et al., *Muon reconstruction efficiency in reprocessed 2010 LHC proton-proton collision data recorded with the ATLAS detector*, ATLAS-CONF-2011-063, 2011.

[92] ATLAS Collaboration, G. Aad et al., *Muon Momentum Resolution in First Pass Reconstruction of pp Collision Data Recorded by ATLAS in 2010*, ATLAS-CONF-2011-046, 2011.

[93] ATLAS Collaboration, G. Aad et al., *Measurement of the top quark-pair production cross section with ATLAS in pp collisions at* $\sqrt{s} = 7$ *TeV*, Eur. Phys. J. **C71** (2011) 1577.

[94] ATLAS Collaboration, G. Aad et al., *Updated Luminosity Determination in pp Collisions at* $\sqrt{s}$*=7 TeV using the ATLAS Detector*, ATLAS-CONF-2011-011, 2011.

[95] J. Campbell et al., *NLO QCD predictions for* $W + 1$ *jet and* $W + 2$ *jet production with at least one b jet at the 7 TeV LHC*, Phys. Rev. **D86** (2012) 034021.

[96] ATLAS Collaboration, G. Aad et al., *Measurement of the cross-section for W boson production in association with b-jets in pp collisions at* $\sqrt{s} = 7$ *TeV with the ATLAS detector*, arXiv:hep-ex/1302.2929, 2013.

[97] CDF Collaboration, T. Aaltonen et al., *First measurement of the production of a W boson in association with a single charm quark in* $p\bar{p}$ *collisions at* $\sqrt{s} = 1.96$ *TeV*, Phys. Rev. Lett. **100** (2008) 091803.

[98] CMS Collaboration, S. Chatrchyan et al., *Study of associated charm production in W final states at* $\sqrt{s} = 7$ *TeV*, CMS-PAS-EWK-11-013, 2011.

[99] ATLAS Collaboration, G. Aad et al., *Measurement of the production of a W bosons in association with a charm hadron in pp collisions at* $\sqrt{s} = 7$ *TeV*, ATLAS-CONF-2013-045, 2013.

[100] CMS Collaboration, S. Chatrchyan et al., *Measurement of associated charm production in W final states at* $\sqrt{s} = 7$ *TeV*, CMS-PAS-SMP-12-002, 2013.

[101] J. Pumplin, D. Stump, J. Huston, H. Lai, P. M. Nadolsky, et al., *New generation of parton distributions with uncertainties from global QCD analysis*, JHEP **0207** (2002) 012.

[102] R. D. Ball, V. Bertone, S. Carrazza, C. S. Deans, L. Del Debbio, et al., *Parton distributions with LHC data*, Nucl. Phys. **B867** (2013) 244.

[103] A. Martin, W. Stirling, R. Thorne, and G. Watt, *Parton distributions for the LHC*, Eur. Phys. J. **C63** (2009) 189.

[104] H1 and ZEUS Collaboration Collaboration, F. Aaron et al., *Combined Measurement and QCD Analysis of the Inclusive* $e^{\pm}p$ *Scattering Cross Sections at HERA*, JHEP **1001** (2010) 109.

[105] V. Radescu et al., *Combined Measurement and QCD Analysis of the inclusive* $e^{\pm}p$ *Scattering Cross Sections at HERA*, H1prelim-10-142 and ZEUS-prel-10-018, `https://www.desy.de/h1zeus/combined_results/index.php`, 2010.

[106] H.-L. Lai, M. Guzzi, J. Huston, Z. Li, P. M. Nadolsky, et al., *New parton distributions for collider physics*, Phys. Rev. **D82** (2010) 074024.

[107] M. Whalley, D. Bourilkov, and R. Group, *The Les Houches accord PDFs (LHAPDF) and LHAGLUE*, arXiv:hep-ph/0508110, 2005.

[108] G. T. Garvey and J.-C. Peng, *Flavor asymmetry of light quarks in the nucleon sea*, Prog. Part. Nucl. Phys. **47** (2001) 203.

[109] New Muon Collaboration Collaboration, P. Amaudruz et al., *The Gottfried sum from the ratio* $F_2(n)$ / $F_2(p)$, Phys. Rev. Lett. **66** (1991) 2712.

[110] NuTeV Collaboration, D. Mason et al., *Measurement of the Nucleon Strange-Antistrange Asymmetry at Next-to-Leading Order in QCD from NuTeV Dimuon Data*, Phys. Rev. Lett. **99** (2007) 192001.

[111] NuTeV Collaboration Collaboration, M. Goncharov et al., *Precise measurement of dimuon production cross-sections in muon neutrino Fe and muon anti-neutrino Fe deep inelastic scattering at the Tevatron*, Phys. Rev. **D64** (2001) 112006.

[112] M. Burkardt and B. Warr, *Chiral symmetry and the charge asymmetry of the s anti-s distribution in the proton*, Phys. Rev. **D45** (1992) 958.

[113] F. Olness et al., *Neutrino dimuon production and the strangeness asymmetry of the nucleon*, Eur. Phys. J. **C40** (2005) 145.

[114] S. Alekhin, S. A. Kulagin, and R. Petti, *Determination of Strange Sea Distributions from Neutrino-Nucleon Deep Inelastic Scattering*, Phys. Lett. **B675** (2009) 433.

[115] A. Sherstnev and R. Thorne, *Different PDF approximations useful for LO Monte Carlo generators*, arXiv:hep-ph/0807.2132, 2008.

[116] N. Kidonakis, *Next-to-next-to-leading-order collinear and soft gluon corrections for t-channel single top quark production*, Phys. Rev. **D 83** (2010) 091503.

[117] N. Kidonakis, *Next-to-next-to-leading-logarithm resummation for s-channel single top quark production*, Phys. Rev. **D 81** (2010) 054028.

[118] N. Kidonakis, *Two-loop soft anomalous dimensions for single top quark associated production with a W- or H-*, Phys. Rev. **D82** (2010) 054018.

[119] ATLAS Collaboration, G. Aad et al., *Performance of the ATLAS Electron and Photon Trigger in p-p Collisions at* $\sqrt{s} = 7$ *TeV in 2011*, ATLAS-CONF-2012-048, 2012.

[120] ATLAS Collaboration, G. Aad et al., *Measurement of the b-tag Efficiency in a Sample of Jets containing Muons with* $5\ \mathrm{fb}^{-1}$ *of Data from the ATLAS Detector*, ATLAS-CONF-2012-043, 2012.

[121] E. Lohrmann, *A Summary of Charm Hadron Production Fractions*, arXiv:hep-ex/1112.3757, 2011.

[122] ATLAS Collaboration, G. Aad et al., *Jet energy resolution and selection efficiency relative to track jets from in-situ techniques with the ATLAS Detector Using Proton-Proton Collisions at a Center of Mass Energy* $\sqrt{s} = 7$ *TeV*, ATLAS-CONF-2010-054, 2010.

[123] A. Glazov, *Averaging of DIS cross section data*, AIP Conf. Proc. **792** (2005) 237.

[124] H1 Collaboration, F. Aaron et al., *Measurement of the Inclusive ep Scattering Cross Section at Low* Q^2 *and* x *at HERA*, Eur. Phys. J. **C63** (2009) 625.

[125] H1 and ZEUS Collaboration, F. Aaron et al., *Combined Measurement and QCD Analysis of the Inclusive e+- p Scattering Cross Sections at HERA*, JHEP **1001** (2010) 109.

Acknowledgements

The last three years have been an important experience both from a professional and from a personal point of view. I would like to thank my supervisor Hubert Kroha for giving me the opportunity to work at the Max-Planck-Institut für Physik, in a team composed of very nice people which also happen to be excellent physicists and in one of the nicest cities I know. I would like to thank Oliver Kortner for his invaluable help during these three years and for all the table tennis matches we had after lunch. I'm also thankful to all other members of the group, we shared a lot of physics and beers and I really enjoyed my time with you.

I would like to thank my former supervisor Paolo Bagnaia for introducing me to the ATLAS experiment during my master thesis. I'm also indebted to Georges Aad, for the thousands of mails he replied to, and to Giacomo Snidero, for the time we spent working together.

And now for something completely different.

Le persone che ho conosciuto qui saranno per sempre importanti per me. Voglio dire grazie a Daniele, perché anche se mai na gioia, ci siamo divertiti. Un grazie ad Elena, per esserci sempre stata. Grazie a Francesca, Laura, Verena, Davide B., Davide R., Giorgio, per tutte le avventure che abbiamo condiviso.

Poi ci sono persone che sono importanti anche a 1000 km di distanza, perché ci sono comunque. Marco, Marco, Damiano e Giordano, non è stato facile stare lontano da voi e da tutti quegli amici che ad ogni ritorno a Roma mi accoglievano come se non fossi mai partito. Ed è stato difficilissimo stare cosí lontano da Alessandra.

Dire che ringrazio la mia famiglia è estremamente riduttivo. Vi voglio bene, davvero.